INVESTIGATING INTERNAL EROSION IN GAP-GRADED GRANULAR SOILS UNDER VARIOUS SHEAR LOADING CONDITIONS WITH CFD-DEM

SONG SHUNXIANG

PhD

The Hong Kong Polytechnic University

2026

The Hong Kong Polytechnic University

Department of Civil and Environmental Engineering

Investigating Internal Erosion in Gap-Graded Granular Soils under Various Shear Loading Conditions with CFD-DEM

SONG Shunxiang

A thesis submitted in partial fulfilment of the requirements for the degree of

Doctor of Philosophy

August 2025

CERTIFICATE OF ORIGINALITY

I hereby declare that this thesis represents my independent work, and to the best of my understanding and conviction, it contains no content that has been previously published or written, nor material that has been accepted for the conferment of any other degree or diploma. Any sources or contributions from external works have been duly acknowledged within the text.

Signature:

Name: Song Shunxiang

ABSTRACT

Internal erosion is one of the primary causes of catastrophic failures in geotechnical structures such as embankments, dams, levees, and offshore foundations. Traditional internal erosion studies have typically been conducted under highly simplified loading conditions, which fail to capture the complex hydro-mechanical interactions present in real engineering environments. This thesis addresses this gap by employing a Computational Fluid Dynamics–Discrete Element Method (CFD–DEM) framework to systematically investigate internal erosion in gap-graded granular soils under various shear loading conditions, including hollow cylinder torsional shear, biaxial shear, direct shear, and ring shear conditions. These loading conditions are strategically chosen to represent key engineering scenarios, ranging from seismic-induced stress rotation to long-term stability of tailings dams.

The thesis focuses on how the initial stress state and loading mode influence internal erosion and how the loss of fine particles due to erosion changes the mechanical behaviors of the post-eroded specimens during subsequent shearing. The results reveal that fines mass loss intensifies as the mobilized shear stress approaches the peak strength. This behavior is driven by the progressive development of fabric anisotropy and the formation of interconnected void channels, which enhance hydraulic conductivity and trigger localized instability. Erosion patterns vary across loading conditions. In erosion simulations under biaxial shear conditions, erosion increases monotonically with shear stress. In contrast, under direct and ring shear conditions, erosion is limited during the initial shearing stage due to the reorientation of force chains perpendicular to the seepage direction, which reduces the pore connectivity along the seepage direction and promotes clogging.

Post-eroded specimens exhibit reduced peak strengths, particularly those subjected to high stress states during erosion and those with high fines contents. This reduction is linked to the erosion-induced microstructural damage and the inability to form strong force chains. The residual shear behavior of the post-eroded specimen is most effectively examined under ring shear conditions. Results show that internal erosion leads to a reduction in the residual shear stress, reflecting a permanent loss of interlocking capacity of the post-eroded specimen. More importantly, post-eroded specimens exhibit greater fluctuation amplitudes and reduced fluctuation frequency in the residual shear stress compared to their non-eroded counterparts. This indicates that the deformation mechanism shifts from frequent, small-scale particle readjustments to

less frequent but large intermittent slips, which are often associated with localized collapses of coarse-dominated force chains. The formation and development of shear bands are significantly influenced by internal erosion. In direct shear tests, where a 'predefined' shear plane exists, erosion leads to a transition of the shear bands from narrow and localized bands to wider and more diffuse zones, especially in the fine-dominated specimens. This happens because the removal of fines disrupts the original force transmission paths, requiring larger deformation to re-establish stable force chains. In contrast, coarse-dominated specimens, particularly those eroded under low stress states, maintain relatively well-defined shear bands, as the coarse skeleton remains largely intact during the whole erosion stage.

Comparative simulations across different shear loading conditions reveal that both mechanical response and erosion susceptibility are strongly influenced by the shear mode. In biaxial shear specimens, stable and continuous force chains among coarse particles result in the highest peak strengths and the lowest fines mass loss. In direct shear specimens, deformation is confined within a narrow band, producing intermediate strength and erosion resistance. Ring shear specimens, in contrast, involve low confinement together with sustained large displacements, leading to frequent disruption of force chains and the greatest cumulative fines mass loss.

The coupled erosion simulations under hollow cylinder torsional shear conditions can capture the combined effects of principal stress rotation (α) and intermediate principal stress ratio (b). Higher α and b promote anisotropic force chains and reduce vertical pore connectivity of the specimen, further leading to localized clogging. Additionally, key influencing factors on internal erosion such as fines content, hydraulic gradient, and confining pressure are systematically evaluated as part of the erosion simulations conducted under various shear loading conditions. High hydraulic gradients cause rapid fine detachment and early clogging, while low gradients result in gradual erosion. In fine-dominated specimens, this slow process may trigger localized instabilities and rearrangements, increasing the risk of sudden fines loss in later stages. Confining pressure consistently suppresses erosion by enhancing interparticle locking and contact force density, thereby maintaining the granular structure integrity under seepage forces.

PUBLICATIONS ARISING FROM THE THESIS

Journal papers:

Song, S. X., Wang, P., Yin, Z. Y., & Cheng, Y. P. 2024. Micromechanical Modeling of Hollow Cylinder Torsional Shear Test on Sand with DEM. *Journal of Rock Mechanics and Geotechnical Engineering*. 16(12): 5193-5208. https://doi.org/10.1016/j.jrmge.2024.02.010.

Song, S. X., Yin, Z. Y., Liu Y. J., Wang, P., & Cheng, Y. P. 2024. Investigation of Suffusion under Torsional Shear Conditions With CFD-DEM. *Journal of Rock Mechanics and Geotechnical Engineering*. 48(17): 4274-4290. https://doi.org/10.1002/nag.3844.

Song, S. X., Yin, Z. Y., Liu Y. J., Wang, P., & Cheng, Y. P. A Coupled CFD–DEM Investigation on the Internal Erosion and Mechanical Behaviors of Gap-Graded Granular Soils under Biaxial Shear Conditions. *Under review*.

Song, S. X., Yin, Z. Y., Liu Y. J., Wang, P., & Cheng, Y. P. Micro-Macro Investigation of Internal Erosion and Shear Instability in Gap-Graded Granular Soils under Direct Shear Conditions: A Coupled CFD–DEM Study. *To be submitted*.

Song, S. X., Yin, Z. Y., Liu Y. J., & Cheng, Y. P. CFD–DEM Analysis of Internal Erosion in Gap-Graded Soils under Ring Shear Conditions: The Role of Stress State in Erodibility and the Effect of Erosion on Residual Stability. *To be submitted*.

Song, S. X., Yin, Z. Y., Liu Y. J., & Cheng, Y. P. Comparative Study of Internal Erosion and Mechanical Response in Gap-Graded Granular Soils under Different Shear Loading Conditions. *To be submitted*.

ACKNOWLEDGEMENTS

Looking back, it's hard to believe that my PhD journey is finally coming to an end. I still remember the excitement and nervousness I felt when I began my doctoral studies during the pandemic. It was a time of global uncertainty and disrupted routines, and starting campus life under such conditions was nothing like I had expected. Starting a research degree under such unusual circumstances was not easy, but it taught me resilience, patience, and the importance of staying focused even in the face of challenges. Though the journey was often tough, every late night in the office room, every unexpected result, and every small breakthrough along the way made it feel worth it. I am deeply grateful for the support I received throughout these years, which helped me grow both as a researcher and as a person.

I would like to express my deepest gratitude to my supervisor, Prof. Zhen-yu Yin, for his unwavering support, expert guidance, and intellectual inspiration throughout my PhD studies. Over the years at PolyU, he has been far more than a supervisor. He has served as a mentor and role model, shaping not only my academic development but also my approach to research and problem solving. Under his supervision, I received rigorous training in geotechnical engineering and gained valuable skills in critical thinking, coding, and scientific communication. Whenever I faced difficulties in my research, he was always approachable and ready to offer timely advice, technical insights, and constructive feedback. His dedication, professionalism, and genuine care for his students have profoundly influenced my academic development and left a lasting impact on my academic growth.

I wish to express my heartfelt gratitude to Professor Pei Wang from East China Jiaotong University, Prof. Yi-Pik Cheng from University College London, and Dr. Ya-Jing Liu from Zhejiang University of Technology, for their invaluable guidance and insightful suggestions throughout my doctoral research. They generously shared their expertise, provided detailed feedback on my manuscripts, and helped refine my research ideas with great patience. Whenever I encountered challenges, big or small, they were always willing to offer timely and thoughtful support. Their encouragement and academic mentorship have been instrumental in advancing my research and sustaining my progress throughout this journey.

I am deeply grateful to all my group members for their care, support, and encouragement throughout my research journey. I am especially thankful to Prof. Yin-Fu Jin, Prof. Jie Yang, Dr. Hao Xiong, Dr. Ning Zhang, Dr. Kai-Qi Li, Dr. Tuo Wang, Dr. Qi Zhang, Dr. Shao-Heng He, Dr. Pin Zhang, Dr. Ze-Yu Wang, Dr. Wang-Qi Xu, Dr. Jing-Cheng Teng, Dr. Chang He, Dr. Peng-Lin Li, Dr. Kai Lou, Dr. Yu Pan, Dr. Lu-Jia Yu, Dr. Yang Cheng, Dr. Qi-Wei Liu, Mr. Rong Yi, Mr. Qian-Yi Zhang, and many other colleagues who have offered me invaluable guidance, insightful discussions, and constant assistance during my academic journey. Your expertise, generosity, and friendship have greatly enriched my research experience. Outside of research, I deeply cherish the wonderful moments we spent together beyond the lab. Playing basketball in our free time and discovering the rich and vibrant food culture of Hong Kong brought joy and balance to my daily life and have become some of the most memorable and treasured experiences of my academic journey.

I would like to extend my heartfelt gratitude to my parents for their unwavering love and support, as well as to my entire family for their constant care and encouragement. Although the pandemic kept us apart for long periods, their silent understanding and unwavering faith in me have sustained me with strength and resilience throughout this journey. I am deeply grateful for their sacrifices and the emotional foundation they have provided. At the same time, I wish to thank my girlfriend, Dr. Ming-Xi Li, for her loving companionship. Her presence has brought joy, warmth, and unexpected moments of happiness to what could have otherwise been a routine and demanding academic life. Her support and kindness have made this path not only bearable but truly meaningful.

Finally, I would like to thank the esteemed experts who kindly reviewed this thesis and attended the defence for their insightful comments and valuable feedback.

TABLE OF CONTENTS

LIST OF FIGURES

LIST OF TABLES

CHAPTER 1: INTRODUCTION

1.1 Background

The long-term stability and safety of earth structures such as embankment dams, levees, and flood containment earthworks are critically governed by the interaction between seepage water and the soil mass. Among various modes of hydro-mechanical failure, internal erosion has been widely recognized as one of the most dangerous mechanisms. Unlike surface erosion, internal erosion takes place beneath the ground surface, making it difficult to detect in its early stages. However, its consequences can be catastrophic, leading to the progressive loss of soil mass, reduction in shear strength, and ultimately, structural instability or failure of geotechnical systems (Foster and Fell 2001).

Internal erosion is responsible for a significant proportion of dam and levee failures worldwide. According to the International Commission on Large Dams (ICOLD), internal erosion accounts for approximately half of all earth dam failures, with a similar proportion observed in levee failures (Bridle 2017). Foster et al. (2000) summarized historical data showing that roughly 47% of embankment dam failures are attributable to internal erosion. ICOLD Bulletin No. 99 further points out that 44% of dam failures internationally result from internal erosion (Brown and Gosden 2008).

The catastrophic potential of internal erosion is illustrated by several historical cases. One of the most notable examples is the failure of the Teton Dam in Idaho, USA, in 1976. During its first reservoir filling, internal erosion occurred along weak zones in the loess core and fractured foundation rock, ultimately causing the complete failure of the dam, as shown in Fig 1.1. The disaster led to significant loss of life and extensive damage to property. The U.S. Bureau of Reclamation (USBR) identified that inadequate erosion protection of the impervious core was a key contributing factor (USBR 1976). Other notable cases include Fontenelle Dam near failure in 1965 (Fig 1.2), the failure of the Tunbridge Dam in 2008 (Fig 1.3) and so on (Babu and Srivastava 2014; Yousefpour and Mojtahedi 2024).

Despite growing awareness, the fundamental mechanisms of internal erosion, especially under complex loading conditions, remain poorly understood. Most existing studies have mainly focused on the effects of hydraulic gradients, fines contents (FC), particle size distributions (PSD), and static confining pressures (Ma et al. 2019; Wang et al. 2024a; Xiong et al. 2020). However, these investigations often overlook the influence of shear loading conditions, which is commonly present in real-world geotechnical engineering. In practice, soils are rarely subjected to pure seepage. Instead, they experience combined hydraulic and complex mechanical loading, such as torsional shear in pile foundations, biaxial stresses in earth slopes, direct shear in fault zones, or ring shear in rotational landslides. These different loading conditions may significantly change the arrangement of particles, contact fabric, and erosion pathways, thereby influencing both the initiation and evolution of internal erosion (Song et al. 2024b). In addition, soils subjected to internal erosion may be at different stress states. In some cases, soils may be near their peak shear strength, whereas in others, they may have only undergone initial stages of shearing. These different stress histories will affect the soil's fabric anisotropy and pore structure. This change in structural stability directly affects the threshold for particle detachment and migration. Consequently, the initiation and progression of internal erosion are governed not only by hydraulic forces but also by the soil's mechanical states.

Furthermore, after erosion, the degraded soil structure is often subjected to subsequent mechanical loading, such as shearing under long-term operational stresses or seismic events. The changes caused by erosion in the mechanical behavior, including the peak strength, residual strength, strain localization and compressibility, are still not well understood, particularly under different loading paths. Fortunately, research in this area is receiving growing attention (Hu et al. 2022; Qian et al. 2021).

Some experimental investigations of the coupling between gap-graded granular soils and seepage flow have been conducted (Chang and Zhang 2013). However, these laboratory setups often cannot achieve the simulation of the complex loading conditions. It is also hard for these apparatuses to simultaneously apply constant controlled shear loads and measure localized erosion accurately. Furthermore, capturing micro-mechanical processes such as particle migration, force chain evolution, and contact buckling/collapse remains difficult with these conventional experimental techniques (Chang and Zhang 2011).

In recent years, computational modelling has proven to be a powerful tool for investigating these complex processes. The coupled Computational Fluid Dynamics–Discrete Element Method (CFD-DEM) enables the explicit simulation of seepage flow and granular mechanics. This method enables the capture of the complex interactions between fluid and individual soil particles. Therefore, the mechanisms of internal erosion can be investigated from the microscopic perspective. As mentioned previously, despite the advantages of the coupled CFD-DEM approach, most existing research on internal erosion has mainly concentrated on the effects of fluid-related parameters such as flow direction and hydraulic gradient, or on factors like particle shape and static confining pressure (Guo et al. 2018; Kim et al. 2019; Liu et al. 2021; Liu et al. 2022; Liu et al. 2020; Wang et al. 2023; Wang et al. 2024b; Xiong et al. 2020; Xiong et al. 2021). However, most of these studies are based on simplified boundary conditions, such as constant confining pressure or unidirectional seepage, and neglect the complex shear paths commonly encountered in real engineering scenarios, and existing models rarely maintain a constant stress state during erosion. In reality, DEM allows flexible control of boundary conditions and realistic modeling of particle interactions, enabling the simulation of soil behavior under various shear loading conditions such as torsional shear, biaxial shear, direct shear, and ring shear along specific stress paths (Farhang and Mirghasemi 2017; Mohajeri et al. 2020; Nitka and Grabowski 2021; Wang et al. 2022b). Moreover, research on the post-eroded response remains limited and has focused mainly on strength reduction, with little attention paid to the changes in the failure patterns (e.g., shear banding) of post-eroded specimens and the altered role of fines. These limitations hinder the ability of current numerical simulations to realistically capture the degradation mechanisms of soils under coupled hydro-mechanical conditions.

1.2 Scope and objectives of the research

This thesis aims to bridge the gap between traditional studies on internal erosion, which are usually conducted under simple boundary conditions, and the complex hydro-mechanical environments found in real geotechnical structures. This research uses the coupled CFD–DEM approach to investigate internal erosion in gap-graded granular soils under several shear loading conditions, including hollow cylinder torsional shear, biaxial shear, direct shear, and ring shear. The study examines how the soil's stress states and the applied loading conditions influence progression of internal erosion. This study also investigates how particle loss caused by erosion affects the soil's mechanical behavior during the subsequent shearing after erosion, including peak strength, residual strength, and shear banding.

Each shear test is chosen to represent specific real engineering situations and to provide complementary insights. Hollow cylinder torsional shear test (HCTST) allows for the independent control of the rotation of major principal stress axis (α) and intermediate principal stress ratio (b), which is useful for offshore foundations, tunnels, or seismic areas where stress directions change. Biaxial shear creates plane-strain conditions and helps to study natural shear band formation and its interaction with seepage flow, which is relevant for earth dams and levees during drawdown or flood events. Direct shear focuses on predefined shear planes, making it suitable to study erosion along existing slip surfaces, such as in reactivated landslides or embankments where water flow weakens fine-rich zones. Ring shear allows continuous large-displacement shearing, which is important for evaluating long-term stability in tailings dams, landfills, and long-runout landslides where fines migration reduces residual strength.

In addition to the loading conditions and the stress states during erosion, this research also studies the effects of key influencing factors like hydraulic gradient, fines content, and confining pressure on internal erosion. Then, the post-eroded specimens are re-sheared to study how their structure has changed. This includes the changes in peak strength, residual strength, shear band development, load transfer mechanisms, and micro-scale behavior such as contact forces and particle arrangement.

Furthermore, this study goes beyond individual case analyses by conducting a systematic comparison across biaxial, direct, and ring shear conditions. This comparative study isolates the effect of loading mode on key processes, including peak strength, fines mass loss, and the recovery of mechanical performance after erosion. By elucidating how boundary constraints and kinematic conditions influence hydro-mechanical degradation, the research provides deeper insight into the role of testing configuration in erosion assessment.

The results are expected to improve the predictive capability of internal erosion models and provide guidance for the design, monitoring, and risk assessment of geotechnical structures such as dams, levees, offshore foundations, and waste barriers under combined hydraulic and mechanical loads.

To achieve the objectives outlined above, this thesis focuses on the following key aspects:

(a) To present coupled CFD-DEM models that integrates different shear tests (hollow cylinder torsional shear, biaxial shear, direct shear, and ring shear) with seepage flow to systematically investigate the internal erosion in gap-graded soils under various loading conditions.

(b) To perform coupled hydro-mechanical simulations in gap-graded granular soils to explore how stress state, principal stress orientation, and loading history affect internal erosion, including particle migration, permeability changes, and formation of seepage channels.

(c) To examine how material and hydraulic factors, such as confining pressure, hydraulic gradient, and fines content, influence erosion susceptibility and rate, and gain deeper insight into the mechanisms governing internal erosion.

(d) To assess the mechanical behavior of post-eroded gap-graded granular soils by re-shearing the specimens, focusing on strength loss, shear band development, and changes in load transfer, especially the role of fine particles in maintaining force chains.

(e) To conduct a comparative analysis of internal erosion and mechanical response across different shear loading conditions, thereby elucidating the influence of boundary constraints and deformation modes on erosion progression and mechanical stability.

1.3 Thesis layout

This thesis investigates internal erosion in gap-graded soils under various loading conditions and its influence on the subsequent shear behavior of post-eroded specimens. Before presenting the main content, the research background is first introduced, relevant literature is reviewed, and the numerical simulation method employed in this study are then described. Aiming at the study on internal erosion under various loading modes and the effect of internal erosion on the post-eroded behavior, the hollow cylinder shear condition, biaxial shear condition, direct shear condition and ring shear condition are introduced individually to simulate a wide range of practical engineering situations as closely as possible. Other influencing factors such as stress state, hydraulic gradient, fines content, and confining pressure are also considered in these coupled CFD-DEM simulations. The main structure of the thesis is outlined as follows:

Chapter 1 presents a brief introduction to the background of the research, highlighting the significance of internal erosion in gap-graded granular soils and the need for the coupled CFD–DEM method to study internal erosion under various shear loading conditions and its influence on the post-eroded behavior of soil.

Chapter 2 reviews key studies on internal erosion, relevant influencing factors, typical shear loading conditions, the effect of erosion on soil’s mechanical behaviors, the coupled CFD-DEM approach and so on.

Chapter 3 focuses on internal erosion in the proposed CFD–DEM HCTST model, aiming to investigate the combined effect of principal stress rotation and the intermediate principal stress ratio on internal erosion, as well as the underlying mechanisms of particle migration under seepage flow.

Chapter 4 presents numerical simulations investigating internal erosion under biaxial shear conditions, with a specific focus on the effects of stress state and confining pressure. The influence of internal erosion on the strength degradation and failure mode of gap-graded granular soil specimens is also analysed from both macro- and micro-scale perspectives.

Chapter 5 is dedicated to the coupled CFD-DEM internal erosion simulations in both fine-dominated and coarse-dominated gap-graded granular soils under direct shear conditions. The impact of stress state and hydraulic gradient on the development of erosion are examined, with particular emphasis on their effects on the formation and development of shear band after erosion.

Chapter 6 focuses on internal erosion simulations by the coupled ring shear conditions, considering the effects of stress state and confining pressure. Particular attention is given to the influence of erosion on the specimen’s sustained large-displacement shearing behavior.

Chapter 7 conducts a comparative study of internal erosion and post-eroded mechanical response across biaxial, direct, and ring shear conditions. This chapter isolates the influence of boundary constraints and deformation mechanisms on peak strength, erosion susceptibility, and structural recovery, providing deep insight into the role of testing configuration in erosion assessment.

Chapter 8 summarizes the principal findings obtained in this research and proposes potential directions for future research.

Fig 1.1 Failure of the Teton Dam due to internal erosion in Idaho, USA, in 1976 (USBR 1976).

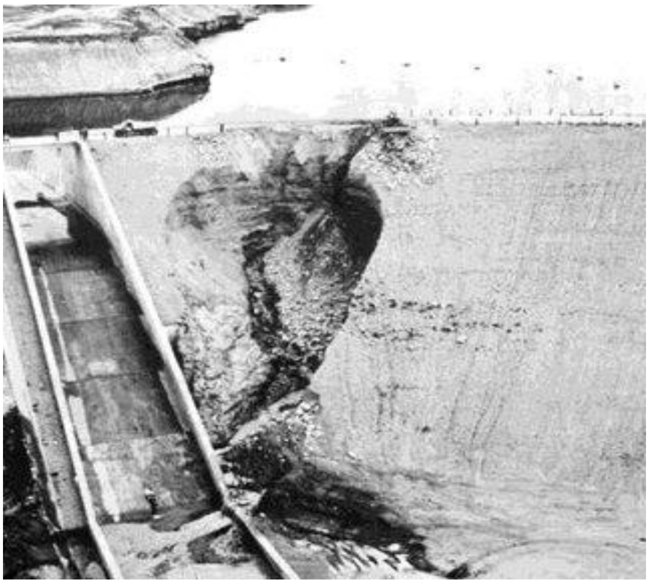

Fig 1.2 Piping failure on the right abutment of Fontenelle Dam in Wyoming, USA, in 1965 (Babu and Srivastava 2014).

Fig 1.3 Failure of the Tunbridge Dam due to internal erosion in Tasmania, Australia, in 2008 (Yousefpour and Mojtahedi 2024).

CHAPTER 2: LITERATURE REVIEW

2.1 Introduction

This chapter presents a comprehensive review of previous research on internal erosion in granular soils, with particular emphasis on gap-graded granular soils subjected to various shear loading conditions. The mechanisms of particle detachment and migration under seepage flow are examined, together with the influencing factors that affect the progression of erosion. Recent studies on the shear behavior of granular soils under different shear modes, including hollow cylinder torsional shear, direct shear, biaxial shear, and ring shear loading conditions, are reviewed to highlight the effects of loading conditions on soil fabric and force chain networks. The distinctive characteristics of gap-graded soils, such as non-uniform particle size distribution and preferential flow paths, are discussed to emphasize their high susceptibility to internal erosion.

Furthermore, the chapter reviews methodologies for investigating erosion processes, including both experimental methods and numerical simulation approaches, particularly the coupled CFD–DEM approach. The limitations of current studies, including the incomplete understanding of mechanical behavior of granular soils after erosion and the combined effects of stress state, fines content, hydraulic gradient and confining pressure on internal erosion, are identified. Finally, this Chapter concludes by highlighting the existing research gaps and stressing the need for a systematic investigation into internal erosion and how it affects the subsequent shear behavior of granular soils under various loading conditions.

2.2 Internal erosion

2.2.1 Definition and mechanisms of internal erosion

Internal erosion denotes the process where fine soil or rock particles are detached, transported, and removed by seepage flow within porous media such as embankments, soils, or rock masses (Foster and Fell 2001; Foster et al. 2000; Liu et al. 2020). This phenomenon typically occurs in granular materials when water flows through interconnected pores or fractures, exerting hydraulic forces strong enough to move fines such as silt and sand. As particle migration progresses, localized voids or channels form and may gradually expand and develop into larger pathways, further reducing the load-bearing capacity of the material. Internal erosion is particularly critical in heterogeneous or gap-graded soils, where the absence of intermediate-sized particles results in large, interconnected voids that facilitate the initiation and progression of particle loss.

As shown in Fig 2.1, four principal mechanisms of internal erosion have been identified: suffusion, concentrated leak, backward erosion and contact erosion (Fell and Fry 2007; Xiong et al. 2021). Suffusion refers to the selective migration of fine particles through the void spaces between coarse particles under seepage flow, without significant disturbance to the overall soil structure. It typically occurs in gap-graded or internally unstable soils, where fines are loosely packed (Bendahmane et al. 2008; Fannin and Slangen 2014). Backward erosion is a surface-initiated process in which shallow pipes form at the downstream toe of a dam or levee and propagate upstream against the flow direction, driven by overtopping or seepage exit gradients (BEEK et al. 2013). Concentrated leak involves the development of localized flow paths or leaks, often at structural discontinuities or interfaces, where water concentrates and rapidly removes soil particles (Benahmed and Bonelli 2012; Bonelli et al. 2013). Concentrated leak is different from backward erosion in that concentrated leak can occur in isolated regions without continuous upstream propagation (Foster and Fell 2001). Contact erosion occurs at the interface between two different soils (e.g., clay and sand), where seepage forces dislodge particles from one material into the other. It is driven by velocity gradients across the boundary and does not require internal instability within a single soil layer (PHILIPPE et al. 2013).

2.2.2 Influencing factors of internal erosion

The initiation and progression of internal erosion are controlled by a combination of soil properties and hydraulic conditions. These factors determine the stability of the soil structure under seepage forces and the potential for particle migration. In general, they can be categorized into soil-related factors and hydraulic-related factors.

The susceptibility of soil to internal erosion is strongly influenced by soil's physical and mechanical characteristics. Among these, particle size distribution plays a critical role, as it governs the pore structure and potential for fine particles to migrate through the voids of a coarse-grained framework (Kim et al. 2019). Gap-graded soils, which exhibit a significant absence of intermediate particle sizes, often form large and interconnected voids, which makes them highly vulnerable to suffusion. According to the previous studies (Fannin and Moffat 2006; Kenney and Lau 1986), the granular soil is regarded as internally unstable when the gap ratio D_{15} / d_{85} > 4 (where D_{15} and

d_{85} represent the particle diameters of 15% mass passing in the coarse particles and 85% mass passing in the fine particles, respectively). When the gap ratio < 4, the soil remains relatively stable, and fine particles are hard to be dislodged or eroded. Xiong et al. (2022) involved a set of coupled CFD-DEM investigations into the effect of PSD on clogging and found that PSD significantly influences the extent and depth of fine particle migration, and the erosion rate generally decreases as the stability of gap-graded soils increases which is consistent with other related studies (Hu et al. 2019; Zou et al. 2020). Particle shape also affects the behavior of internal erosion. Angular particles tend to interlock and form a more stable structure, while rounded particles corresponds to the reduced interparticle friction and larger pore channels that facilitate migration (Guo et al. 2018; Xiong et al. 2021). The investigation conducted by Qian et al. (2021) found that greater particle angularity improves the soil's resistance to internal erosion, with a marked reduction in fine particle loss observed as angularity increases. Fines content (FC) is another key factor. The behavior of internal erosion differs markedly between fine-dominated and coarse-dominated specimens, particularly when additional influencing factors are involved (Liu et al. 2020; Wang et al. 2023; Xiong et al. 2022). Considering the complex in situ stress conditions in different zones of the hydraulic structures, some physical experiments have been conducted to investigate the effect of stress states and loading conditions on suffusion.(Chen et al. 2016; Kuwano et al. 2021; Luo et al. 2019; Zhou et al. 2022a). For example, Chang and Zhang (2011) conducted a series of laboratory tests using a stress-controlled apparatus, and found that the increase of the deviatoric stress would result in the increase of the maximum erosion rate and deformation of the soil specimen. Then, some hydro-mechanical coupling tests on gap-graded soils under triaxial extension, triaxial compression and isotropic stress paths were designed. A higher initiation hydraulic gradient was observed in the suffusion test under the extension stress condition.(Chang and Zhang 2013). Luo et al. (2019) further found that there is a piecewise linear relationship between the critical initiation hydraulic gradient and deviator stress by a series of physical suffusion tests. The effect of confining pressure internal erosion in both fine-dominated and coarse-dominated specimens was studied by Liu et al. (2020). Song et al. (2024b) investigated the combined effects of α and b on internal erosion, and found that the fines mass loss decreases with both α and b.

Hydraulic-related factors primarily control the driving forces for particle detachment. The hydraulic gradient is the most direct factor. Seepage forces exert greater drag and lift on particles as the increase of hydraulic gradient, eventually overcoming interparticle resistance (Liu et al. 2020; Mu et al. 2023). Based on Chang and Zhang (2013) and Zhou et al. (2022a), the internal erosion process comprises four phases, i.e., stable, initiation, development, and failure. These phases are characterized by three critical hydraulic gradients corresponding to fine particle removal, force chain buckling, and structural collapse. Under compression, the erosion initiation gradient initially rises with increasing shear stress ratio, peaks at an intermediate value, and subsequently decreases as the stress state approaches failure. In addition, under isotropic stress conditions, both the erosion initiation gradient and the skeleton deformation gradient peak at a specific porosity.

2.3 Shear loading conditions of granular soils

Granular soils in geotechnical practice are often subjected to complex stress states arising from various loading conditions, such as those induced by foundation loads, slope instability, seismic events, or hydraulic fluctuations. To simulate these conditions in the laboratory, several specialized shear testing methods have been developed, each designed to replicate specific stress paths and deformation modes. Among them, biaxial shear, direct shear, ring shear, and hollow cylinder torsional shear tests are widely used to investigate the mechanical behavior of soils under controlled conditions. These tests enable researchers to examine not only strength and deformation properties but also the evolution of soil fabric, pore pressure, and localized failure zones such as shear bands. It is noted that triaxial testing has been extensively used in previous studies on internal erosion and remains a fundamental method for assessing erodibility under axisymmetric compression. This thesis focuses on the aforementioned other shear tests that enable more diverse stress path simulations.

2.3.1 Biaxial shear

Biaxial shear conditions commonly arise in geotechnical structures where deformation is constrained in one lateral direction, leading to a plane strain state. This stress path is representative of many practical situations, such as earth retaining walls, embankments, levees, and foundation margins, where the longitudinal strain is negligible compared to the transverse and vertical components. In such cases, the soil experiences differential horizontal stresses, making the biaxial shear test an appropriate laboratory method for simulating realistic stress and strain conditions (Hanna and Ayadat 2019; Zhang and Lou 2024). In the laboratory, the biaxial shear test is typically conducted in a rectangular cell equipped with movable pistons on two opposite vertical walls and rigid boundaries on the other two sides. Vertical load is applied through a top platen, while horizontal stress is controlled via lateral rams, enabling precise manipulation of the stress ratio and shear direction (see Fig 2.2). This setup allows for the measurement of stress–strain response, volume change, and the evolution of shear bands under controlled drainage conditions (Alshibli et al. 2003; Esmaeili et al. 2023; Labuz et al. 1996).

Numerous studies have employed the biaxial shear test to address fundamental questions in soil mechanics. For example, Han and Drescher (1993) studied the formation, orientation, and growth of shear bands by conducting biaxial compression tests on sand. It was concluded that both the shear strain at the onset of shear banding and the resulting shear-band orientation are influenced by the confining pressure. The research by Tatsuoka et al. (2003) emphasized the role of plane-strain conditions in evaluating strength and deformation properties of sands under realistic loading paths encountered in earth structures. Imaging tools, such as PIV and X-ray CT, have been integrated with biaxial apparatuses to visualize internal deformation and shear band formation in real time (Alshibli and Hasan 2008). Huang et al. (2008) employed DEM to capture the behavior of sand from the under the biaxial shear condition and provided insights into shear-induced anisotropy at the particle scale. The DEM study by Mukherjee et al. (2017) investigated the onset of both localized and liquefaction-related failure modes in sand under undrained plane-strain conditions. Wang et al. (2022b) employed a series of DEM simulations on the particle-size effect of granular material in biaxial test and investigated the effect of particle breakage on strength and shear band.

Overall, due to its ability to simulate plane-strain compression conditions and provide detailed insight into localized deformation mechanisms, the biaxial shear test remains a valuable tool for both experimental and calibration purposes in geomechanics, particularly when studying complex soil behavior beyond the limitations of axisymmetric triaxial testing.

2.3.2 Direct shear

Direct shear conditions are commonly encountered in geotechnical structures where a well-defined slip plane develops under loading, such as in the stability of slopes, retaining walls, foundations, and interfaces between different soil layers or between soil and structural elements. These conditions occur when relative displacement takes place along a predetermined failure surface under constant or controlled normal stress, often observed in shallow landslides, embankment stability problems, and pavement systems (Liu et al. 2005; Potts et al. 1987; Scarpelli and Wood 1982).

Among soil testing methods, the direct shear test is both simple and extensively utilized to measure shear strength. As shown in Fig 2.3, the device consists of a shear box split into two halves, with the soil specimen under a constant normal load as horizontal movement generates shear along a predetermined plane (Barla et al. 2010; Liu 2006). This configuration provides a straightforward means to assess the Mohr–Coulomb shear strength parameters, including cohesion and internal friction angle. The test is particularly suitable for studying interface behavior, where frictional resistance and displacement-dependent strength are critical design parameters. Meanwhile, its simplicity, cost-effectiveness, and ability to impose large displacements make it a standard procedure in geotechnical practice.

Numerous studies have employed the direct shear test to study the stress–strain characteristics of granular materials under various conditions. Gan et al. (1988) conducted a series of direct shear tests to obtain the strength parameter of a kind of unsaturated soil. Xu et al. (2011) employed digital image processing to quantitatively assess the proportion and spatial distribution of rock blocks in soil-rock mixtures and conducted large-scale direct shear testing to investigate how rock block content influences shear strength, deformation mechanisms, and shear band development. In addition to monotonic loading, the direct shear test has been adapted for cyclic loading conditions and soil-structure interface behavior investigation (Al-Douri and Poulos 1992; Yin et al. 2021a). For instance, Pra-ai and Boulon (2017) performed cyclic two-dimensional direct shear tests to study sand-structure interface behavior under repeated loading. The research proposed a new test interpretation method, analysed cyclic contraction and stress degradation, and emphasized the role of cyclic amplitude, initial density, and centre of stress cycles.

In this thesis, the direct shear test is emphasized for its significant advantage in the investigation of shear banding. The predefined failure plane and the capability to impose large displacements allow clear visualization and quantification of localized deformation. The DEM direct shear tests conducted by Cui and O'Sullivan (2006) revealed the initiation and evolution of shear bands through the analysis of localized strain, particle displacement, and force chains. The study highlighted the sensitivity of shear banding to micro-scale fabric and boundary conditions in granular materials. Furthermore, Wang et al. (2007) conducted a series of DEM direct shear test and revealed that shear bands develop from boundaries toward the centre, with primary bands forming near peak state.

2.3.3 Ring shear

Ring shear conditions occur in geotechnical scenarios where soils undergo extremely large displacements along a failure surface, often under constant or near-constant shear stress. Such conditions are characteristic of rapid landslides, long-runout debris flows, and progressive failure in slopes or embankments (Sassa et al. 2004; Toyota et al. 2009). Unlike direct shear or biaxial loading, which generally involve limited displacement before peak and post-peak strength behavior is assessed, ring shear conditions replicate the sustained movement that takes place after initial failure, making them particularly relevant for studying residual strength and post-failure mobility of soils (Bishop et al. 1971; Dong et al. 2020; Mohajeri et al. 2020; Stark and Eid 1994).

In the laboratory, the ring shear apparatus is specifically used to investigate the mechanical behavior of soils under large-displacement and post-peak deformation conditions. As shown in Fig 2.4, the apparatus typically is composed of an annular shear box divided into upper and lower rings, with the soil specimen placed between them. The specimen is subjected to a controlled normal stress while the lower ring is rotated continuously, inducing shear along the circular plane (Bishop et al. 1971; Sassa et al. 2004). Unlike conventional shear tests, this configuration allows for unrestricted horizontal displacement, enabling the soil to reach extremely large strains. By maintaining a constant normal load during shearing, the ring shear apparatus effectively simulates conditions similar to those in real landslides, where soil generally experiences continuous movement under nearly constant normal stress. A comparison between ring shear and shear box tests was conducted by Okada et al. (1998), which showed that their results in peak friction angles and liquefaction detection were consistent, while some discrepancies were observed with triaxial tests.

Progress in ring shear testing has greatly enhanced knowledge of residual shear strength which is a key parameter in slope stability and landslide mobility analysis. Early pioneering investigations by Skempton (1964) and Bishop et al. (1971) introduced the concept of residual strength and highlighted its relevance in analysing progressive failures. These studies found that soil properties like clay mineralogy and particle orientation strongly influence the residual state. Subsequent studies further provided insights into the roles of effective normal stress, water content and other factors in determining the post-failure behavior of soils (Gibo et al. 1987; Lupini 1980;

Stark and Eid 1994). In recent years, some ring shear tests have been conducted with DEM simulations. For example, Mohajeri et al. (2020) combined DEM with ring shear testing to capture stress history dependence in cohesive materials. Using multi-objective optimization, the study successfully calibrated micromechanical parameters, enabling accurate simulation of shear stress, density, and wall friction under large displacements. A series of DEM ring shear tests was conducted by Dong et al. (2020) to investigate granular flow phase transitions. The study identified critical shearing rates for the quasi-static to slow flow transition and revealed their dependence on normal stress, providing insights into the initiation mechanisms of landslides and debris flows.

2.3.4 Hollow cylinder torsional shear

Hollow cylinder torsional shear conditions occur in geotechnical situations where soils are subjected to complex loading paths, including principal stress rotation and multidirectional loading, such as in offshore foundations, embankments under seismic loads, and tunnels experiencing stress redistribution (Miura et al. 1986a). In these cases, soil elements are not only loaded in simple shear but also experience rotation of the principal stresses, as shown in Fig 2.5 .

The hollow cylinder torsional shear test (HCTST) is a sophisticated laboratory technique that enables independent control of rotational, vertical, radial and circumferential stresses, allowing for the application of complex, non-axisymmetric stress paths that cannot be replicated by conventional triaxial or direct shear apparatuses (Brosse 2012; Hight et al. 1983; Yang et al. 2015). The test employs a cylindrical soil specimen with a central hole, confined by fluid pressure on the inner and outer boundaries, while shear is induced through the controlled rotation, as shown in Fig 2.6. With the aid of the hollow cylinder apparatus (HCA), the mechanical behaviors of soil under various combination of α and b were investigated (Gutierrez et al. 1991; Hight et al. 1983; Symes et al. 1984). Unfortunately, previous studies on HCTSTs usually kept the internal and external cell pressures equal during the shearing process, leading to the simultaneous variation of α and b (Cai et al. 2013; Saada 1988), and thus could not reveal their respective influences. To focus on the independent effect of the rotation of the major principal stress, some HCTSTs with constant b-values were conducted (Kumruzzaman and Yin 2010; Miura et al. 1986a; Miura et al. 1986b; Xiong et al. 2016). Yang et al. (2016) further conducted an experimental investigation of Leighton Buzzard sand using HCA and found the respective effects of α and b on strength, non-coaxiality, and shear banding.

In recent years, some DEM HCTST models have been proposed, enabling the investigation of the significant influence α and b on soil behaviors from the microscopic perspective. Li et al. (2014) proposed an HCTST model in DEM and conducted a series of parametric studies, with subsequent work investigating the difference between the global mechanical response from the boundaries and localized response measured at different locations of the DEM specimen (Li et al. 2015; Li et al. 2017). Shi et al. (2021) developed a DEM HCTST model to simulate complex stress paths in rocks. This study investigated the macro-micromechanical responses and energy evolution of sandstone under various unloading conditions. Furthermore, Song et al. (2024a) developed a DEM model of HCTST. A bonded-sphere assembly in a hexagonal arrangement was developed to simulate the flexible boundaries that allow real-time control of both internal and external cell pressures and capture the inhomogeneous deformation in the radial direction. With this DEM HCTST model, the effects of α and b on both macroscopic and microscopic behaviors of granular sand are investigated and discussed in detail.

Overall, the HCTST is a powerful tool for studying soil's mechanical behaviors under complex stress conditions. It enables detailed examination of anisotropic behavior, principal stress rotation effects, and the development of localized deformation, providing critical insights for geotechnical design under multidirectional and dynamic loading scenarios. Thus, it is a good choice when investigating the combined effect of α and b on internal erosion.

2.4 Methodology on internal erosion investigation

The study of internal erosion has advanced significantly due to improvements in experimental and computational techniques. With the development of precise laboratory equipment and manufacturing technologies, it has become possible to replicate erosion processes under controlled conditions, enabling systematic investigation of soil behavior in laboratory. Concurrently, the rapid growth of computing power and numerical algorithms has allowed researchers to model complex fluid–solid interactions inherent in internal erosion. Numerical approaches, including those adapted from other scientific fields, are now widely applied in geotechnical engineering to simulate multiphase processes with high accuracy. These advancements have facilitated both experimental and numerical studies, providing deeper insight into the mechanisms of internal erosion.

2.4.1 Experimental method

In internal erosion research, conventional experimental approaches for simulating soil seepage erosion mainly include flume experiments (Zhan and You, 2003; Ahmadi-Adli et al., 2014) , artificial rainfall tests on slopes (Ng et al. 2003), and soil column tests (Chang and Zhang 2011; Kim et al. 2013).

As the most commonly adopted experimental method for studying seepage-induced erosion, soil column test apparatus has continued to evolve in recent years. Early soil column tests did not account for the influence of stress but were solely used to investigate the amount of fine particle erosion and the variation of permeability (Cividini et al. 2009). In recent years, several soil column test apparatuses capable of considering stress effects have been developed (Ke and Takahashi 2014; Marot et al. 2024; Wang et al. 2022a). Typically, these devices place the soil specimen within a triaxial cell where confining pressure and axial load can be simultaneously applied during seepage flow. These apparatuses have enabled the simulation of certain simple stress conditions. For example, a stress-controlled internal erosion testing apparatus was developed by Chang and Zhang (2011), as shown in Fig 2.7. With this apparatus, some hydro-mechanical coupling tests on gap-graded soils under isotropic, triaxial compression, and triaxial extension stress paths were designed. A higher initiation hydraulic gradient was observed in the suffusion test under the extension stress condition in the study (Chang and Zhang 2013). Luo et al. (2019) further found that there is a piecewise linear relationship between the critical initiation hydraulic gradient and deviator stress with the same stress-controlled erosion apparatus. Then, Liang et al. (2023) proposed a similar stress-controlled apparatus, and further studied the development of internal erosion and the strength reduction of the soil specimen after erosion.

In addition, advanced techniques such as transparent soil visualization and nuclear magnetic resonance have been increasingly employed to study internal erosion (Duan et al. 2024; Feng et al. 2020; Gu et al. 2025; Irons et al. 2014; Liu and Iskander 2010; Sui and Zheng 2018; Wang et al. 2019). However, these experimental tests are generally time-consuming and labour-intensive, and they remain limited in their ability to provide detailed insights into erosion mechanisms at the microscale.

2.4.2 Numerical simulations

Numerical methods for internal erosion research can be broadly categorized into continuum-based approaches, which incorporate erosion constitutive models, and coupled DEM–fluid methods that simulate fluid–particle interactions at the microscale. The finite element method (FEM) (Vandenboer et al. 2014) and the material point method (MPM) (Liang et al. 2020; Yerro et al. 2017) are commonly used continuum-based approaches. Both can be applied to simulate material loss at the slope scale, but they cannot capture the true interactions between fluid and individual particles. Therefore, these methods are not suitable for investigating the microscopic mechanisms of internal erosion.

The coupled DEM–fluid methods can effectively capture the mechanical behavior of particles during internal erosion. Among these, the Darcy-DEM method, which couples seepage equations with DEM, is commonly used to simulate internal erosion at the unit scale or in small-scale experimental setups (Pirnia et al. 2020; Yin et al. 2021b). However, this method cannot accurately resolve the interactions between particles and fluid, as it requires the fluid to satisfy the assumptions of Darcy flow. The coupled Lattice Boltzmann Method-Discrete Element Method (LBM-DEM) can resolve complex particle boundaries and capture both pore fluid motion and particle transport (Han and Cundall 2013; Lominé et al. 2013; Xiong et al. 2014; Zhou et al. 2020). Therefore, it is often used to study the migration of fine particles within pore channels. However, this method involves a high computational cost when simulating complex porous media.

The coupled CFD-DEM approach is another DEM-related method. The unresolved CFD–DEM approach does not resolve the detailed fluid flow around individual particles and therefore cannot accurately capture the localized fluid–particle interactions or the geometry of pore channels. In contrast, the resolved CFD–DEM method explicitly models the fluid flow around particle surfaces, but it faces significant challenges in resolving complex particle boundary conditions and suffers from low computational efficiency (Hu et al. 2023; Kuruneru et al. 2019; Mao et al. 2020). Despite these limitations, the unresolved CFD–DEM method is capable of simulating element-scale internal erosion processes under realistic stress conditions while accounting for two-way coupling between the fluid and granular phases (Hu et al. 2022; Wang et al. 2024a; Zhao and Shan 2013). Due to the balance between computational efficiency and physical fidelity, the unresolved CFD–DEM approach is adopted in this thesis. The governing equations and coupling scheme of this method will be introduced in detail in the following sections.

2.5 Coupled CFD-DEM numerical method

The coupled CFD-DEM approach enables the detailed modelling of fluid-solid interactions by simulating fluid flow using CFD and particle dynamics using DEM. This methodology is particularly suited for capturing the complex processes involved in internal erosion, such as particle detachment, transport, and clogging within the pore structure (Cheng et al. 2023; Zhao and Shan 2013). In this thesis, the DEM code Particle Flow Code (PFC3D) is employed to compute the translational and rotational motion of individual soil particles, including their velocities, positions, and other kinematic properties. Concurrently, the open-source CFD solver OpenFOAM is employed to simulate the fluid phase by numerically solving the volume-averaged Navier–Stokes (N–S) equations enabling quantitative determination of key fluid parameters, including the velocity field, pressure gradient, and local hydraulic gradients, which are essential for capturing the hydrodynamic forces acting on soil particles during internal erosion (Ge et al. 2024; Wang et al. 2023; Xie et al. 2023; Zhou et al. 2022b; Zhou et al. 2019a). The ccoupling between the fluid and solid phases is achieved through a two-way interaction framework implemented via TCP sockets. The governing equations used in the coupled CFD-DEM method are introduced as follow.

2.5.1 Governing equations for particle system

Within the DEM framework, the dynamic behavior of a given particle *i* at any time step *t* is governed by the Newton's laws of motion, which accounts for both translational and rotational motion (Cundall and Strack 1979). These equations are expressed as follows:

$$m_i \frac{d\boldsymbol{U}_i}{dt} = \sum_{j=1}^{n_i^c} \boldsymbol{F}_{ij}^c + \boldsymbol{F}_i^f \tag{2.1}$$

$$I_i \frac{d\omega_i}{dt} = \sum_{j=1}^{n_i^c} \boldsymbol{M}_{ij} \tag{2.2}$$

where m_i denotes the particle mass; n_i^c represents the total number of contacts acting on particle *i*; $\boldsymbol{U}_i$, I_i and ω_i are the translational velocity vector, moment of inertia tensor and angular velocity vector of the particle *i*, respectively; $\boldsymbol{F}_{ij}^c$ and $\boldsymbol{M}_{ij}$ represent the contact force and torque, respectively, exerted on the given particle *i* by the neighbouring particle *j*; and $\boldsymbol{F}_i^f$ is the fluid-solid interaction force acting on the particle *i* due to the surrounding fluid phase.

2.5.2 Governing equations for liquid system

The fluid phase is simulated within the CFD framework. The governing equations for fluid flow consist of the locally averaged N-S equations and the continuity equation, which explicitly incorporate the influence of the particulate phase on the fluid at any time *t* (Jasak et al. 2007; Wang et al. 2023):

$$\rho_f \frac{\partial n\boldsymbol{v}}{\partial t} + \rho_f \boldsymbol{v} \bullet \nabla (n\boldsymbol{v}) = -n\nabla p + \mu \nabla^2 (n\boldsymbol{v}) + \boldsymbol{f}_b \tag{2.3}$$

$$\frac{\partial n}{\partial t} + \nabla (n\boldsymbol{v}) = 0 \tag{2.4}$$

where ρ_f denotes the density of fluid; n is the local porosity, which evolves as particles move and rearrange; $\boldsymbol{v}$ and p represent the volume-averaged velocity and pressure of the fluid element, respectively; μ is the dynamic viscosity of the fluid. $\boldsymbol{f}_b$ is the body force per unit volume exerted on the fluid by the particles located within the fluid domain.

2.5.3 Governing equations for particle-fluid interaction forces

This body force $\boldsymbol{f}_b$ accounts for the momentum exchange between the fluid and particle phases due to drag and other interphase interactions and is essential for achieving two-way coupling between the CFD and DEM domains. It can be computed by the following equation:

$$\boldsymbol{f}_b = \frac{\sum_{i=1}^{m} \boldsymbol{f}_{fluid}^{i}}{V} \tag{2.5}$$

where V denotes the volume of CFD computational cell. $\sum_{i=1}^{m} \boldsymbol{f}_{fluid}^{i}$ is the total particle-fluid interaction forces that act on this particle. The force $\boldsymbol{f}_{fluid}$ comprises two dominant components:

$$\boldsymbol{f}_{fluid} = \frac{4}{3}\pi r^3 \left(\nabla p - \rho_f \boldsymbol{g}\right) + \boldsymbol{f}_{drag} \tag{2.6}$$

where r is the particle radius; $\boldsymbol{g}$ is the gravitational acceleration vector; ∇p denotes the local pressure gradient. In this equation, the first term on the right-hand side corresponds to the pressure gradient force, while the second term represents the drag force. The force $\boldsymbol{f}_{drag}$ is defined as:

$$\boldsymbol{f}_{drag} = \boldsymbol{f}_0 n^{-\chi} \tag{2.7}$$

where $\boldsymbol{f}_0$ denotes the drag force applied to a single particle which can be calculated based on the semi-empirical model proposed by Di Felice (1994):

$$\boldsymbol{f}_0 = \frac{1}{2} C_d \rho_f \pi r^2 \left|\boldsymbol{u}-\boldsymbol{v}\right|\left(\boldsymbol{u}-\boldsymbol{v}\right) \tag{2.8}$$

where C_d is the drag coefficient, defined as:

$$C_d = \left(0.63 + \frac{4.8}{\sqrt{Re_p}}\right)^2 \tag{2.9}$$

with Re_p being the Reynolds number, given by:

$$Re_p = \frac{2\rho_f r\left|\boldsymbol{u}-\boldsymbol{v}\right|}{\mu} \tag{2.10}$$

In addition, $n^{-\chi}$ is an empirical term used to account for the influence of local porosity on the fluid–solid interaction, and the coefficient χ is defined as follow:

$$\chi = 3.7 - 0.65\exp\left[-\frac{\left(1.5-\lg Re_p\right)^2}{2}\right] \tag{2.11}$$

With the above equations, the information of the particle and fluid phases can be calculated in DEM and CFD in real time.

In addition, the Courant number *C*, expressed in the following equation, should be below 1 to ensure the numerical stability and accuracy throughout the whole simulation process (Liu et al. 2023b):

$$C = \frac{\sum_F U_F \Delta S}{2\Delta V}\Delta t_f < 1 \tag{2.12}$$

where $\sum_F U_F \Delta S$ denotes the sum of the face fluxes of a fluid cell; ΔV is the volume of the cell; and Δt_f is the timestep in the CFD solver. Meanwhile, the timestep Δt_p

in the DEM part should satisfy the following criteria (Cundall and Strack 1979):

$$\Delta t_p \leq 2\sqrt{\frac{M}{k}} \tag{2.13}$$

where M and k denote the mass of particle and stiffness, respectively.

It is noted that the lift and added-mass forces are neglected in the CFD-DEM coupling. The interaction between fluid and each particle is primarily modeled using the drag force that depends on relative velocity, local porosity, and particle size. Meanwhile, all particles are assumed rigid and spherical, ignoring particle breakage and realistic shape effects that could influence local pore structure and fluid flow. The CFD domain uses a fixed Eulerian mesh, and porosity changes are updated at discrete time intervals rather than continuously, assuming quasi-steady flow. The pore fluid is modeled as a continuum, which is valid for moderate particle Reynolds numbers.

The following operation sequence is performed with the DEM code and CFD solver in a two-way CFD-DEM coupling simulation. As shown in Fig 2.8, the particle system and the fluid field are firstly generated based on the designed simulation program. The fluid mesh information is then sent to the DEM part, and the CFD module is initialized in DEM. After the initial calculation of the porosity and drag force, the CFD solver will update the information including the velocity, pressure, and pressure gradient of the fluid phase based on the data obtained from DEM, and the updated information will be sent to the DEM part. Then, the DEM solver will cycle forward a time increment which is same as the coupling interval. During the interval, the information of the particle system is updated, and the fluid-solid interaction force will be added to the particles. The above steps will be repeated until the required coupling time.

2.5.4 Validation of the coupled CFD-DEM method

Regarding the validation of numerical simulations of internal erosion, Liu et al. (2021) compared experimental results with CFD–DEM simulations but were only able to reproduce the overall trend of fines loss, mainly because particle number, shape, and gradation in physical tests cannot be fully replicated in numerical models. In fact, due to the scarcity of suitable experimental data, most existing studies rely on indirect verification of the coupled CFD–DEM framework using the sedimentation test (Liu et al. 2020), repose angle test (Zhou et al. 2022b), free settling test (Guo et al. 2018) and fluidization test (Zhou et al. 2022a). Moreover, the Ergun test and drop test were conducted in our previous studies for the validation work (Song et al. 2024b; Wang et al. 2023), as shown in Fig 2.9 and Fig 2.10. The good agreement between the numerical result from the coupled CFD-DEM simulations and analytical solution indicates that coupled CFD-DEM approach used in this thesis can well capture the interaction behavior between the particle system and fluid phase.

2.6 Summary

In this chapter, a comprehensive review of internal erosion in granular soils has been presented, beginning with the definition as a seepage-induced process of particle detachment and migration within porous media. The mechanisms and key influencing factors of internal erosion in gap-graded granular soils are discussed, including the role of particle size distribution, fines content, hydraulic gradient, and stress state in determining the erodibility of soil specimens. The Chapter also examines various shear loading conditions commonly encountered in geotechnical practice, including biaxial shear, direct shear, ring shear, and hollow cylinder torsional shear loadings. Each of these corresponding tests enables the simulation of different stress paths and deformation modes, offering valuable insights into how mechanical loading affects soil fabric and subsequent erosion.

Experimental methods, including soil column tests and advanced visualization techniques, used to investigate internal erosion are reviewed, along with their limitations. Numerical approaches, particularly the coupled CFD–DEM method, have been highlighted as effective tools for modeling fluid-particle interactions at the microscale. The unresolved CFD–DEM approach, which balances computational efficiency and physical fidelity, has shown strong potential for simulating internal erosion under complex shear loading conditions.

The review also covers experimental and numerical approaches used to study internal erosion. While traditional soil column tests and advanced visualization techniques provide valuable macro-scale data, they are often limited in capturing micro-mechanical responses of gap-graded granular soils under controlled stress conditions. Numerical methods, particularly the coupled CFD–DEM approach, have emerged as powerful tools for simulating fluid–particle interactions at the pore scale. The unresolved CFD–DEM method, which balances computational efficiency and physical fidelity, has shown promise in modeling internal erosion under complex hydromechanical conditions.

Overall, the literature review indicates that while considerable advances have been achieved in understanding the macroscopic behavior of gap-graded granular soils under internal erosion, there remain gaps in quantifying microscale particle-fluid interactions and the effects of different stress paths on erosion and subsequent mechanical behavior after erosion. This review provides a solid foundation for the following Chapters, which will employ coupled CFD-DEM simulations to systematically investigate internal erosion under various shear loading conditions and examine the resulting changes in the mechanical behavior of the post-eroded soil specimens.

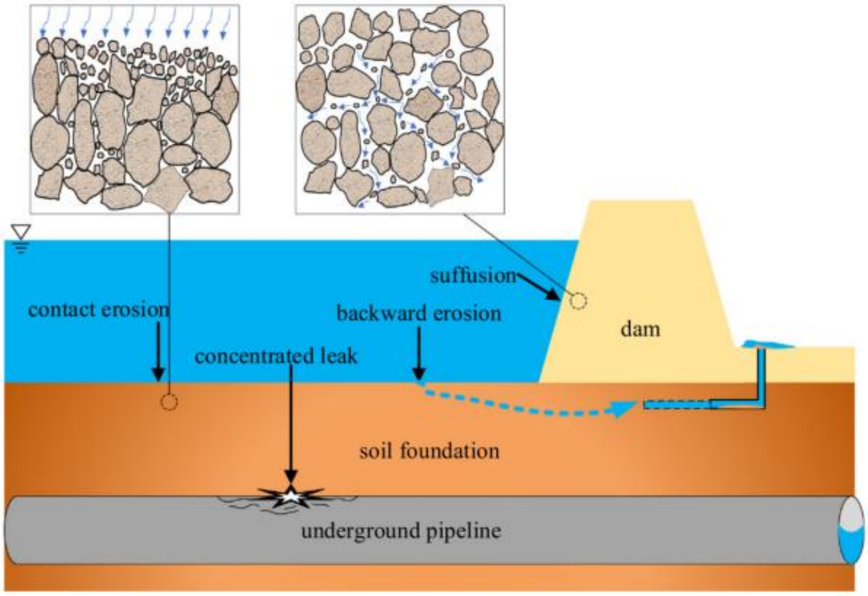

Fig 2.1 Schematic diagram of different seepage erosion in a dam (Xiong et al. 2021).

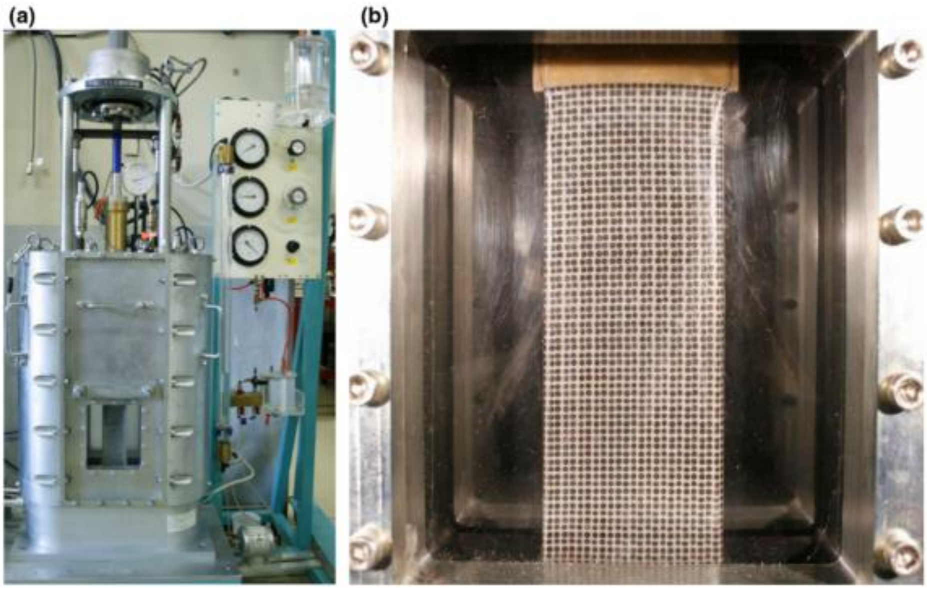

Fig 2.2 Photographs of (a) biaxial shear test apparatus and (b) installed soil specimen (Zhuang et al. 2013).

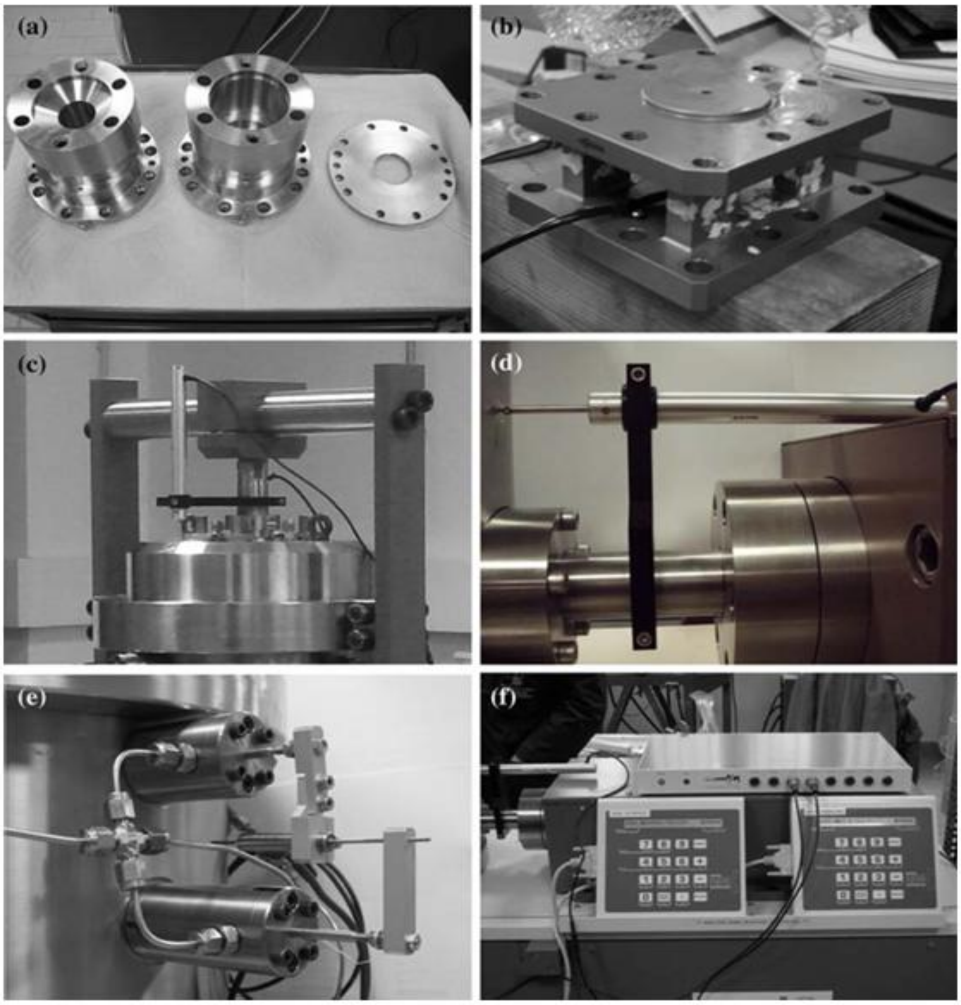

Fig 2.3 Photographs of a direct shear apparatus: (a) Shear boxes and plate, (b) Shear load cell, (c) vertical potenziometer, (d) horizontal potenziometer (EXT2), (3) LVDT transducer, (f) Control panels and load actuators (Barla et al. 2010).

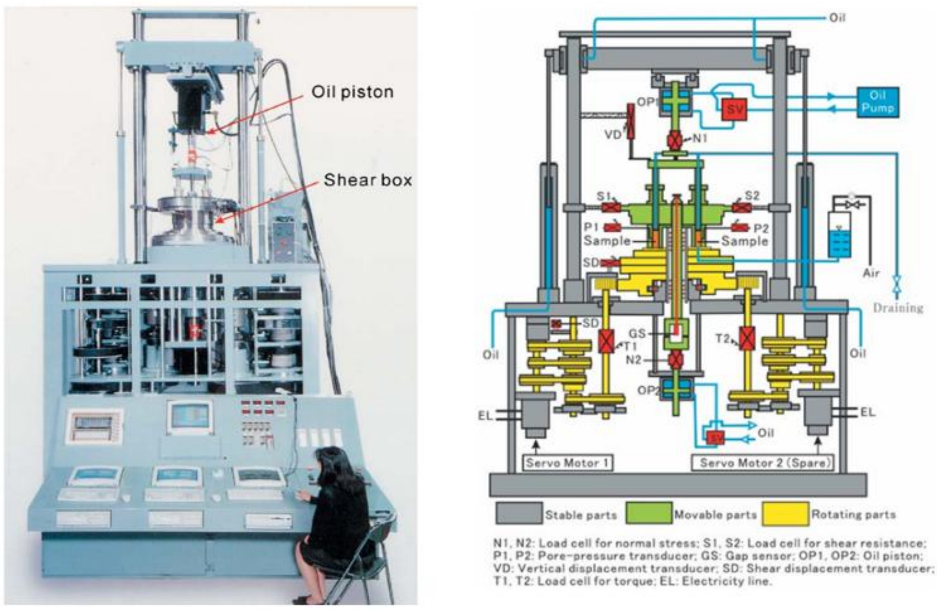

(a) (b)

Fig 2.4 (a) Photo and (b) mechanical structure of the dynamic-loading ring-shear apparatus (Sassa et al. 2004).

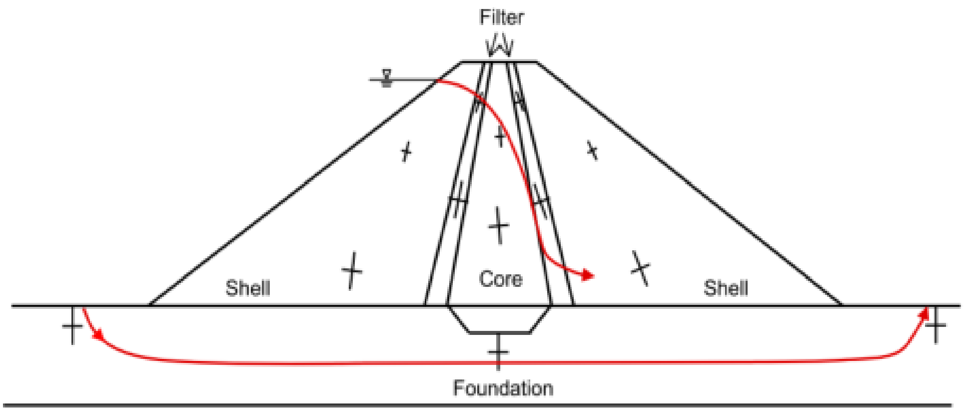

Fig 2.5 Illustration of the distribution and orientation of principal stresses in various zones and at the foundation after the reservoir is filled (Chang and Zhang 2013).

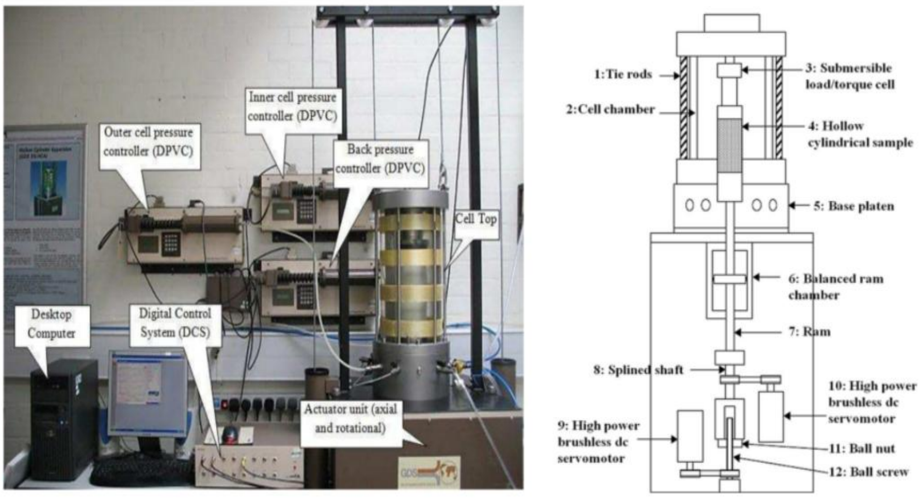

(a) (b)

Fig 2.6 (a) Photo and (b) schematic cross section of HCA (Yang 2013).

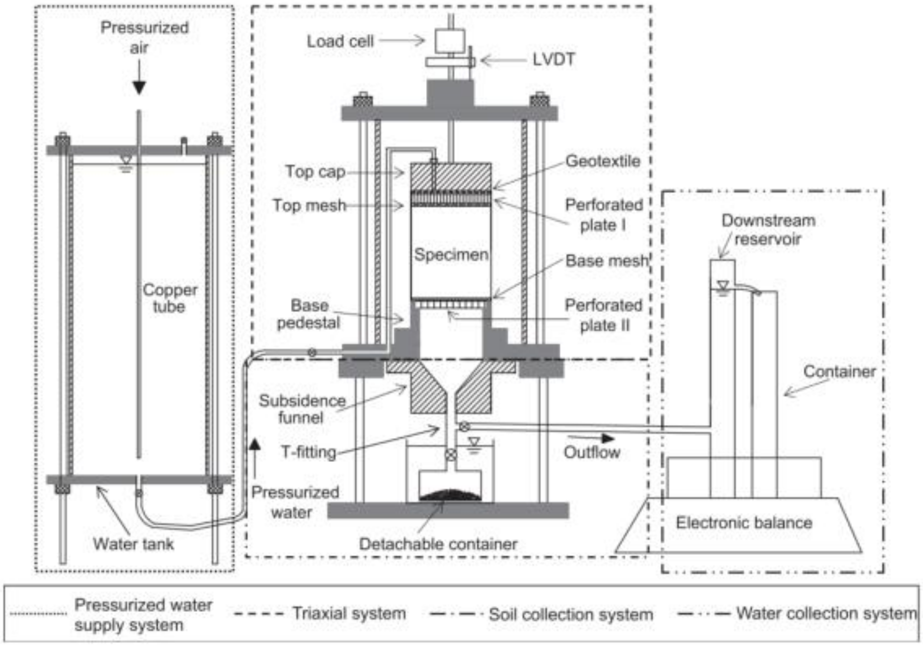

Fig 2.7 Diagram of the stress-controlled apparatus for internal erosion testing.

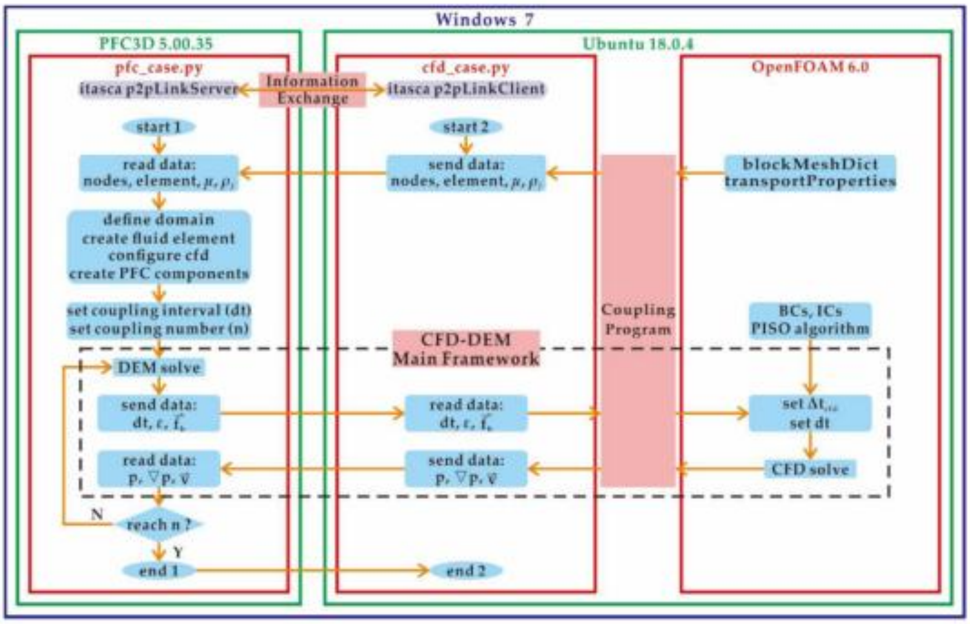

Fig 2.8 Algorithm flowchart of CFD-DEM coupling (Zhou et al. 2019a).

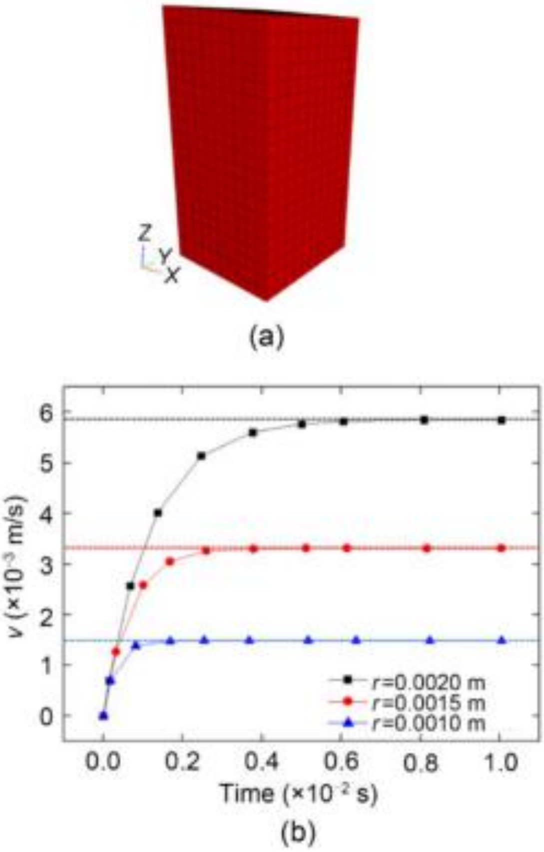

Fig 2.9 (a) Schematic diagram of the drop test and (b) variation of particle velocities and theoretical values (Wang et al. 2023).

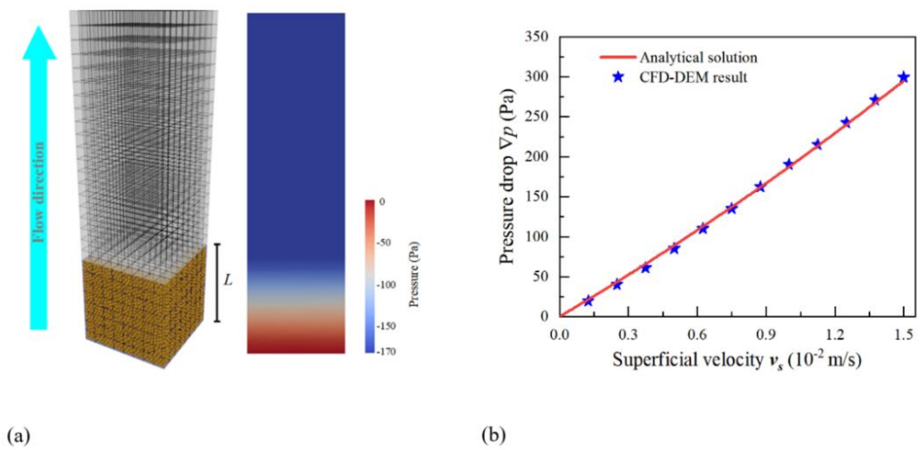

Fig 2.10 (a) Ergun test and (b) pressure drop and theoretical values (Song et al. 2024b).

CHAPTER 3: COUPLED CFD-DEM INVESTIGATION ON INTERNAL EROSION IN GRANULAR SOILS UNDER HOLLOW CYLINDER TORSIONAL SHEAR CONDITION

3.1 Introduction

Internal erosion usually initiates and continues in gap-graded soils under complicated stress states. This process also often involves the rotation of the major principal stress axis and various combinations of the three principal stresses. Fortunately, the hollow cylinder apparatus (HCA) is an effective tool to capture these complex stress states in geotechnical research. Compared with other available apparatuses, the main advantage of HCA lies in its ability to allow the investigation of soil mechanical behaviors under various stress conditions through the independent control of the vertical, rotational, radial and circumferential stresses (Gutierrez et al. 1991; Hight et al. 1983; Symes et al. 1984). Apart from some of the physical tests and simulations which considered some simple stress states, few of the existing studies have investigated the combined effect of α (the angle between the major principal stress and vertical axis) and b (given by $(\sigma_2 - \sigma_3) / (\sigma_1 - \sigma_3)$) due to the difficulty in developing the physical apparatus and numerical CFD-DEM model.

To gain a deeper insight into the effect of loading conditions on internal erosion, a stress-controlled hollow cylinder torsional shear test (HCTST) DEM model with flexible membrane boundaries allowing for the independent control of α and b is first developed in this Chapter. After the validation of the DEM model, nine specimens are then sheared under various loading paths with fixed α (25°, 45°, and 65°) and b (0.2, 0.5, and 0.8), and the confining pressure p are the same and kept constant at 50 kPa during the whole simulation process in all specimens. When the deviatoric stress q reaches 55 kPa, the shearing process is paused, and the seepage flow is introduced for the erosion simulations. The results will be analysed in detail to find the relationship between macroscopic internal erosion and microscopic evolution of internal fabric of the gap-graded soil.

3.2 Simulation procedure

3.2.1 DEM HCTST model

As a widely used tool in geotechnical research, HCA can help to independently control the stress components (the vertical stress σ_z, torsional shear stress $\tau_{z\theta}$, circumferential stress σ_θ and radial stress σ_r) by adjusting the external loads (the vertical load W, torque T, internal cell pressure p_i, and external cell pressure p_o) in real time. The formulas used to calculate the stress and corresponding strain components are summarized in Table 3.1. Furthermore, to better understand the stress states in HCTSTs, the following equations are used to describe the stress states in the stress space of mean normal stress p and deviatoric stress q (Brosse 2012; Song et al. 2024a):

$$\sigma_z = p - \frac{1}{3}q(b - \frac{1}{2}) + \frac{1}{2}q\cos(2\alpha) \tag{3.1}$$

$$\sigma_r = p + \frac{2}{3}q(b - \frac{1}{2}) \tag{3.2}$$

$$\sigma_\theta = p - \frac{1}{3}q(b - \frac{1}{2}) - \frac{1}{2}q\cos(2\alpha) \tag{3.3}$$

$$\tau_{z\theta} = \frac{1}{2}q\sin(2\alpha) \tag{3.4}$$

Therefore, many loading conditions with various of α and b can be achieved by combining the two sets of stress states and adjusting the corresponding external loads in HCTSTs. More details about the principle of HCTST can be found in previous studies (Brosse 2012; Hight et al. 1983; Li et al. 2014; Song et al. 2024a; Yang 2013).

Based on the above principle, a DEM HCTST model, where an algorithm for simulating the real inner and outer rubber membranes of the HCA is proposed, as shown in Fig 3.1, to achieve the simulations under various stress conditions. In this model, the vertical load is applied by the top and bottom rigid plates, and the torque is applied by rotating the top and bottom short vertical plates. Meanwhile, the internal and external cell pressures are applied by applying forces on the sphere elements of the flexible membrane boundaries (Fig 3.1). The bond between the membrane sphere particles (MM) is governed by the linear parallel bond contact model. This contact model is featured with linear force-displacement behaviors in the normal and shear directions, and the bond can break if the tensile or shear stress exceeds the corresponding strength. On the other hand, the linear elastic contact model, which provides linear relationship in the normal and shear direction without bonding and cohesion, is used to capture the interactions between particles (PP), particle and wall (PW), particle and membrane (PM), and membrane and wall (MW). In addition, to achieve high-fidelity simulation results and ensure a realistic stress distribution in the HCA sample, the dimension of the DEM sample is designated to be the same as that of the physical test (Hight et al. 1983; Saada 1988), namely, 100 mm in height, and 30 mm and 50 mm respectively in the inner and outer diameters.

The inner and outer flexible membrane boundaries are composed of sphere elements bonded in a hexagonal arrangement, as shown in Fig 3.1. Each sphere element can be considered as a central node, and the force acting on is determined by the confining pressure and its force-bearing area. During the shearing process, the applied external force is updated in each timestep to achieve the real-time control of the internal and external cell pressures. Herein, one central node and its surrounding sphere elements are taken as an example (red line in Fig 3.1) to elucidate this algorithm in detail. First, the sphere elements are numbered from 0 to 7. The vector pointing from the central sphere element 0 to the sphere element i (= 0,1…7) is denoted as $\vec{l}^{\,i}$ here, and it is defined as:

$$\vec{l}^{\,i} = x^i - x^0 \tag{3.5}$$

where x^i is the coordinate of node i. The outward normal $\vec{n}^{012}$ and the area A^{012} of the triangular mesh element 012 in Fig 3.1 can be expressed as:

$$\vec{n}^{012} = \frac{\vec{l}^{\,1} \times \vec{l}^{\,2}}{\left|\vec{l}^{\,1} \times \vec{l}^{\,2}\right|} \tag{3.6}$$

$$A^{012} = \frac{1}{2}\left|\vec{l}^{\,1} \times \vec{l}^{\,2}\right| \tag{3.7}$$

Therefore, the force acting on the node 0 credited to the triangle mesh element 012, i.e., $\vec{F}^{012-0}$, is:

$$\vec{F}^{012-0} = -\frac{1}{3} p_c A^{012} \vec{n}^{012} = -\frac{1}{6} p_c \vec{l}^{\,1} \times \vec{l}^{\,2} \tag{3.8}$$

where p_c is the confining pressure. Then, the total applied force acting on the node 0, $\vec{F}^{0}$, can be obtained by summarizing the forces from the six surrounding triangular mesh elements:

$$\vec{F}^0 = -\frac{1}{6} p_c \sum_{i=1}^{6} \vec{l}^{\,i} \times \vec{l}^{\,i+1} \tag{3.9}$$

By continuously adjusting the forces applied on the sphere elements, the desired internal and external cell pressures can be precisely maintained, further allowing for the independent control of α and b during the HCA test. Meanwhile, the deformation of the specimen in the radial direction can be captured effectively by monitoring the positions of all membrane sphere elements. Thus, with the flexible boundaries, this DEM model enhances the fidelity of simulation results and allow to impose complex loading paths in the hollow cylinder torsional shear tests. Similar flexible membrane algorithms have been previously demonstrated to accurately reproduce the mechanical characteristics of the real membrane (Wang et al. 2022c; Zhang et al. 2020b). The flexible membrane boundary can be generated as follows: 1) generate the DEM HCA sample with rigid wall boundaries; 2) determine the node positions of the triangular meshes surrounding the rigid sample boundaries according to the packing of spheres and select appropriate size of the membrane spheres (1.0 mm in diameter in this study); 3) create and bond the spheres with high bond strengths; 4) delete the rigid wall boundaries.

3.2.2 Validation of the DEM HCTST model

The HCTST simulation with the fixed major principal stress direction (α = 60°) and intermediate principal stress ratio (b = 0.5) is conducted for the validation work of the proposed DEM HCTST model. It is noted that the mean normal stress p is also kept unchanged at 98 kPa during the shearing process, and more details about the test can be found in the experimental study by Miura et al. (1986a). The particle size distribution (PSD) used in the validation is shown in Fig 3.2 (the blue dashed line). Fig 3.3 presents the comparison between the numerical simulation and experimental results. The good agreements in both stress and strain components demonstrate the ability of the proposed DEM HCTST model in the description of the mechanical behavior of granular materials in the HCTSTs.

More validation work can be found in our previous study (Song et al. 2024a). It is noted that the parameters related to the flexible membrane boundaries have been determined before shearing with the same method as the one in Zhang et al. (2020a). In short, tensile and suspension simulation tests are performed to determine the effective modulus E_{PP}, normal bond stiffness $\bar{k}_n$, tangential bond stiffness $\bar{k}_s$, and other related parameters. Meanwhile, a set of sliding tests was carried out to measure the friction coefficients between the membrane spheres, the soil particles, and the rigid walls. These parameters and the calibrated parameters related to soil particles used in the validation are listed in Table 3.2, and they will be also used in the following coupled CFD-DEM simulations of suffusion under various loading conditions considering different values of both α and b.

3.2.3 Simulation program

Based on the DEM HCTST model, nine suffusion simulations are designed with different α and b, as summarized in Table 3.3. As the main objective of this thesis is to study the suffusion under different loading conditions, the variation of FC is not considered, and all erosion cases have the same FC of 16%. As mentioned in Chapter 2, the granular soil is considered internally stable when the gap ratio D_{15} / d_{85} < 4 (Fannin and Moffat 2006; Kenney and Lau 1986) where the fine particles are difficult to be dislodged. Thus, the gap ratio of the gap-graded soil is set as 5.6 in this paper, as shown in the PSD curve (the red solid line in Fig 3.2).

The HCTST specimen used in the coupling simulation matches the size of the DEM model used in the validation process. Before coupling, the specimen is first generated with a relative density D_r (= (e_{max} - e) / (e_{max} - e_{min})) of around 64.3%. The specimen is then sheared under different loading paths with various fixed α and b, and the confining pressure p is kept constant at 50 kPa during the whole shearing process. When the deviatoric stress q reaches 55 kPa, the shearing process is paused, and the CFD domain is then introduced for the suffusion simulations. Meanwhile, the bottom rigid boundary is replaced by a filter wall with apertures approximately 5 times the radius of the largest fine particle, designed to permit fine particle migration while retaining the coarse fraction (Fig 3.4), so that the fine particles can be washed out of the specimen by the fluid flow. The stress states of the nine cases are kept the same except for the major principal stress direction and intermediate principal stress ratio during the suffusion process. In addition, the shearing will restart to adjust the stress components if the stress states of the specimens have deviated from the pre-determined values due to the seepage flow and loss of the fine particles.

The introduced CFD domain has the same inner and outer diameters as the particle assembly, while the height is set as 1.5 times that of the DEM sample. The free slip boundary condition is applied on both the inner and outer lateral CFD boundaries, and the fluid flows from top to bottom by applying the fluid pressures at the inlet and outlet boundaries. The hydraulic gradient i (= Δp / ρgL, where Δp denotes the differential pressure between the inlet and outlet boundaries, and L denotes the length of the particle assembly along the flow direction) is set as 2.0 in this study.

3.3 Simulation results and discussions

3.3.1 Mass loss of fine particles

Fig 3.5 shows the cumulative mass loss of fine particles during suffusion and the ultimate values in the nine cases having different α and b. It is concluded that the cases with smaller α have more fine particles eroded. In other words, as the major principal stress gradually rotates from the vertical direction to the horizontal direction, fewer fine particles are washed away by the fluid flow. Meanwhile, the fines mass loss is also influenced by the value of b. In detail, more fine particles are eroded in the cases having smaller b under otherwise same loading conditions, which is consistent with the observation in Liu et al. (2022). The differences of the fines mass loss in cases having different α and b can be explained by the stress-controlled HCTST loading system. In short, the circumferential stress σ_θ whose direction is perpendicular to the fluid flow increases with α, and another applied stress perpendicular to the vertical direction, the radial stress σ_r, increases as b increases (Yang 2013). Therefore, the restriction on the particles on the horizontal plane is more significant in cases having larger α and b, resulting that the largest cumulative eroded fines mass (10.8%) is observed in the case with α = 25° and b = 0.2, while the fines mass loss (8.3%) is the smallest when α = 65° and b = 0.8. The microscopic explanations for the macroscopic difference in the fines mass loss are given in the following sections.

Under the applied hydraulic gradient, the fine particles are not migrated uniformly through the pores due to the restriction by the clogging, applied stress and other factors (Wang et al. 2024a; Xiong et al. 2022; Zhou et al. 2022a). The DEM specimen is divided into nine equal layers along the vertical direction, as shown in Fig 3.6, to facilitate the investigation of the fines mass loss under different loading conditions. The cases with b = 0.2 and having α = 65° are taken as examples here. The distributions of the particle numbers in the nine layers before and after erosion are plotted in Fig 3.7. In general, most fine particles are eroded in layer 1 which is near the filter wall in all cases, and the loss of fine particles in layer 9 is also significant. By contrast, the variations of the particle numbers in middle layers are much smaller, which is consistent with Liu et al. (2020) and Zhou et al. (2022a). The possible explanation for this phenomenon is that the clogging in middle layers has restricted the movement of fine particles along the vertical direction. To have a clearer understanding, three coarse particles and the surrounding connected fine particles in layer 5 at t = 0s and 6s are shown in Fig 3.7. In comparison with the initial state, some fine particles are observed blocked in the pore between coarse particles at the moment t = 6s, resulting in that other fine particles cannot be migrated downward through this pore after the clogging occurs (Xiong et al. 2022). Meanwhile, the distribution of particle numbers along the vertical direction is affected by both α and b. As α increases from 25° to 65°, more particles are observed in the middle layers after erosion. Similarly, more fine particles are blocked in the middle layers with the increase of b. This can be also explained by the aforementioned different applied stress components in cases having various α and b: the increased restriction from the direction perpendicular to the fluid flow with the increases of both α and b results in more significant clogging in the middle layers, especially in layers 4 and 5 where there are more particles after erosion than the initial state.

3.3.2 Volume flow rate

There is a strong mutual influence between the fluid phase and particle system during the process of suffusion. Thus, the behavior of fluid phase should be also considered. The evolutions of the volume flow rate Q (= $\boldsymbol{v} \cdot A$, where A is defined as the area of the ring in the middle of layer 2 in this study; the flow velocity $\boldsymbol{v}$ is defined as $\boldsymbol{v} = \boldsymbol{k} \cdot \boldsymbol{i}$, and $\boldsymbol{k}$ is the hydraulic conductivity) in cases under different loading paths are shown in Fig 3.8. It is concluded that the volume flow rates all increase during the suffusion process despite the different loading conditions. The smallest rates in all cases are observed at the moment t = 0s, indicating that fines mass loss can increase the hydraulic conductivity $\boldsymbol{k}$ of the HCTST specimens. In addition, the increasement of permeability decreases with the increases of both α and b. The greatest value of the volume flow rate is observed in the case having α = 25° and b = 0.2, while the permeability is the smallest in the case with α = 65° and b = 0.8. In other words, greater fines mass loss corresponds to a higher volume flow rate.

3.3.3 Strong force chains

The force transmission and contact anisotropy are mainly contributed by the strong force chains in the granular packing, while the weak ones are mainly responsible for the maintenance of the stability of the strong force chains (Qian et al. 2021; Radjai et al. 1998). For the gap-graded materials Liu et al. (2020), further found that the fine particles with higher contact forces and connectivity are more difficult to be washed away by the fluid flow. To facilitate the investigation of the contributions of particles with different sizes to the strong force chains, three types of contacts are categorized in this study: the contact between coarse particles (*c-c* contact), the contact between fine particles (*f-f* contact) and the contact between coarse and fine particles (*c-f* contact) (Qian et al. 2021; Zhou et al. 2022a). The cut-off point between the strong and weak forces is set as the average contact force f_a here,(Liu et al. 2020; Minh et al. 2013) defined as:

$$f_a = \frac{\sum_{N_c} f_i}{N_c} \tag{3.10}$$

where N_c is the total number of contacts and f_i is the contact force at a contact. The forces which are greater than f_a are the strong contact forces, while the ones less than f_a are defined as the weak contact forces. In addition, the proportion P_s which denote the percentages of strong force chains in different types of contacts to the total strong force chains can be calculated by the following equation:

$$P_s = \frac{N_s^{ct}}{N_s} \tag{3.11}$$

where N_s^{ct} is the number of strong force chains in each contact type and N_s is the number of total strong chains.

Fig 3.9 shows the contributions of the three types of contacts to the strong force network for the same cases as those in Fig 3.7 before and after erosion. In general, the type of *c-c* contact plays a dominant role in both non-eroded and post-eroded particle assemblies in all cases, while the type of *f-f* contact accounts for the smallest proportion. On the other hand, fine particles have made more contributions to the strong force chains after the suffusion process, proved by the increases of the percents of the *c-f* and *f-f* contacts (Fig 3.9 (b) and (c)). This phenomenon can be attributed to that some of fine particles are clogged in the pores between coarse particles and may overfill the pores during the suffusion process. These fine particles will then bear greater contact forces (Liu et al. 2020), which further makes it more difficult for fine particles to be washed away.

The percents of the *c-f* and *f-f* contacts in strong force chains in layers of these post-eroded samples are plotted in Fig 3.10 and Fig 3.11 for further analysis. In general, fine particles are found to contribute more to the strong force chains in the middle layers, which is consistent with the particle number distribution shown in Fig 3.7. This means that some of the fine particles moved from the upper layers have overfilled the pores and been obstructed in the middle layers, further bearing greater loads. Meanwhile, the percents of the two types of contacts related to fine particles increase with both α and b in most layers, implying that more fine particles are strongly connected with other surrounding particles, and less fine particles are washed away as both α and b increase.

3.3.4 Anisotropy of contact force and force chain network

To have a deep understanding of the differences in suffusion under various loading conditions, the spatial distribution of the microscopic contact orientation is considered in this study (Xiong et al. 2020; Xiong et al. 2021; Zhou et al. 2022a). The distribution function which can quantify the contact information can be defined by the following Fourier series:

$$E(\varphi) = \frac{1}{2\pi}\left[1 + \mathrm{A}\cos(\varphi - \mathrm{B})\right] \tag{3.12}$$

where φ denotes the angle between the directions of the contact and vertical axis; A and B are the magnitude and the corresponding principal direction of the anisotropy, respectively, and they can be calculated by the following equations (Qian et al. 2021; Xiong et al. 2020):

$$\mathrm{A} = 2\sqrt{\left[\int_0^{2\pi} E(\varphi)\cos 2\varphi d\varphi\right]^2 + \left[\int_0^{2\pi} E(\varphi)\sin 2\varphi d\varphi\right]^2} \tag{3.13}$$

$$\mathrm{B} = \frac{1}{2}\arctan\frac{\int_0^{2\pi} E(\varphi)\sin 2\varphi d\varphi}{\int_0^{2\pi} E(\varphi)\cos 2\varphi d\varphi} \tag{3.14}$$

Fig 3.12 and Fig 3.13 show the spatial distributions of normal contact force and contact normal for three cases before and after suffusion. After suffusion, the principal directions of both normal contact force and contact normal rotate slightly to the vertical direction in the three cases, and more contacts are generated along the vertical direction due to the seepage flow. Meanwhile, the specimens with α = 45° and 65° tend to be less anisotropic with the decreased anisotropy magnitudes, while the anisotropy magnitude of the sample with α = 25° shows a slight increase. To have a better understanding, the evolutions of the two anisotropy parameters of both normal contact force (A_n and B_n) and contact normal (A_c and B_c) for all cases during the suffusion process are plotted in Fig 3.14 and Fig 3.15. In general, the applied fluid flow is observed to be able to reduce the anisotropy levels although constant anisotropic stresses are continually imposed on the specimens in cases with α = 45° and 65°. For cases with α = 25°, the anisotropy magnitudes also decrease although there is a slight increase during the initial seconds. The slightly decreased anisotropy magnitudes and the corresponding directions which are slightly rotating to the fluid direction suggest that some contacts along the major principal stress directions are destroyed, and some new contacts are generated along the vertical direction under the action of fluid flow. Furthermore, the possible explanation of the initial increase in magnitude in cases with α = 25° is that the contacts in the horizontal plane are not as strong as those in the cases where α = 45° and 65° due to the smaller circumferential stress σ_θ (Yang 2013), and some of the horizontal contacts are easier to be destroyed in the initial stage. The free particles are then quickly connected with the surrounding particles along the flow direction which is close to the initial principal direction of anisotropy. Thus, the anisotropy principal directions rotate to the vertical direction quickly, and the specimens become more anisotropic at the initial stage. Like the cases with α = 45° and 65°, some of the contacts along the anisotropy principal direction break during the following suffusion process, and the magnitudes begin to decrease.

The anisotropy magnitudes before suffusion show a decreasing trend with b when α = 25° and 45°, while an opposite trend is observed when α = 65°, as shown in Fig 3.16. This arises from the fact that when α = 65°, the radial stress σ_r is relatively large. Concurrently, the vertical stress σ_z decreases as the increase of b. This reduction in σ_z results in a higher number of inherent contacts distributed along the vertical direction breaking, and the generation of new contacts along the horizontal direction in the cases with larger b-values during shearing (Brosse 2012; Song et al. 2024a; Yang 2013). On the other hand, although the majority of loads are resisted by the contacts distributed vertically when α = 25° and 45°, more contacts are observed along the horizontal direction due to the increase of the radial stress σ_r with b, resulting in the decrease of the anisotropy magnitude with b. Consequently, it becomes increasingly challenging for fine particles to overcome the horizontal constraints in cases with larger b-values, consistent with the observation in Fig 3.5. Similarly, for cases having the same b, the more the principal direction deviates from the fluid (vertical), the higher restriction from the horizontal direction, and the fewer the fines mass loss. More information about the contact distribution can be seen in the force chain network analysis in Fig 3.17.

Local contact force networks (the zone highlighted by the red dashed line) of some cases are shown in Fig 3.17 for the microscopic analysis. From the front views, the stress anisotropy is clearly captured by the force chains which are gradually rotating to be close to the horizontal direction as α increases from 25° to 65° (Fig 3.17(d) – (f)), consistent with Fig 3.14 and Fig 3.15. Meanwhile, more strong force chains are observed in the horizontal plane from the top views due to the increased restriction by the radial stress σ_r with the increase of b (Fig 3.17 (a) – (c)).

3.3.5 Pore structure and erosion path

For the specimens under different loading conditions, the internal particles undergo rotation and sliding during the shearing process, and the contacts between particles exhibit varying degrees of buckling and collapse (Song et al. 2024a; Tordesillas 2007). In other words, the internal structures of these granular systems have undergone varying degrees of change, and correspondingly, the pores between the particles have also exhibited differences. To describe the pore structures of the particle assemblies, the maximal ball (MB) method which can be used to extract pore networks from generic and arbitrary 3D images is introduced (Dong and Blunt 2009). With this method, Silin et al. (2003) and Silin and Patzek (2006) studied the dimensionless capillary pressure during drainage processes. Xiong et al. (2022) investigated the pore structure of porous media, further analysing the effect of pore size on the degree and position of clogging. In this study, the HCTST specimen is first divided into many voxels. Then, the MB method operates by finding the largest inscribed ball at each voxel coordinate whose radius is equivalent to the minimal distance to the particle phase or boundaries (Xiong et al. 2022). Then, the balls that are included in the largest inscribed balls are regarded as inclusions and are removed. The rest ones, referred to as the maximal balls, provide a non-redundant representation of the pore space. The maximal ball clusters are then extracted and plotted to outline the porous skeletons, thereby offering a depiction of the attributes of pores. More details about the MB method can be found in previous studies (Arand and Hesser 2017; Dong and Blunt 2009; Silin and Patzek 2006).

Fig 3.18 shows the local pore structures of some cases, and the local zone is the same as that in Fig 3.17. Compared to the case with α = 25° and b = 0.2, the pores in the specimen having α = 25° and b = 0.8 are narrower in the radial direction (see the pores highlighted by the black circles), resulting in that the pores in the specimen with a larger b have a poorer connectivity along both the radial and vertical directions. Meanwhile, the pores in the specimen with a larger α are narrower in the circumferential direction (white circles in Fig 3.18 (b) and (c)). The variations in the pore structures and connectivity can be explained by the same reason that accounts for the different distributions of force chains. As the radial stress σ_r increases with b, particles undergo greater compression, consequently generating more contacts and reducing the pore cavities in the radial direction. Similarly, the increased circumferential stress σ_θ and torsional stress $\tau_{z\theta}$ with α lead to a reduction in pore cavities in the circumferential direction.

It is noted that the larger the minimal distance, the larger the local pore size. When the value of distance of a voxel is larger than the sizes of fine particles, the fine particles can migrate through this voxel. In this study, a statistical index P_{vf}, i.e., the percentage of voxels that allow fine particles to pass through to all voxels in layers, is defined in the following equation to better describe the connectivity of the pores along the vertical direction:

$$P_{vf} = \frac{N_{vf}}{N_v} \times 100\% \tag{3.15}$$

where N_{vf} is the number of voxels allowing fine particles to pass through in one layer, and N_v is the number of all voxels in this layer. When the value of P_{vf} is zero, there is no chance for fine particles to pass through this layer. Conversely, if P_{vf} is 100%, all fine particles have the potential to migrate through under the effect of seepage flow. The HCTST specimens are divided into about 650 layers along the vertical direction here. Fig 3.19 shows the distribution of P_{vf} in layers for the same cases as those in Figure 20. Notably, the values represented in Fig 3.19 are the minimal ones observed in the three cases. The values of P_{vf} are always the smallest in many layers when α = 65° and b = 0.8. This suggests an increased propensity for fine particles to be obstructed within these layers, thereby impeding their ability to migrate a long distance. In contrast, the P_{vf} values are larger in the other cases, indicating enhanced connectivity along the vertical direction.

The various pore structures further cause that the fine particles are migrated by the fluid along different paths, as shown in Fig 3.20. In this figure, the dots with different colours and shapes represent the positions of one fine particle in cases having various α and b at different suffusion moments. In general, when α and b are large, particles suffer more restriction in the horizontal plane which is perpendicular to the fluid flow, and the connectivity of pores along the vertical direction is poor (Chang and Zhang 2013). Thus, the fine particles are more difficult to be washed away compared to those in the cases having smaller α and b. For example, the fine particles in the cases with α = 25° move a longer distance along the vertical direction, while the fine particles in the cases with larger α move a shorter distance, especially in the case with α = 65° and b = 0.8 where the fine particle is clogged after a short movement (Fig 3.20). Moreover, Fig 3.21 plots the average vertical displacement of the fine particles, showing that the fine particles in the specimens with smaller α and b travel a greater distance under the effect of seepage flow. The provided different pore structures and migration paths in the HCTST specimens under different loading conditions can to some extent explain the various fines mass loss in Fig 3.5.

3.4 Conclusions

A stress-controlled HCTST model in DEM which can achieve the independent control of the major principal stress direction and intermediate principal stress ratio is first developed in this Chapter. Then, the CFD solver was introduced to conduct coupled CFD-DEM simulations on gap-graded granular soils aiming to reveal the suffusion under complex loading conditions. Both macroscopic and microscopic responses during the suffusion were investigated and discussed in detail. The main findings are summarized as follows:

1. Both α and b have influences on the fines mass loss. In general, fewer fine particles are washed away by the fluid as both α and b increase. The variations of the particle numbers in layers show that most eroded particles are from the layer near the CFD domain outlet, and clogging is observed in the middle layers. Meanwhile, more particles are found clogged in the middle layers as both α and b increase. In addition, the permeability of the HCTST specimens shows an increasing trend during the suffusion process, and the volume flow rates are larger in the cases having more particles loss, illustrated by the decrease of permeability with α and b.

2. Compared with coarse particles, fine particles make smaller contribution to the strong force chains, while more fine particles are observed to be strongly connected after the suffusion process. The percents of the contacts related to fine particles in strong contacts increase with α and b, implying that more fine particles are clogged and difficult to be eroded in cases having larger α and b.

3. From the microscopic perspective, the magnitudes of contact anisotropy are to some extent weakened by the fluid flow, and the corresponding principal directions slightly rotate to the fluid direction during suffusion in all cases. In addition, more fine particles are washed away in cases whose anisotropy principal directions are close to the fluid flow direction.

4. With the increase of α, the force chains are distributed more along the horizontal direction, and the restriction on the particles from the horizontal direction increases. Meanwhile, the increased radial stress σ_r with b enhances the restriction. In addition, the pore structures also exhibit differences, and the vertical connectivity of the pores in the specimens with larger α and b is poorer.

5. The various pore structures and distributions of the contacts in specimens under different loading conditions induce fine particles to migrate along different paths, further resulting in the differences in fines mass loss and variations in particle numbers in layers.

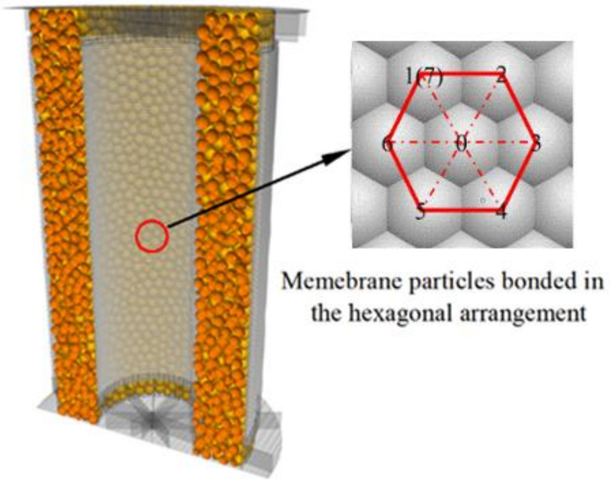

Fig 3.1 DEM HCTST model and the flexible membrane boundary.

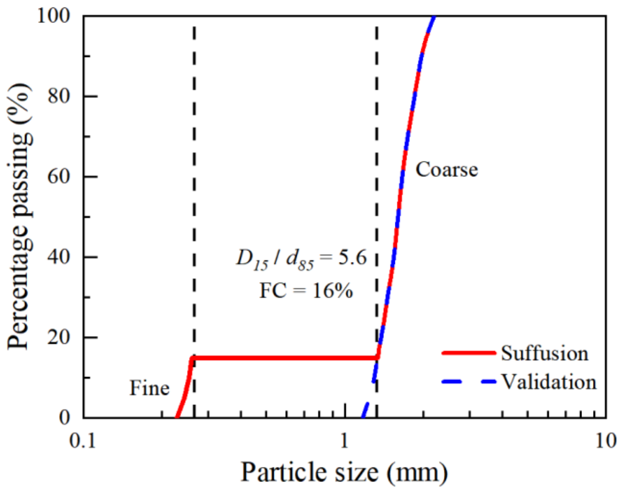

Fig 3.2 Particle size distribution employed in the validation and suffusion simulations.

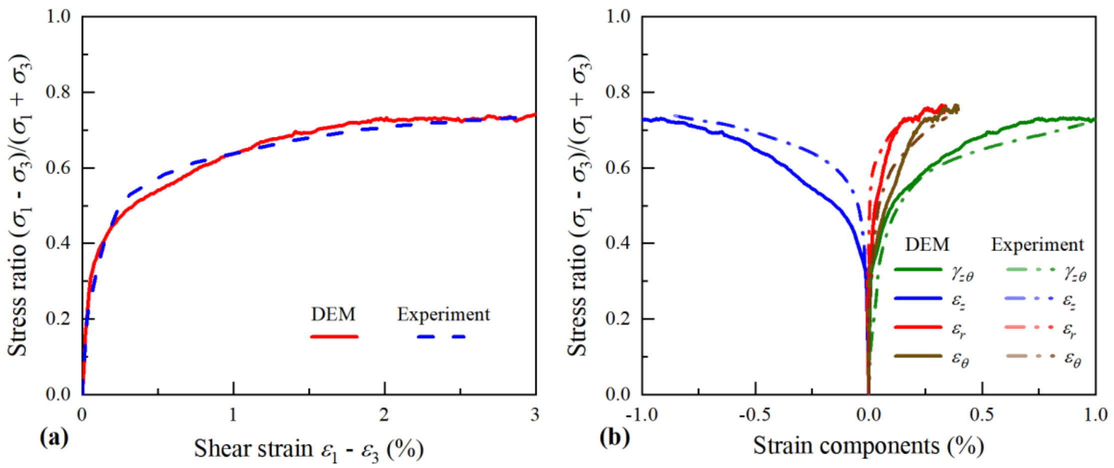

Fig 3.3 Comparison between the experimental and numerical results: (a) Stress ratio; (b) Strain components.

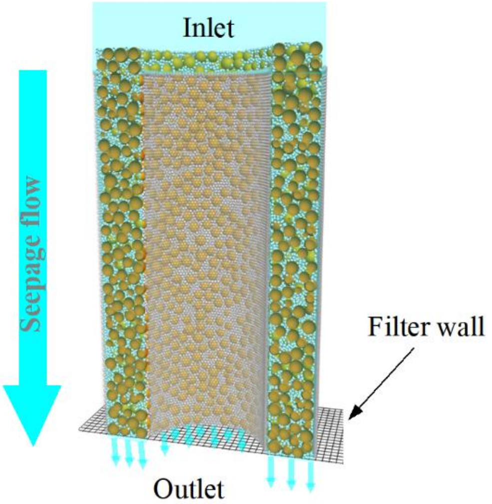

Fig 3.4 The coupled CFD-DEM suffusion model.

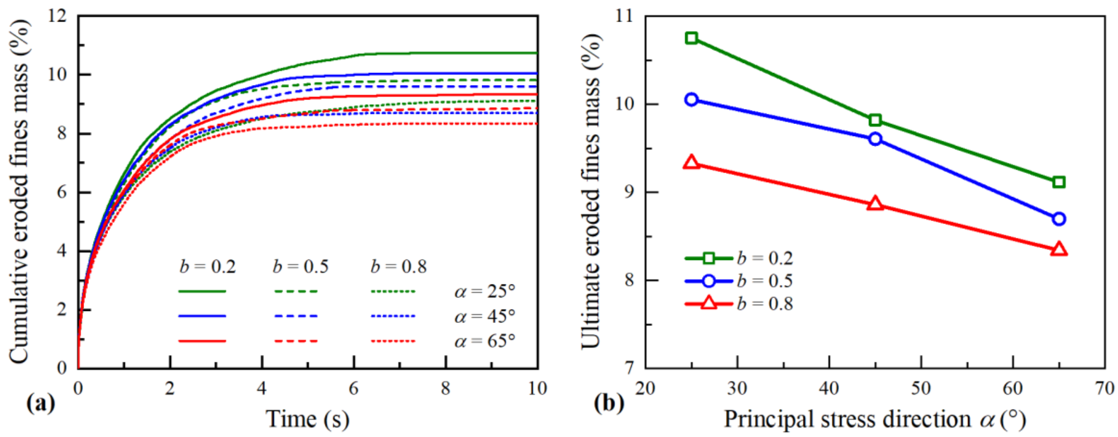

Fig 3.5 (a) Cumulative eroded fines mass during suffusion and (b) the ultimate values for cases with different α and b.

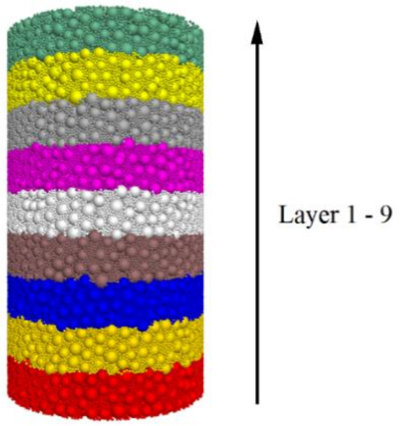

Fig 3.6 Classified layers of the DEM sample along the vertical direction.

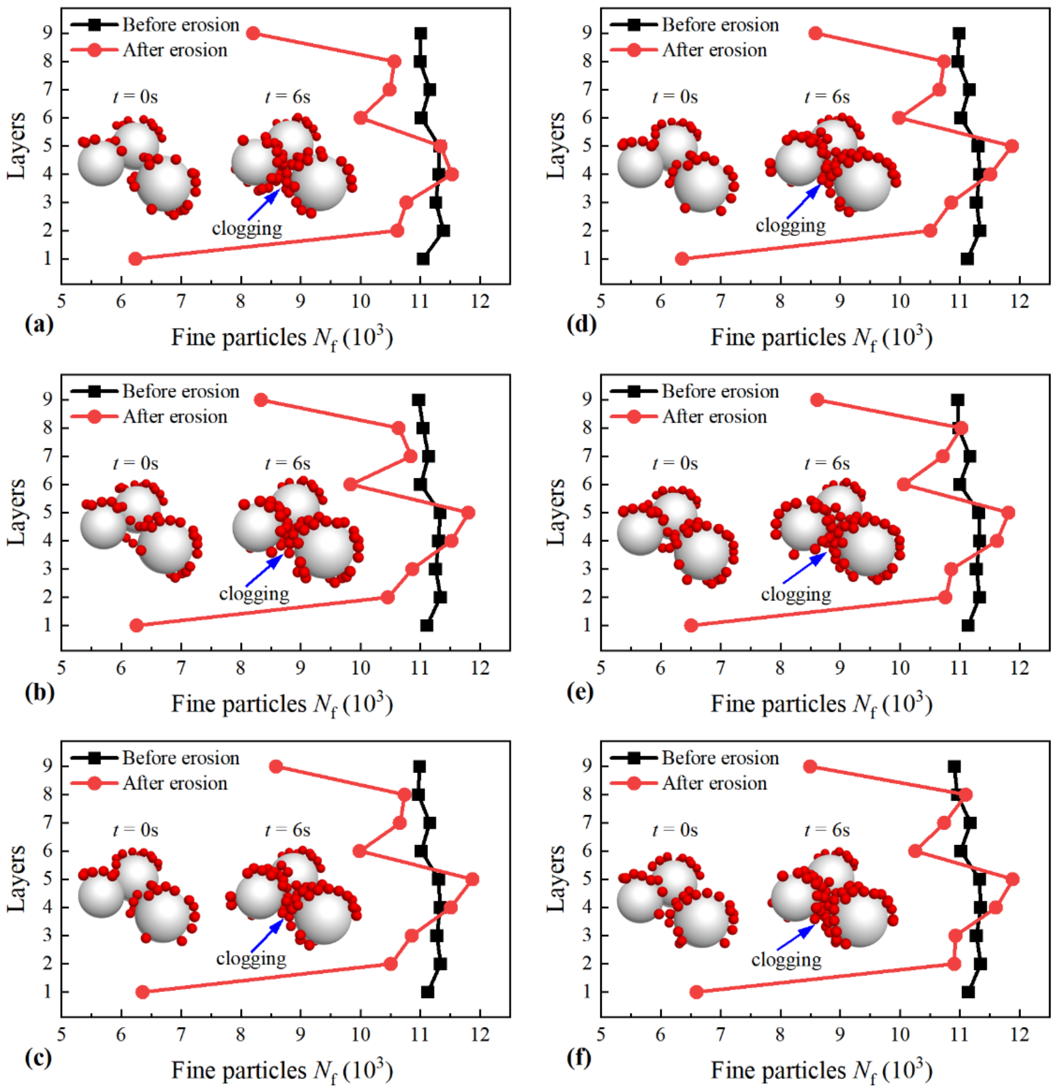

Fig 3.7 Distribution of particle numbers in layers for cases: (a - c) b = 0.2 with α = 25°, 45°, and 65°, respectively; (d - f) α = 65° with b = 0.2, 0.5 and 0.8, respectively.

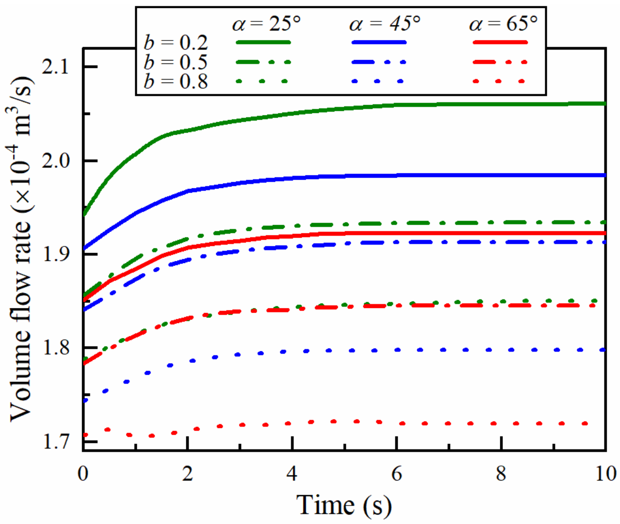

Fig 3.8 Evolution of the volume flow rate for all cases.

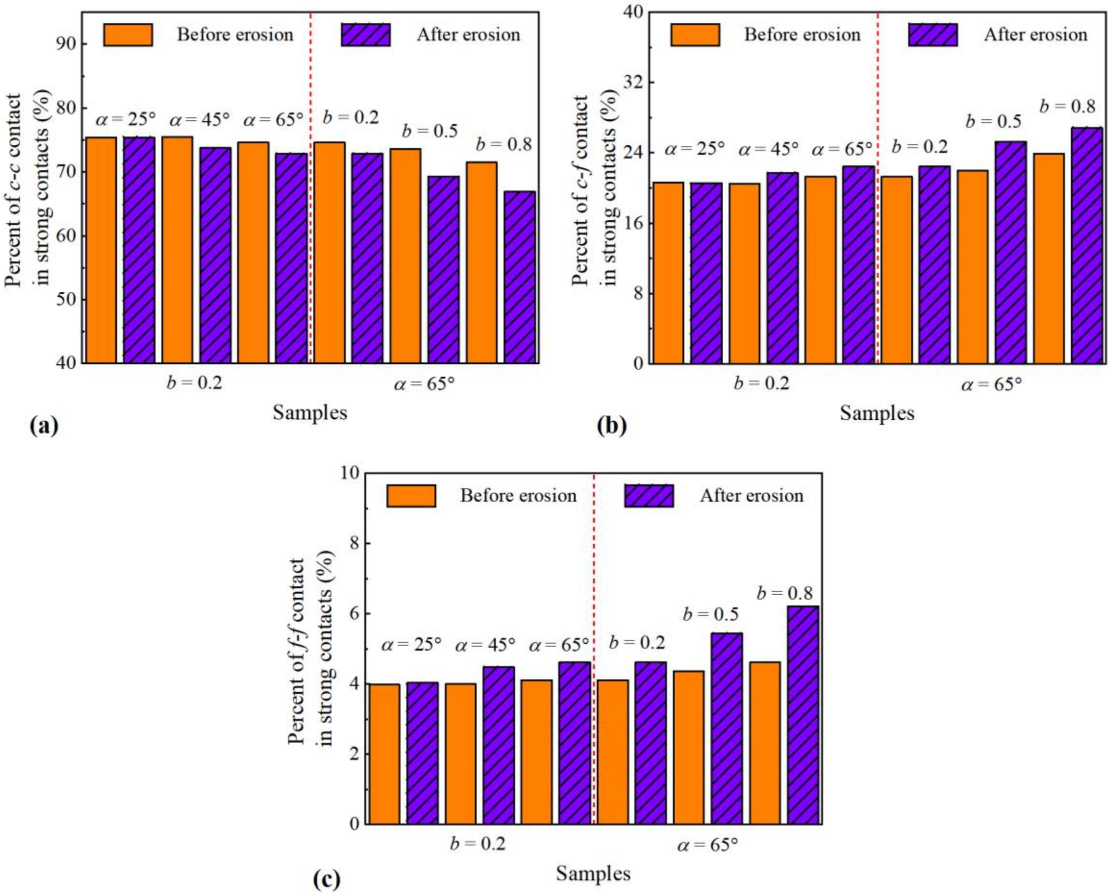

Fig 3.9 Contributions of (a) *c*-*c*, (b) *c*-*f* and (c) *f*-*f* contacts to the strong force chain network before and after erosion.

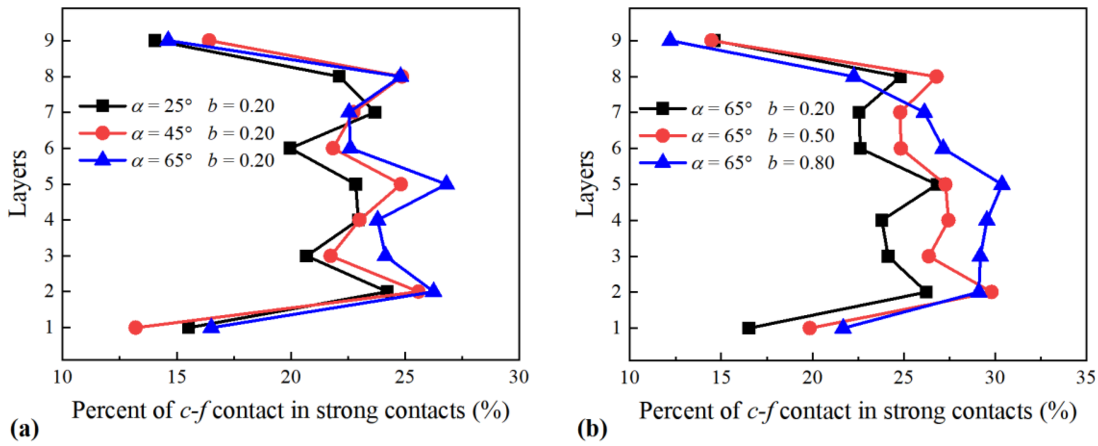

Fig 3.10 Percent of *c*-*f* contact in the strong contacts in layers for cases: (a) $b = 0.2$ with $\alpha = 25°$, 45°, and 65°, respectively; (b) $\alpha = 65°$ with $b = 0.2$, 0.5 and 0.8, respectively.

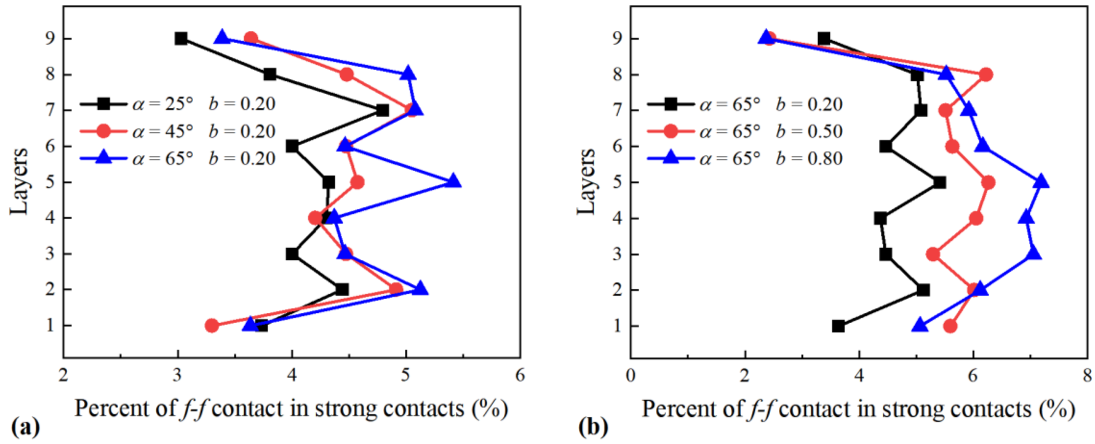

Fig 3.11 Percent of *f-f* contact in the strong contacts in layers for cases: (a) $b = 0.2$ with $\alpha = 25°$, 45°, and 65°, respectively; (b) $\alpha = 65°$ with $b = 0.2$, 0.5 and 0.8, respectively.

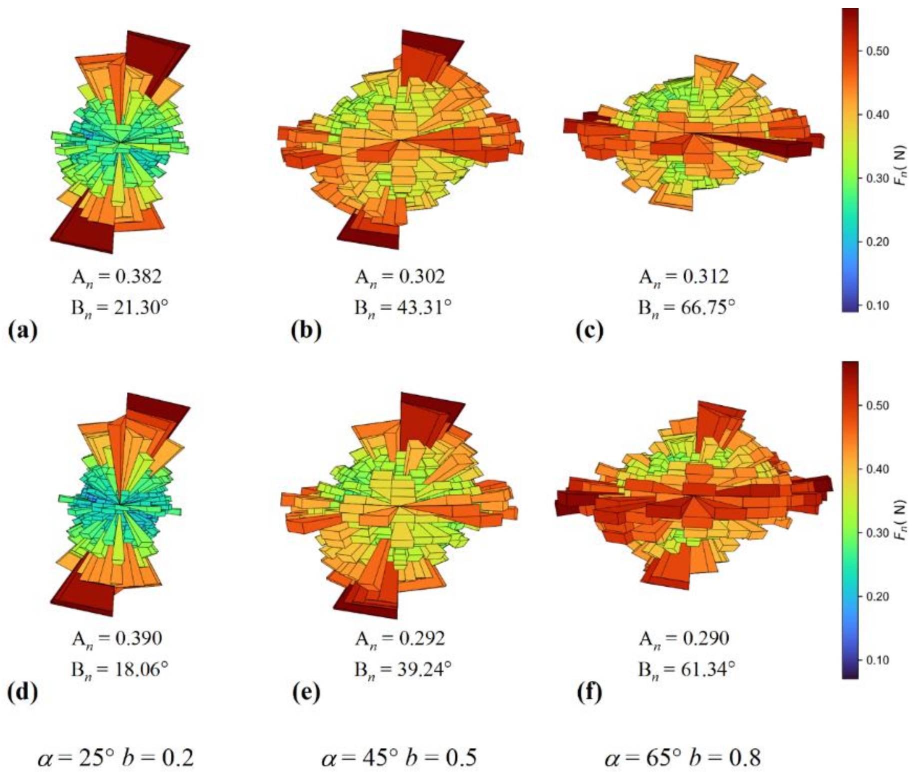

Fig 3.12 Spatial distribution of normal contact force (a - c) before and (d -f) after suffusion: $\alpha = 25°$ and $b = 0.2$ (left); $\alpha = 45°$ and $b = 0.5$ (mid) and $\alpha = 65°$ and $b = 0.8$ (right).

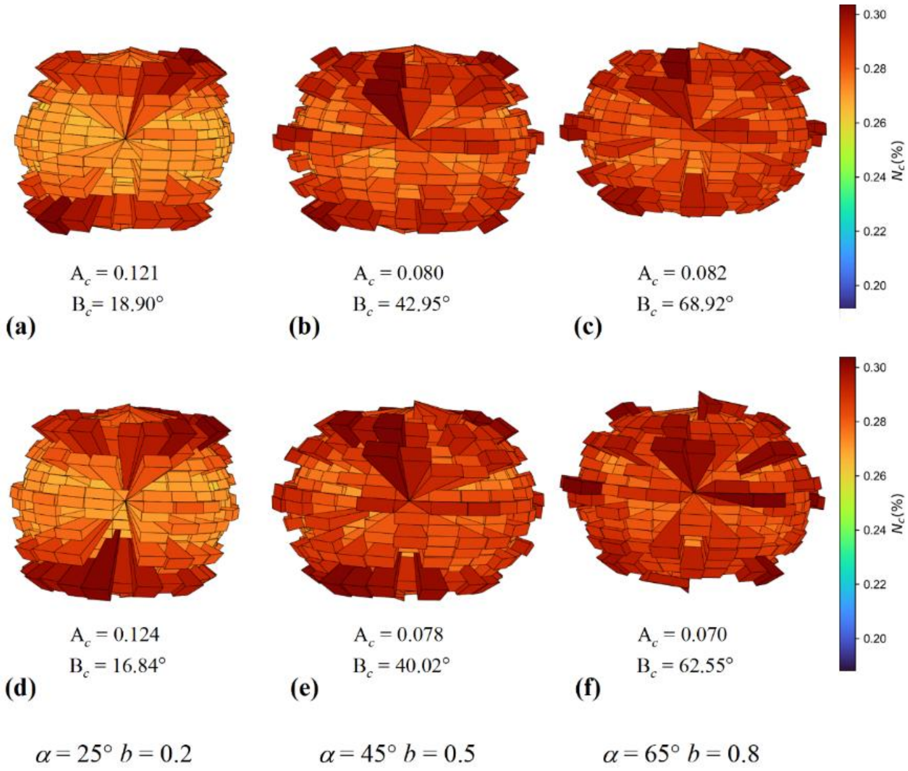

Fig 3.13 Spatial distribution of contact normal (a - c) before and (d -f) after suffusion: $\alpha = 25°$ and $b = 0.2$ (left); $\alpha = 45°$ and $b = 0.5$ (mid) and $\alpha = 65°$ and $b = 0.8$ (right).

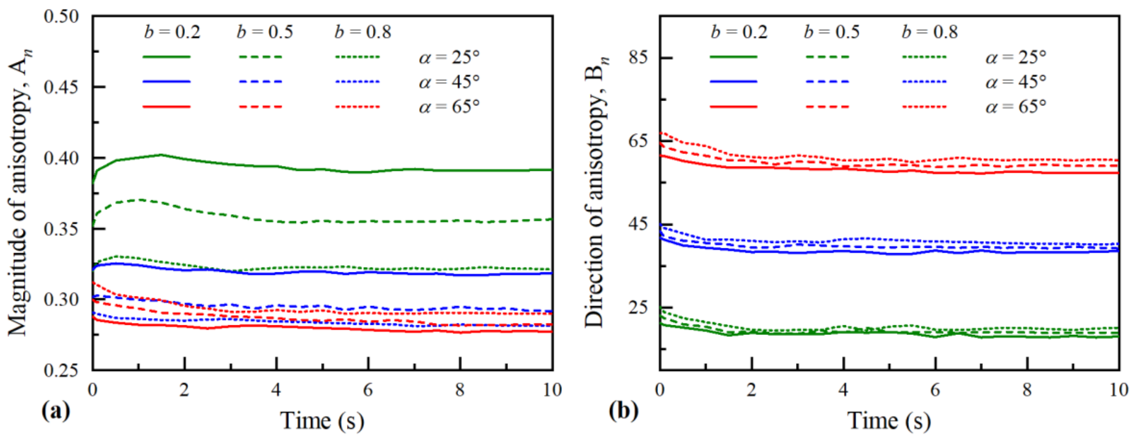

Fig 3.14 Evolution of the (a) anisotropy magnitude and (b) principal direction of normal contact force during suffusion.

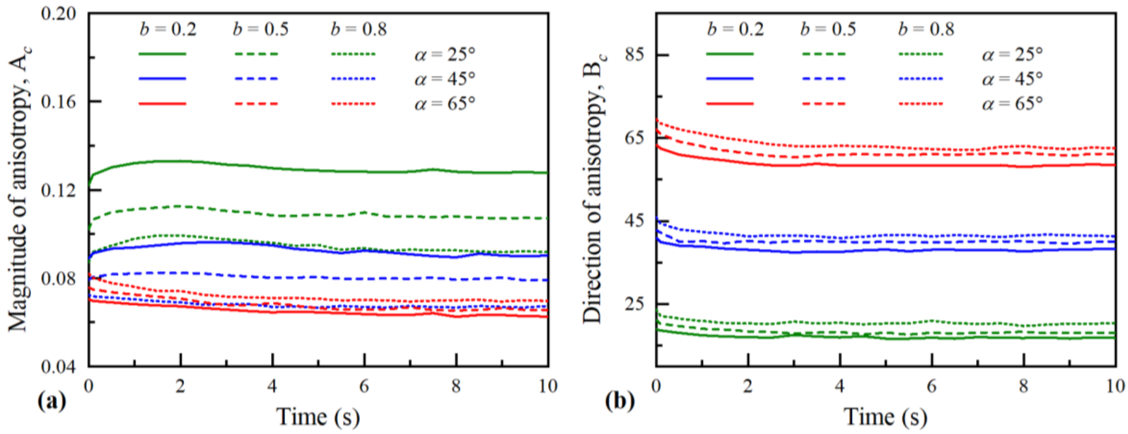

Fig 3.15 Evolution of the (a) anisotropy magnitude and (b) principal direction of contact normal during suffusion.

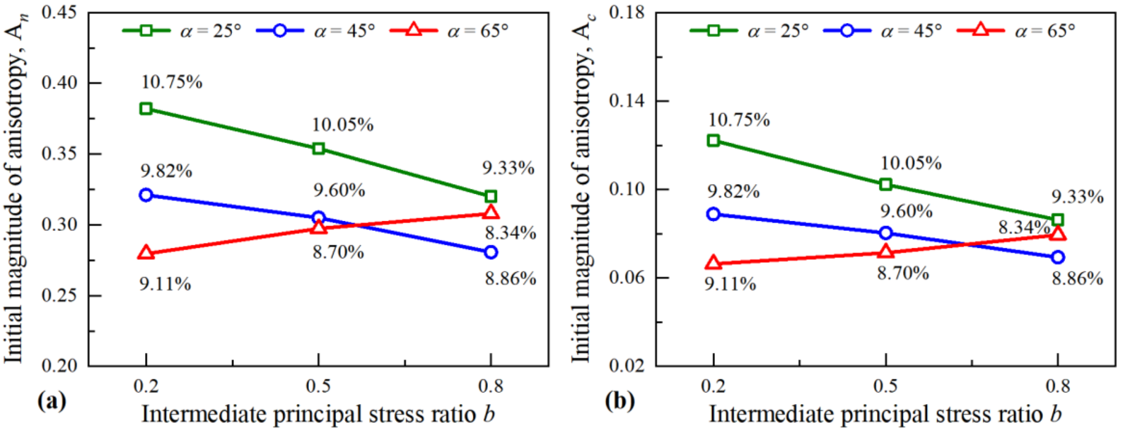

Fig 3.16 Relationship between the initial anisotropy magnitude and intermediate principal stress ratio: (a) normal contact force; (b) contact normal (the number near the point is the percentage of ultimate fines mass loss).

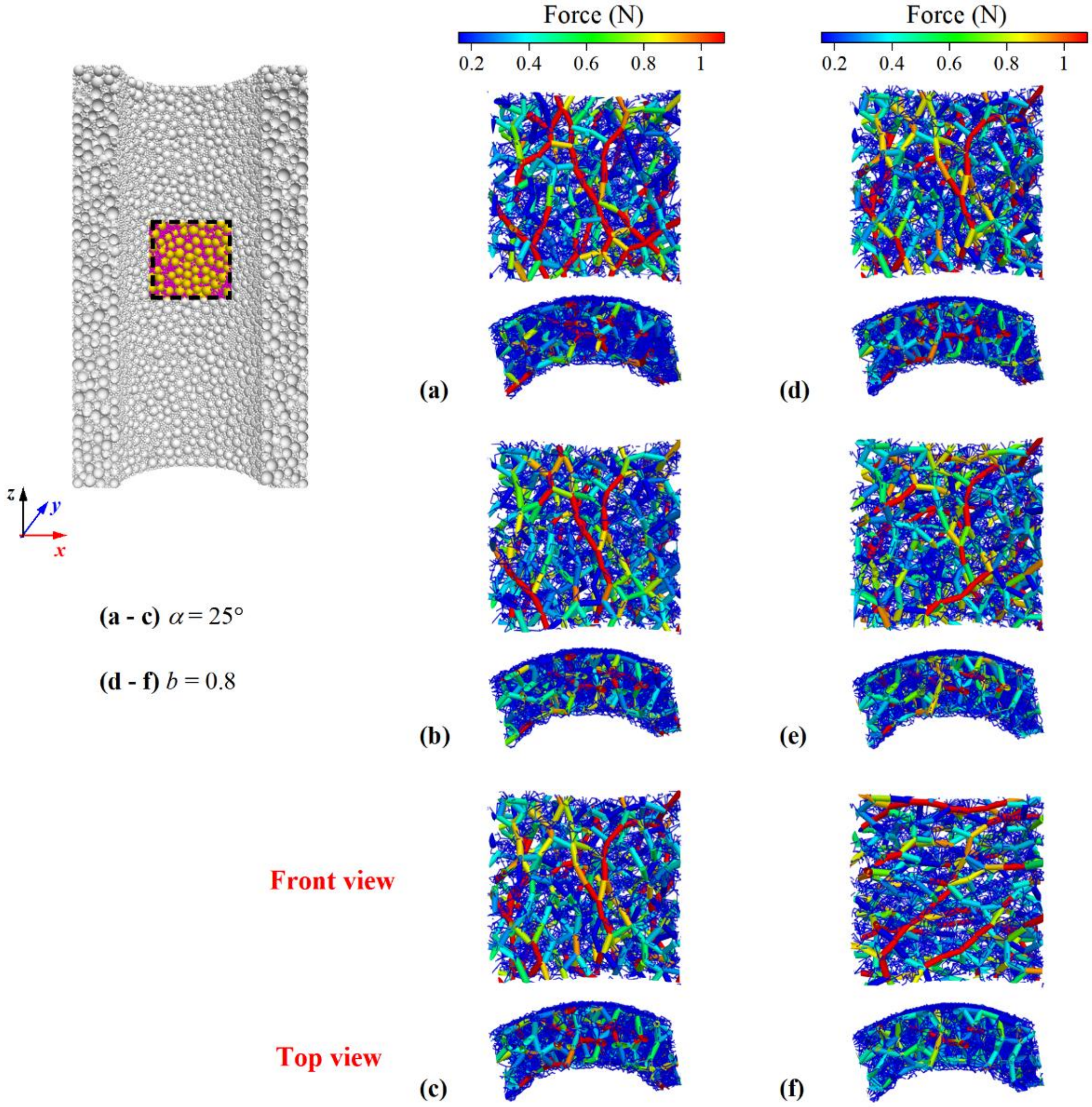

Fig 3.17 Local contact force networks for cases: (a - c) α = 25° with b = 0.2, 0.5 and 0.8, respectively; (d - f) b = 0.2 with α = 25°, 45°, and 65°, respectively.

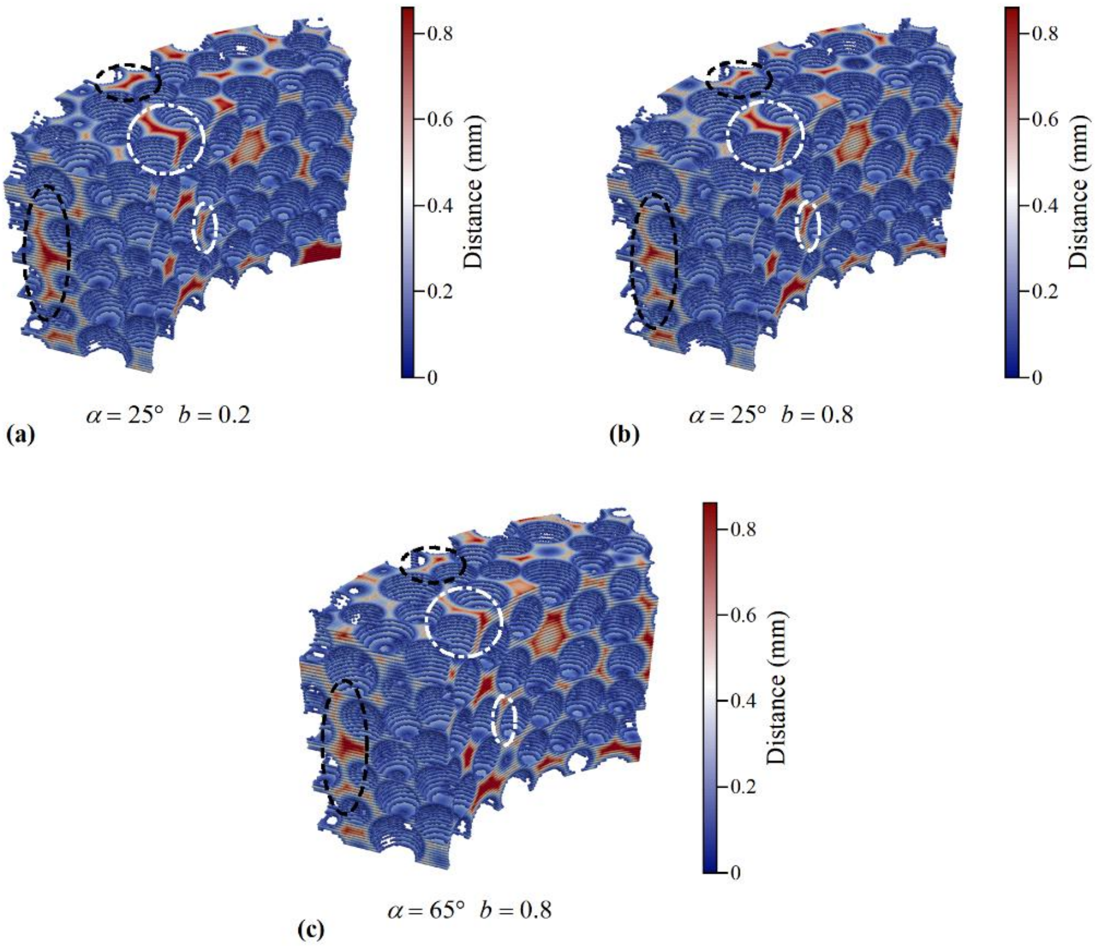

Fig 3.18 Pore structures for cases: (a) α = 25° with b = 0.2; (b) α = 25° with b = 0.8; and (c) α = 65° with b = 0.8.

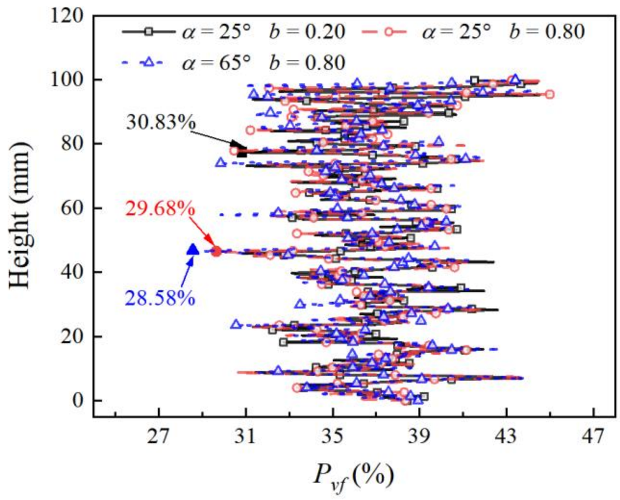

Fig 3.19 Percent of voxels allowing fine particles to pass through in layers.

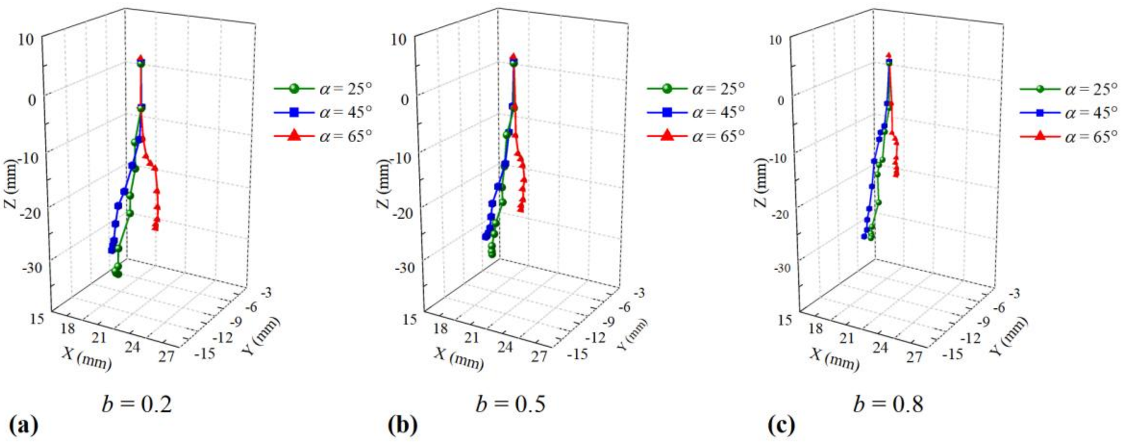

Fig 3.20 Erosion paths of a fine particle in cases with different α and b.

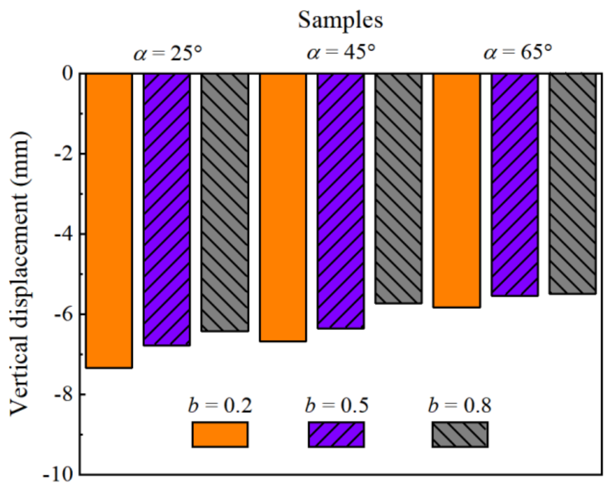

Fig 3.21 Average vertical displacement of fine particles for all cases.

Table 3.1 Formulas employed to determine stresses and strains in the HCTST

Vertical	$\sigma_z = \dfrac{W}{\pi(r_o^2 - r_i^2)}$	$\varepsilon_z = \dfrac{z}{H}$
Radial	$\sigma_r = \dfrac{p_o r_o + p_i r_i}{r_o + r_i}$	$\varepsilon_r = -\dfrac{\mu_o - \mu_i}{r_o - r_i}$
Circumferential	$\sigma_\theta = \dfrac{p_o r_o - p_i r_i}{r_o - r_i}$	$\varepsilon_\theta = -\dfrac{\mu_o + \mu_i}{r_o + r_i}$
Torsional	$\tau_{z\theta} = \dfrac{3T}{2\pi(r_o^3 - r_i^3)}$	$\gamma_{z\theta} = \dfrac{\theta}{3H(r_o^2 - r_i^2)}$
Major principal	$\sigma_1 = \dfrac{\sigma_z + \sigma_\theta}{2} + \sqrt{(\dfrac{\sigma_z + \sigma_\theta}{2})^2 + \tau_{z\theta}^2}$	$\varepsilon_1 = \dfrac{\varepsilon_z + \varepsilon_\theta}{2} + \sqrt{(\dfrac{\varepsilon_z + \varepsilon_\theta}{2})^2 + \gamma_{z\theta}^2}$
Intermediate principal	$\sigma_2 = \sigma_r$	$\varepsilon_2 = \varepsilon_r$
Minor principal	$\sigma_3 = \dfrac{\sigma_z + \sigma_\theta}{2} - \sqrt{(\dfrac{\sigma_z + \sigma_\theta}{2})^2 + \tau_{z\theta}^2}$	$\varepsilon_3 = \dfrac{\varepsilon_z + \varepsilon_\theta}{2} - \sqrt{(\dfrac{\varepsilon_z + \varepsilon_\theta}{2})^2 + \gamma_{z\theta}^2}$

Note: ε_z, ε_r, ε_θ and $\varepsilon_{z\theta}$ are the vertical, radial, circumferential and torsional shear strain components, respectively; z, θ, μ_o and μ_i are the vertical, angular circumferential, outer and inner radial displacements, respectively; H, r_o, and r_i are the initial height, outer and inner radii of the HCTST specimen, respectively.

Table 3.2 Parameters used in the coupled CFD-DEM simulations

Parameters			Value
DEM	Elastic modulus	E_{PP} (Pa)	2.0×10^8
		E_{PW} (Pa)	2.0×10^8
		E_{PM} (Pa)	2.0×10^6
		E_{MM} (Pa)	1.00×10^6
		E_{MW} (Pa)	1.00×10^6
	Stiffness ratio	k_{PP}	3.0
		k_{PW}	3.0
		k_{PM}	3.5
		k_{MM}	3.0
		k_{MW}	4.0
	Friction coefficient	μ_{PP}	0.30
		μ_{PW}	0.20
		μ_{PM}	0.35
		μ_{MM}	0.90
		μ_{MW}	0.65
	Rolling friction coefficient	μ_r	0.1
	Normal stiffness of the linear parallel bond	$\bar{k}_n$ (Pa/m)	3.0×10^8
	Tangential stiffness of the linear parallel bond	$\bar{k}_s$ (Pa/m)	1.00×10^8
	Density of particles	ρ_p (kg/m^3)	2650
	Density of membrane particles	ρ_m (kg/m^3)	809
CFD	Cells	Radial × circumferential × vertical directions	3 × 12 × 25
	Fluid viscosity	μ (Pa $*$ s)	1.0×10^{-3}
	Density of fluid	ρ_f (kg/m^3)	1000

Table 3.3 Simulation program

Test	1	2	3	4	5	6	7	8	9
α	25°	25°	25°	45°	45°	45°	65°	65°	65°
b	0.2	0.5	0.8	0.2	0.5	0.8	0.2	0.5	0.8

CHAPTER 4: COUPLED CFD-DEM INVESTIGATION ON THE INTERNAL EROSION AND MECHANICAL BEHAVIORS OF GAP-GRADED GRANULAR SOILS UNDER BIAXIAL SHEAR CONDITION

4.1 Introduction

The loading condition of soil is acknowledged to be varying both temporally and spatially in hydraulic earth structure engineering (Hu et al. 2022; Liu et al. 2022; Luo et al. 2019). For example, soil is often subjected to biaxial shear conditions when the deformation is constrained in one principal direction while shear stresses develop predominantly along the other two directions. Typical situations include embankments, retaining structures, and tunneling, where lateral displacements are restricted, leading to a state dominated by two principal stresses. In addition, from the perspective of the stress-strain behavior, soil at different spatial locations may reside at different stress states relative to the peak stress. The differences in stress history may lead to varied responses of soil when subjected to external disturbances such as internal erosion. Furthermore, soil with different stress history may exhibit different mechanical behaviors after the same internal erosion. In this Chapter, a novel coupled CFD–DEM framework capable of capturing various stress states of soil under biaxial shear conditions is proposed, aiming to investigate the differences in erodibility of gap-graded soil specimens under different stress states and to study the influence of internal erosion on the mechanical behaviour of soil from both macroscopic and microscopic perspectives. It is noted that the effect of confining pressure is also considered in the stress state. Therefore, the stress states are characterized by the confining pressure σ_3 and the stress ratio mobilization $\beta = (\eta - 1) / (\eta_c - 1)$ in this Chapter (Liu et al. 2022). Here, $\eta = \sigma_1 / \sigma_3$ represents the principal stress ratio, and η_c is the critical principal stress ratio.

A total of 12 CFD-DEM simulations considering various confining pressures and stress ratio mobilizations are conducted. During the erosion process, the stress states are kept constant by adjusting the DEM biaxial shear model. After erosion, all specimens are re-sheared form their current stress states. The results are then compared to the non-eroded soil specimens under different confining pressures. The relationship effect of stress state on fines loss, the variations of the mechanical behaviour of the specimens after erosion and other results are discussed in detail.

4.2 Simulation procedure

This Chapter focuses on the internal erosion of gap-graded granular soil under various stress states and its subsequent shear behaviours under the biaxial shear condition. The following four consecutive stages, as shown in Fig 4.1, are performed in each simulation.

4.2.1 Specimen generation

The DEM model of the biaxial shear test is generated with the gap-graded soil. The DEM specimen has a size of 15 mm in both length and width, while the height is twice the length/width (Fig 4.2 (a)). The variation of FC is not considered in this paper, and the fine particles underfill the voids among the coarse particles with a FC of about 25% in all specimens. The particle size distribution (PSD) of the soil is plotted in Fig 4.3. The gap ratio of the gap-graded soil used in this Chapter is set as approximately 5.6 which is as same as that in Chapter 3.Then, the six surrounding walls of the specimen are precisely controlled by the servo algorithm, ensuring that the particles inside the container are subjected to the targeted isotropic compression, thereby achieving the desired confining pressure (Wang et al. 2022b; Zhou et al. 2019b). In addition, the relative densities D_r are consistently maintained within a range of 64.5% to 68.5% for all samples (Zhou et al. 2019b).

4.2.2 Biaxial shear before erosion

The front and back walls are fixed after the generation stage, and the confining pressure σ_3 is maintained constant by adjusting the forces applied on the lateral walls during the shearing process. Then, the specimens are sheared by moving the top wall downward until the predetermined stress ratios are reached. Fig 4.4 plots the stress ratio evolution of the specimens under the confining pressures of 25 kPa, 50 kPa, and 100 kPa, and the stress states used in the following erosion process are listed in Table 4.1. Like Chapter 3, the inter-particle contact behaviour (PP) is described by the rolling resistance linear contact model, while the linear elastic contact model is employed to describe the interaction between particle and wall (PW) in this study. The relevant parameters including the stress ratio of PP contact (k_{PP}) and stress ratio of PW contact (k_{PW}) are summarized in Table 4.2.

4.2.3 Internal erosion

During the erosion stage, the bottom boundary wall of the DEM specimen is changed to a filter wall containing holes smaller than the coarse particles but larger than the fine particles, so that only the fine particles can be washed away (see Fig 4.2 (b)). With the DEM specimens under the predetermined stress states, the CFD part is then introduced. The introduced CFD domain has the same length and width as the DEM samples, while the height is 1.5 times that of the particle assembly. The free slip boundary conditions are applied on the lateral CFD boundaries, and the water flows along the vertical direction by applying the differential pressure between the inlet and outlet boundaries. In this Chapter, the hydraulic gradient i is set as 2.0. Related CFD parameters used in the erosion simulations are summarized in Table 4.2.The erosion stage lasts for 10 seconds, and the stress states in all samples are kept constant during the erosion process.

4.2.4 Biaxial shear after erosion

After erosion, the CFD domain is removed, and the filter wall is replaced by an impermeable rigid boundary which is same as the one used in the second stage. Subsequently, the biaxial shear tests are restarted on these post-eroded specimens, proceeding from their current stress states until an axial strain of 25% is achieved. Then, a comprehensive analysis is conducted to investigate both the macroscopic and microscopic behaviours of the post-erosion specimens. The findings are then compared with the results from the specimens that do not undergo the erosion stage. This comparative study aims to elucidate the effects of internal erosion under various stress states on the mechanical behaviours and failure mechanisms of gap-graded soil.

4.3 Numerical results and discussions

4.3.1 Result from erosion stage

Fines loss

Fig 4.5 shows the evolutions of percentage of cumulative fines loss during erosion and the ultimate values for all specimens. It is concluded that more fine particles are eroded at lower confining pressure due to the lower restrictions by the surrounding particles on fine particles. Meanwhile, with the same σ_3, more fine particles are transported through the voids and exit the filter wall as β increases, which is consistent with the investigations by Qian et al. (2021) and Hu et al. (2022). In some cases, there are some pronounced increases of the eroded fines mass at some erosion moments. For example, the specimen with σ_3 = 100kPa and β = 1.00 undergoes a considerable mass reduction within the time interval t = 3 – 4.5s. This reduction is not observed in cases with β = 0.35 and 0.70, where the erosion of fine particles has ceased within this time interval. This phenomenon can be attributed to the local collapse and rearrangement of the specimen fabric during the erosion stage. Fig 4.6 and Fig 4.7 plot the local packings of the specimens with β = 0.35 and 1.00 under σ_3 = 100kPa. These two figures show the changes of both the particles (left column) and contacts (right column) at the moments t = 2, 3 and 4s. In comparison with the local packing with β = 0.35, the contact between the blue coarse particles in the cases having β = 1.00 collapses at t = 3s when the sharp mass reduction initiates. Then, the contact between the blue and red coarse particles also collapses during the subsequent erosion (t = 4s), which will further induce the surrounding fine particles to easily migrate through the voids and be eroded away by the fluid flow. In general, the specimen undergoes more local collapses and rearrangements in the process of shearing to failure (Gu et al. 2014; Song et al. 2024a; Tordesillas 2007). More fine particles are therefore freed as β increases during this process, so that the erosion rate increases with β in the initial erosion stage. For specimens with large β, the internal structures are not as stable as those in specimens having small β, and they are easier to be destroyed by the seepage flow during erosion. Meanwhile, the local collapse during erosion will result in the rearrangement and adjustment of the specimens to the required constant stress states. Therefore, more new free fine particles will be released and washed away by the seepage flow during the erosion process.

Distribution of the contact orientation

The spatial distributions of both contact number (N_c) and normal contact force (F_n) (calculated by the same equations as those in Chapter 3) for the cases with σ_3 = 100kPa with different β before erosion are shown in Fig 4.8. In general, the anisotropy magnitude of contact number A_c is smaller than that of normal contact force A_n in all cases. The anisotropies of both contact number and normal contact force are aligned with the vertical direction, and the corresponding magnitudes increase with the increase of the stress ratio β from 0.35 to 1.35. It means that more new contacts have been generated along the loading direction to resist the external loads with shearing and more inherent contacts have buckled or collapsed as β increases (Li and Yu 2009;

Song et al. 2024a). Consequently, this process results in that more fine particles have been released from the constraints imposed by the confining pressure. These free fine particles are more susceptible to being dislodged and transported out of the specimen under the effect of seepage flow. In other words, an increase in the initial anisotropy magnitude corresponds to an enhanced erosion of fine particles. This correlation indicates the important role of contact anisotropy during the process of internal erosion, where the fabric anisotropy induced by stress application can intensify the erosion susceptibility of the gap-graded soil specimens.

Further insights into the effect of internal erosion on the soil fabric are provided by the anisotropy evolution of both N_c and F_n with erosion, as shown in Fig 4.9. In general, the corresponding principal directions of the two anisotropy components in most specimens gradually rotates to the erosion direction (vertical), which means that more new contacts are generated along the vertical direction under the effect of seepage flow. For the cases with higher values of β (1.00 and 1.35), the specimens gradually become less anisotropic while there is an increase in anisotropy magnitude in the initial stage, which is consistent with Zhou et al. (2022a). However, specimens with lower β values (0.35 and 0.70) do not exhibit significant changes in anisotropy magnitude during the later stage of erosion, especially for the normal contact force. This is due to that the specimen is relatively stable when β is small, making it resistant to structural damage induced by seepage flow. In contrast, when β is large, many inherent contacts have already buckled and collapsed before erosion, and the structures in some local zones have become relatively fragile. The seepage flow will further intensify this disparity, i.e., it is easier for the seepage force to destroy the fragile local contact structures when β is large, as depicted in Fig 4.7. This leads to the sudden changes in both the magnitude and direction of anisotropy in Fig 4.9. Meanwhile, local collapse of the eroded specimen usually coincides with the change in the stress state, and external loading is then continually adjusted and applied to the specimen to maintain the required constant β during erosion. As a result, both the magnitude and direction of anisotropy exhibit some fluctuations. Additionally, these fluctuations in specimens with large β coincides with the significant changes in local distribution of contact orientation (Fig 4.18 and Fig 4.19) which further leads to a different failure mode of the specimens compared to the non-eroded specimens (Fig 4.12 and Fig 4.13).

Contact buckling and collapse

As mentioned before, the contacts buckle and collapse during both the shearing and erosion processes. Meanwhile, the contact anisotropy and force transmission are mainly contributed by the strong contact force chains in granular assemblies (Radjai et al. 1998). For the gap-graded materials, Liu et al. (2020) found that the collapse and buckling of strong contacts would significantly intensify the erosion of fine particles. In this study, the cut-off point between the strong and weak force chains is set as f_a (f_a is the average contact force) (Minh et al. 2013). The condition for determining the occurrence of force chain buckling is consistent with that of Liu et al. (2020) and Tordesillas (2007), which is a change of more than 1° in the intersection angle of the chains in a short time (0.001s).

The variations in the fractions of buckling and collapse of the strong contacts during the erosion process in the two cases, with β = 0.35 and 1.00 under the confining pressure of 100 kPa, are taken as example and plotted in Fig 4.10. In this figure, the vertical axes represent the ratios of buckled or collapsed force chains to all force chains. It is noted that contacts are also classified into three types like those in Chapter 3: *c-c* contact, *f-f* contact and *c-f* contact. In general, massive force chain buckling and collapse occur during the initial erosion stage when the erosion rate exhibits a high magnitude. Among the contact types, the *f-f* contacts exhibit the highest fractions of buckling and collapse, while the *c-c* contacts demonstrate the lowest. Meanwhile, for all three types of contacts, the fractions of both force chain buckling and collapse in the case with β = 0.35 are smaller than those in the case with β = 1.00, which aligns with the differential fines mass loss observed between the two cases in Fig 4.5. Additionally, it is observed that a pronounced phase of fluctuation is present in the case with β = 1.00, occurring within the temporal interval ranging from t = 3 to 5s. This fluctuation is associated with the detachment and release of a substantial number of fine particles, some of which are then subject to migration away from the specimen under the effect of seepage flow. This phenomenon highlights the interplay between contact stability, stress-induced anisotropy, and the erosion effect of fluid flow within the gap-graded granular system.

4.3.2 Result from shear stage

Mechanical behaviour of non-eroded and post-eroded specimens

After erosion, these post-eroded specimens are then reloaded at the same shear rate as that in the second stage from the current stress states until reaching an axial strain ε_z of 25%. The principal stress ratio η and volumetric strain ε_v versus the axial strain ε_z

for both the non-eroded and post-eroded specimens are plotted in Fig 4.11. In general, the specimens with a higher value of β require a greater axial strain to maintain the constant stress state during internal erosion. With the sameσ_3, the peak stress ratios of the post-eroded specimens are found to be smaller than those in the non-eroded ones, with this disparity being particularly pronounced for the specimens with a larger β. Meanwhile, the stress-strain curves of the post-eroded specimens exhibits greater fluctuations compared to the non-eroded specimens. This observed discrepancy can be attributed to that the post-eroded specimens have become locally unstable under the effect of seepage flow. As for the volumetric strain ε_v, specimens that have undergone erosion demonstrate a greater degree of shrinkage compared to their non-eroded counterparts during the initial shearing stage. As the shearing progresses, these post-eroded specimens exhibit less volumetric dilatancy than those non-eroded specimens. These observations are found to align with some previous research results (Chang and Zhang 2011; Chen et al. 2016; Hu et al. 2022; Ke and Takahashi 2015; Qian et al. 2021).

Particle rotation fields of non-eroded and post-eroded specimens

As a precursor to failure, the shear banding process is thought to have a significant correlation with some local characteristics, including void ratio, force chains, and particle rotation (Oda and Kazama 1998; Song et al. 2024a; Tordesillas 2007). Consistent with the approach in Wang et al. (2022b) and Zhu and Yin (2019), this section employs the particle rotation field as an indicator for characterizing the shear band. Fig 4.12 shows the particle rotation fields of the three non-eroded specimens at axial strain ε_z = 20%. It is worth noting that the coarse particles play the dominant role in the whole specimen with the fines content of 25% (Hu et al. 2022; Qian et al. 2021). Thus, the analysis of particle rotation is focused on the coarse particles here. It is seen that particles with higher rotation gradient are predominantly aligned along the diagonal axis, i.e., the shear bands are distinctly oriented in the diagonal direction in all three specimens, irrespective of the confining pressure applied.

However, for the post-eroded specimens, especially those with higher β-values, the shapes of the shear bands have undergone certain changes. The particle rotation fields of the specimens with the confining pressure of 100kPa are taken as examples, as shown in Fig 4.13. It is seen that the shear band maintains its alignment along the diagonal direction when β = 0.35. However, with the increase of β, the difference between the shear band in the post-eroded specimen and that of the non-eroded specimen becomes increasingly more pronounced. Specifically, an increase in β is found associated with more particles with higher rotation gradients beyond the diagonal zone in the specimen. In other words, the post-eroded specimen with a large β does not merely fail along the diagonal direction, especially for the specimen with β = 1.35 which exhibits an absence of discernible shear bands. This is attributed to the fact that the internal structures of specimens with larger β values are subject to a more pronounced influence from the seepage flow.

Local buckling and collapse of force chains

Shear banding is highly associated with the buckling and collapse of force chains (Iwashita and Oda 2000). To better investigate the relationship between the formation of shear band and the evolution of force chains in the granular gap-graded soil specimen, the DEM model is divided into 12 equal local zones based on their relative positions in the cubic specimen, as shown in Fig 4.14. With the same definition of contact buckling and collapse as that in previous sections, the average fractions of the buckling and collapse of force chains during the 0 to 20% axial strain stage are calculated for the non-eroded specimens, as shown in Fig 4.15. In this figure, the left column represents the average fraction of contact buckling, and the right column represents that of contact collapse. For the non-eroded specimens, the higher fractions of both the contact buckling and collapse are found to be distributed along the diagonal direction, which is consistent with the distribution of particles with higher rotation gradients. In other words, the formation of shear band is the process of the collapse and buckling of inherent force chains and the generation of new force chains to resist the external loads.

For the post-eroded specimens, the specimens with σ_3 = 100kPa are taken as examples here, and the local average fractions of contact buckling and collapse are plotted in Fig 4.16 and Fig 4.17, respectively. In general, more contacts buckle or collapse in the post-eroded specimens than the non-eroded ones during shearing. It seems that the fractions of both contact buckling and collapse increase as β increases from 0.35 to 1.35. Meanwhile, like the non-eroded specimens, the higher values are distributed along the diagonal direction when β is small (Fig 4.16 (a - b) and Fig 4.17 (a - b)). However, when β = 1.00 and 1.35, significant contact buckling and collapse are also found in other local zones (Fig 4.16 (c - d) and Fig 4.17 (c - d)). This can be attributed to the fact that when β is small, the specimen is at a relatively stable state before erosion, with contact buckling and collapse occurring uniformly throughout the entire specimen. Under this condition, it is hard for seepage flow to trigger local failures in the specimen. As a result, when the specimen is sheared after the erosion stage, the internal skeleton is similar to the non-eroded one, leading to similar failure patterns. However, the specimen with a large β is not that stable and homogeneous, and it is easy for the seepage flow to destroy the local structures of the specimen. This can further result in that the local structure of the specimen after erosion diverges from that of the non-eroded specimen at the same axial strain. This difference in the effect of seepage flow on the local structures of specimens with different β can be observed in the change of local distribution of normal contact force orientation before and after erosion (Fig 4.18 and Fig 4.19).

Fig 4.18 and Fig 4.19 illustrate the anisotropies of the strong normal contact forces within the 12 local zones (Fig 4.14) for the cases subjected to a confining pressure of σ_3 = 100kPa, with β = 0.35 and 1.35, respectively, before and after erosion. Compared to the specimen with β = 1.35, the microstructural anisotropy within most local zones of the specimen with a β-value of 0.35 demonstrates insignificant variations after the erosion process. This suggests that the main microstructural structure of the specimen with β = 0.35 remains largely unaffected by the seepage flow. As a result, the post-eroded specimen exhibits a failure mode analogous to that of the non-eroded specimen. When the specimen is sheared to β = 1.35, the specimen has already exhibited a more pronounced state of inhomogeneity and instability before erosion. This pre-existing condition intensifies the influence of the seepage flow on the specimen's fabric, which is further evidenced by the significant changes in microstructural anisotropy observed within the local zones (Fig 4.19). Then, this post-eroded specimen, which has undergone significant internal structural changes under the influence of seepage flow, will exhibit a different failure mode compared to the non-eroded specimen (Fig 4.12 and Fig 4.13).

4.4 Conclusions

This Chapter has conducted a series of coupled CFD-DEM internal erosion simulations on gap-graded granular soils under various biaxial shear stress states which is characterized by the stress ratio mobilization β and confining pressure. After erosion, these post-eroded specimens were further sheared to failure under the current stress states. Both macroscopic and microscopic responses of the specimens during the internal erosion and following shear processes were investigated and discussed in detail, including the relationship between stress state and fines mass loss, the variations of the stress-strain curves of the post-eroded specimens, and the changes of shear bands. The main conclusions of this study are summarized as follows:

1. The influence of internal erosion on the shear behaviour of gap-graded soil specimens intensifies as the stress ratio β increases. This trend is evidenced by a more pronounced difference between the shear bands of the post-eroded specimens and those of the non-eroded ones. Specifically, the specimens that have undergone internal erosion but have small β exhibit similar shear bands to the non-eroded specimens, while the soil specimens under high stress states do not exhibit discernible shear bands.

2. The local structural failure defined by the extensive buckling and collapse of the strong force chains under the effect of seepage flow is found to contribute to the different shear bands in the specimens with various β in the subsequent shearing. In short, compared to the soil specimens with small β-values, the specimens under high stress states are usually at more inhomogeneous and unstable states before erosion. This difference is then intensified by the seepage flow in some local zones where more inherent contacts buckle and collapse in the specimens under high stress states. Different degrees of local structural failure in the specimens under various stress states further result in the shear band becoming more indiscernible as β increases. Additionally, erosion-induced structural failures also lead to reduced peak stress ratios and less volumetric dilatancy in the post-eroded specimens.

3. For the erosion stage, the increased stress ratio β in gap-graded soil specimens is associated with an intensified loss of fine particles, which negatively correlates with the confining pressure. The increased β renders the contacts between coarse particles more vulnerable to seepage-induced failure, further resulting in a sharp increase in the mass of eroded fines in specimens with large β during the erosion process. Meanwhile, the specimens with large β-values are found to require greater strains to sustain the constant stress states throughout the erosion process.

4. From the microscopic perspective, the anisotropies in both normal contact force and contact number increase with the initial stress ratio β, with their principal directions closely aligned to the erosion direction (vertical). Seepage forces are found to enhance the contact anisotropy during the initial erosion stage, while a

subsequent slight reduction in anisotropy magnitude with erosion is observed. Furthermore, erosion-induced anisotropy fluctuations are accompanied by the buckling and collapse of contacts. The greater the initial anisotropy magnitude, and the more the contacts buckle and collapse during the erosion process.

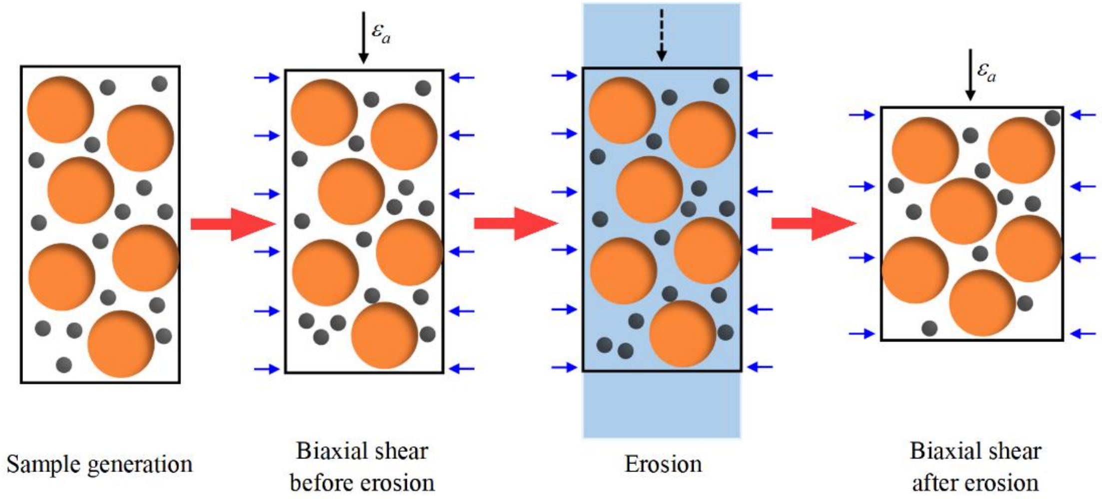

Fig 4.1 Stages of the simulation.

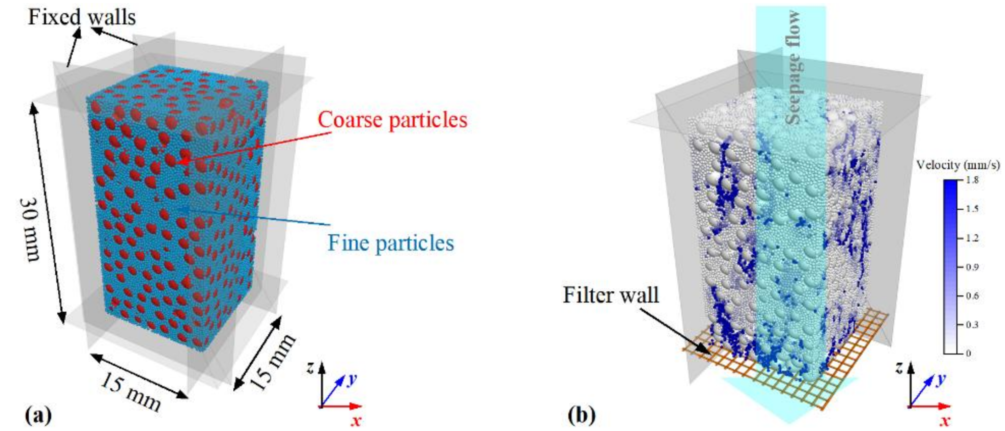

Fig 4.2 Model of the (a) biaxial shear test and (b) coupled CFD-DEM simulation test.

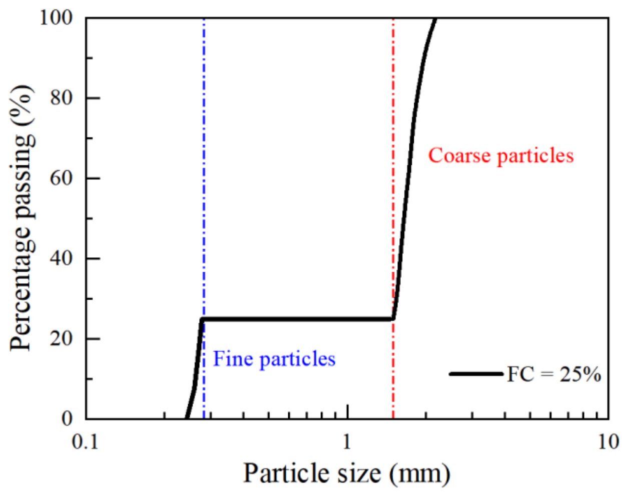

Fig 4.3 Particle size distribution of the gap-graded granular soil.

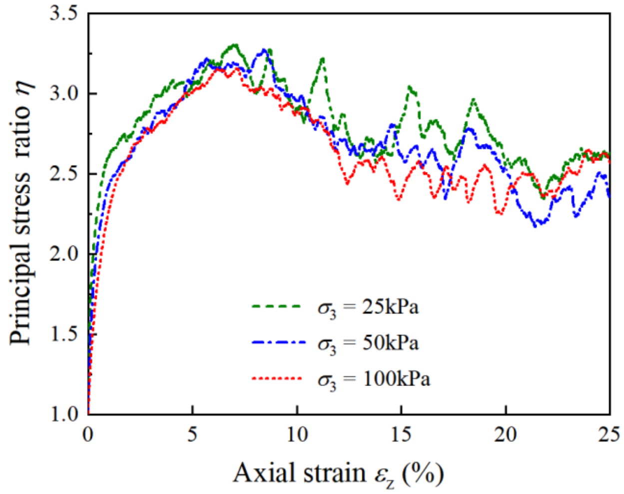

Fig 4.4 The stress-strain relationship for cases with σ_3 = 25 kPa, 50 kPa, and 100 kPa without erosion.

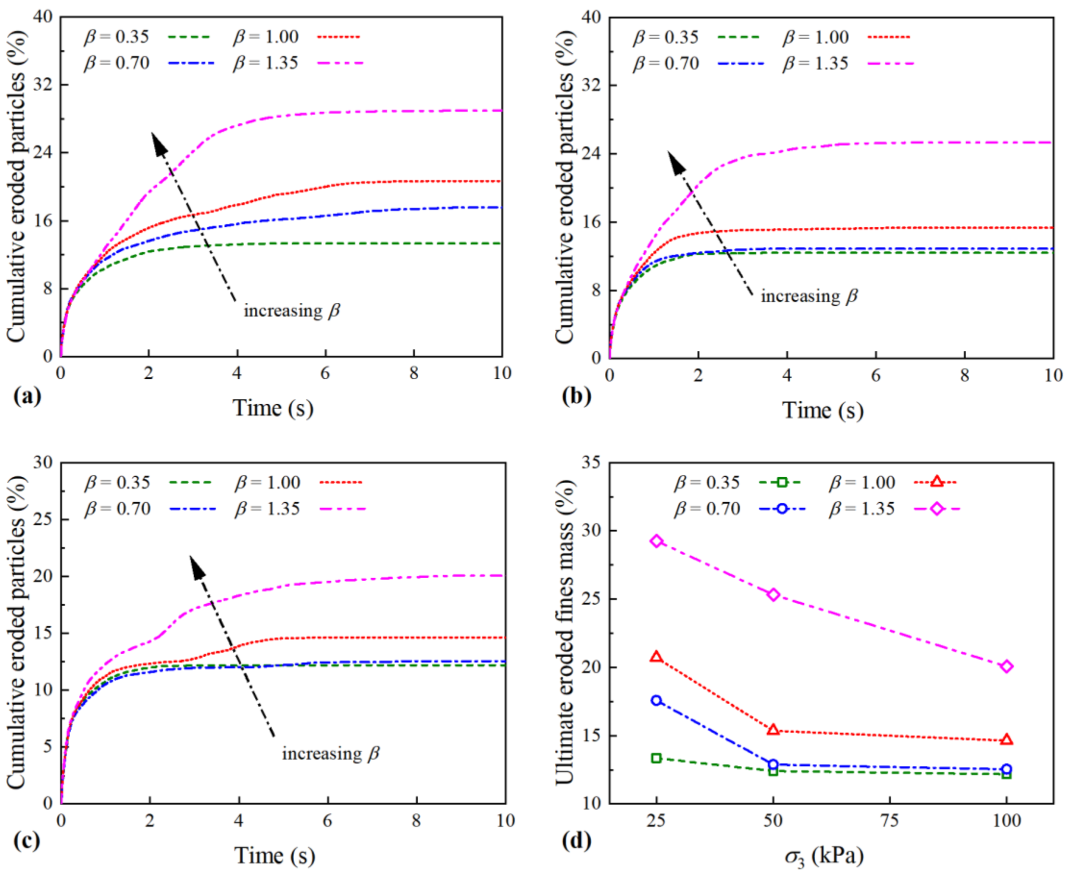

Fig 4.5 Cumulative eroded fines mass during erosion: (a) σ_3 = 25kPa; (b) σ_3 = 50kPa; (c) σ_3 = 100kPa; (d) ultimate values for all cases.

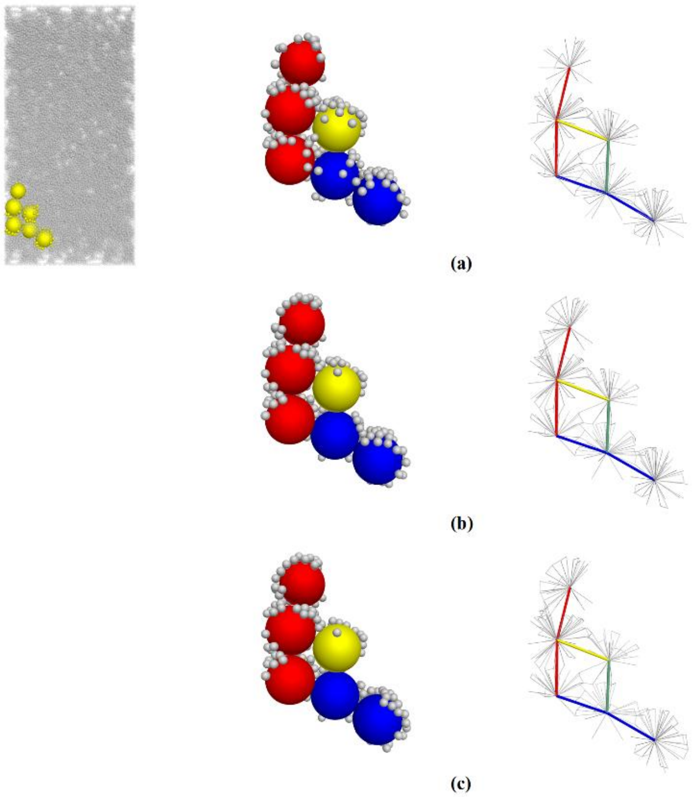

Fig 4.6 Local packings of the case with σ_3 = 100kPa and β = 0.35 at (a) t = 2s; (b) t = 3s; (c) t = 4s.

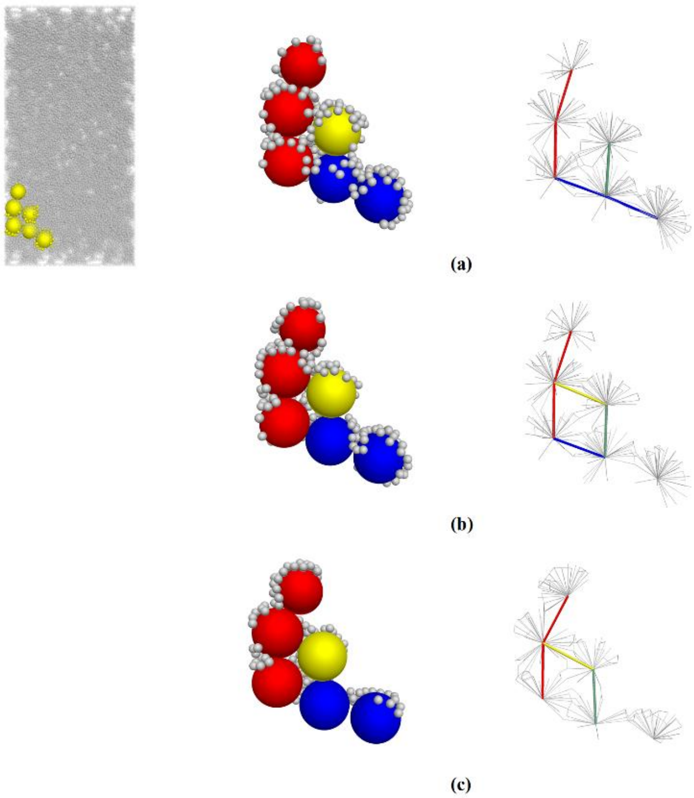

Fig 4.7 Local packings of the case with σ_3 = 100kPa and β = 1.00 at (a) t = 2s; (b) t = 3s; (c) t = 4s.

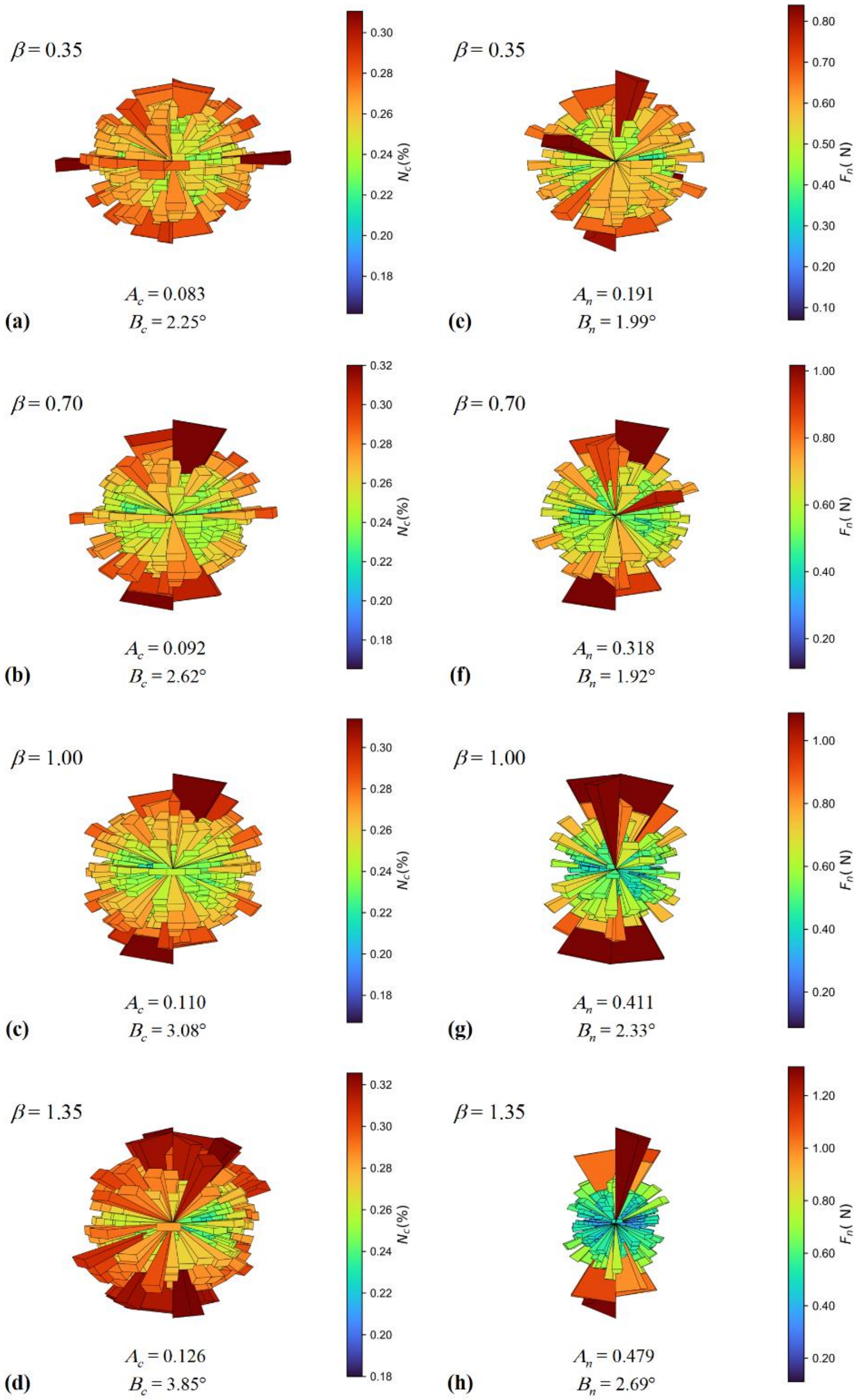

Fig 4.8 Distribution of (a - d) contact normal and (e - h) normal contact force before erosion for cases with σ_3 = 100kPa.

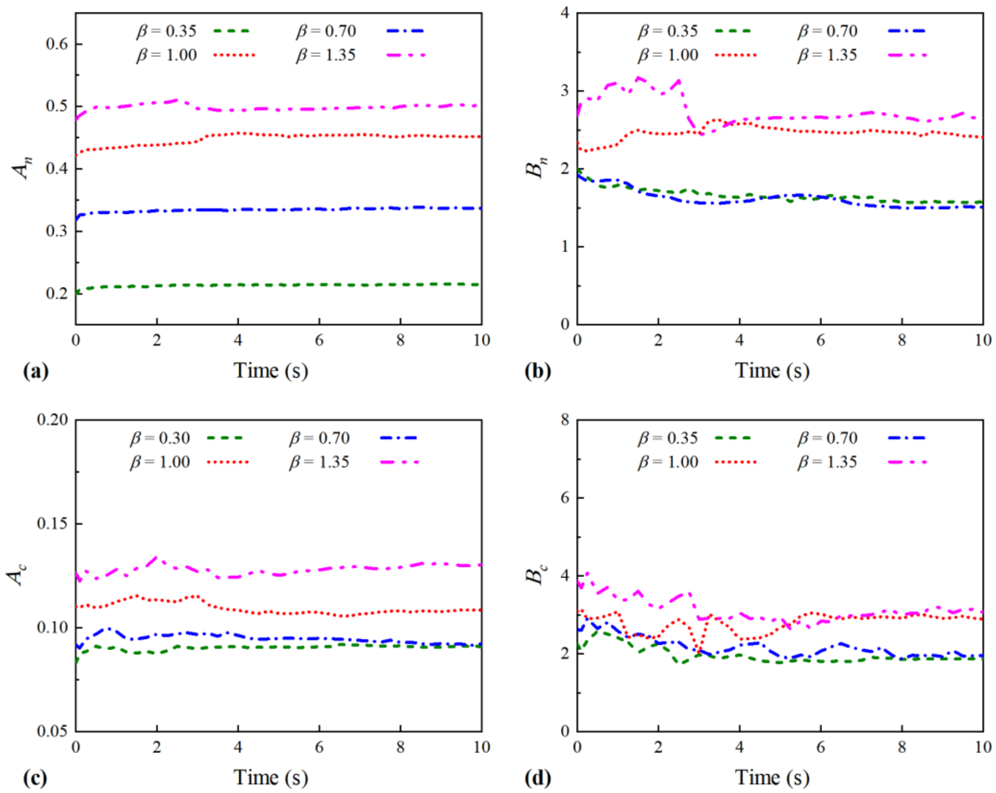

Fig 4.9 Evolutions of the anisotropy magnitudes and principal directions of (a - b) normal contact force and (c - d) contact normal for cases with σ_3 = 100kPa.

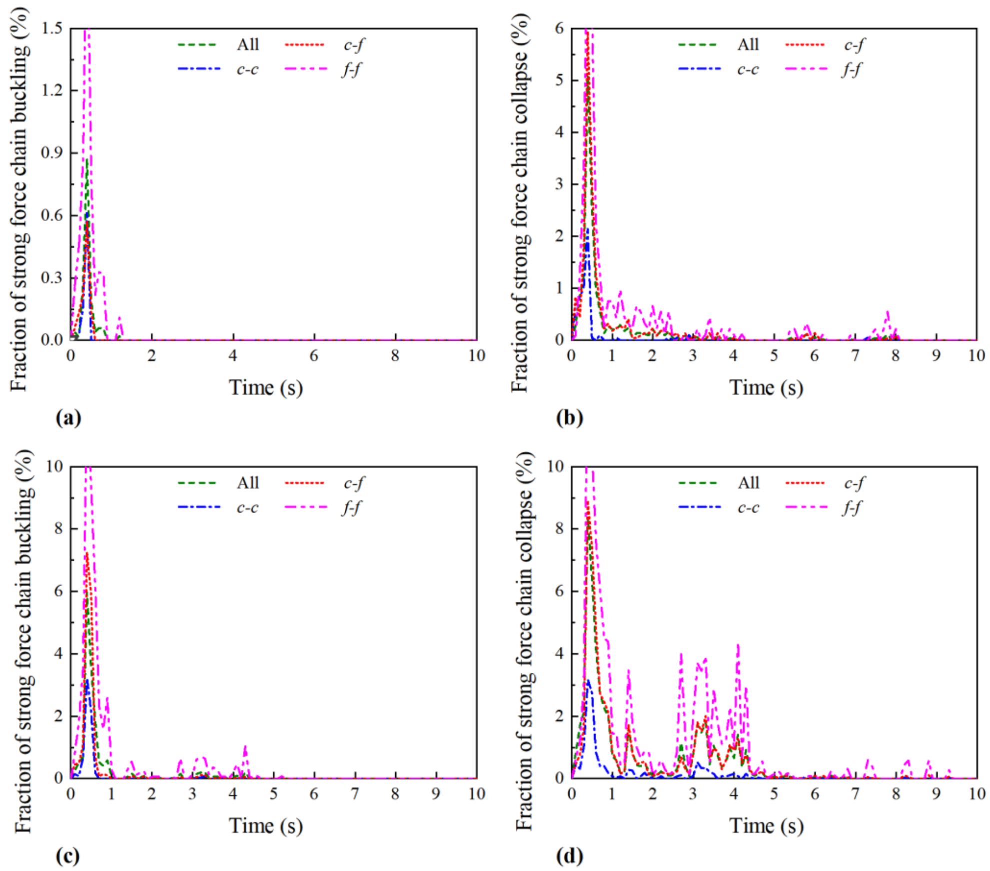

Fig 4.10 Fraction of strong force chain buckling and collapse during erosion for cases with (a - b) β = 0.35 and (c - d) β = 1.00 under σ_3 = 100kPa.

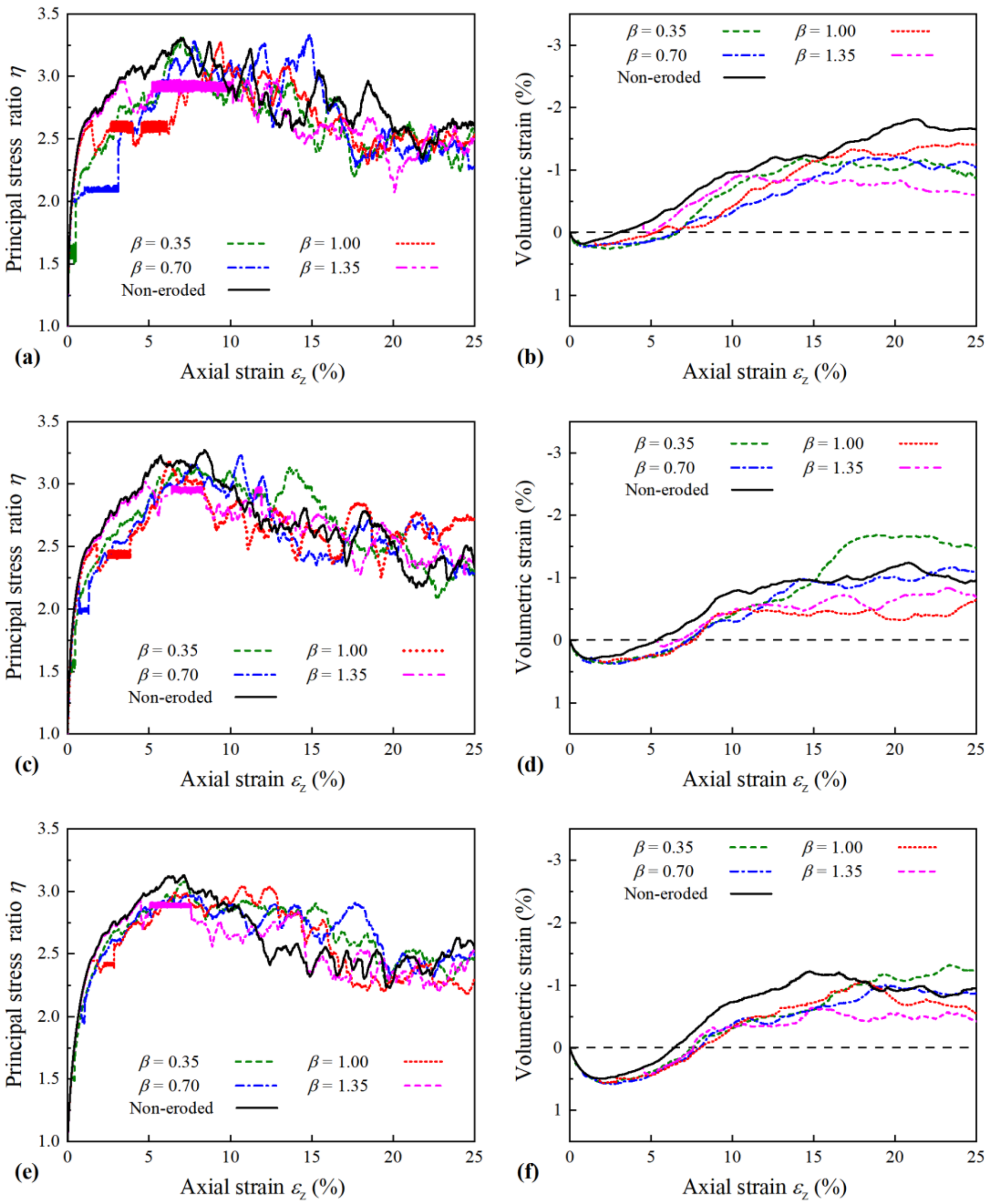

Fig 4.11 Evolutions of principal stress ratio η and volumetric strain ε_v versus axial strain ε_z before and after erosion for cases with (a - b) σ_3 = 25kPa; (c - d) σ_3 = 50kPa; and (e - f) σ_3 = 100kPa.

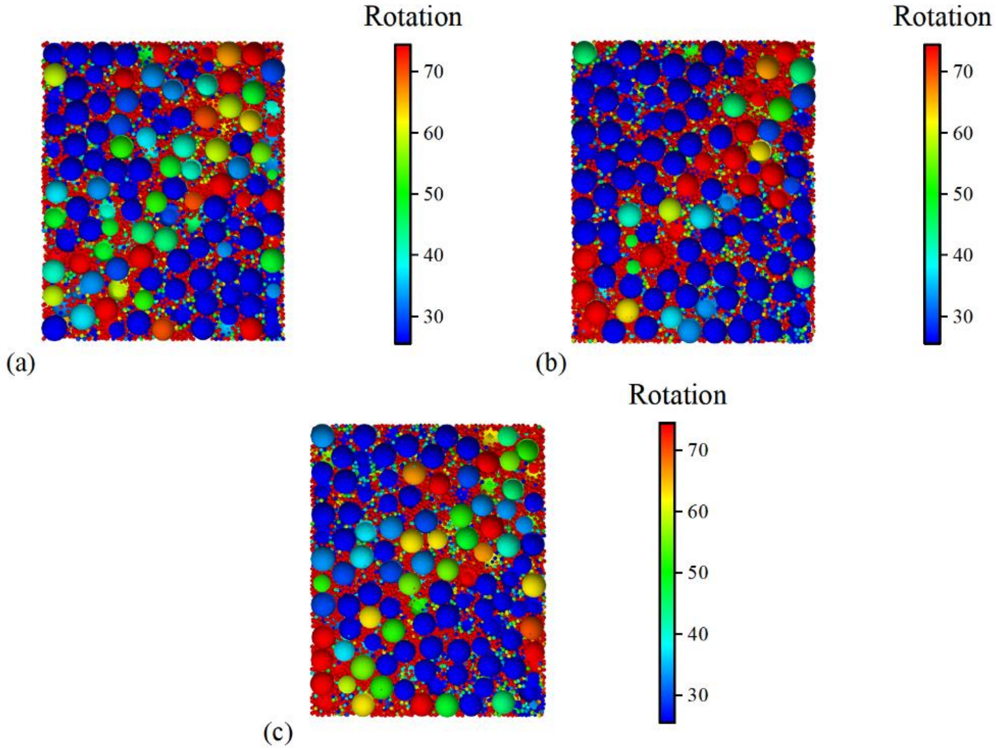

Fig 4.12 Particle rotation fields of non-eroded specimens with (a) σ_3 = 25kPa; (b) σ_3 = 50kPa; and (c) σ_3 = 100kPa at axial strain ε_z = 20%..

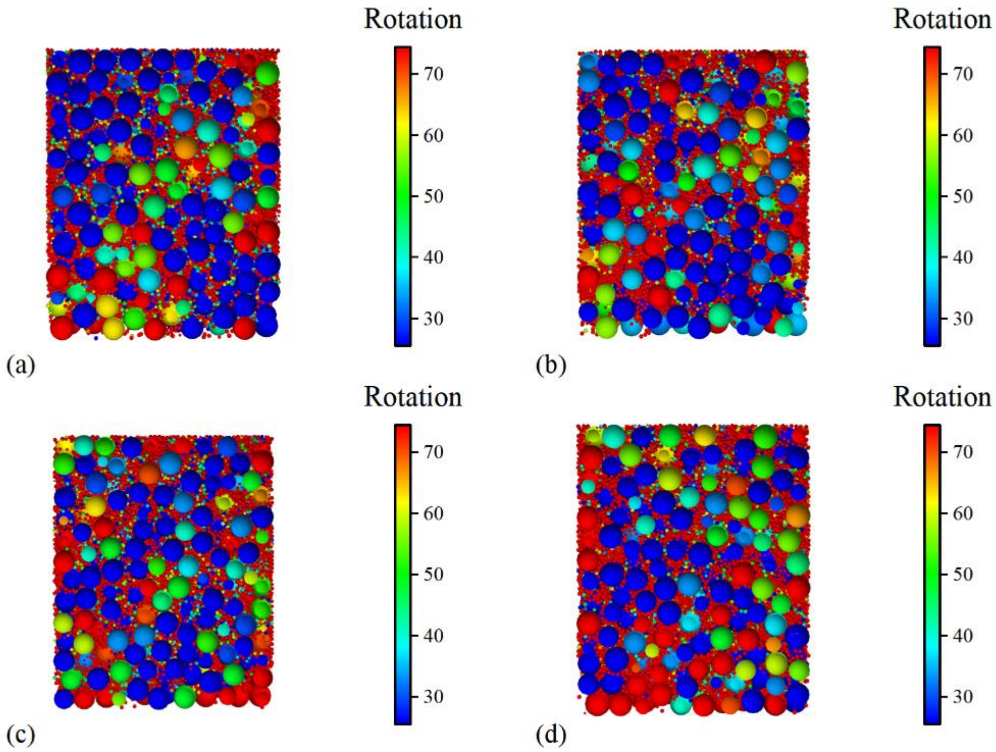

Fig 4.13 Particle rotation fields of post-eroded specimens with (a) β = 0.35; (b) β = 0.70; (c) β = 1.00 and (d) β = 1.35 under σ_3 = 100kPa at axial strain ε_z = 20%..

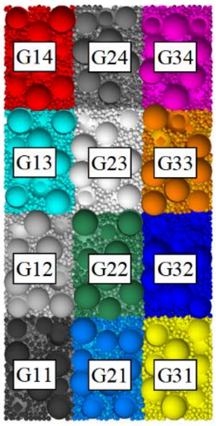

Fig 4.14 Classified zones of the DEM specimen.

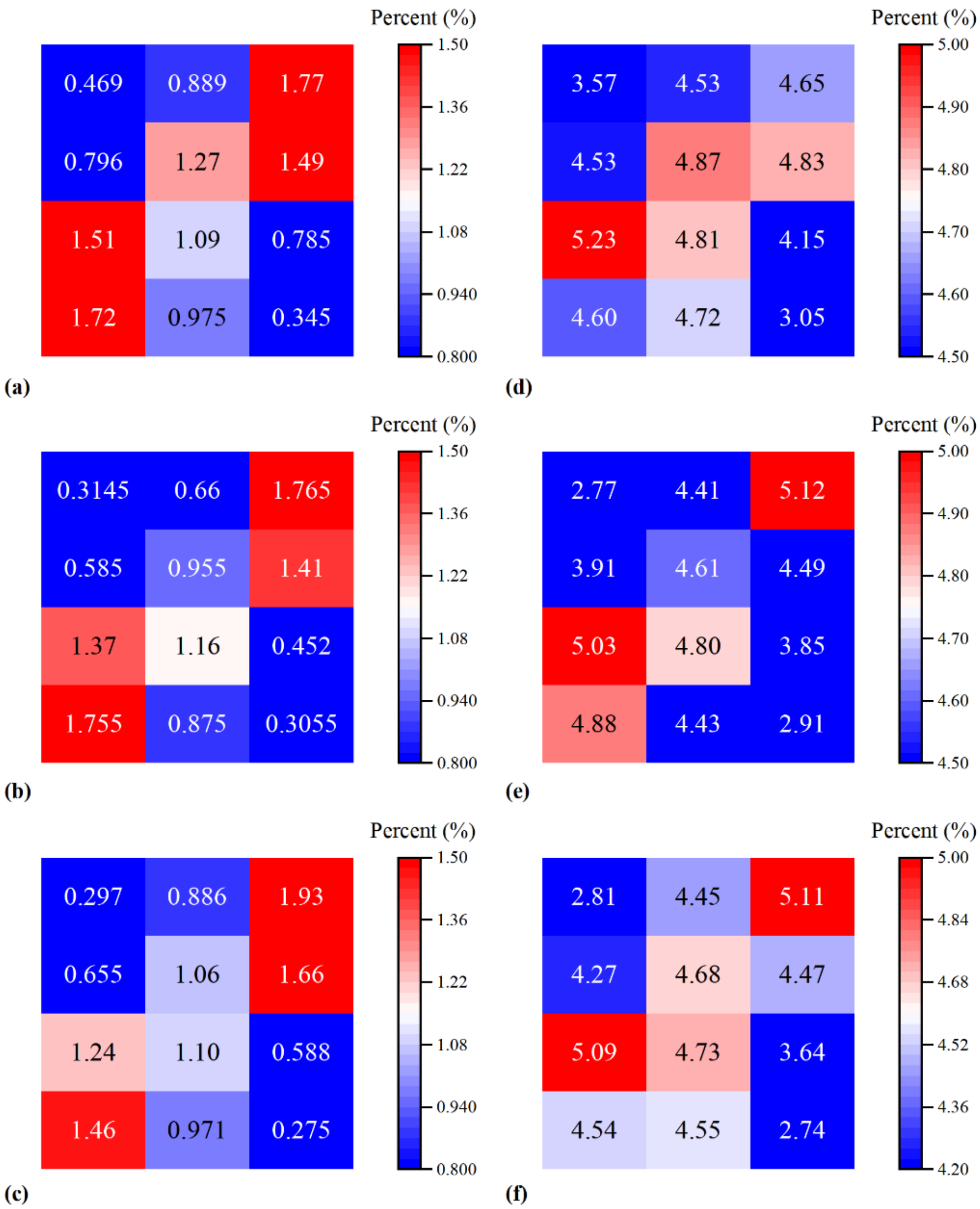

Fig 4.15 Local average fractions of contact buckling and collapse for the non-eroded

specimens with (a - b) σ_3 = 25kPa; (c - d) σ_3 = 50kPa; and (e - f) σ_3 = 100kPa.

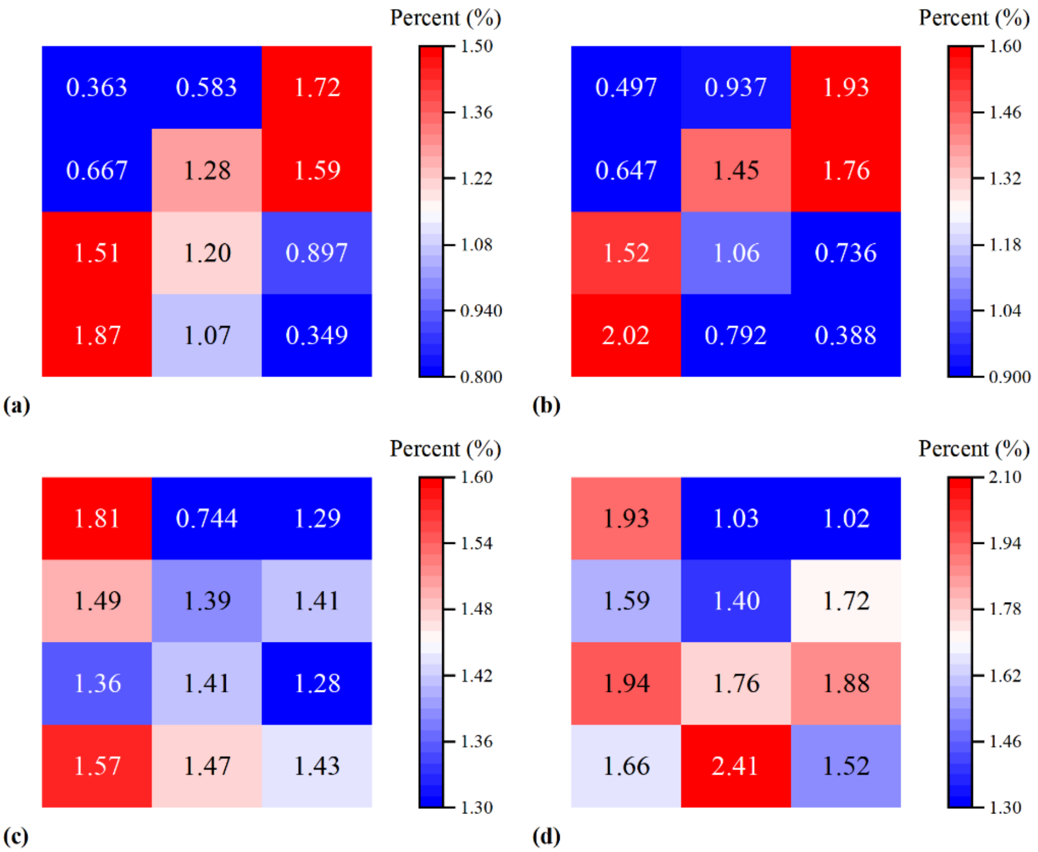

Fig 4.16 Local average fractions of contact buckling for the post-eroded specimens with (a) β = 0.35; (b) β = 0.70; (c) β = 1.00 and (d) β = 1.35 under σ_3 = 100kPa.

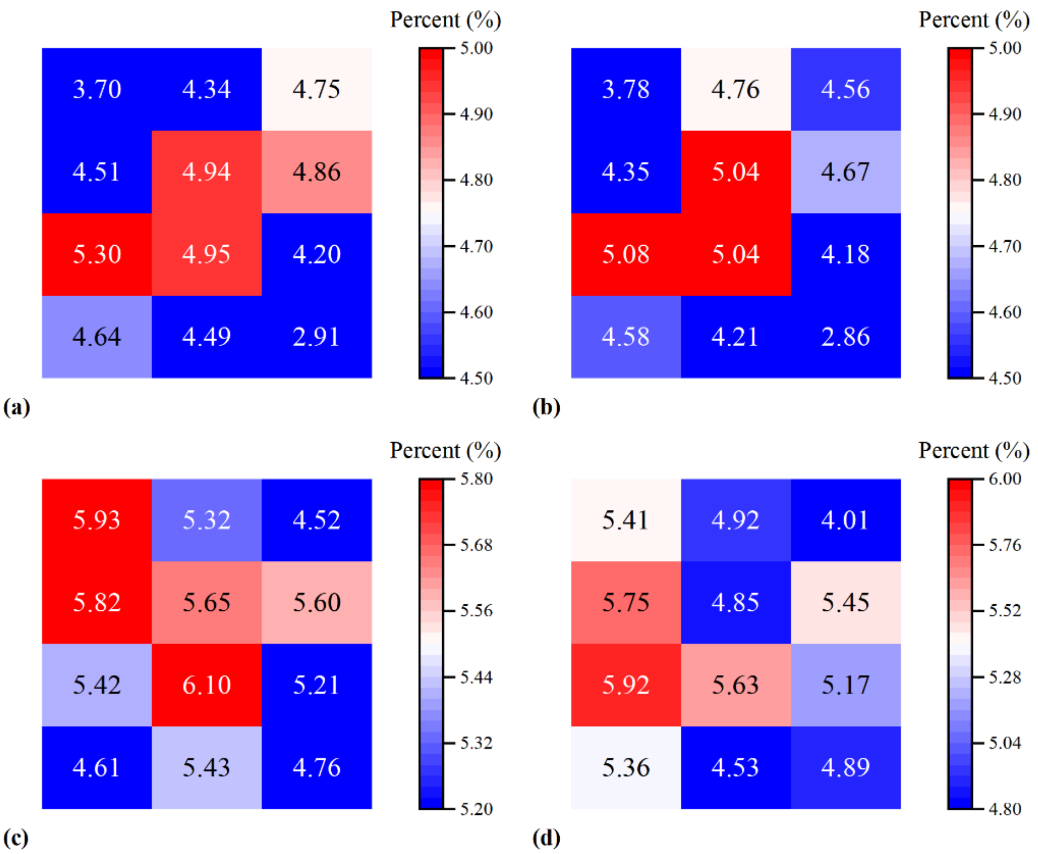

Fig 4.17 Local average fractions of contact collapse for the post-eroded specimens with (a) $\beta = 0.35$; (b) $\beta = 0.70$; (c) $\beta = 1.00$ and (d) $\beta = 1.35$ under $\sigma_3 = 100$kPa.

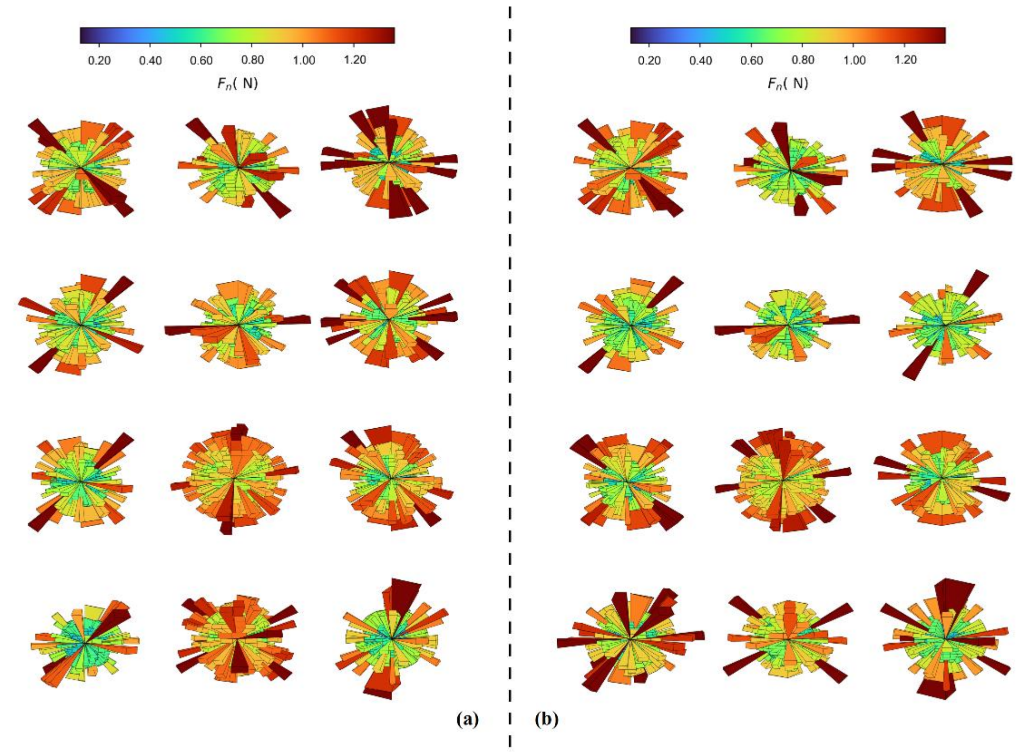

Fig 4.18 Local distribution of strong normal contact force (a) before and (b) after erosion for the case with $\sigma_3 = 100$kPa and $\beta = 0.35$.

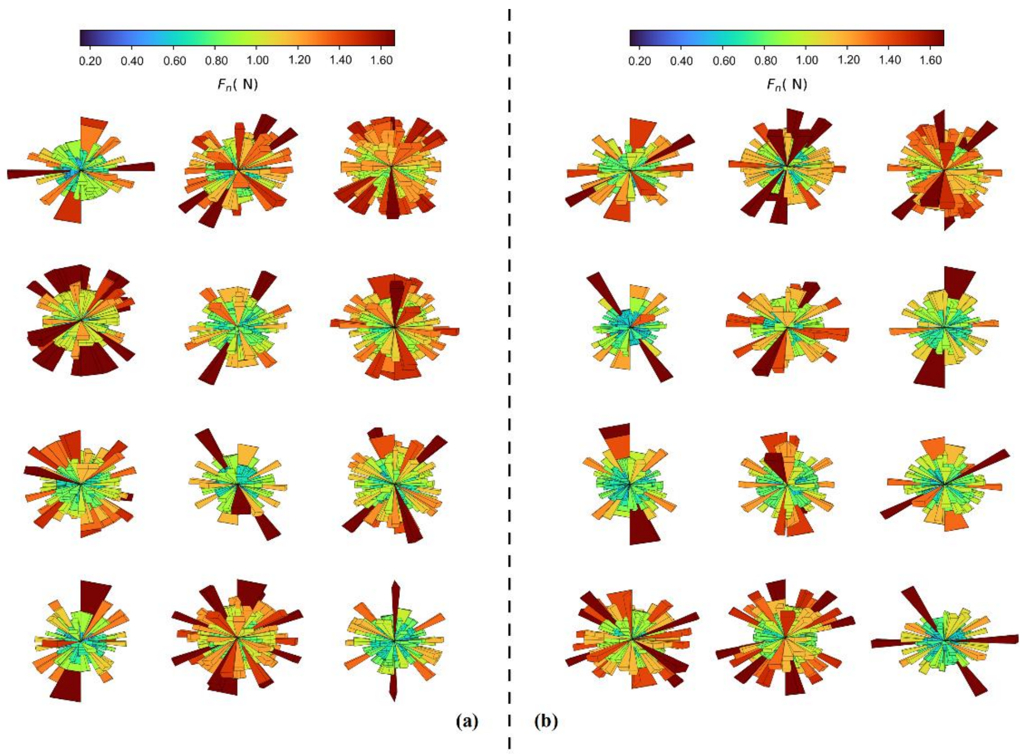

Fig 4.19 Local distribution of strong normal contact force (a) before and (b) after erosion for the case with $\sigma_3 = 100$kPa and $\beta = 1.35$.

Table 4.1 Summary of specimens in the internal erosion simulations

Test	1	2	3	4	5	6	7	8	9	10	11	12
σ_3 (kPa)	25	25	25	25	50	50	50	50	100	100	100	100
β	0.2	0.6	0.8	1.2	0.2	0.6	0.8	1.2	0.2	0.6	0.8	1.2

Table 4.2 Parameters used in the coupled CFD-DEM simulations

Parameters			Values
DEM	Elastic modulus	E_{PP} (Pa)	2.0×10^8
		E_{PW} (Pa)	2.0×10^8
	Stiffness ratio	k_{PP}	3.0
		k_{PW}	3.0
	Friction coefficient	μ_f	0.3
	Rolling friction coefficient	μ_r	0.1
	Density of particles	ρ (kg/m^3)	2650
	Time step	Δt_p (s)	1.0×10^{-7}
CFD	Cells	Length × Width × Height	5 × 5 × 15
	Fluid viscosity	μ (Pa $*$ s)	1.0×10^{-3}
	Density of fluid	ρ_f (kg/m^3)	1000
	Time step	Δt_f (s)	1.0×10^{-5}

CHAPTER 5: COUPLED CFD-DEM INVESTIGATION ON THE INTERNAL EROSION AND SHEAR INSTABILITY IN GAP-GRADED GRANULAR SOILS UNDER DIRECT SHEAR CONDITION

5.1 Introduction

When relative displacement is localized along a predefined shear plane under approximately constant normal stress, soil is subjected to direct shear conditions. This type of loading is commonly encountered at soil–structure interfaces, along potential slope failure surfaces, or between foundations and the underlying soil. Among common laboratory shear tests, the direct shear test enables more explicit control of displacement and stress boundary conditions. As a result, it is particularly well suited for studying the initiation, development, and localization of shear bands (Kodicherla et al. 2019; Kozicki et al. 2013). For gap-graded soils, the content of fine particles has a significant effect on the formation and development of shear bands under direct shear condition, especially after internal erosion. This influence should be carefully investigated. Moreover, the stress state during internal erosion plays a crucial role in determining the subsequent mechanical response of the soil. Soils that experience different stress states before or during erosion may develop different shear band patterns in post-eroded shearing. Additionally, hydraulic gradient also plays an important role and should not be ignored, as it can influence the migration of fine particles and the resulting changes in strength and failure modes.

In this Chapter, a series of erosion simulations considering different fines contents, hydraulic gradients and stress ratio mobilizations is conducted with the coupled CFD-DEM method, aiming to investigate the effect of stress state on internal erosion under direct shear condition from both macroscopic and microscopic perspectives. Moreover, the subsequent influence of erosion on the shear behaviour of post-eroded soils is also studied in detail, with particular attention given to shear banding under direct shear conditions in both non-eroded and post-eroded states.

5.2 Simulation procedure

The CFD-DEM simulations in this Chapter are conducted to study the effect of stress state on internal erosion in gap-graded soil specimens and the mechanical behaviours of the post-eroded soil specimens under direct shear conditions. To describe the stress state of the specimens, a coefficient stress ratio mobilization, $\beta = \eta / \eta_c$, is introduced (Liu et al. 2022). Here, $\eta = \tau / \sigma_N$ represents the stress ratio, and η_c is the critical stress ratio. In this Chapter, the normal stress σ_N for all specimens remains constant at 25 kPa throughout the entire simulation process. Similar to Chapter 4, the entire simulation process is divided into four steps: specimen preparation, initial shearing, erosion simulation, and post-eroded shearing, as illustrated in Fig 5.1.

5.2.1 Specimen preparation

A DEM gap-graded soil specimen is first generated within a cubic direct shear box with a side length of 20 mm, as shown in Fig 5.2 (a). The particle size distribution (PSD) of the gap-graded soil is shown in Fig 5.3, with a gap ratio of approximately 5.6, indicating an internally unstable state (Fannin and Moffat 2006; Kenney and Lau 1986; Song et al. 2024b). Two fines contents are considered in this study: 25% fines (by mass), representing a coarse-dominated mixture where fines underfill the voids of coarse grains, and 35% fines, representing a fine-dominated configuration where fines overfill the voids of coarse grains (Li and Fannin 2012; Liang et al. 2019; Liu et al. 2020). In this study, the relative density (D_r) is maintained at approximately 65.5% for all specimens (Liu et al. 2021; Song et al. 2024b; Zhou et al. 2019b).

5.2.2 Initial shearing

After specimen generation, the prepared specimens are subjected to direct shear. Shearing is performed at a constant rate to reach predefined stress states, characterized by stress ratio mobilization values of β = 0.2, 0.6, 1.0 and 1.2. These stress states are selected to induce varying fabric anisotropy magnitudes and contact force networks. Once the desired stress state is reached, the shearing process is paused to transition into the erosion simulation phase. Fig 5.4 presents the evolution of the stress ratio for specimens with FC = 25% and 35%. The specific stress states selected for the subsequent erosion simulations are summarized in Table 5.1. Key parameters associated with the contact models are summarized in Table 5.2.

5.2.3 Erosion simulation

Once the target stress state is reached, the shearing process is paused, and the DEM specimen's bottom boundary wall is replaced by a filter wall. Holes in the filter wall are designed to be intermediate in size between coarse and fine particles, enabling selective removal of fines while keeping coarse particles in place (see Fig 5.2 (b)). The CFD module is then introduced to simulate internal erosion. The CFD domain matches the DEM specimen in length and width, with a height 1.8 times the particle assembly. A steady-state vertical seepage flow is applied to the specimens, with the hydraulic gradient i set as 0.5 and 2.0 to investigate the effect of hydraulic gradient on internal erosion. The erosion stage lasts for 14 seconds, during which the stress states of all specimens are maintained constant. In this Chapter, the time step for the DEM simulation (Δt_p) is approximately 1×10^{-7} seconds, while the CFD time step (Δt_f) is also set as 1×10^{-5} seconds to ensure numerical stability. Additional parameters related to the erosion simulations are summarized in Table 5.2.

5.2.4 Post-eroded shearing

After the erosion stage, the CFD module is deactivated, and the filter wall is replaced with an impermeable rigid boundary, identical to the one used during the initial shearing stage. Direct shearing is then resumed from the current stress state and continues until a shear strain of 25% is reached. During the re-shearing stage, the evolutions of stress-strain relationship, shear band, force chain and other information are measured in real time.

5.3 Result analysis

5.3.1 Result from erosion stage

Fines mass loss

Fig 5.5 presents the cumulative fines mass loss of all specimens, with results demonstrating a complex interplay between fines content, hydraulic gradient, and mechanical stress state. Under the same hydraulic gradient i and stress state β, fine-dominated specimens (FC = 35%) experience higher relative fines loss than coarse-dominated specimens (FC = 25%). In fine-dominated specimens, the higher proportion of fine particles results in a denser pore structure. However, these fine particles may exist in a loose or weakly constrained state, rendering the soil structure prone to localized collapse under seepage forces, thus reducing its resistance to erosion. Conversely, in coarse-dominated specimens, the overall structure is less likely to experience localized collapse due to the erosion of some specific fine particles. The fine particles are more effectively stabilized by the contact network of coarse particles, further resulting in a lower percentage of fines mass loss (Liu et al. 2020).

In general, fines mass loss decreases at $\beta = 0.6$ compared to $\beta = 0.2$, but increases at $\beta = 1.0$ and peaks at $\beta = 1.2$ for both FC = 25% and 35%. This non-monotonic trend reflects the evolution of soil fabric under shearing. At $\beta = 0.2$, the soil remains relatively isotropic with larger pore spaces, facilitating fine particle migration under seepage. At $\beta = 0.6$, shear-induced fabric anisotropy strengthens contact force chains in the shear direction, constricting pore throats and enhancing particle interlocking, which reduces fines mass loss. This stabilizing effect shows that moderate shear stresses enhance resistance to erosion, which has rarely been observed in earlier studies. This highlights the importance of microstructural evolution, which is often oversimplified in theoretical models. At higher stress ratio mobilizations ($\beta = 1.0$ and 1.2), the increase in fines mass loss indicates a critical transition in soil behaviour. As β increases and approaches 1.2, the specimen nears the failure envelope, potentially inducing localized dilation or shear band formation. During this process, many fine particles cease to contribute to the load-bearing skeleton and are freed (Gu et al. 2014; Iwashita and Oda 2000; Song et al. 2024a; Tordesillas 2007; Xu et al. 2015). Meanwhile, dilation enlarges pore spaces, creating preferential flow paths that enhance fine particle transport. At $\beta = 1.2$, the peak fines mass loss likely results from significant shear-induced local collapses and rearrangements of the internal contact skeleton, which reduces the coordination number of fine particles and thereby weakens their interlocking retention capacity. This observation is supported by Liu et al. (2022) indicating that high shear stresses exacerbate fines mass loss by changing the pore connectivity.

The faster fines mass loss rate in the first several seconds at a hydraulic gradient of $i = 2.0$ (Fig 5.5 (b) and (d)) compared to $i = 0.5$ (Fig 5.5 (a) and (c)), for both fines contents, is driven by the larger seepage force, which causes rapid detachment of loosely bound fines near pore throats in the initial stage. This rapid mobilization likely depletes the most susceptible fines early, after which clogging or stabilization mechanisms may reduce the loss rate. At $i = 0.5$, the lower seepage force leads to a slower, more gradual detachment process. Fig 5.6 shows the local specimen profile and contact force chains for the specimen with a fines content of FC = 35% and $\beta = 1.2$ before erosion. Prior to erosion, fine particles are dispersed around the coarse particles, with some fine particles confined within the pores between coarse particles. At this moment, certain fine particles at this location contribute to the skeletal framework, transmitting forces between coarse particles. However, the local packing configurations under different i gradually exhibit differences as erosion progresses. Fig 5.7 presents the local specimen profiles and contact force chains at the same location within the specimens with FC = 35% subjected to hydraulic gradients of $i = 0.5$ and 2.0 at several different erosion time points. After the initial erosion phase ($t = 4$s), fine particles are eroded from both local packing configurations, accompanied by changes in the contact force chain structures (Fig 5.7 (a) and (d)). Compared to the specimen with $i = 0.5$, the specimen with $i = 2.0$ experiences greater loss of fine particles that contributes to the skeleton structure between coarse particles due to the larger seepage force. This results in increased direct contact between the coarse particles, leading to smaller inter-particle pores, which subsequently cause the remaining fine particles to become clogged. Consequently, the local packing configuration in the specimen with $i = 2.0$ remains structurally stable during the subsequent erosion, with no significant loss of fine particles (Fig 5.7 (e) and (f)). For the specimen with $i = 0.5$, the smaller seepage force results in a relatively gradual collapse and rearrangement of internal contacts compared to the rapid changes observed in the specimen with $i = 2.0$. This slower process prevents the pores between coarse particles from closing quickly, allowing sufficient time for fine particles to be eroded away at a relatively slow rate. However, this may lead to localized collapses within the specimen's internal structure during subsequent erosion stages, initiated by the removal of certain critical fine particles (Liu et al. 2020; Song et al. 2024a; Song et al. 2024b; Tordesillas 2007). During the following structural rearrangement, many fine particles in these regions are released and then rapidly washed away by water flow (Fig 5.7 (a) – (c)), leading to an increase in the fines mass loss rate, as observed in the specimen with $i = 0.5$ and $\beta = 1.2$ between 4s and 6s (pink curve in Fig 5.5 (c)). These findings highlight the interplay between stress-induced fabric evolution and seepage-driven particle mobilization in governing internal erosion and mechanical stability. A more detailed microscopic explanation of the varying degrees of fines mass loss in specimens under different conditions will be presented in the following sections.

Anisotropy of contact

Fig 5.8 and Fig 5.9 show the spatial distributions of contact number (N_c) and normal contact force (F_n) for specimens with FC = 25% and 35% under varying β prior to erosion. For the two specimens with different fines contents, the magnitudes of both the contact number and normal contact force anisotropies increase with shearing, while the corresponding principal directions gradually deviate from the vertical direction.

This means that an increasing number of inherent contacts collapse with shearing, accompanied by the generation of new contacts that distribute along the shear direction to resist the loads (Li and Yu 2009). During this process, many fine particles are released from the constraints, making them more susceptible to being eroded. The observation that cumulative fines mass loss increases with the contact anisotropy is broadly consistent with the findings of Liu et al. (2022) and Hu et al. (2022). However, Fig 5.5 indicates that the specimen with β = 0.2 does not strictly follow this trend, as it exhibits a relatively higher fines mass loss in some cases. This is because, although the anisotropy magnitude plays a critical role in determining the specimen's susceptibility to erosion, the influence of the anisotropy direction cannot be neglected. For specimens under anisotropic stress conditions, the greater the deviation between the directions of anisotropy and seepage flow, the more susceptible the specimen becomes to erosion (Ma et al. 2021; Wautier et al. 2019; Xiong et al. 2020). In this study, although the specimen with β = 0.2 has the smallest anisotropy magnitude, its principal direction is most closely aligned with seepage flow. The internal pore channels of the β = 0.2 specimen, being more consistent with the seepage direction, allow water to pass through more directly and carry away fine particles more easily compared to those in other specimens (Chang and Zhang 2013; Song et al. 2024b). Overall, the combined effect of anisotropy magnitude and direction accounts for the differences in fines mass loss under various stress states observed in Fig 5.5.

Contact buckling and collapse

As previously discussed in Chapter 4, contacts within granular assemblies undergo buckling and/or collapse during both shearing and erosion processes, significantly influencing the microstructural evolution and macroscopic behaviour of gap-graded soils. For the gap-graded soils, Liu et al. (2020) reported that the buckling and eventual collapse of contacts can significantly intensify the erosion of fines, as the loss of key load-bearing contacts (strong force chains) disrupts the force network and weakens the resistance of the matrix to internal erosion.

Fig 5.10 and Fig 5.11 respectively illustrate the evolution of buckling and collapse in strong force chains during the erosion process for specimens with fine contents of FC = 25% and FC = 35% at the stress ratio mobilization of β = 1.2. In these figures, the vertical axes represent the proportion of buckled or collapsed force chains relative to the total number of force chains. In general, *f-f* contacts exhibit the highest susceptibility to buckling and collapse, while *c-c* contacts show the greatest stability.

This difference results from the weaker mechanical interlocking and smaller size of fine particles, which make *f-f* contacts more vulnerable to seepage forces. Extensive buckling and collapse of force chains occur during the initial erosion stage (0 - 2s). Compared to the specimens under i = 0.5, the ones subjected to i = 2.0 experience stronger seepage forces, leading to more intense structural degradation. This internal breakdown and reorganization process releases more fine particles from their original load-bearing positions, making them susceptible to being washed away by the seepage flow. This observation aligns with the higher initial erosion rate shown in Fig 5.5 for the cases with i = 2.0, further highlighting the significant influence of seepage intensity on microstructural stability and particle migration.

As erosion progresses, the extent of contact buckling and collapse gradually diminishes, indicating a progressive stabilization of the specimens. This trend is particularly evident in the coarse-dominated specimens with FC = 25%, which exhibit almost no further contact buckling or collapse in the later erosion stages, except for a minor occurrence of contact collapse between 8-9s in the case of i = 2.0 (Fig 5.10 (d)). For the specimens with FC = 35%, pronounced fluctuations are observed in the fine particle-related contacts (i.e., *c-f* and *f-f* contacts), even after the *c-c* contacts have stabilized. This behaviour is evident in Fig 5.11 (a) and (b) between 7 - 9s, as well as in Fig 5.11 (c) and (d) at around 7s. These more pronounced fluctuations can be attributed to the higher fines content in the fine-dominated specimens, which leads to an increased number of *f-f* contacts and a more interconnected but relatively weaker fine particle network compared to the coarse particle network. As a result, even after the coarse skeleton has stabilized, the migration of certain fine particles under the influence of seepage forces can trigger local force chain reorganizations. This sustained microstructural activity keeps the fine-dominated regions dynamically active throughout the later stages of erosion, further leading to a continuous release and subsequent erosion of the fine particles. This behaviour is evident in the specimen with FC = 35%, β = 1.2, and i = 0.5, which exhibits an increase in erosion rate at around 5s (Fig 5.5 (c)). In addition, although the initial contact buckling and collapse are more pronounced in the specimen under the higher hydraulic gradient of i = 2.0 compared to that under i = 0.5, the rapid filling and clogging of pores by fine particles quickly lead to a relatively stable state. This reduces the likelihood of subsequent severe contact instability, thereby decreasing fines mass loss. This corresponds to the higher initial erosion rate and lower fines mass loss observed in the FC = 35% specimen under i = 2.0, as shown in Fig 5.5 (c) and (d).

5.3.2 Result from shear stage

Mechanical behaviour of non-eroded and post-eroded specimens

After the erosion process, the post-eroded specimens are subjected to resumed direct shear testing under the same normal stress and shear rate as those applied to the non-eroded specimens, starting from their respective post-eroded stress states. Fig 5.12 plots the principal stress ratio η against shear strain γ for both the non-eroded and post-eroded gap-graded soils. For coarse-dominated specimens (FC = 25%), the loss of fine particles results in a slight reduction in peak strength compared to the non-eroded specimen, consistent with previous studies (Chang and Zhang 2011; Chen et al. 2016; Hu et al. 2022; Ke and Takahashi 2015). The effect of seepage flow on the residual strength after erosion appears to be limited. Although the strength curves exhibit greater fluctuations in the later stage of shearing, the residual strength remains close to that of the non-eroded one. For the fine-dominated cases (FC = 35%), specimens under higher β require greater shear strain increments during the erosion process to maintain the required constant stress states. When the stress ratio is low (β = 0.2 and 0.6), the fines mass loss does not lead to significant changes in either peak or residual strength. This can be attributed to internal structural rearrangement and localized clogging, where migrating fine particles accumulate and densify in specific zones during the erosion process, thereby partially offsetting the weakening caused by fines migration (Liu et al. 2023a; Liu et al. 2021; Mu et al. 2023). However, due to the increased role of fine particles in the load-bearing skeleton and their tendency to slip and rotate more easily, the post-eroded shear stress curves exhibit more pronounced fluctuations. For the post-eroded specimens under high stress ratios (β = 1.0 and 1.2), both the peak and residual strengths are reduced compared to the non-eroded specimen. This indicates that under high stress conditions, the internal structure undergoes more intense and widespread erosion-induced damage. In such cases, the particle rearrangements and localized densification caused by erosion are insufficient to offset the overall loss of load-bearing capacity, resulting in a reduction in mechanical strength.

Particle rotation fields of non-eroded and post-eroded specimens

As discussed in Chapter 4, particle rotation has proven particularly useful in DEM simulations for highlighting shear banding. This Chapter also adopts the rotation field as a proxy to identify early signs of shear localization, following methods used by

Wang et al. (2022b) and Zhu and Yin (2019), aiming to reveal how internal erosion influences the onset and progression of shear instability.

Fig 5.13 shows the two particle rotation fields of the non-eroded specimens at shear strain γ = 20%. The shear bands of fine-dominated and coarse-dominated specimens exhibit some differences under direct shear conditions without erosion. The coarse-dominated specimen (FC = 25%) exhibits a load-bearing framework mainly composed of coarse particles, where *c-c* contacts are responsible for transmitting most of the shear stress, as shown in Fig 5.14. The rotation of particles is concentrated within the *c-c* network, resulting in a narrow and well-defined shear band (indicated by red particles). Fine particles in this specimen mostly act as passive fillers with low rotation. In the fine-dominated specimen (FC = 35%), however, a higher proportion of *c-f* and *f-f* contacts allows fine particles to actively participate in force transmission. This contact network weakens the integrity of the load-bearing skeleton, reduces local stiffness, and facilitates particle sliding and rotation. Consequently, the shear band becomes wider and more diffuse, with an active rotation field among fine particles. Additionally, *c-f* contacts in both specimens act as transitional or lubricating zones, which disturb interlocking and result in irregular shear band boundaries.

Fig 5.16 and Fig 5.16 show the particle rotation fields of several post-eroded specimens under varying erosion or shear conditions. After erosion, specimens subjected to direct shear exhibit some changes in the shear bands compared to their non-eroded counterparts. These changes are particularly pronounced in fine-dominated specimens, while coarse-dominated specimens retain a more stable shear band structure. In the post-eroded specimens with FC = 25%, the erosion-induced structural disturbances are limited. The primary *c-c* contact networks remain largely intact, preserving the narrow and well-defined shear bands in the middle of the specimens. Under higher β and i, localized erosion slightly disturbs the internal structure, leading to the appearance of secondary particle rotation hotspots away from the primary shear path. These zones reflect incipient or newly developed shear trajectories, likely forming around stress concentrations or newly generated voids, but overall deformation still concentrates along the preexisting skeleton-dominated shear band.

In contrast, post-eroded specimens with FC = 35% show more pronounced changes due to the significant loss and redistribution of fine particles. When the hydraulic gradient is low, fine particles are more likely to be eroded without forming significant clogging, especially in the lower portion of the specimen (Fig 5.5). This causes a substantial loss of *f-f* and *c-f* contacts and allows the shear band to extend into previously stable or eroded regions, resulting in wider, more diffuse rotation fields. However, under higher *i*, erosion occurs more rapidly and promotes more intense clogging in narrow pore spaces, as noted earlier. This redistribution of fine particles generates complex and irregular contact topologies, leading to multi-centered rotation hotspots away from the primary shear band. Additionally, when β is also high, the specimen is already approaching or entering shear localization. In this case, the original shear band continues to dominate the deformation, but it now coexists and interacts with erosion-induced secondary rotation zones. Moreover, under high β, the substantial loss of fine particles in certain regions leads to a local transition toward a coarse-dominated load-bearing skeleton. This structural reorganization changes the local stiffness and load transfer capacity in these regions, thereby altering the development of the shear band. Depending on the surrounding fabric, this may either reinforce the original shear band or redirect deformation into newly formed weaker zones, contributing further to the asymmetric and spatially diffuse nature of the post-eroded rotation field.

Overall, internal erosion breaks the original contact structures. The resulting shear responses become less stable and more spatially heterogeneous. Rather than a single, well-defined shear band, the post-eroded specimens may develop multiple deformation paths, reflecting the coupling between preexisting structural weaknesses and erosion-induced rearrangements.

Force chain in shear band

As previously noted, the initiation and development of the shear band is a fundamental feature of the direct shear test. It determines the transition between peak and residual strength and serves as a micro-mechanical indicator of particle rearrangement, contact loss, stress redistribution, etc. In direct shear tests, shear localization typically initiates and develops near the mid-height of the specimen. While not explicitly predefined, this central region consistently experiences the highest shear strain due to boundary-induced stress concentration, making it the natural location for shear band formation (Kodicherla et al. 2019; Kozicki et al. 2013). In this thesis, the middle layer of the specimen (layer L2 in Fig 5.17) is selected to investigate the roles of coarse and fine particles in the shear band and the evolution of the contacts during shearing.

Fig 5.18 and Fig 5.19 respectively illustrate the contribution of each contact type to the strong force chain network within the shear band for specimens with FC = 25% and FC = 35%, including both non-eroded and some post-eroded cases. For the specimens with FC = 25%, both non-eroded and post-eroded specimens exhibit a shear band dominated by coarse particles throughout the shearing process. The contribution of *c-c* contacts gradually increases as shearing progresses, although a slight decrease is observed in the later stages. In contrast, the contributions of *c-f* and *f-f* contacts first decrease and then increase with shearing. This trend may be attributed to the evolving mechanical role of fine particles during shearing. Initially, many *c-f* and *f-f* contacts collapse due to fine particle sliding or rotation. As shearing continues, some fine particles originally constrained by *c-f* contacts may detach and migrate into pore spaces within the coarse skeleton. Once stabilized in these locations, they form new contacts and resume participation in load transmission. Additionally, in post-eroded specimens, some fine particles are released from *c-f* and *f-f* contacts under the influence of seepage force and are subsequently washed away. As a result, erosion enhances the dominance of coarse particles in the strong force chain network within the shear bands, particularly in specimens with greater fines mass loss.

In the non-eroded specimens with FC = 35%, the contribution of *c-c* contacts progressively increases during shearing, while that of *c-f* contacts shows a declining trend. The contribution of *f-f* contacts remains relatively stable throughout the shearing process. Despite the observed trends, fine particles continue to dominate the strong force chain network, highlighting their significant role in load transmission within the shear band. However, in post-eroded specimens with FC = 35%, a notable structural transition is observed, where coarse particles become the primary load-bearing agents. The contribution of *c-c* contacts increases significantly and surpasses that of *c-f* and *f-f* contacts. This change is primarily driven by the substantial loss of fine particles under seepage forces, which triggers widespread structural collapse and reorganization within the specimens. As fine particles are removed, coarse particles come into direct contact, forming a more stable and interconnected force chain network. This indicates a shift from a fine-dominated granular structure to a coarse-dominated framework after erosion. Moreover, the specimen with $\beta = 1.2$ and $i = 0.5$ exhibits the most significant increase in *c-c* contact contribution. However, this increase requires the greatest shear strain to develop, indicating that this specimen has experienced the most frequent shear loading cycles during the erosion process to maintain the target stress state. The most pronounced structural degradation and reorganization during erosion then results in the most substantial fines mass loss and the strongest dominance of *c-c* contacts within the shear band. The evolving role of fine particles reflects the process of particle rearrangement and force chain reorganization during both erosion and shearing processes. It also highlights that even in specimens with relatively low fines content, fine particles can play a non-negligible role in the formation and development of the shear band.

5.4 Conclusions

In this chapter, a micro-macro investigation based on coupled CFD–DEM analysis of gap-graded granular soils under direct shear conditions is presented, focusing on the effects of fines content (FC), hydraulic gradient (i), and stress state (β) on internal erosion and shear mechanical behaviour. The influence of internal erosion on the formation and development of shear bands in specimens with different FC during the post-eroded shearing process is thoroughly discussed, with particular emphasis on the underlying microscopic mechanisms. The main findings are listed as follows:

1. For both fine-dominated and coarse-dominated specimens, the fines mass loss initially decreases and subsequently increases as β increases, indicating that both the fabric anisotropy and its orientation significantly influence erosion behaviour. A high hydraulic gradient leads to rapid detachment of fine particles and early clogging, after which the structure tends to stabilize. In contrast, a low hydraulic gradient results in gradual erosion and delayed structural collapse. In fine-dominated specimens, this progressive process can induce localized instability and particle rearrangement, making the specimen more susceptible to sudden fines mass loss during the late stage of erosion.

2. Contact buckling and collapse are most pronounced during the initial erosion stage, with *f-f* contacts exhibiting the highest susceptibility to failure. Under a high hydraulic gradient, specimens undergo more severe structural degradation during this early phase. As erosion progresses, coarse-dominated specimens rapidly stabilize, while fine-dominated specimens continue to show fluctuations, particularly in *c-f* and *f-f* contacts. This sustained microstructural activity leads to continuous fine particle release, especially under a low hydraulic gradient.

3. After erosion, fines mass loss in coarse-dominated specimens results in only a

minor reduction in peak strength, with the residual strength remaining largely unchanged. In fine-dominated specimens, internal rearrangement and localized clogging partially compensate for the structural weakening under low stress states ($\beta = 0.2$ and 0.6), helping to maintain overall strength stability. However, greater strength degradation is observed under higher stress states ($\beta = 1.0$ and 1.2), indicating more extensive erosion-induced damage. In these cases, particle rearrangements and localized densification are insufficient to restore the original load-bearing capacity, particularly under high stress conditions.

4. The formation and development of shear bands are significantly influenced by internal erosion, with notable differences between coarse-dominated and fine-dominated specimens. In specimens with FC = 25%, the coarse skeleton remains dominant, and erosion slightly alters the contact network, with *c-c* contacts maintaining primary load transmission. In contrast, specimens with FC = 35% exhibit a structural transition after erosion, where many fine particles are washed away, leading to increased *c-c* contact dominance and a shift from fine-dominated to coarse-dominated load-bearing framework. This transition, especially under high β and low i, requires greater shear strain to re-establish stable force chains, indicating extensive microstructural reorganization. Particle rotation fields reveal that erosion leads to wider, more diffuse shear bands in fine-dominated specimens, while coarse-dominated ones retain narrow, well-defined bands.

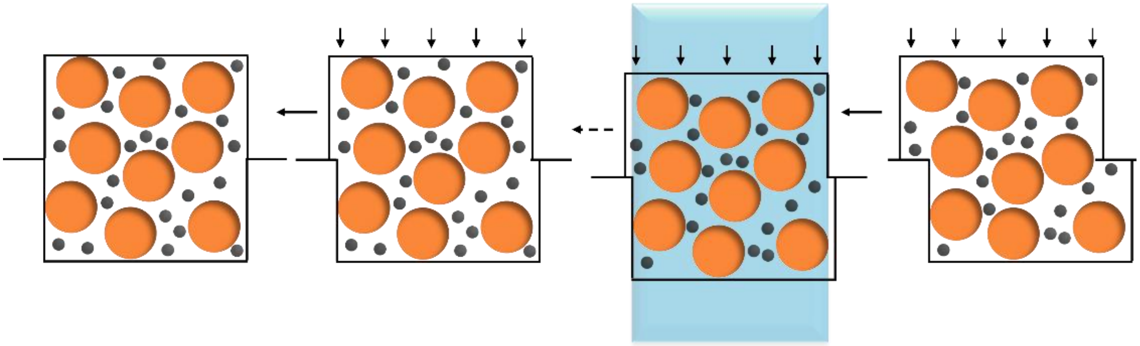

Fig 5.1 Stages of the simulation.

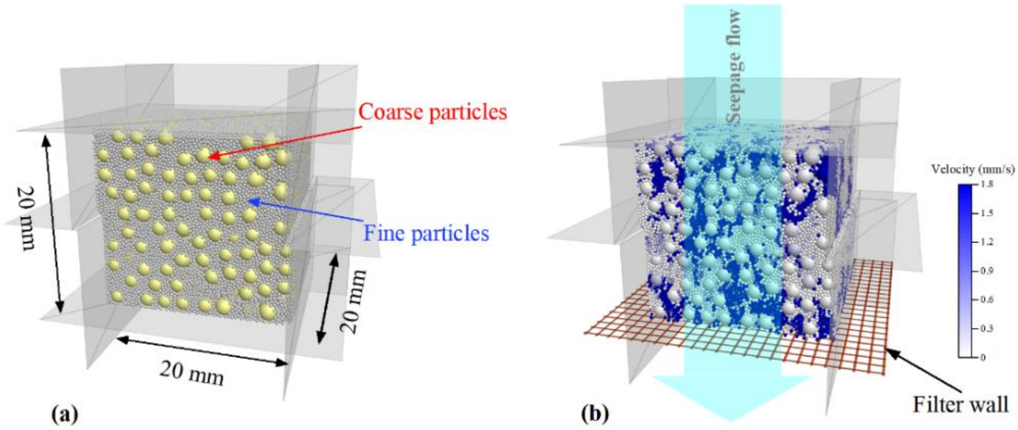

Fig 5.2 Model of the (a) direct shear test and (b) coupled CFD-DEM simulation test.

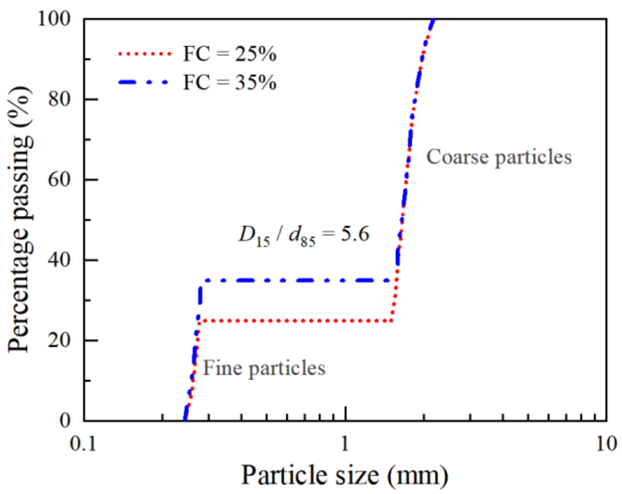

Fig 5.3 Particle size distribution of the gap-graded soil.

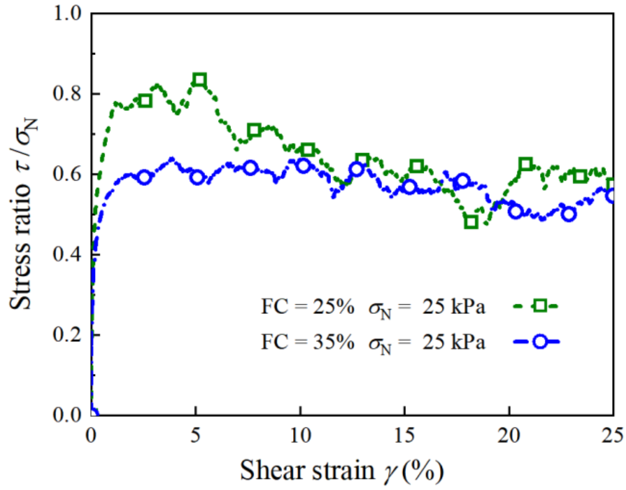

Fig 5.4 Stress-strain relationships for soils with FC = 25% and 35% without erosion.

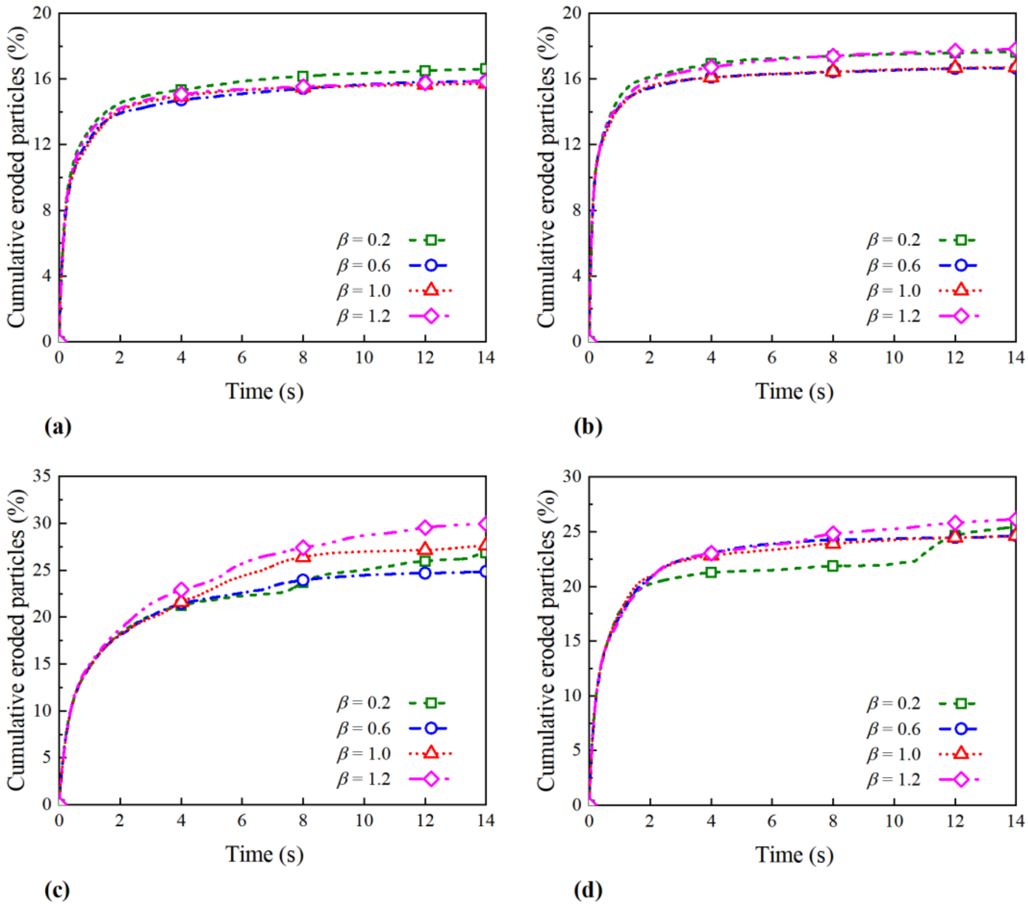

Fig 5.5 Cumulative eroded fines mass during erosion: (a) FC = 25% and $i = 0.5$; (b) FC = 25% and $i = 2.0$; (c) FC = 35% and $i = 0.5$; (d) FC = 35% and $i = 2.0$.

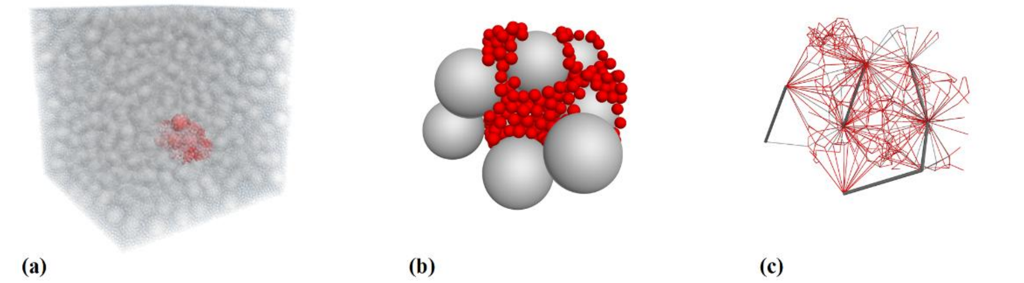

Fig 5.6 Local packings of the case before erosion with FC = 35% and β = 1.2.

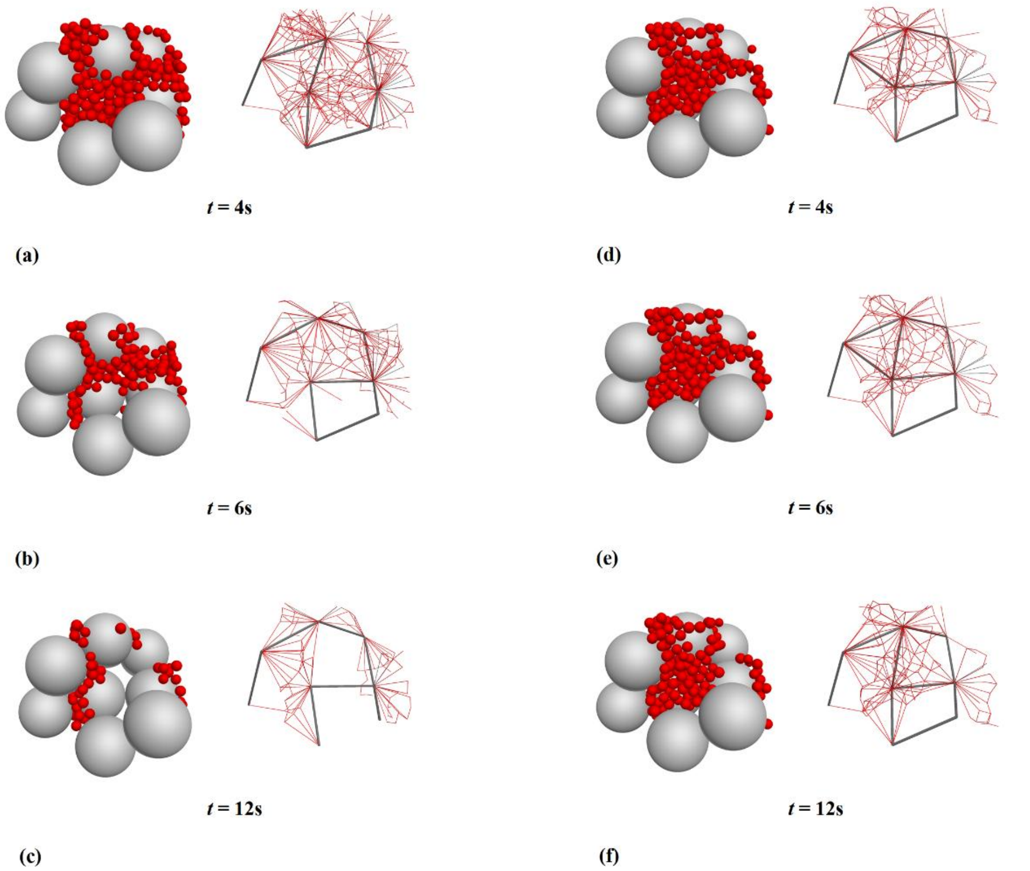

Fig 5.7 Local packings of the case with FC = 35% and β = 1.2, under hydraulic gradients of (a - c) i = 0.5 and (d - f) i = 2.0, at t = 4s, 6s and 12s.

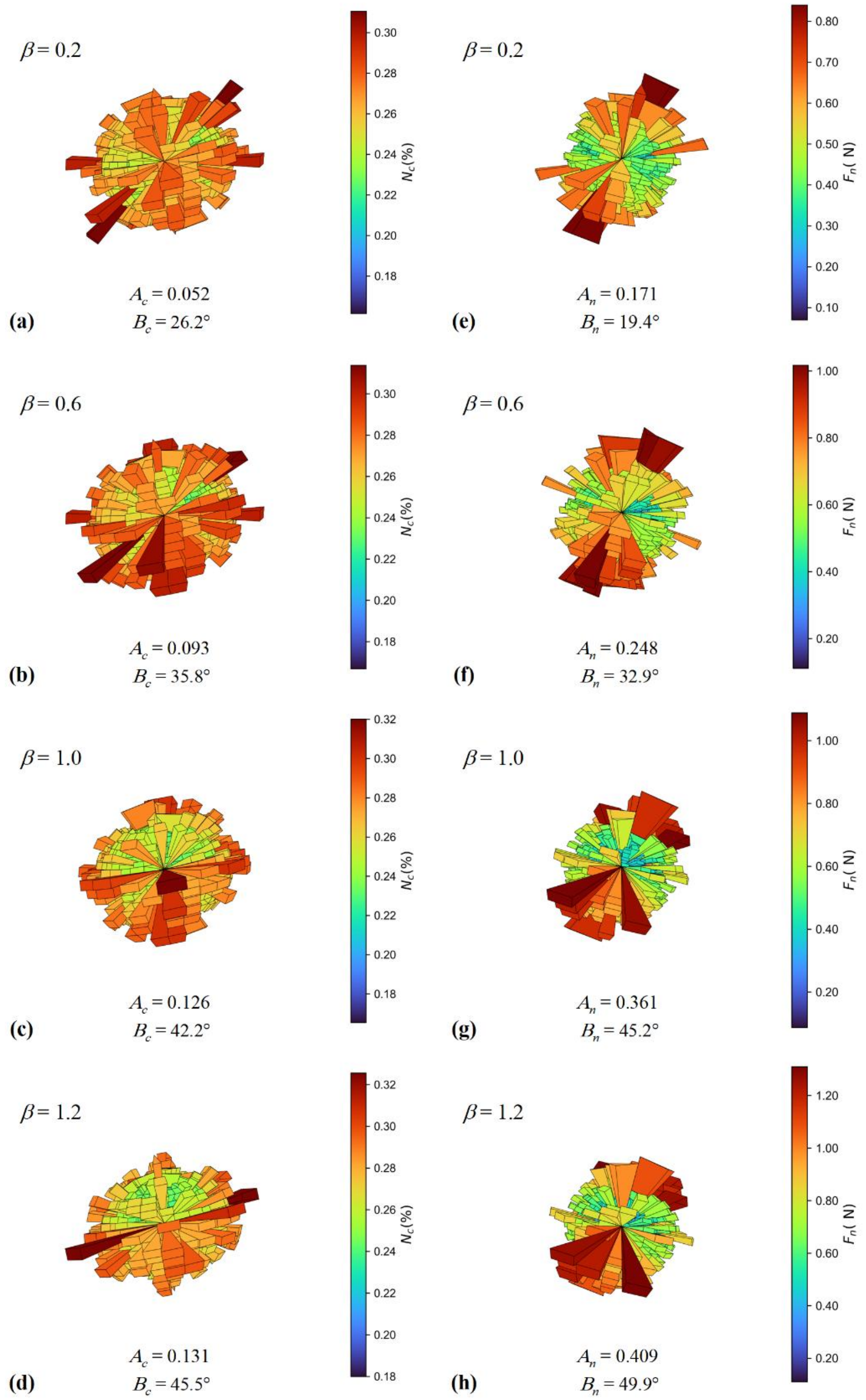

Fig 5.8 Distribution of (a - d) contact normal and (e - h) normal contact force before erosion for specimens with FC = 25%.

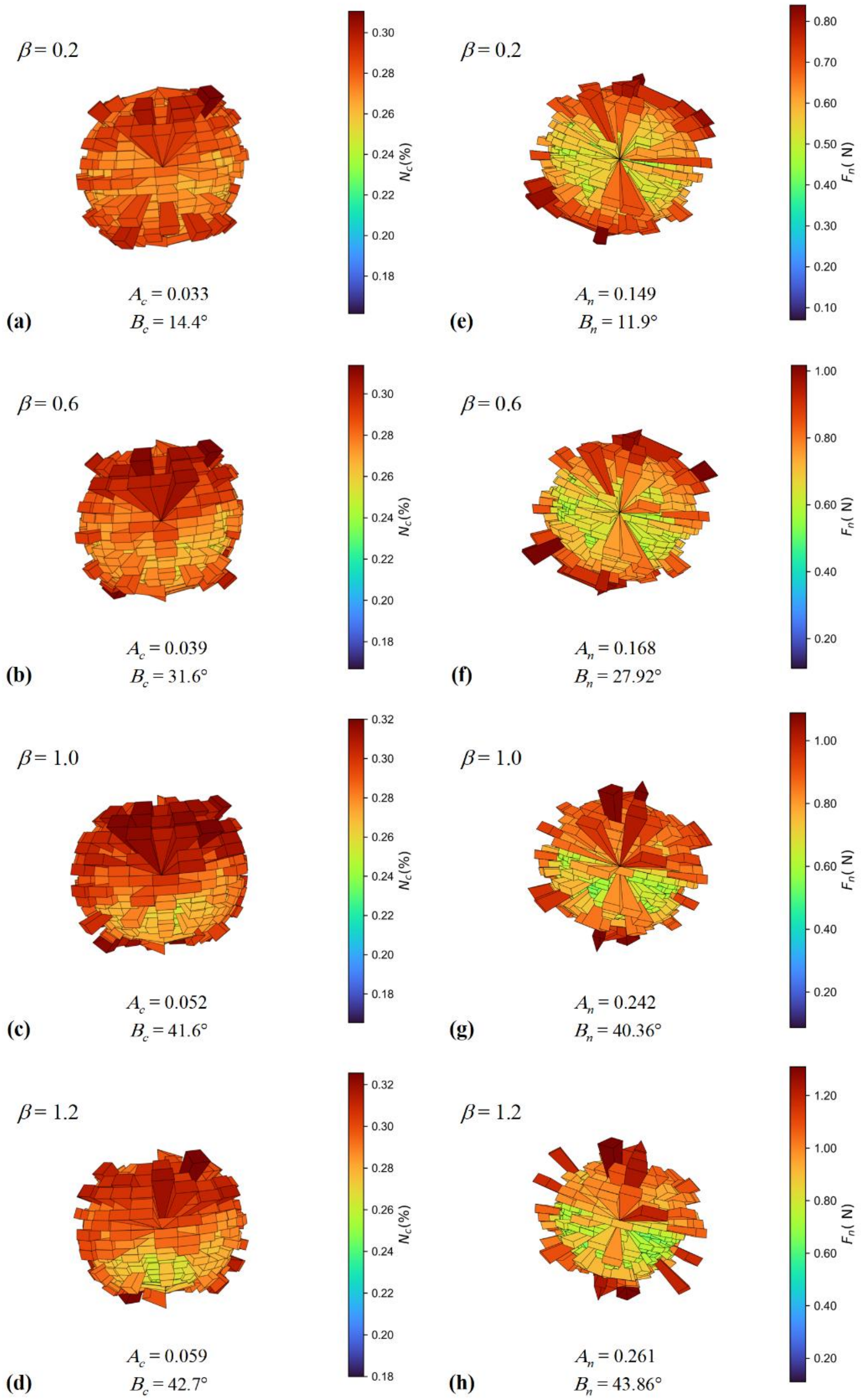

Fig 5.9 Distribution of (a - d) contact normal and (e - h) normal contact force before erosion for specimens with FC = 35%.

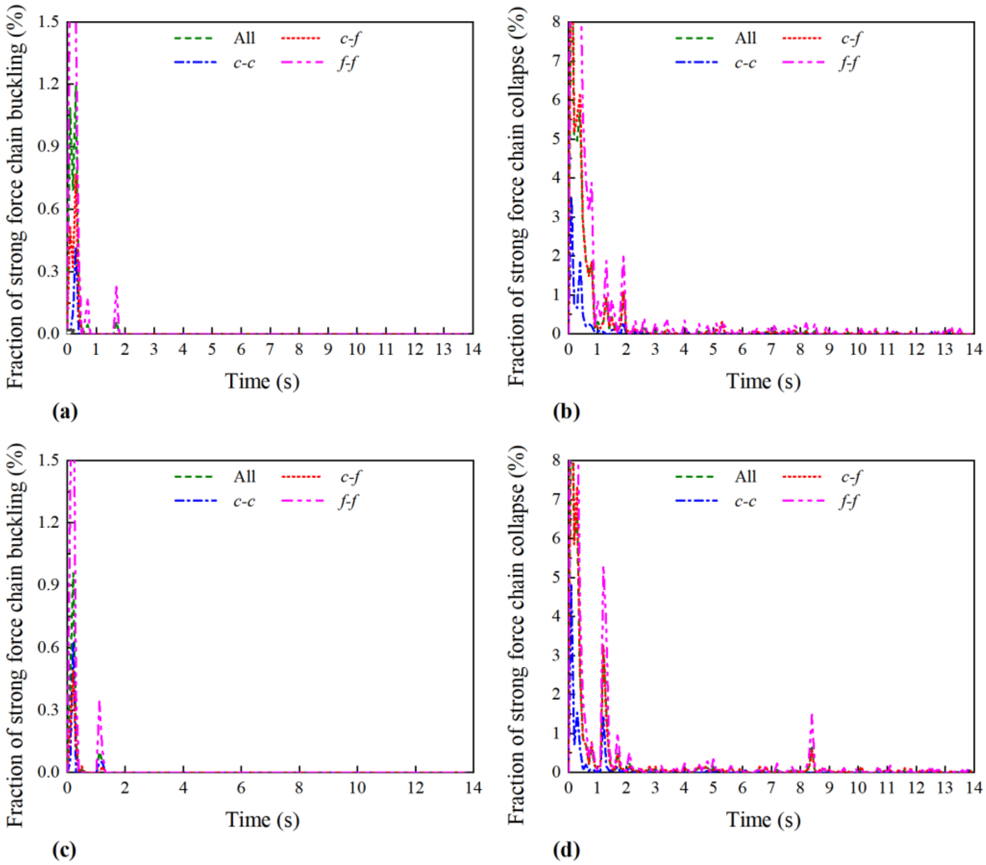

Fig 5.10 Fraction of strong force chain buckling and collapse during erosion in specimens with $\beta = 1.2$ and FC = 25%, under (a–b) $i = 0.5$ and (c–d) $i = 2.0$.

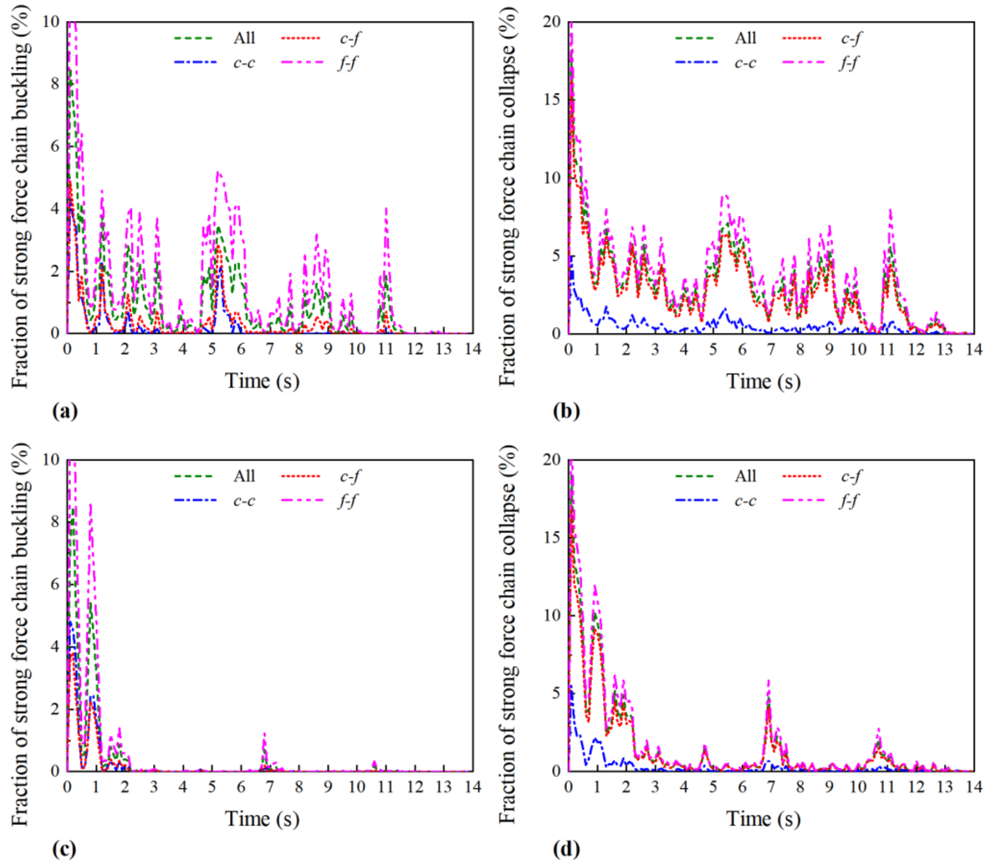

Fig 5.11 Fraction of strong force chain buckling and collapse during erosion in specimens with $\beta = 1.2$ and FC = 35%, under (a–b) $i = 0.5$ and (c–d) $i = 2.0$.

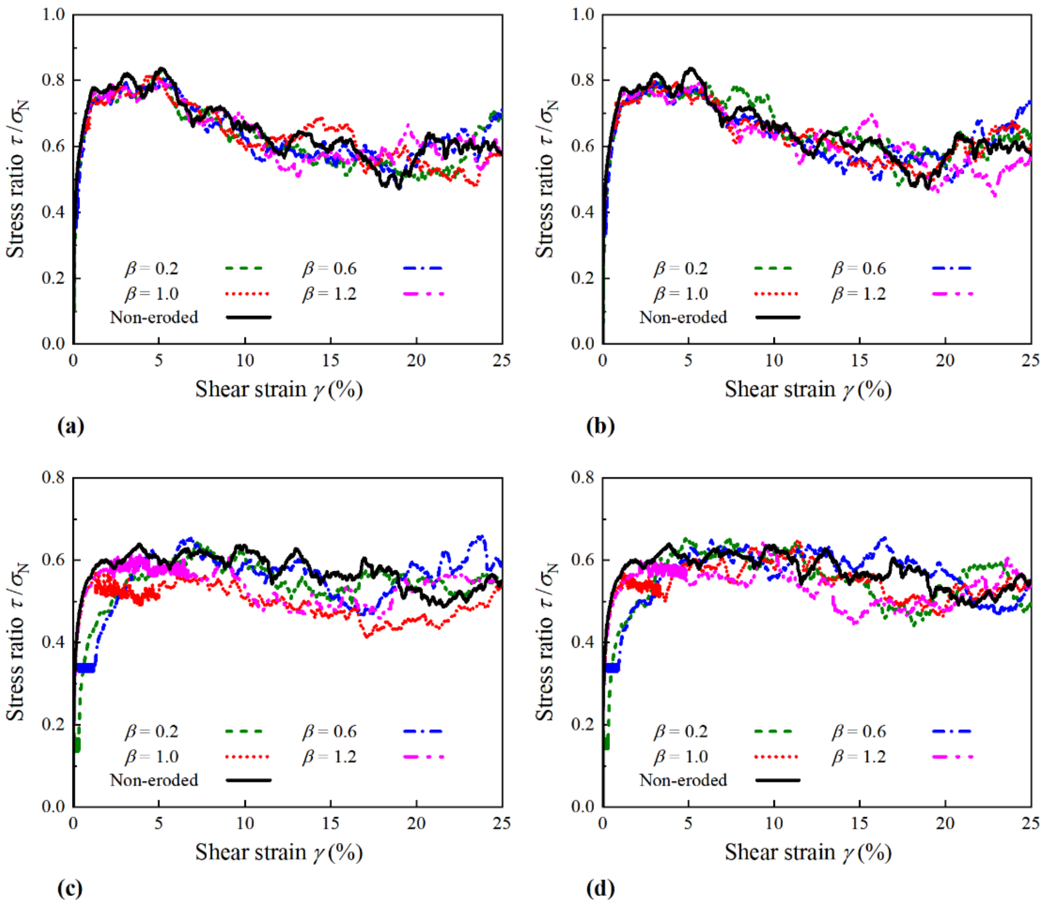

Fig 5.12 Evolutions of principal stress ratio $\eta = \tau / \sigma_N$ versus shear strain before and after erosion: (a) FC = 25% and i = 0.5; (b) FC = 25% and i = 2.0; (c) FC = 35% and i = 0.5; (d) FC = 35% and i = 2.0.

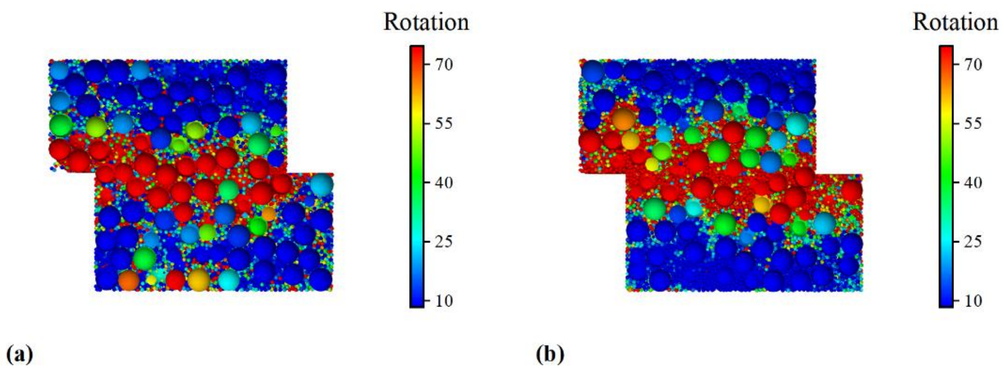

Fig 5.13 Particle rotation fields of non-eroded specimens with (a) FC = 25% and (b) FC = 35%.

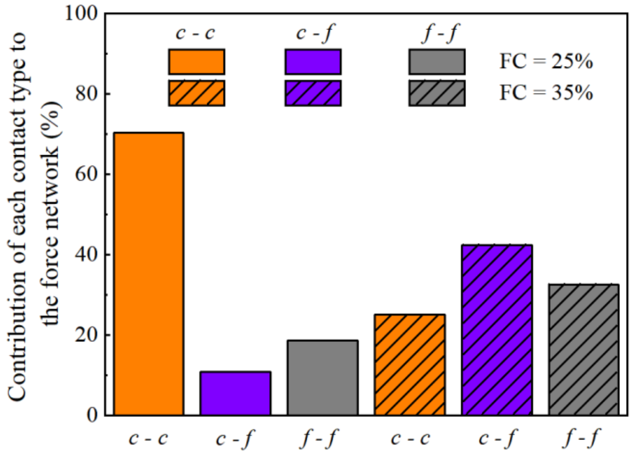

Fig 5.14 Contribution of each contact type to the force chain structure in non-eroded specimens.

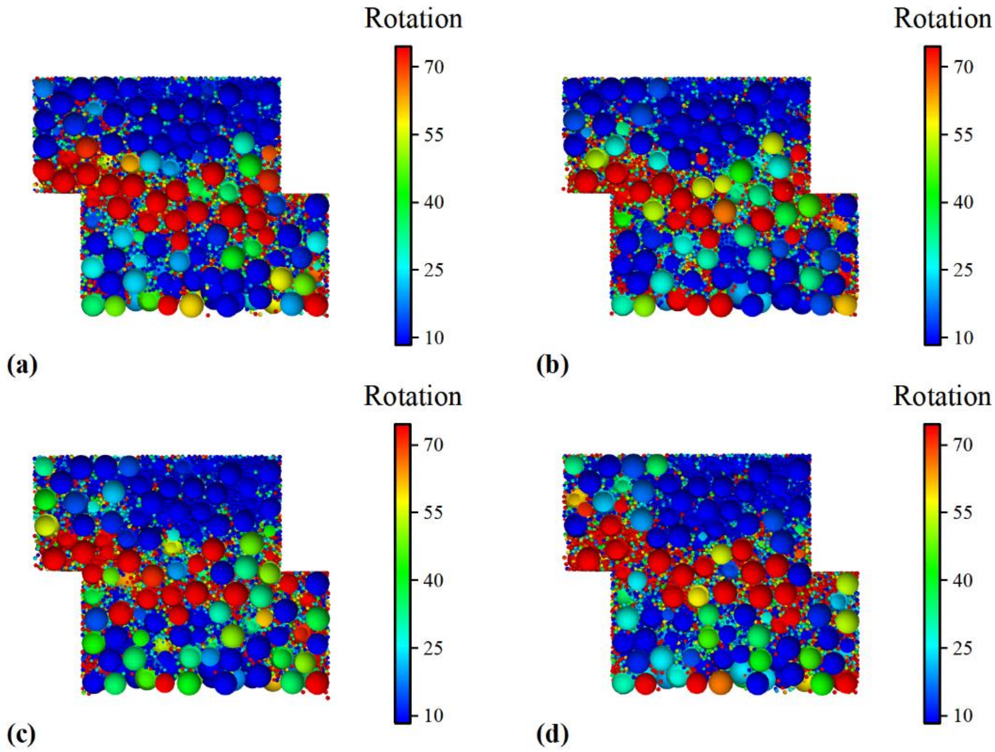

Fig 5.15 Particle rotation fields of post-eroded specimens with FC = 25%: (a) $\beta = 0.6$ and $i = 0.5$; (b) $\beta = 1.2$ and $i = 0.5$; (c) $\beta = 0.6$ and $i = 2.0$; and (d) $\beta = 1.2$ and $i = 2.0$.

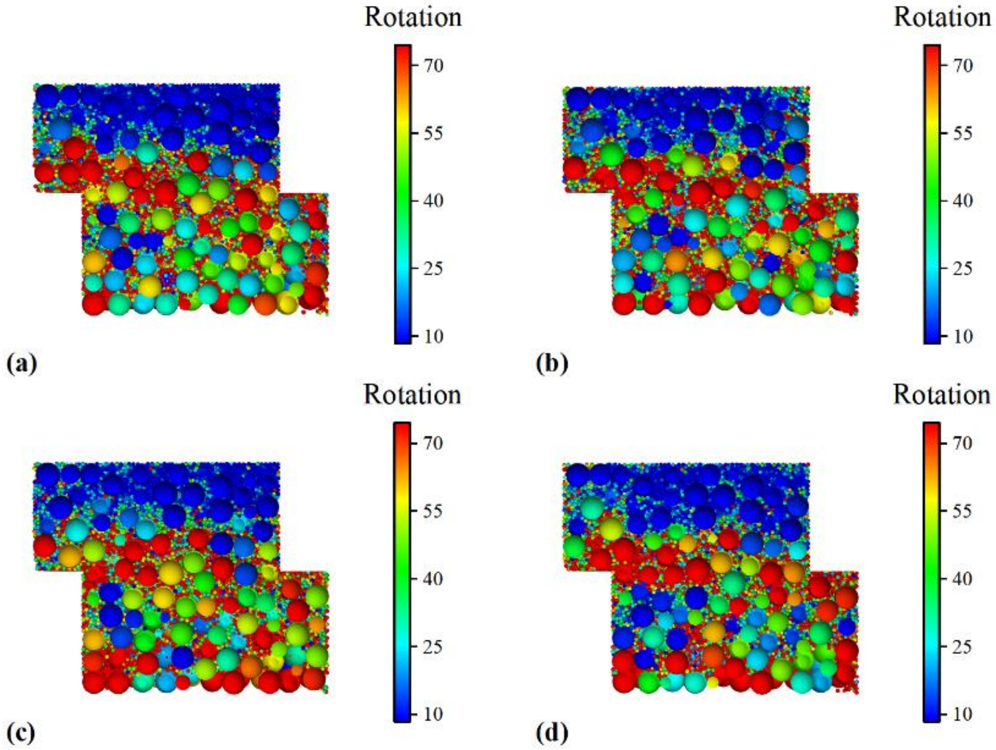

Fig 5.16 Particle rotation fields of post-eroded specimens with FC = 35%: (a) β = 0.6 and i = 0.5; (b) β = 1.2 and i = 0.5; (c) β = 0.6 and i = 2.0; and (d) β = 1.2 and i = 2.0.

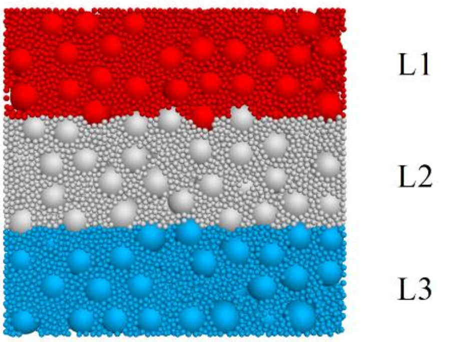

Fig 5.17 Classified layers of the DEM specimen.

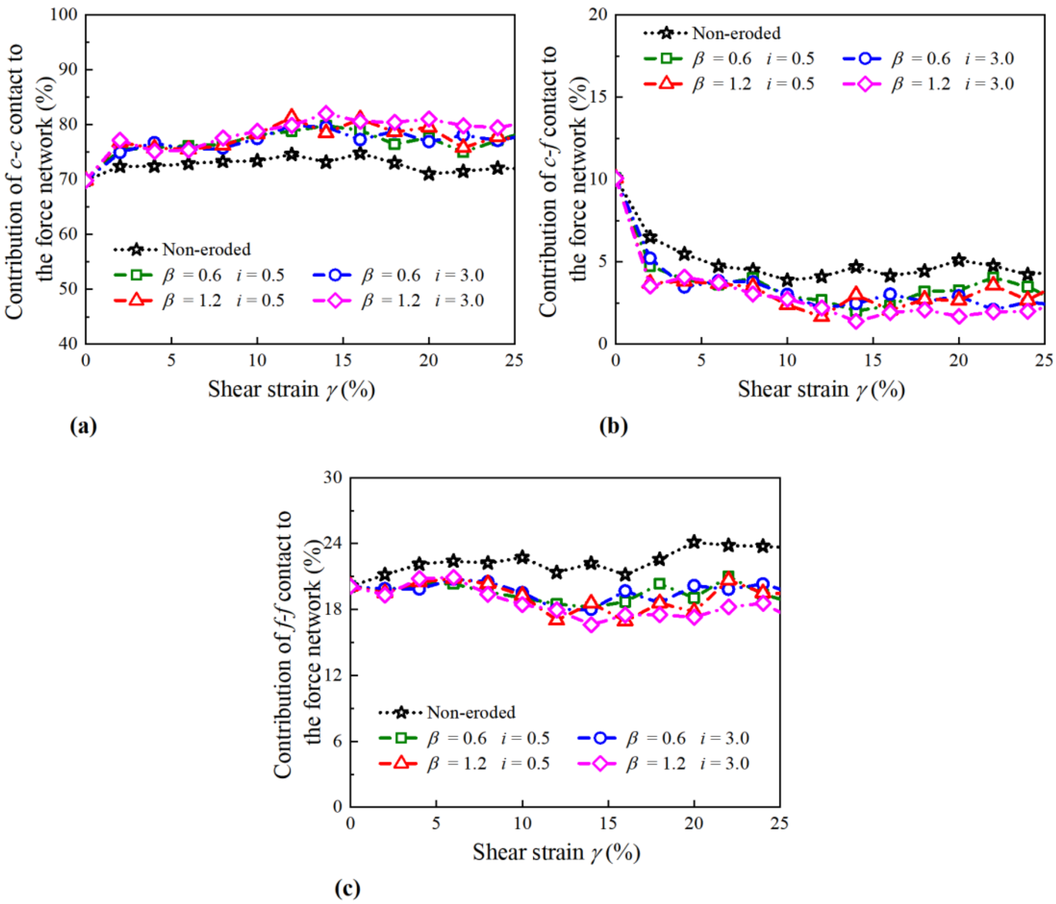

Fig 5.18 Contribution of each contact type to the strong force chain network in the shear band for specimens with FC = 25%: (a) *c-c*; (b) *c-f*; and (c) *f-f* contacts.

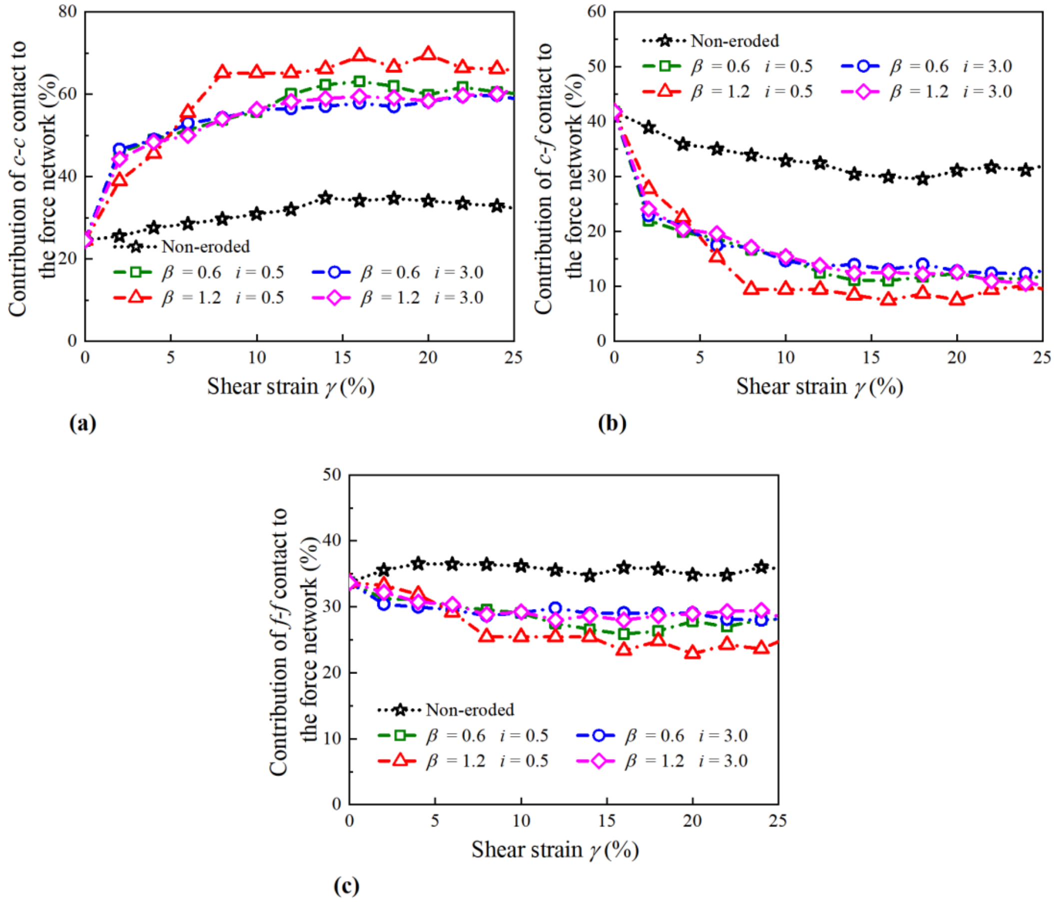

Fig 5.19 Contribution of each contact type to the strong force chain network in the shear band for specimens with FC = 35%: (a) *c-c*; (b) *c-f*; and (c) *f-f* contacts.

Table 5.1 Summary of samples in the internal erosion simulations

ID	1	2	3	4	5	6	7	8	9	10	11	12	13	14	15	16
FC (%)	25	25	25	25	25	25	25	25	35	35	35	35	35	35	35	35
i	0.5	0.5	0.5	0.5	2.0	2.0	2.0	2.0	0.5	0.5	0.5	0.5	2.0	2.0	2.0	2.0
β	0.2	0.6	1.0	1.2	0.2	0.6	1.0	1.2	0.2	0.6	1.0	1.2	0.2	0.6	1.0	1.2

Table 5.2 Parameters used in the coupled CFD-DEM simulations

Parameters			Values
DEM	Elastic modulus	E_{PP} (Pa)	2.0×10^{8}
		E_{PW} (Pa)	2.0×10^{8}
	Stiffness ratio	k_{PP}	3.0
		k_{PW}	3.0
	Friction coefficient	μ_f	0.3
	Rolling friction coefficient	μ_r	0.1
	Density of particles	ρ (kg/m^3)	2650
	Time step	Δt_p (s)	1×10^{-7}
CFD	Cells	Length × Width × Height	5 × 5 × 9
	Fluid viscosity	μ (Pa $*$ s)	1.0×10^{-3}
	Density of fluid	ρ_f (kg/m^3)	1000
	Time step	Δt_f (s)	1.0×10^{-5}

CHAPTER 6: COUPLED CFD–DEM INVESTIGATION OF INTERNAL EROSION AND RESIDUAL SHEAR BEHAVIOUR IN GAP-GRADED SOILS UNDER RING SHEAR CONDITION

6.1 Introduction

Soil is subjected to ring shear conditions when it undergoes large deformations with continuous shearing along a cylindrical or annular surface. This condition is commonly observed in shear zones of landslides, fault gouges, or soil layers subjected to repeated or long-term loading, where shear strain localizes into a narrow zone and evolves toward residual strength. Investigating the residual stress of soil is of great significance, as it represents the minimum shear strength that the soil can sustain after large displacement, which is critical for assessing the long-term stability and reactivation potential of landslides. Compared to other shear testing methods, the ring shear test allows continuous rotation without loss of shear surface continuity, enabling the simulation of unlimited shear displacement. This unique feature makes it particularly suitable for studying the transition from peak to residual strength and the long-term mechanical behaviour of soils under progressive failure (Dong et al. 2020; Mohajeri et al. 2020). In addition, soil may experience internal erosion prior to entering the large deformation stage. This process can disrupt the original particle arrangement and the load-bearing structure, leading to internal restructuring and the development of preferential flow paths, thereby significantly altering both the peak and residual strength of the soil. Notably, the residual stress may not only change in magnitude but also exhibit altered fluctuation patterns during shearing. The fluctuation of residual stress reflects the dynamic process of particle rearrangement, interlocking, and sliding within the shear zone, and its stability directly influences the soil's mechanical response under long-term or cyclic loading. Therefore, investigating both the magnitude and the fluctuation behaviour of residual stress is essential for understanding the post-eroded strength evolution and long-term stability of soil, which has important implications for assessing landslide reactivation potential and the durability of geotechnical structures.

In this Chapter, a CFD-DEM framework is presented that integrates ring shear loading history with internal erosion simulation to systematically investigate the influence of shear stress and normal stress on internal erosion in gap-graded soils. The study further examines how internal erosion, occurring under ring shear conditions and normal stresses, subsequently affects the post-eroded shear strength and sustained large-displacement shearing behaviour. By pausing the shearing process at defined stress levels under different normal stresses, applying controlled fluid flushing via CFD module, and then resuming ring shear testing, the proposed approach effectively captures the coupled interaction between mechanical loading and hydraulic processes from both macroscopic and microscopic perspectives.

6.2 Simulation program

The numerical simulations in this Chapter follow a four-stage procedure like that in Chapter 4 and Chapter 5 to systematically investigate the coupled effects of stress states and internal erosion in gap-graded soils. As illustrated in Fig 6.1, the process begins with specimen preparation and proceeds sequentially through: (1) generating a gap-graded soil specimen, (2) applying ring shear loading to achieve predefined stress states, (3) introducing fluid flow under sustained mechanical loading to simulate internal erosion, and (4) resuming shear deformation to assess the post-eroded mechanical behaviour. This staged approach enables a comprehensive analysis of the bidirectional coupling between stress history and erosion-induced fabric degradation.

6.2.1 Specimen preparation

The first step involves generating a numerical specimen representative of gap-graded soils within a ring shear configuration using DEM (Fig 6.2 (a)). The DEM model features an inner cylindrical wall with a diameter of 36 mm and an outer cylindrical wall with a diameter of 56 mm, forming a specimen with a height of 18 mm. The top rigid wall is vertically movable to apply and maintain the target normal stress. Short vertical walls are attached to both the top and bottom boundaries and are aligned circumferentially to transmit torque, with torsional shear applied through the rotation of the top short vertical walls (Mohajeri et al. 2020; Simons et al. 2015). Coarse and fine particles are randomly packed within this numerical apparatus according to PSD shown in Fig 6.3. The fines content is 25% by mass and the gap ratio of the gap-graded soil is also approximately 5.6, indicating that the soil is internally unstable (Fannin and Moffat 2006; Song et al. 2024b; Zhao et al. 2024). Moreover, the relative density (D_r) is uniformly maintained at about 63% across all specimens, ensuring consistent initial packing conditions (Liu et al. 2021).

6.2.2 Ring shear before erosion

Following specimen preparation, torsional shear is initiated by rotating the short vertical walls at a constant angular velocity under a constant normal stress of 25 kPa, 50 kPa, or 100 kPa. Similarly, the stress ratio mobilization coefficient, defined as $\beta = \tau / \tau_c$, is introduced to characterize the stress state of the particle assembly, where τ denotes the current shear stress and τ_c is the residual shear strength under each corresponding normal stress. Fig 6.4 shows the shear stress-strain curves for specimens under the three normal stress levels. The shearing process is paused at predefined stress states of β = 0.4, 0.7, 1.0, and 1.2, which correspond to progressively evolving fabric anisotropy and contact force network configurations. These selected stress states are designed to represent distinct stages along the shear strength development path and are summarized in Table 6.1 for reference. Key parameters used in the DEM ring shear model are listed in Table 6.2.

6.2.3 Internal erosion

In this stage, the bottom wall of the DEM specimen is replaced with a porous filter wall designed to mimic a physical retention boundary as shown in Fig 6.2 (b). Subsequently, the CFD module is activated to impose a steady seepage flow through the specimen. The CFD domain is geometrically aligned with the DEM sample in terms of inner and outer diameters and extends vertically to 1.8 times the height of the particle assembly to ensure sufficient space for flow development and pressure stabilization. A constant hydraulic gradient of i = 2.0 is applied here. This gradient is chosen to be sufficiently high to initiate internal erosion, yet below the threshold for full liquefaction. The erosion process is simulated for a duration of 10 seconds. During this period, the mechanical state of the specimen, particularly the torsional shear stress and normal stress, is actively maintained at the predefined target levels (i.e., β = 0.4, 0.7, 1.0, and 1.2). If particle loss due to erosion causes a reduction in shear stress, the torsional shear boundary is temporarily reactivated to restore the target stress state, ensuring that erosion occurs under sustained mechanical loading (Liu et al. 2023b; Song et al. 2024b). Simulation parameters used in CFD module, such as fluid viscosity and fluid density, are summarized in Table 6.2.

6.2.4 Ring shear after erosion

After the erosion process is completed, the fluid phase is deactivated, and the porous filter wall is replaced with an impermeable rigid boundary identical to that used in the initial shear stage. The torsional shearing process is then resumed from the current deformed and eroded configuration, using the same angular velocity as before. The post-eroded stress-strain response is recorded to evaluate the changes in mechanical properties, including peak shear strength, residual strength, and the evolution of fabric anisotropy. By comparing these responses with those of the intact specimen without erosion, this stage quantitatively assesses the extent of mechanical changes induced by internal erosion under different initial stress states and normal stresses.

6.3 Simulation results and discussions

6.3.1 Result from erosion stage

Fines mass loss

The cumulative eroded fines mass during erosion and the ultimate loss in all specimens with different β and σ_N are plotted in Fig 6.5 and Fig 6.6, respectively. The fines mass loss observed in the simulations exhibits a strong dependence on the pre-shearing stress state β and the confining normal stress σ_N. For all levels of σ_N, the mass loss increases only marginally as β rises from 0.4 to 0.7. However, a significant increase in erosion is observed when β reaches 1.0 and further intensifies at β = 1.2. This pronounced threshold behaviour cannot be attributed solely to the magnitude of the applied seepage flow. Instead, it is significantly influenced by the pre-existing microstructural state of the gap-graded soil, which is a direct consequence of the prior shear deformation history.

The initial microstructure, established during the shearing phase prior to erosion, plays a decisive role in determining the soil's erodibility. In specimens with low β values (β = 0.4 and 0.7), the particle assembly remains in a pre-failure regime. The coarse particle skeleton maintains a relatively stable and isotropic contact network. Although minor local rearrangements occur, the overall structure is robust, and the number of broken contacts is limited. As a result, the population of fines that are liberated and become susceptible to transport by fluid forces is small. Under these conditions, the subsequent application of seepage flow acts as a perturbation, but the inherent stability of the contact structure effectively limits particle mobilization, resulting in only a modest amount of erosion. In contrast, specimens subjected to high β values (β = 1.0 and 1.2) have undergone significant shear deformation and internal structural reorganization. This results in a highly anisotropic and damaged microstructure.

To quantify this damage, the concept of contact collapse is employed here. Contact collapse usually liberates many fine particles that were previously confined within the interstices of the coarse skeleton. Importantly, this release is not limited to non-load-bearing fines. Many fine particles that were actively participating in the load-bearing force chain are also dislodged due to the adjustments of surrounding coarse particles. The collapse of contacts involving these load-bearing fine particles constitutes a direct degradation of the structural integrity of the granular skeleton. This destabilization triggers a cascade of internal reorganizations, further weakening the fabric and releasing additional fines into the seepage flow, thereby amplifying the erosion process.

The evolution of contact collapse, as illustrated in Fig 6.7 for the specimens with σ_N = 50 kPa, provides critical evidence for this mechanism. The fraction of contact collapse is highest during the initial stages of erosion and increases with the initial β value. This early burst of microstructural degradation coincides with the rapid increase in fines mass loss, indicating a causal relationship. This figure further reveals that the proportion of contact collapse is highest for *f-f* contacts, followed by *c-f* contacts, while *c-c* contacts exhibit the lowest proportion of collapse. This reflects the relative strength and stability of the contact types, with *c-c* contacts forming the primary load-bearing skeleton of the particle assembly. In the later stages of erosion, the rate of contact collapse for all contact types tends toward zero. The *c-c* contact collapse decreases rapidly and stabilizes at a very low level. This indicates that the core internal contact network, although partially damaged during earlier shearing and erosion, has reorganized into a stable configuration capable of sustaining the applied stress without further significant degradation. The collapse of fine-related contacts (*c-f* and *f-f*) also gradually approaches zero but exhibits small fluctuations. These fluctuations are more pronounced for *f-f* contacts, suggesting ongoing, localized adjustments among the fine particles, likely due to fluid-induced rearrangements or the collapse of small and fine-dominated clusters.

The influence of normal stress σ_N is also evident. For a given β, the cumulative fines mass loss is consistently lower at higher σ_N. This stabilizing effect of confining pressure is supported by Fig 6.8, which compares the average contact force at β = 1.0 for specimens under different σ_N levels. The data show that the average contact forces for both *c-f* and *f-f* contacts increase with σ_N. This indicates that under higher confining stress, fine particles are more tightly confined and interlocked within the coarse matrix. The enhanced contact forces increase the energy barrier required for seepage forces to dislodge fine particles, thereby improving the overall stability of the granular assembly and mitigating internal erosion, even when the soil is under high stress states (Liu et al. 2020).

Anisotropy of contact

For internal erosion in gap-graded soils, contact anisotropy plays a critical role. It not only describes the geometric arrangement of the particle skeleton but also affects several key macro-mechanical processes, such as the pathways of seepage flow, the transport of fine particles, and the redistribution of internal force chains. A highly anisotropic contact fabric can facilitate the formation of aligned void spaces or shear bands, which in turn may serve as dominant erosion channels, especially under coupled hydro-mechanical loading (Chang and Zhang 2013; Song et al. 2024b).

The number of contact normal (N_c), normal contact force (F_n), and shear contact force (F_s) are fundamental indicators of the microstructural state of a granular assembly. The spatial distributions of these quantities, as illustrated in the 3D rose diagrams (Fig 6.9) for specimens with different β values under σ_N = 25 kPa, reveal the progressive development of anisotropy in both the particle fabric and the internal force chains before erosion. The initial anisotropy of the contact normal, normal contact force, and shear contact force increases with β. This growing anisotropy reflects a progressive alignment of the particle structure and the force transmission network along the developing shear plane. Specimens with higher β exhibit a more pronounced anisotropic fabric, resulting in mechanically heterogeneous zones characterized by unevenly distributed force chains. These zones of reduced strength are highly susceptible to seepage-induced particle detachment. The resulting microstructural heterogeneity facilitates the formation of preferential flow paths, thereby accelerating the migration and loss of fines (Chang and Zhang 2013; Qian et al. 2021; Song et al. 2024b). Furthermore, higher β values correspond to stress states closer to failure, where shear-induced damage diminishes the soil skeleton’s resistance to fluid forces. As a result, the interplay between pre-shear-induced microstructural anisotropy and hydraulic loading significantly intensifies the erosion process.

To further investigate the influence of seepage flow on the internal structure of the specimen, the changes in the magnitudes and principal directions of the three anisotropies before and after erosion under different stress states and normal stresses are plotted in Fig 6.10 to Fig 6.12. Before erosion, the anisotropy magnitudes of N_c, F_n, and F_s all increase during shearing, indicating the progressive development of directionally oriented contact fabric and force chain network within the granular assembly. The principal directions of both contact normal anisotropy and normal contact force anisotropy gradually decrease in angle relative to the vertical direction, indicating a progressive reorientation of contact normals and normal contact forces toward steeper inclinations. In contrast, the principal direction of shear contact force anisotropy rotates toward the horizontal direction, consistent with the circumferential shear direction in the ring shear test, which indicates that particle sliding becomes more organized and synchronized with increasing shear strain. It is noted that when $\beta = 1.2$, the evolution of shear contact force anisotropy deviates from the monotonic trend observed at lower stress states, as its magnitude exhibits a slight reduction. This reduction indicates that the spatial concentration of shear forces is weakening and localized slip and contact relaxation become increasingly prevalent, leading to a more heterogeneous distribution of shear forces. This suggests the onset of microstructural instability, indicating that the system can no longer sustain stable shear resistance through particle rearrangement and is approaching macroscopic failure.

After erosion, the anisotropy magnitudes of most specimens decrease, indicating that fines mass loss disrupts the established contact fabric and shifts the system toward a less anisotropic state (Zhou et al. 2022a). However, in specimens with $\beta = 1.2$ under $\sigma_N = 25$ kPa and 50 kPa, both the normal and shear contact force anisotropy magnitudes exhibit an unexpected increase. This means that the specimens with higher β become more susceptible to seepage flow, and seepage-induced stress reduction further triggers the resumption of shearing. This drives particle reorganization that may lead to the formation of more concentrated force chains and shear paths. This indicates that the granular assembly can reorganize itself into a more ordered and efficient load-bearing structure. For the contact normal anisotropy, the anisotropy magnitudes of all specimens decrease after erosion, and the corresponding principal directions rotate toward the direction of seepage flow. This is due to the fact that many fine particles are eroded from their original positions and subsequently deposited in a more vertical alignment within the voids of the coarse particle matrix. This unusual increase in anisotropy is not observed in the specimens under $\sigma_N = 100$ kPa. Even when $\beta = 1.2$, all anisotropy values continue to decrease. This behaviour may be attributed to tighter particle interlocking under higher confining pressure, which results in a more stable granular skeleton with greater resistance to the migration of fine particles. Meanwhile, the potential for structural reorganization under seepage flow is constrained.

6.3.2 Result from shear stage

Stress-strain relationship

Starting from the current stress states, the post-eroded specimens are re-sheared under the same normal stress and shear rate as the non-eroded ones. The stress-strain responses of both the non-eroded and post-eroded gap-graded soils are plotted in Fig 6.13. In general, compared to the stress-strain responses of the non-eroded specimens, the responses of the post-eroded specimens show reduced peak and residual strengths, consistent with the findings of Hu et al. (2020) and Qian et al. (2021). Due to the pre-existing microstructural damage caused by the migration of fine particles, the post-eroded granular assemblies are unable to develop robust force chain networks during continued shearing as effectively as the non-eroded specimens, which weakens their strength development. Consequently, the peak stress is reached at lower stress levels. Then, the non-eroded specimens undergo more pronounced and rapid softening. The shear stress drops from the peak to the residual state are steeper, which indicates more abrupt and unstable structural collapses. This accelerated softening reflects the degradation of the granular skeletons after erosion, where the remaining inter-particle contacts are weaker and fewer, further resulting in a diminished capacity to sustain loads and leading to more catastrophic failure modes. Furthermore, the residual strengths are also reduced after erosion, indicating a diminished long-term load-bearing capacity for the post-eroded specimens. Additional analysis of residual strength behaviours is presented in the subsequent sections.

Residual stress

Residual strength is crucial for stability of slopes and geotechnical systems, as it governs the post-peak behaviour of soils under large-displacement conditions, such as landslides and reactivated shear surfaces. The ring shear test is widely regarded as one of the most effective experimental methods for investigating residual strength in soils (Dong et al. 2020; Mohajeri et al. 2020). The ring shear apparatus allows for continuous and large-displacement shearing under controlled normal stress conditions. This means that the specimen can reach and maintain a true residual state, in which the shear stress stabilizes after significant particle rearrangement and the internal fabric evolves toward a critical state configuration. In this study, the fluctuation characteristics of residual shear stress are analyzed for both non-eroded and post-eroded specimens to investigate how seepage-induced fine particle migration influences the mechanical behaviour of the gap-graded soils. Comparisons of fluctuation amplitude and frequency between non-eroded and post-eroded specimens are used to assess whether fines mass loss induces greater structural instability or facilitates particle reorganization toward a more stable fabric configuration. In this study, the relative peak-to-peak (P-P) amplitude and the mean-crossing rate (MCR) are employed. The relative peak-to-peak amplitude is defined as the ratio of the fluctuation range to the average residual shear stress (Ramsdell and Hinos 1971):

$$Relative\,P-P=\frac{\tau_{max}-\tau_{min}}{\bar{\tau}}\times 100\% \tag{6.1}$$

where τ_{max} and τ_{min} are the maximum and minimum shear stresses during the residual stress stage, respectively; $\bar{\tau}$ is the mean shear stress. The mean-crossing rate is defined as the number of times the shear stress crosses the corresponding mean residual shear stress per unit of residual shear strain (Barnett 2001; Yura and Hanson 2010):

$$MCR=\frac{N_{cross}}{\Delta\gamma} \tag{6.2}$$

where N_{cross} is the number of times the residual shear stress curve crosses $\bar{\tau}$ and $\Delta\gamma$ is the strain interval in the residual stress stage. In short, the normalized relative P-P amplitude can measure fluctuation intensity while minimizing the influence of normal stress. A higher relative P-P amplitude means larger sudden slips or localized collapse, especially at coarse-particle contacts, which suggests greater instability in the gap-graded soil specimens. The MCR can reflect how often fluctuations occur and indicate the level of microscale particle activity such as rolling, sliding and contact rearrangement. A high MCR suggests frequent small adjustments and an evolving internal structure.

Fig 6.14 and Fig 6.15 present the relative peak-to-peak amplitudes and mean-crossing rates, respectively, showing the effects of stress and erosion history on the amplitude and frequency of stress fluctuations during the residual stage. The relative P-P amplitudes in post-eroded specimens are generally higher than those in non-eroded ones. This increase is more pronounced in specimens with higher stress states (β = 1.0 and 1.2), while specimens with lower β show only minor changes. Meanwhile, the fluctuation amplitude decreases as the normal stress increases, suggesting that higher normal stress can help to stabilize the internal structure of the granular assembly and reduce stress variations. The higher P-P amplitudes in post-eroded specimens, especially those with β = 1.0 and 1.2, suggest stronger fluctuations in residual shear stress and reflect the occurrence of larger intermittent slips or localized collapse within the internal structures. As shown in Fig 6.16 which shows the evolution of coarse particle contribution to the shear stress, after seepage-induced removal of fine particles, coarse particles contribute more to the shear load. This means that the load-bearing force chain network becomes more dependent on a small number of contacts between coarse particles. When some of these important contacts buckle or collapse, it can trigger a chain of local rearrangements of force chains, further leading to sudden and large drops in the shear stress.

The MCR values remain close to those of non-eroded specimens in post-eroded specimens with lower β, while the values decrease noticeably in high-β specimens which have experienced significant fines mass loss. A lower MCR means fewer stress fluctuations around the average residual shear stress, which suggests reduced microscale particle activity such as particle rolling, sliding, and small contact rearrangements. This finding agrees with the results shown in Fig 6.17, which shows that fine particles contribute less to shear stress transmission after erosion. Fine particles are more prone to rolling and sliding under external loading compared to coarse particles. As a result, they typically participate in frequent and small movements that help stabilize the granular fabric structure. The removal of fine particles reduces the number of these small adjustments, further leading to a less active mechanical response during shearing. Therefore, residual shear stress fluctuations in post-eroded specimens become less frequent but more abrupt.

Overall, the reduced peak strength and increased fluctuation amplitude in residual shear stress after internal erosion are caused by microstructural degradation and a shift from fine-mediated to coarse-dominated load transfer. In the residual stage, the remaining coarse particles carry most of the load through fewer, highly stressed c–c contacts. These chains undergo intermittent failure and reformation, resulting in large-amplitude, low-frequency stress fluctuations. At the same time, the absence of fines reduces microscale adjustments (e.g., rolling/sliding), decreasing small-scale fluctuation frequency. Each sudden slip temporarily reduces the load-bearing capacity and can trigger localized instability. Over time, repeated events lead to cumulative damage, promoting progressive failure even under constant loading conditions. Each stress drop is associated with a displacement pulse, contributing to accelerated permanent deformation. In slopes and embankments, such irregular large- amplitude movement increases the risk of chain-reaction instability, where local collapses evolve into large-scale sliding. Large-amplitude local deformation may reopen collapsed or constricted flow paths. When seepage flow resumes, such as during recurrent rainfall, flood cycles, or rising water levels, these reactivated channels allow higher local fluid velocities, enhancing fine particle mobilization and accelerating internal erosion.

6.4 Conclusions

This Chapter provides a micro–macro analysis based on a coupled CFD-DEM framework to explore the internal erosion behaviour and post-eroded mechanical response of gap-graded soils under ring shear conditions, with a focus on the effects of pre-shearing stress state (β) and confining stress (σ_N). By integrating controlled shearing, seepage flow, and re-shearing, this study systematically examines the interplay between mechanical loading and hydraulic degradation. Detailed analyses were conducted to understand how residual stress changes after internal erosion. The main findings are listed as follows:

1. The cumulative eroded fines mass exhibits a strong dependence on the pre-shearing stress state β. For all normal stress levels, fines mass loss remains relatively stable when β is small but rises sharply when β reaches 1.0 and further intensifies when β = 1.2, indicating a threshold effect. The initial fabric and contact force anisotropy emerge as critical indicators of the gap-graded soil's susceptibility to internal erosion, as higher magnitudes of anisotropy observed at higher β values exhibit a clear correlation with increased fines mass loss. Additionally, higher σ_N consistently reduces fines mass loss due to stronger particle interlocking and higher average contact forces, which improves the resistance against fine particle removal.

2. The evolutions of fabric and contact force anisotropies reveal a complex interplay between stress history and seepage flow. Before erosion, all anisotropy magnitudes increase with shearing, which suggests the development of oriented fabric and force chains. When β = 1.2, a slight decrease in shear force anisotropy magnitude indicates the onset of microstructural instability. After erosion, most specimens exhibit reduced anisotropy. However, in specimens with β = 1.2 under σ_N = 25 kPa and 50 kPa, both normal and shear contact force anisotropies increase, suggesting that stress relaxation triggers shear resumption and promotes structural reorganization into more efficient load paths. In contrast, no such enhancement occurs in the specimen with β = 1.2 and σ_N = 100 kPa, where tighter particle interlocking limits the rearrangement.

3. Compared to the non-eroded specimens, post-eroded specimens exhibit lower peak and residual strengths. Pre-existing microstructural damage due to erosion hinders the development of robust force chains, resulting in more abrupt strain softening. Steeper stress drops after the peak indicate unstable structural collapse, reflecting a weakened granular skeleton with reduced load-bearing capacity.

4. Residual shear stress fluctuations in post-eroded specimens exhibit higher relative peak-to-peak amplitudes but lower mean-crossing rates, particularly under high stress states. This indicates that fluctuations become less frequent but more intense after erosion. The increased fluctuation amplitude reflects larger intermittent slips or localized collapses. This occurs as the removal of fine particles during erosion which causes force chains to become increasingly dependent on contacts among coarse particles. Meanwhile, the reduced fluctuation frequency suggests diminished microscale activity, as the loss of fine particles reduces the number of small adjustments such as rolling and sliding. This erosion-induced shift from high-frequency, small-scale rearrangements to low-frequency, large-magnitude slips indicates progressive internal degradation and a higher risk of abrupt and large-scale structural instability during the residual stress stage.

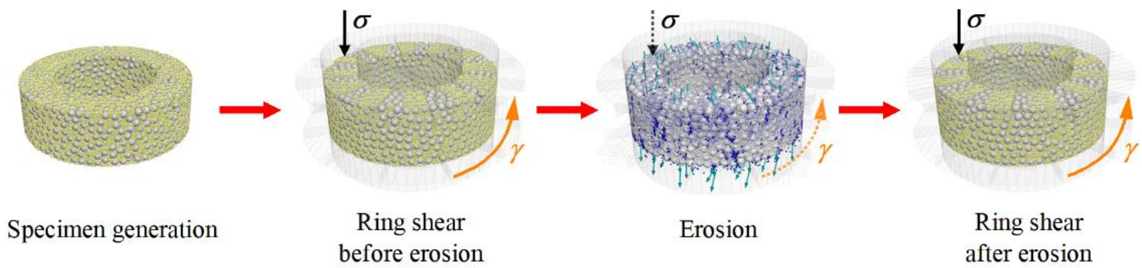

Fig 6.1 Simulation procedure.

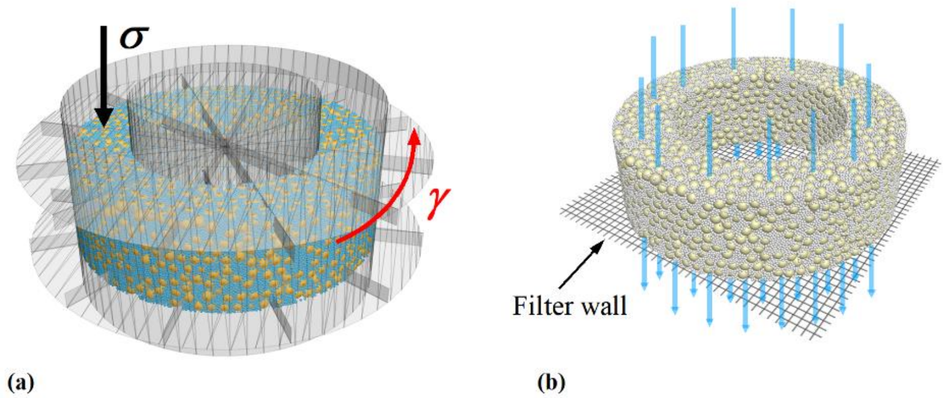

Fig 6.2 Numerical model of the (a) ring shear test and (b) coupled CFD-DEM simulation test.

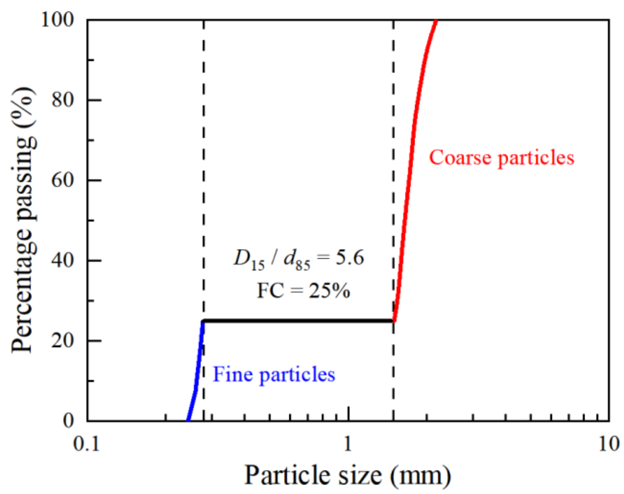

Fig 6.3 Particle size distribution of the gap-graded soil.

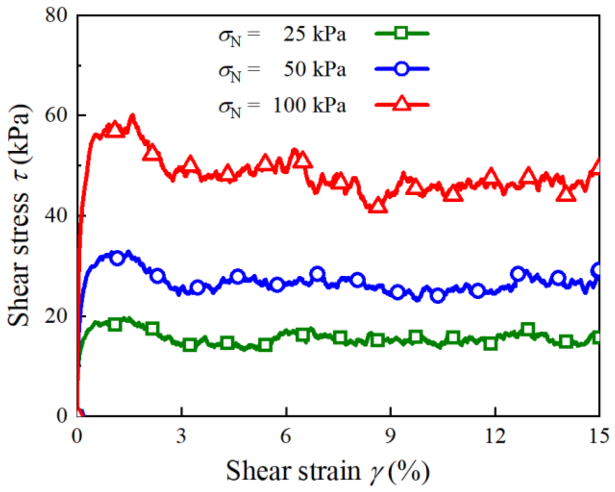

Fig 6.4 The stress-strain relationship for non-eroded specimens.

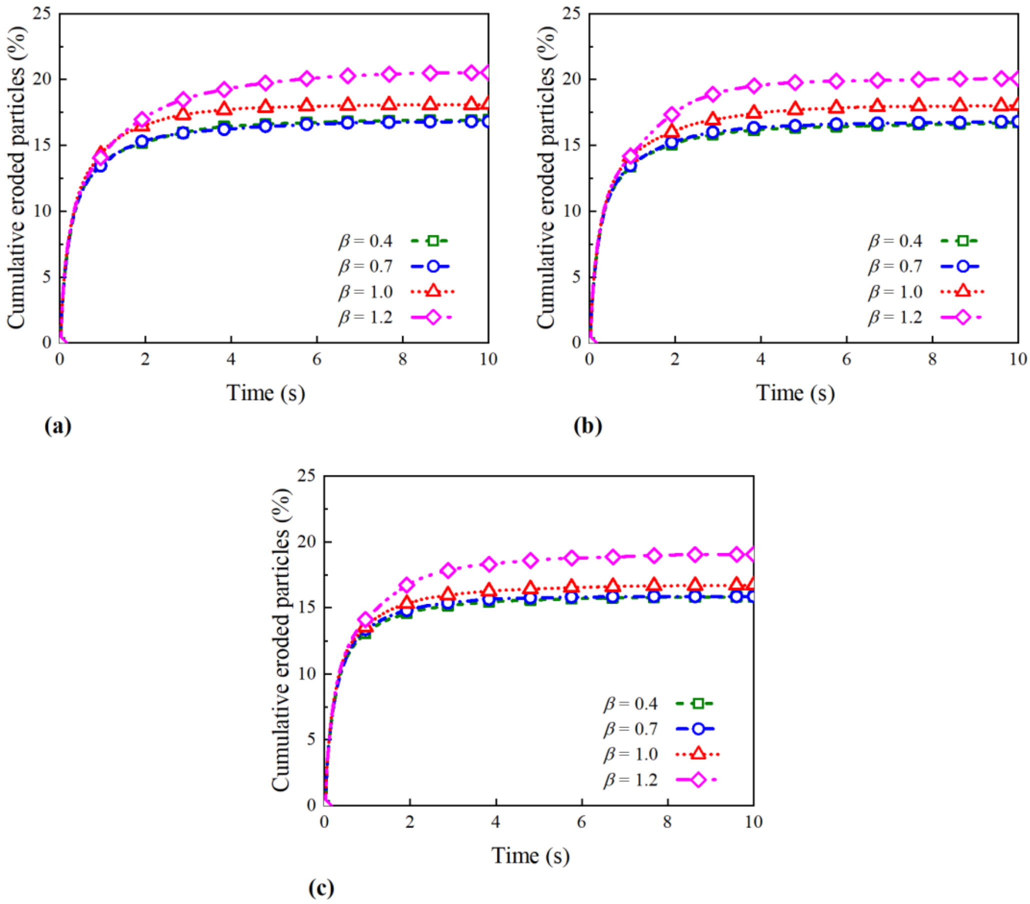

Fig 6.5 Cumulative eroded fines mass for specimens with (a) σ_N = 25 kPa, (b) σ_N = 50 kPa, and (c) σ_N = 100 kPa.

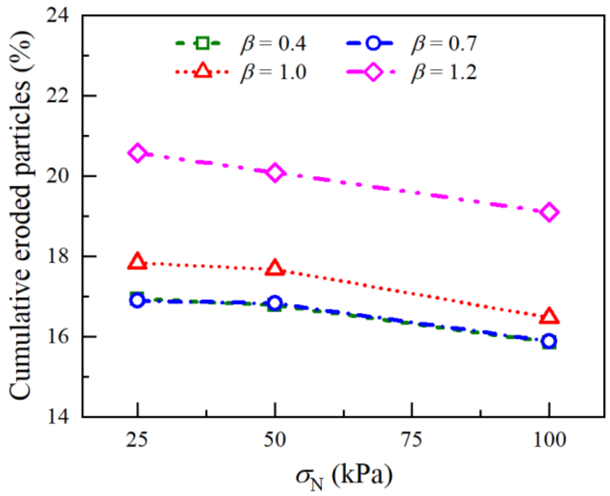

Fig 6.6 Ultimate fine mass loss for all specimens.

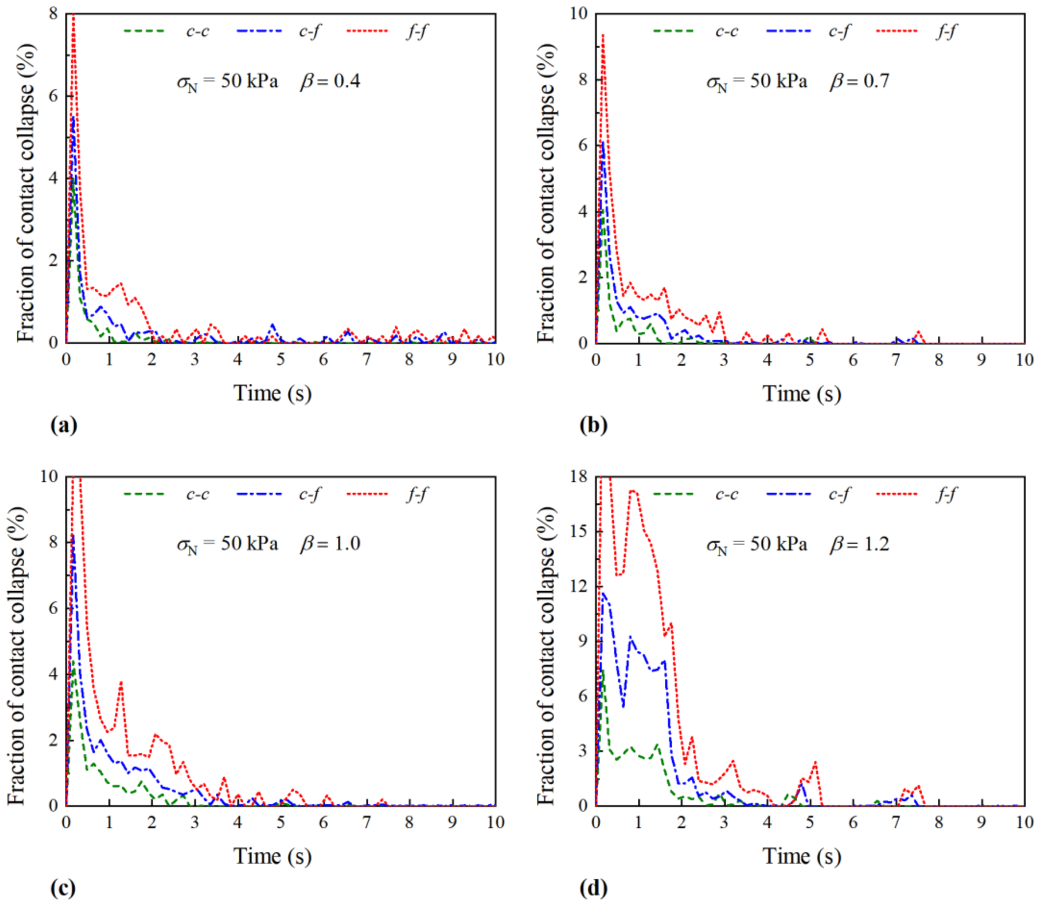

Fig 6.7 Fraction of force chain collapse during erosion in specimens with σ_N = 50 kPa.

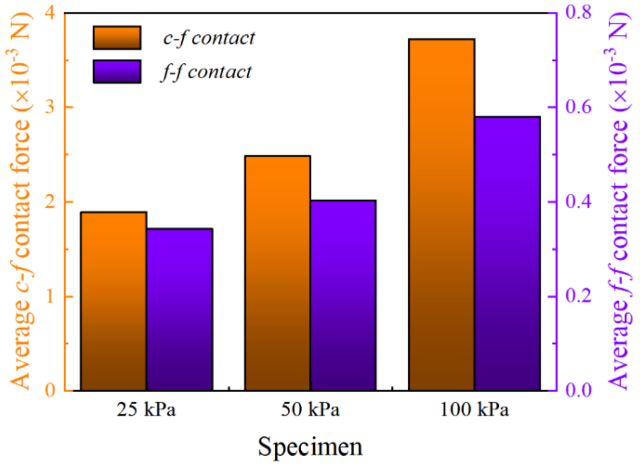

Fig 6.8 Average contact forces for c-c and c-f contacts at β=1.0 under varying normal stress before erosion.

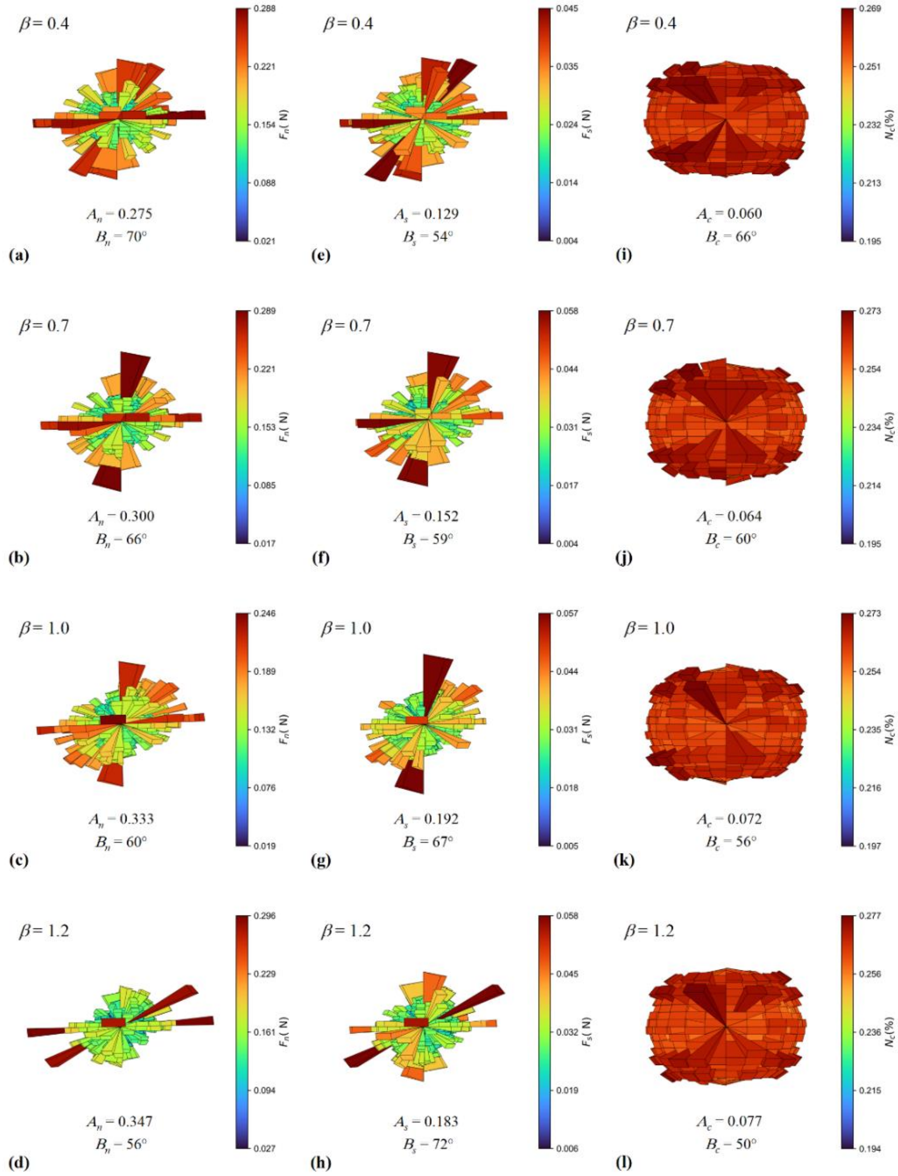

Fig 6.9 Distribution of (a - d) normal contact force, (e - h) shear contact force before and (i - l) contact normal before erosion for specimens under σ_N = 25 kPa.

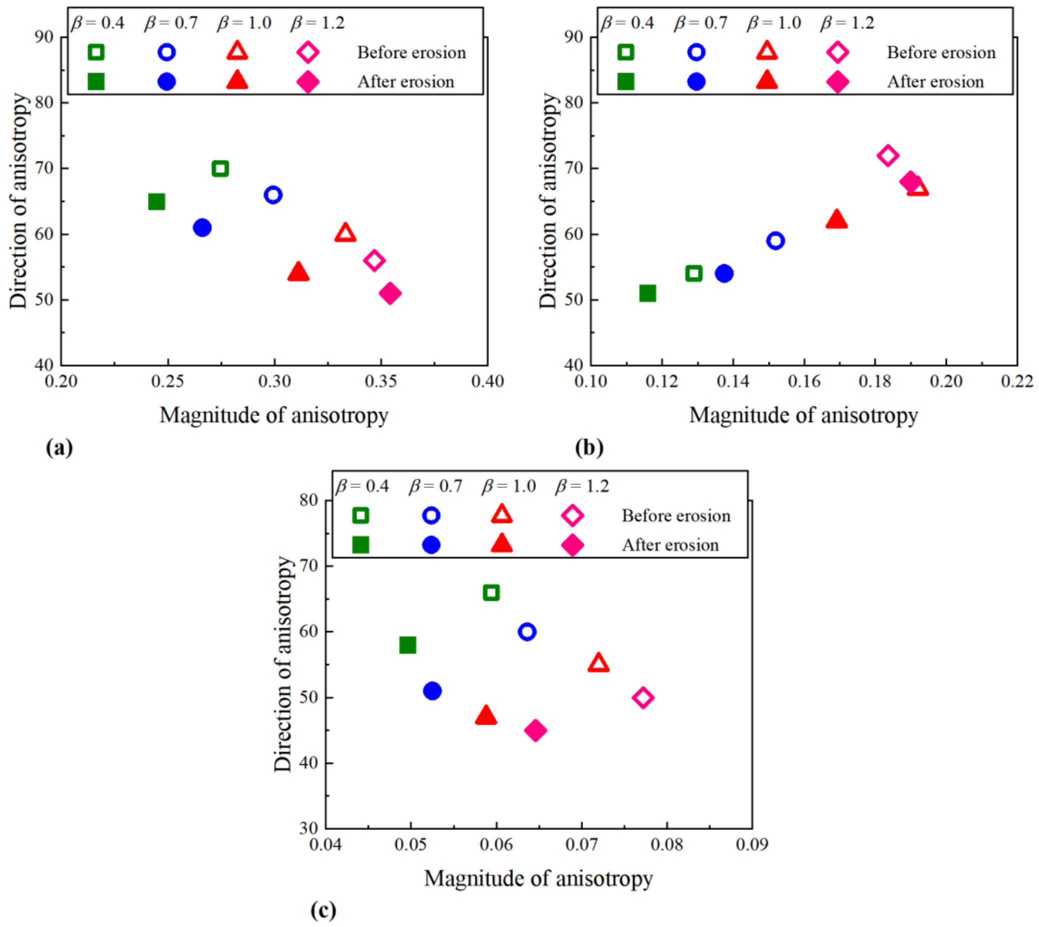

Fig 6.10 Changes in (a) contact normal, (b) normal contact force and (c) shear contact force anisotropies before and after erosion for specimens with σ_N = 25 kPa.

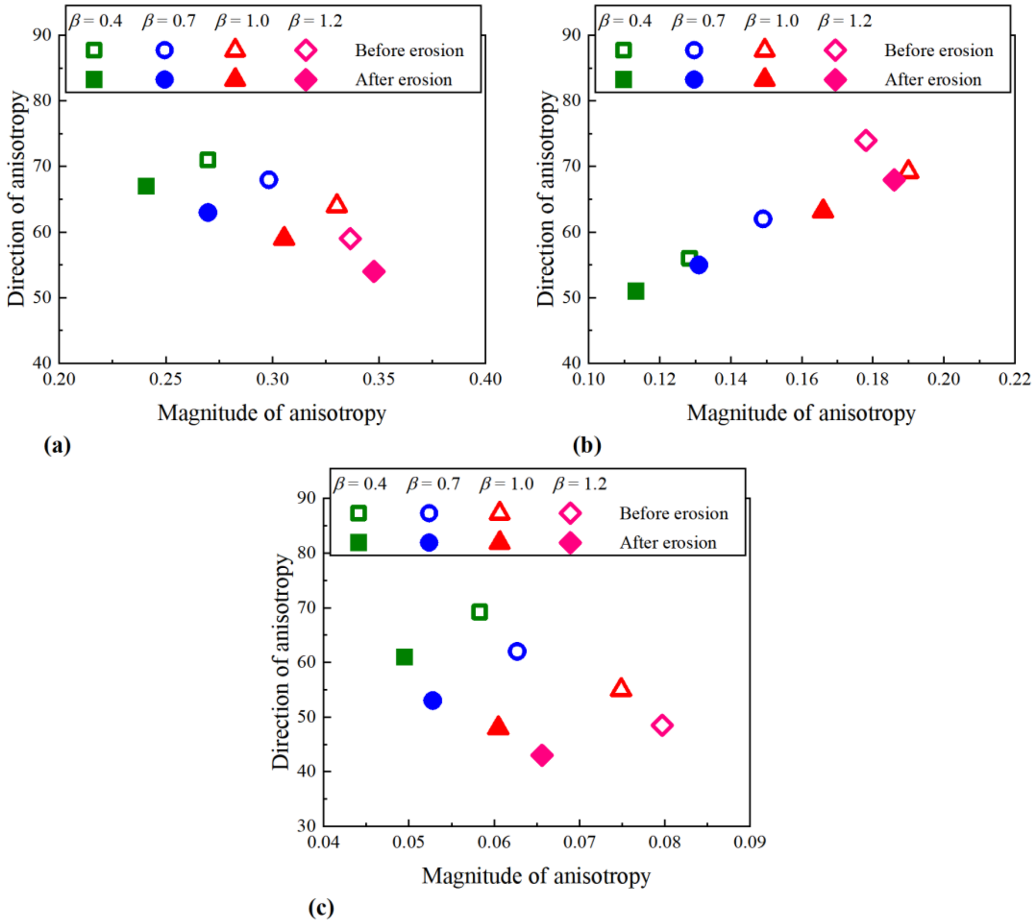

Fig 6.11 Changes in (a) contact normal, (b) normal contact force and (c) shear contact force anisotropies before and after erosion for specimens with σ_N = 50 kPa.

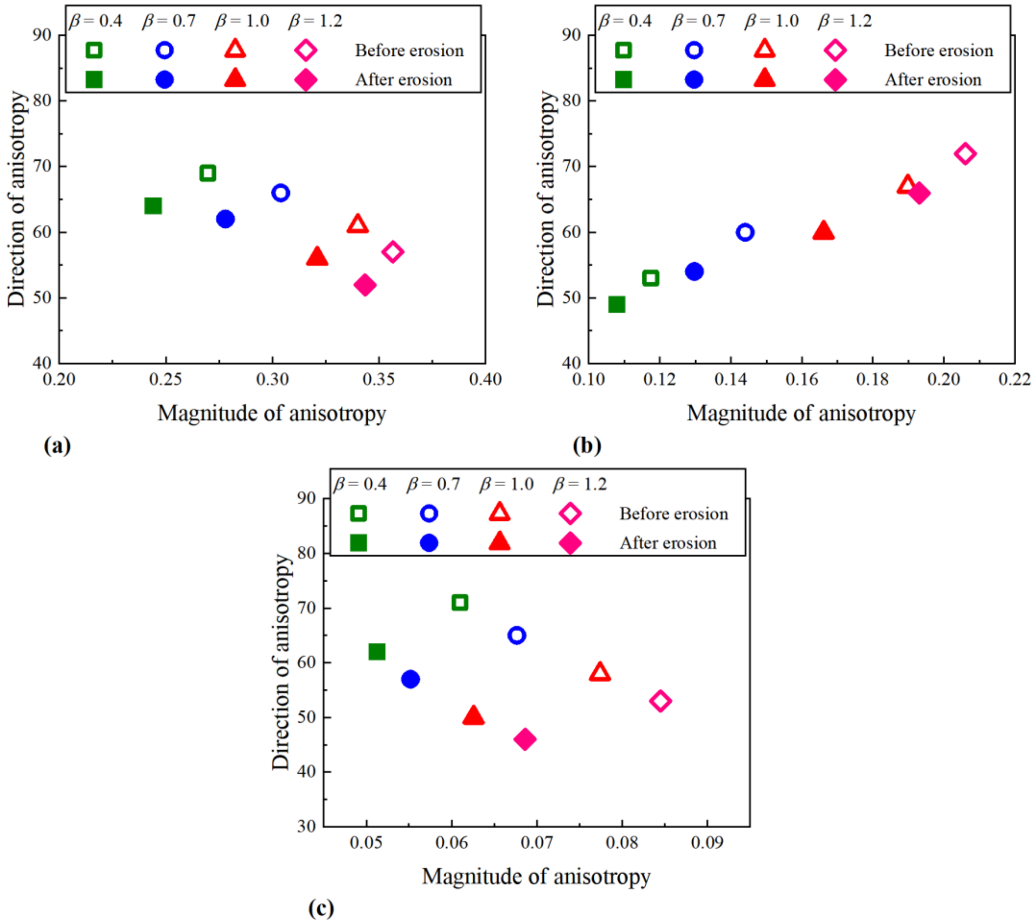

Fig 6.12 Changes in (a) contact normal, (b) normal contact force and (c) shear contact force anisotropies before and after erosion for specimens with σ_N = 100 kPa.

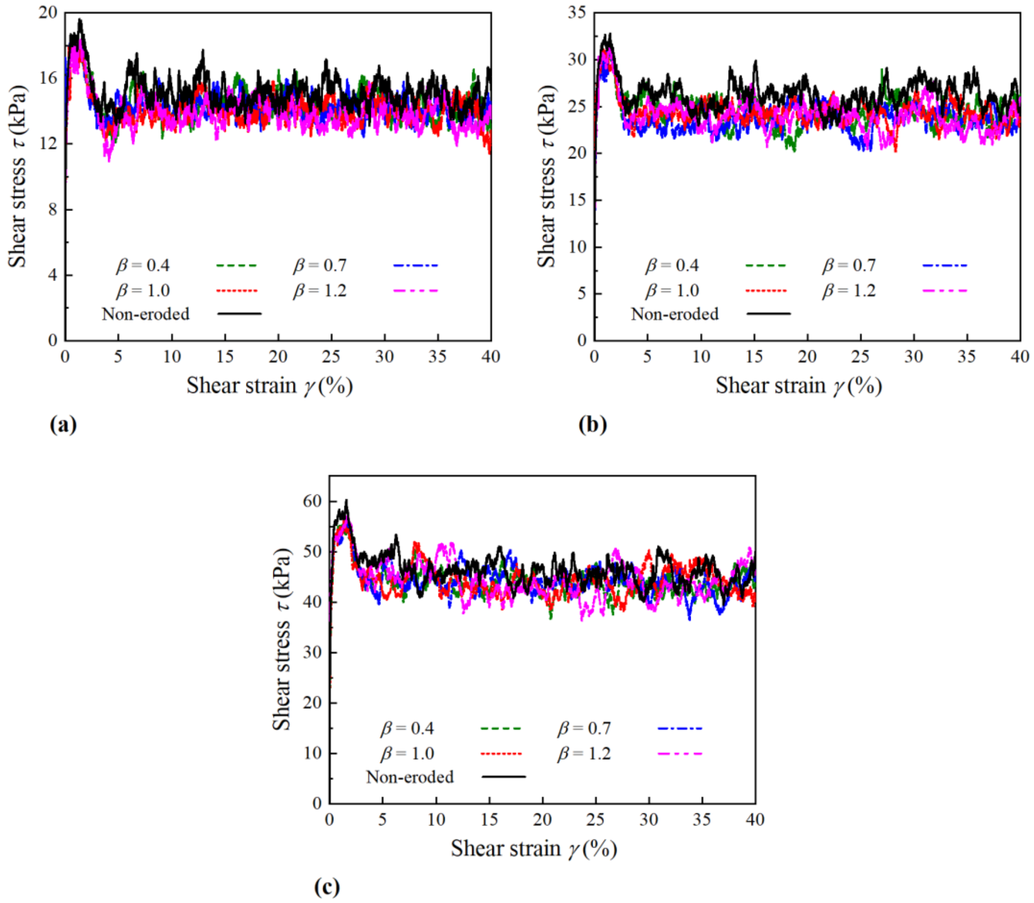

Fig 6.13 Evolutions of stress-strain relationships before and after erosion: (a) σ_N = 25 kPa, (b) σ_N = 50 kPa, and (c) σ_N = 100 kPa.

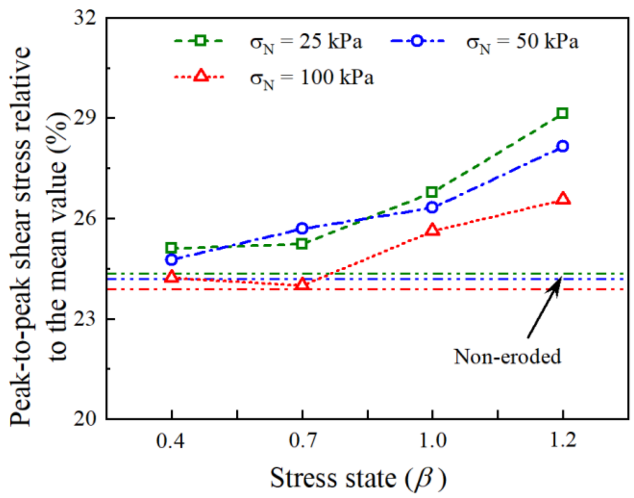

Fig 6.14 Relative peak-to-peak amplitudes in the residual stage under different stress states.

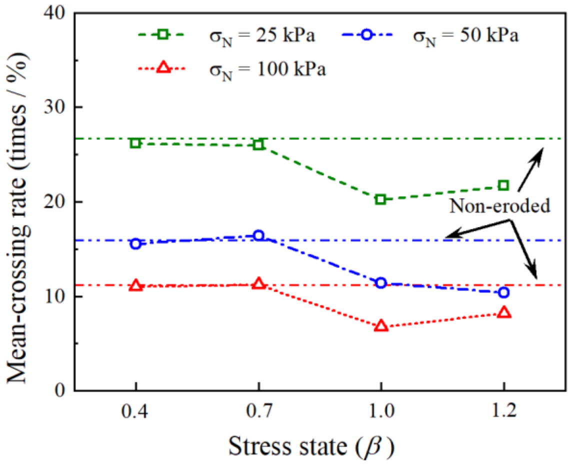

Fig 6.15 Mean-crossing rates during residual shearing for all specimens.

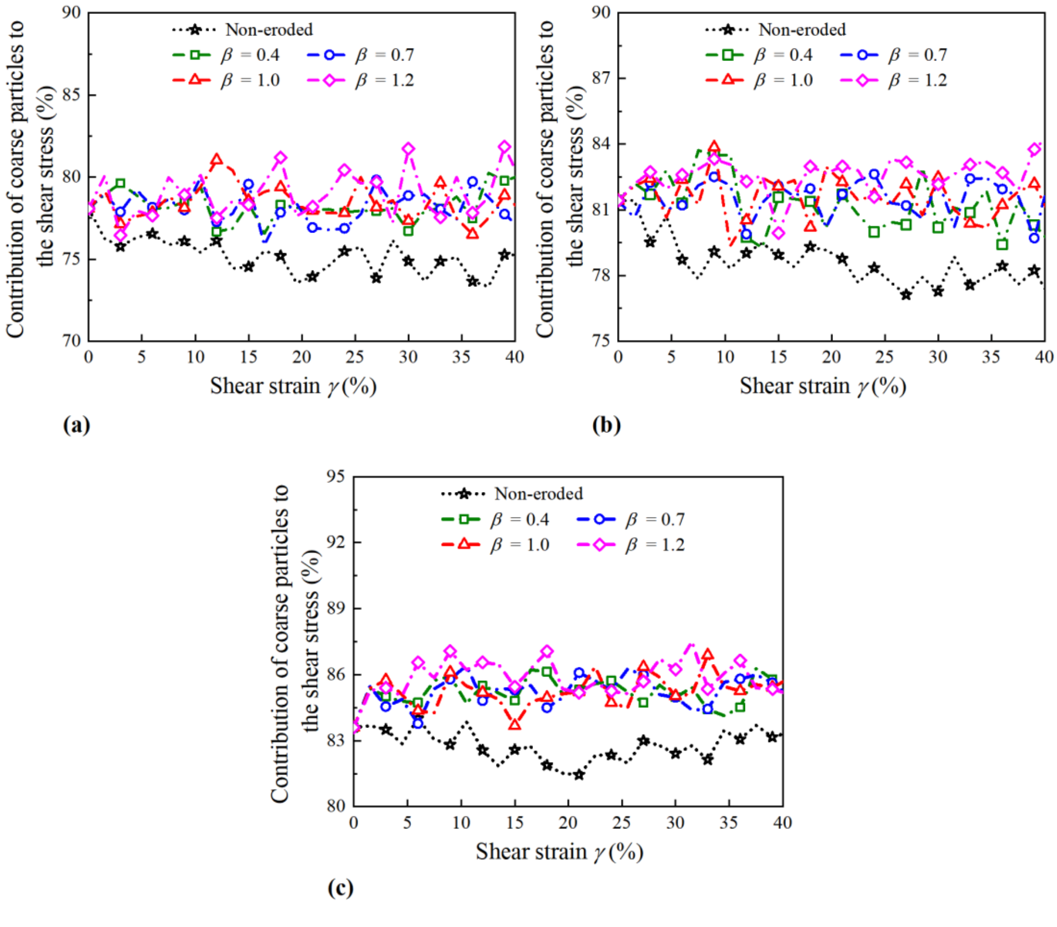

Fig 6.16 Contribution of coarse particles to the shear stress during shearing for specimens with (a) σ_N = 25 kPa, (b) σ_N = 50 kPa, and (c) σ_N = 100 kPa.

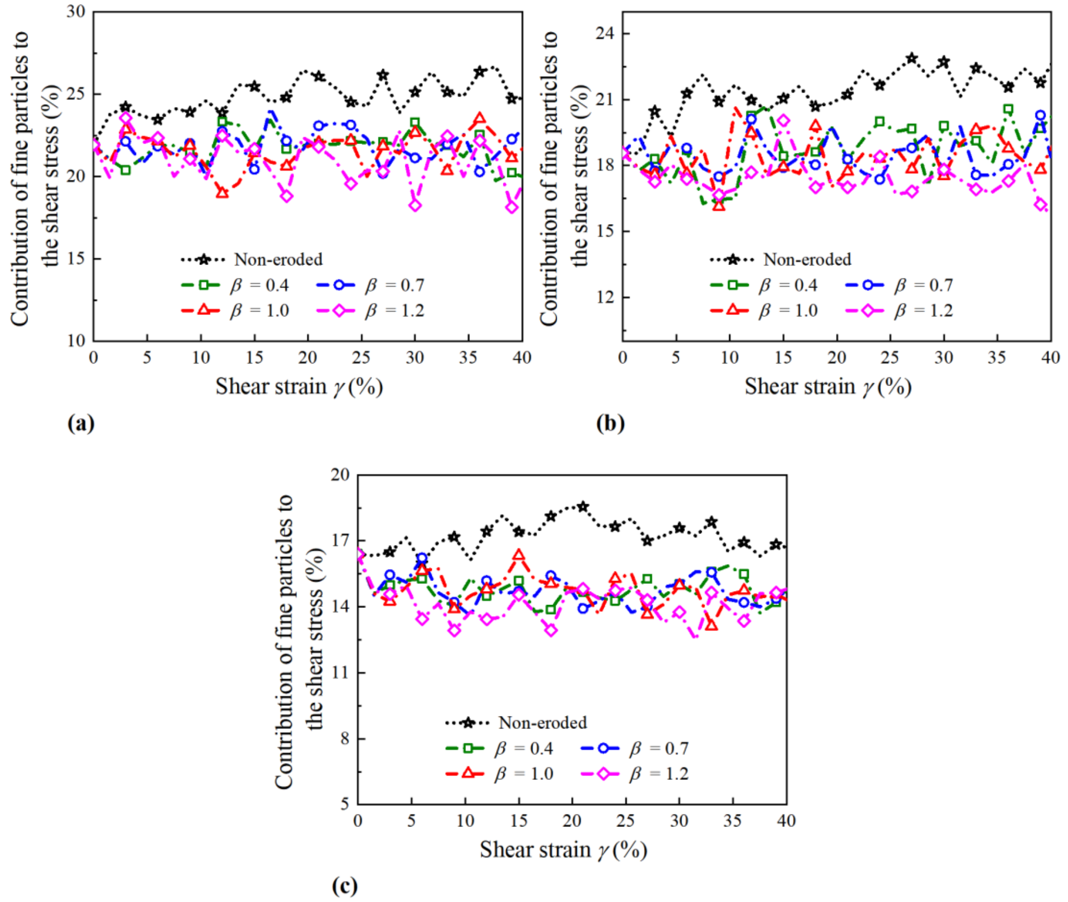

Fig 6.17 Contribution of fine particles to the shear stress during shearing for specimens with (a) σ_N = 25 kPa, (b) σ_N = 50 kPa, and (c) σ_N = 100 kPa.

Table 6.1 Summary of the stress states

ID	1	2	3	4	5	6	7	8	9	10	11	12
σ_N (kPa)	25	25	25	25	50	50	50	50	100	100	100	100
β	0.4	0.7	1.0	1.2	0.4	0.7	1.0	1.2	0.4	0.7	1.0	1.2

Table 6.2 Input parameters used in the simulations

Parameters			Values
DEM	Elastic modulus	E_{PP} (Pa)	2.0×10^8
		E_{PW} (Pa)	2.0×10^8
	Stiffness ratio	k_{PP}	3.0
		k_{PW}	3.0
	Friction coefficient	μ_f	0.3
	Rolling friction coefficient	μ_r	0.1
	Density of particles	ρ (kg/m^3)	2650
	Time step	Δt_p (s)	1.0×10^{-7}
CFD	Cells	Radial × circumferential × vertical directions	3 × 12 × 9
	Fluid viscosity	μ (Pa $*$ s)	1.0×10^{-3}
	Density of fluid	ρ_f (kg/m^3)	1000
	Time step	Δt_f (s)	1.0×10^{-5}

CHAPTER 7: COMPARATIVE STUDY OF INTERNAL EROSION AND MECHANICAL RESPONSE IN GAP-GRADED GRANULAR SOILS UNDER DIFFERENT SHEAR LOADING CONDITIONS

7.1 Introduction

Biaxial shear, direct shear, and ring shear tests are widely used laboratory methods for evaluating the mechanical behavior of granular soils. Each imposes distinct boundary and kinematic constraints that govern the evolution of deformation patterns and stress transmission. In biaxial shear tests, rigid lateral boundaries restrict horizontal deformation, enabling controlled application of both axial and confining stresses. Direct shear tests localize deformation along a predefined horizontal plane through the relative displacement of upper and lower boxes. Ring shear tests employ an annular configuration that facilitates continuous rotation about a central axis, thereby maintaining a persistent shear zone throughout the test.

Due to these fundamental differences in constraint and deformation mode, the evolution of microstructure can vary significantly across the three test setups (Hanna and Ayadat 2019). As a result, the hydro-mechanical response of soil under seepage flow may also differ with loading configuration. For instance, variations in boundary flexibility and particle mobility could influence pore connectivity, fine particle mobilization, and the potential for clogging during internal erosion. However, despite the widespread use of these tests in geotechnical investigations, there has been limited comparative study on how the choice of shear mode affects the initiation and progression of internal erosion under otherwise identical conditions. It remains unclear to what extent shear modes influence the erosion behavior, whether results from one shear configuration can be generalized to others, and what effects these differences have for evaluating post-eroded strength degradation.

In this Chapter, a CFD–DEM framework is employed to systematically compare the mechanical response, erosion susceptibility, and post-eroded behavior of gap-graded granular soils under biaxial, direct, and ring shear loading conditions. By maintaining consistent initial relative density, fines content, confining pressure, and mobilized stress level, the simulations isolate the effect of loading mode on key processes, including force chain development, fine particle migration, and re-shearing mechanical response after erosion. This comparative study aims to provide insight into how the selection of shear test configuration influences the hydro-mechanical degradation, thereby supporting more informed choices in future erosion-related studies.

7.2 Model setup and simulation procedure

This chapter examines how different shear modes influence the microstructural characteristics of gap-graded granular soil and explores their effects on the migration of fine particles under hydraulic erosion. After the erosion process, shear is reapplied to evaluate whether the mechanical response of the material can be reconstructed, thereby demonstrating that the shear mode not only governs the initial microstructure, but also has a strong impact on the material's evolution and ability to recover after internal erosion. It is noted that all numerical specimens were generated using the same PSD, with identical fines content and gap ratio. This can help to eliminate gradation-induced variability in pore structure and erodibility. The relative density of each specimen is carefully controlled within a narrow range by adjusting the isotropic consolidation pressure during DEM sample preparation (Zhou et al. 2019b). This high degree of uniformity minimizes differences in initial void ratio and contact network development. In addition, the number of particles in each specimen are kept as consistent as possible across different shear modes. Therefore, comparisons between different simulations can be as fair and meaningful as possible.

7.2.1 Soil preparation and model setup

In this chapter, two gap-graded granular soils with fines contents of 17% and 34% by mass are investigated under each of the three shear modes, namely biaxial, direct and ring shear. The PSD curves of the soils are shown in Fig 7.1. Despite the difference in fines content, both soils exhibit the same gap ratio (D_{15} / d_{85}) of about 5.1. A total of six specimens is first generated in DEM. As illustrated in Fig 7.2, two specimens are prepared for each shear mode. All specimens are then consolidated under a constant confining pressure of 50 kPa. The relative density (D_r) of each specimen is controlled within a range of 58.7% to 59.5%.

7.2.2 Simulation procedure

Similar to the simulation program in the previous Chapters, once the DEM models are generated, they are subjected to shear loading. When each of the six specimens has been sheared to a stress state of $\beta = 0.75$ (where $\beta = \tau / \tau_p$, and τ_p represents the peak shear strength of the specimen), the shearing process is temporarily paused. At this same stress state, the rigid walls at the bottom of each specimen are replaced with filter walls of appropriately sized openings to allow fine particles to pass through the bottom of the specimen while leaving coarse particles unaffected (Hu et al. 2022; Liu et al. 2022). It should be noted that, in addition to the above, the biaxial and direct shear specimens are sheared up to 20% strain, whereas the ring shear specimens are sheared up to 40% strain, in order to enable a comparative study of the effects of different shear modes on gap-graded granular soils.

Subsequently, the CFD module is introduced and activated to perform the flushing simulation. The CFD domains are geometrically aligned with the DEM specimens in the x–y plane, but extend vertically in the z-direction to a height approximately twice that of the DEM specimen, ensuring adequate flow development. Two erosion cases are conducted for each specimen, corresponding to hydraulic gradients of $i = 0.3$ and 3.0, respectively. Therefore, during the internal erosion stage, a total of 12 cases is conducted, with detailed information for each case provided in Table 7.1. Each specimen is subjected to erosion for 10 seconds. During this period, if any specimen experiences a reduction in strength due to particle loss and internal structural collapse, shear loading is then reapplied to maintain the designated stress state of $\beta = 0.75$.

Following the internal erosion simulation, the CFD module is removed. The filter walls at the bottom of the DEM specimens are replaced with impermeable rigid walls. Subsequently, the specimens resume shearing in their respective modes, starting from the current stress states after erosion. The relevant DEM and CFD parameters used during the shearing and erosion processes are summarized in Table 7.2.

7.3 Result analysis

7.3.1 Effect of shear mode on soil's mechanical response

Strength

Fig 7.3 shows the stress-strain relationships of the non-eroded gap-graded granular soils under different shear loading conditions. Overall, the specimens with FC = 34% exhibit lower peak strengths than those with FC = 17% across all three shear modes. This indicates that increasing the fine content weakens the load-bearing capacity of the granular skeleton. The FC = 17% specimens show a distinct peak strength followed by a strain-softening phase. Their stress-strain curves also show greater fluctuations, which reflect frequent and abrupt breakage and reorganization of force chains among coarse particles. Such behavior is characteristic of strong particle interlocking and high frictional resistance. In contrast, the FC = 34% specimens exhibit smoother stress-strain responses. The peak strength is less pronounced or nearly absent, and post-peak softening is minimal, especially in biaxial and direct shear tests. This smoother response suggests that fines act as a buffering medium that promotes continuous particle sliding and suppresses sudden collapse of force chains. These observations indicate a shift in mechanical behavior. At lower fine content, the gap-graded soils exhibit a more brittle and structure-sensitive manner governed by coarse-particle interactions. At higher fine content, the specimens display a steady-state response mediated by the fine particle network.

To better compare the strength differences under different loading conditions, the angles of shearing resistance for the six non-eroded specimens are plotted in Fig 7.4. Overall, biaxial shear test yields the highest strength, followed by direct shear test, with ring shear test producing the lowest values. This ordering is primarily governed by the degree of constraint imposed on particle motion. In biaxial shear test, the boundaries along the y-direction are fixed, which restricts particle displacement and rotation in this direction, thereby reducing the degrees of freedom for particle rearrangement. As a result, the coarse particle skeleton develops highly continuous and robust force chains, and interparticle interlocking is maximized, further leading to the highest peak shear strength (Hanna and Ayadat 2019). In contrast, direct shear test and ring shear test provide greater freedom for particle motion. This reduces the effectiveness of interlocking and limits the potential for dilation. In direct shear test, deformation is concentrated within a relatively narrow shear band. The localized force chains can remain partially intact, which allows the specimen to maintain a moderate peak strength. In ring shear test, continuous and intense shearing promotes extensive particle rearrangement throughout the whole specimen. The coarse particle force chains are frequently destroyed and reorganized, which results in the lowest peak shear strength among the three shear modes.

While increasing fines content reduces the overall load-bearing capacity of the coarse particle skeleton and peak strengths, the relative ranking of the three shear modes remains unchanged. The peak strength of a granular assembly is determined by the boundary-induced constraint on particle motion, which controls the development and stability of force chains and dilation.

Force chain network

Fig 7.5 and Fig 7.6 show the strong force chain networks at peak strength for specimens with FC = 17% and 34%, respectively. When FC = 17%, the strong force chain network is dominated by *c-c* contacts. These contacts form a continuous, high-stress skeleton that bears the majority of the external load. Fine particles contribute minimally to the strong network, acting primarily as fillers. In contrast, when FC = 34%, the strong force chain network undergoes a structural transition. Fine particles become significant contributors to the strong force chain network. The dominance of *c-c* contacts is reduced, and force transmission becomes diffuse. *c-f* contacts act as force bridges between coarse and fine particles, while *f-f* contacts develop into a load-bearing network of their own. This indicates a shift from a coarse-dominated skeleton to a hybrid mechanical framework involving all contact types.

The strong force chain networks at peak strength exhibit distinct spatial architectures across the three shear modes. In biaxial shear test, the strong force chains are well developed and connected, and predominantly aligned with the axial loading direction, forming a continuous and load-efficient skeleton throughout the specimen. In direct shear test, strong force chains localize within a narrow shear band and orient obliquely, consistent with the shear plane. Outside this zone, the network is sparse and discontinuous, indicating that particles surrounding the shear zone are relatively unconstrained and contribute less to load bearing. In ring shear test, the strong force chains are relatively short, fragmented, and lack a dominant orientation. They are more diffusely distributed, without forming continuous load-bearing paths across the whole specimen. The continuous rotation of the shear plane and the higher particle freedom result in frequent disruption and reorganization of force chains, resulting in lower peak strength and less pronounced stress localization. Overall, the differences in force chain structure correspond well with the peak strength ranking, with biaxial shear exhibiting the most robust and continuous network, direct shear showing localized strong chains, and ring shear displaying the weakest, most fragmented network.

Fig 7.7 and Fig 7.8 illustrate the 3D rose diagrams of contact normal for the non-eroded specimens at peak strength with FC of 17% and 34%, respectively. Distinct differences in contact anisotropy are observed among the three shear modes. Specimens under biaxial shear condition exhibit the strongest anisotropy, confirming that its strong lateral constraint forces the load-bearing contacts into a highly efficient and axial alignment. This highly oriented fabric is the microstructural basis for the observed superior strength (Fig 7.4) and the continuous force chains (Fig 7.5). In contrast, the ring shear specimens show more isotropic contact distributions at peak strength, as continuous rotation and low confinement disrupt the directional stability of contacts. Furthermore, specimens with FC = 17% show more pronounced anisotropy than those with FC = 34%, implying that higher fines content tends to fill voids and weaken the directional fabric of the coarse skeleton.

Fig 7.9 and Fig 7.10 show the evolution of the collapse ratio of strong contacts with shear strain for non-eroded specimens with FC of 17% and 34%, respectively. The collapse ratio quantifies the proportion of strong force chains that fail with shearing, reflecting the stability of the load-bearing structure. Among the three shear modes, ring shear specimens exhibit the highest collapse ratios throughout shearing, followed by direct and biaxial shear specimens. This trend suggests that continuous rotation and limited confinement in the ring shear tests promote frequent contact breakage and microstructural renewal, while the biaxial specimens maintain the most stable and long-lived force chains under plane-strain confinement. Increasing fines content from 17% to 34% further amplifies the collapse ratio, indicating that excess fine particles weaken interparticle interlocking and reduce contact persistence. Interestingly, the collapse ratio curves for ring shear specimens fluctuate less than those of biaxial and direct shear specimens after the peak strength, indicating that deformation in ring shear tests tend toward a stable restructuring regime, where contact breakage and formation become balanced over time. In contrast, the pronounced fluctuations observed in the biaxial and direct shear specimens reflect the microstructural expression of brittle behavior. The strongly anisotropic and well-consolidated skeleton resists failure effectively, but once instability initiates, it fails abruptly and intermittently, leading to the larger stress drops.

To further quantify the contributions of different contact types to the strong force chain network, Fig 7.11 and Fig 7.12 illustrate the evolution of these contributions during the shear process for specimens with FC = 17% and 34%, respectively. When FC = 17%, *c-c* contacts consistently dominate the load transfer, emphasizing the dominance of the coarse particle skeleton. The contribution's initial increase of *c-c* contacts followed by a subsequent decrease in biaxial and direct shear tests reflects the formation and collapse of interlocking. The contribution by *c-f* contacts gradually increases after an initial decrease, indicating the essential role of *c-f* bridges in maintaining residual strength. Meanwhile, in ring shear test, the contribution by *f-f* contacts increases with significant fluctuations, reflecting the structural instability of the fine particle network under continuous and large-displacement shearing. For specimens with FC = 34%, the evolution reveals a general decline of the contribution by *c-c* contacts across all shear loading conditions, suggesting a transfer of load to the mixed skeleton. Both direct and ring shear tests show a continuous decrease in contribution by *c-c* contacts, accompanied by increases in contributions by *c-f* and *f-f* contacts, demonstrating the effective dispersion of load across the hybrid network. In biaxial shear test, however, the strong boundary constraint maintains stress transfer primarily through robust *c-c* and *c-f* contacts. Consequently, the contribution by *f-f* contacts slightly rises initially but then decreases and stabilizes, as the strong constraint suppresses the participation of the relatively weak *f-f* network. These differences in constraint and network evolution explain the variations in the stability of load path, the observed ranking of shear strength, and the smoothness of the macroscopic stress response.

7.3.2 Influence of shear mode on internal erosion

Cumulative fine particle loss

Fig 7.13 and Fig 7.14 present the evolution of fines mass loss during internal erosion and the total mass of eroded fine particles, respectively. At low fines content (FC = 17%), the ranking of mass loss of fine particles remains consistent across shear modes, with ring shear showing the highest loss, followed by direct shear, and biaxial shear the lowest. This reflects the role of boundary constraints in stabilizing the force chain skeleton. In detail, fragmented and discontinuous force chains provide little resistance to particle migration in the ring shear specimen, while the continuous skeleton in the biaxial shear specimen effectively restricts fine loss. A higher hydraulic gradient of i = 3.0 accelerates early erosion and slightly increases the total loss, but the process quickly plateaus once the movable fines are exhausted. This rapid stabilization occurs because fine particles in specimens with low fines content mostly act as free fillers with little structural involvement.

When FC = 34%, the total fines mass loss is significantly greater, as more erodible particles are available within the pore space. Meanwhile, higher hydraulic gradient of

i = 3.0 amplifies both the rate and total amount of fines mass loss Although the same ranking of fines mass loss across the three shear modes is maintained, the erosion dynamics differ fundamentally. The initial erosion rates in the cases with FC = 34% are slower than those in the corresponding cases with FC = 17%, due to the partial participation of fine particles in load bearing through *c-f* and *f-f* contacts, which stabilizes the structure initially. However, once erosion initiates, the process becomes sustained and progressive, particularly under the ring shear condition.

Coordination numbers

Coordination number is the average number of contacts a particle has with its neighbors, which can be further categorized by contact type (*c-c*, *c-f* and *f-f*). Coordination number reflects the connectivity and load-bearing capacity of the particle network. The evolution of coordination number helps to quantify microstructural stability, particle rearrangement, and the role of fine particles during erosion (Zhou et al. 2022a). Fig 7.15 and Fig 7.16 respectively show the evolutions of coordination numbers for the specimens with FC = 17% and 34% under i = 0.3 during erosion.

For specimens with FC = 17%, $Z_{c\text{-}c}$ remains nearly constant, indicating the stability of the coarse skeleton. $Z_{c\text{-}f}$ exhibits a transient decrease followed by partial recovery, reflecting the initial detachment and subsequent reorganization of fines around coarse particles. Notably, $Z_{f\text{-}f}$ increases slightly with erosion, indicating that the remaining fine particles become more locally concentrated as loosely bounded particles are preferentially eroded. In specimens with FC = 34%, biaxial shear tests show minimal changes in all coordination numbers, consistent with their high resistance to erosion. In direct shear conditions, $Z_{c\text{-}c}$ initially decreases but gradually recovers as coarse particles re-establish contacts following the removal of fine particles. Meanwhile, $Z_{f\text{-}f}$ first increases during the early to mid-stage of erosion, due to the reorganization and local densification of fine particles in pore spaces. It subsequently declines as the clogged fine particles are progressively mobilized and eroded. In additions, ring shear specimens exhibit a continuous decrease in both $Z_{c\text{-}f}$ and $Z_{f\text{-}f}$. This decline directly correlates with the high and continuous erosion rate and indicates the progressive and sustained disruption of the fine-particle network.

7.3.3 Stress-strain relationships of the post-eroded specimens

After erosion, post-eroded specimens are re-sheared starting from their current stress states. Fig 7.17 presents the stress-strain relationships of both non-eroded and post-eroded gap-graded soils across the three shear modes. The results demonstrate a clear dependence of the post-eroded mechanical behavior on both fines content and shear mode. For specimens with low fines content (FC = 17%), the peak shear strength remains largely unchanged compared with their non-eroded counterparts. At the initial stage of shearing, the stress-strain curves closely overlap with the non-eroded response, indicating that the coarse particle skeleton continues to govern load transfer. Deviations from the non-eroded curves appear at larger strains, suggesting local rearrangements of the remaining fines after erosion within the particle network.

Specimens with high fines content (FC = 34%) are more affected by erosion. Peak shear strength decreases noticeably, and some cases, particularly the ring shear specimens with i = 3.0, do not exhibit a clear peak, suggesting the substantial disruption of the mixed particle skeleton during erosion. The stress-strain curves at larger strains show greater fluctuations compared with non-eroded specimens, especially in direct and ring shear tests, which reflects the progressive collapse and reorganization of force chains as fines are removed. Biaxial shear specimens which are constrained by strong lateral boundaries and experience lower fines loss, show smaller fluctuations. Additionally, during the erosion process, FC = 34% specimens accumulate larger shear strains due to repeated reloading necessary to maintain the target stress state, while the specimens with FC = 17% experience minimal additional deformation.

These observations demonstrate that fines content primarily governs the susceptibility of the particle skeleton to erosion, while the imposed shear mode influences how the residual microstructure accommodates the loss of fine particles. Biaxial shear test provides strong confinement that preserves coarse particle load paths. Direct shear test exhibits moderate susceptibility with localized structural disruption. Ring shear is the most vulnerable to removal of fine particles and progressive microstructural degradation due to weak confinement and continuous large-displacement shearing.

7.4 Conclusions

This Chapter investigates the influence of different shear modes, i.e., biaxial, direct, and ring shear, on the microstructural characteristics, internal erosion susceptibility, and post-eroded mechanical response of gap-graded granular soils with FC of 17% and 34%. The main conclusions are summarized as follows:

1. The peak shear strength of gap-graded granular soils follows the order of biaxial shear test, followed by direct shear test, and then ring shear test, regardless of fines content. This ranking reflects the degree of kinematic constraint imposed by each shear mode. Biaxial shear test provides lateral strain confinement, which enhances particle interlocking and maintains continuous coarse particle force chains, resulting in the highest strength. Direct shear test exhibits moderate strength, as the deformation is localized within a narrow shear band, allowing partial preservation of continuous force chains. Ring shear test shows the lowest strength, as the weak confinement and continuous large-displacement shearing lead to frequent force chain reorganization.

2. The structure, connectivity, and anisotropy of force chains are influenced by both fines content and shear mode. Low fines content specimens are dominated by *c-c* contacts, forming a continuous and highly anisotropic skeleton, while higher fines content specimens exhibit increased contributions from *c-f* and *f-f* contacts, creating a hybrid load-bearing framework. Furthermore, biaxial shear specimens have the strongest anisotropy, while ring shear specimens display the most isotropic and fragmented contact network. The evolution of strong contact collapse ratio further confirms that ring shear experiences the highest proportion of failed contacts, whereas biaxial shear maintains the most stable force chains. Meanwhile, fluctuations in the collapse ratio of strong contacts are smaller in ring shear specimens, while biaxial and direct shear specimens show pronounced intermittent failure, reflecting the brittle structural behavior.

3. Fines mass loss is influenced by both shear mode and fines content. Ring shear specimens undergo the most severe erosion, followed by direct shear specimens, while biaxial shear specimens exhibit the least fines mass loss. In specimens with low fines content, the total fines loss is limited and stabilizes rapidly, whereas high fines content leads to sustained and progressive erosion, particularly under weakly constrained shear conditions. The evolution of coordination numbers corroborates the observations, showing minimal disruption in biaxial shear, moderate changes in direct shear, and continuous decline in both *c-f* and *f-f* contacts in ring shear specimens, reflecting progressive degradation of the fine particle network.

4. Re-shearing after erosion shows that specimens with low fines content maintain

similar peak strength and stress-strain behavior to their non-eroded counterparts, with small deviations at large strains. By contrast, post-eroded specimens with high fines content suffer pronounced strength loss and display greater fluctuations, especially under direct and ring shear conditions. These results indicate that the capacity to recover mechanical performance after erosion depends strongly on both fines content and the degree of confinement imposed by the shear mode.

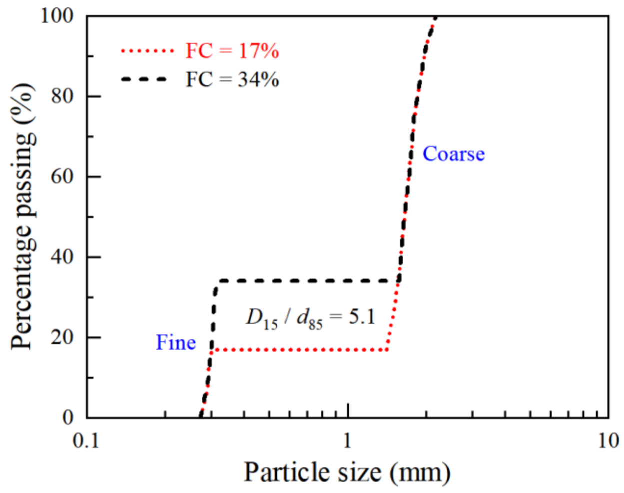

Fig 7.1 Particle size distribution of the gap-graded soil.

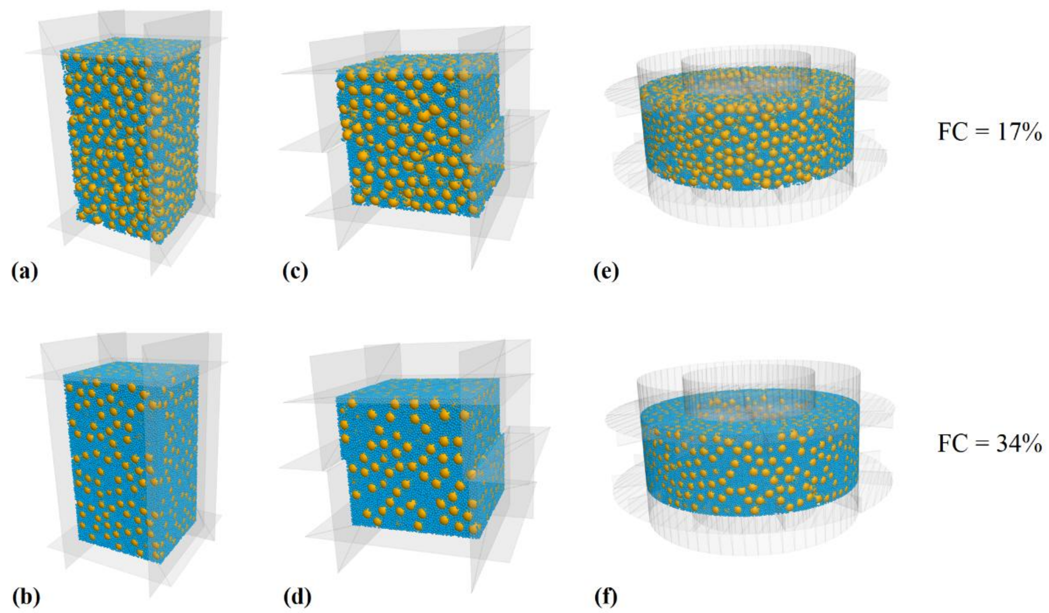

Fig 7.2 DEM specimens of (a - b) biaxial shear tests; (c - d) direct shear tests and (e - f) ring shear tests.

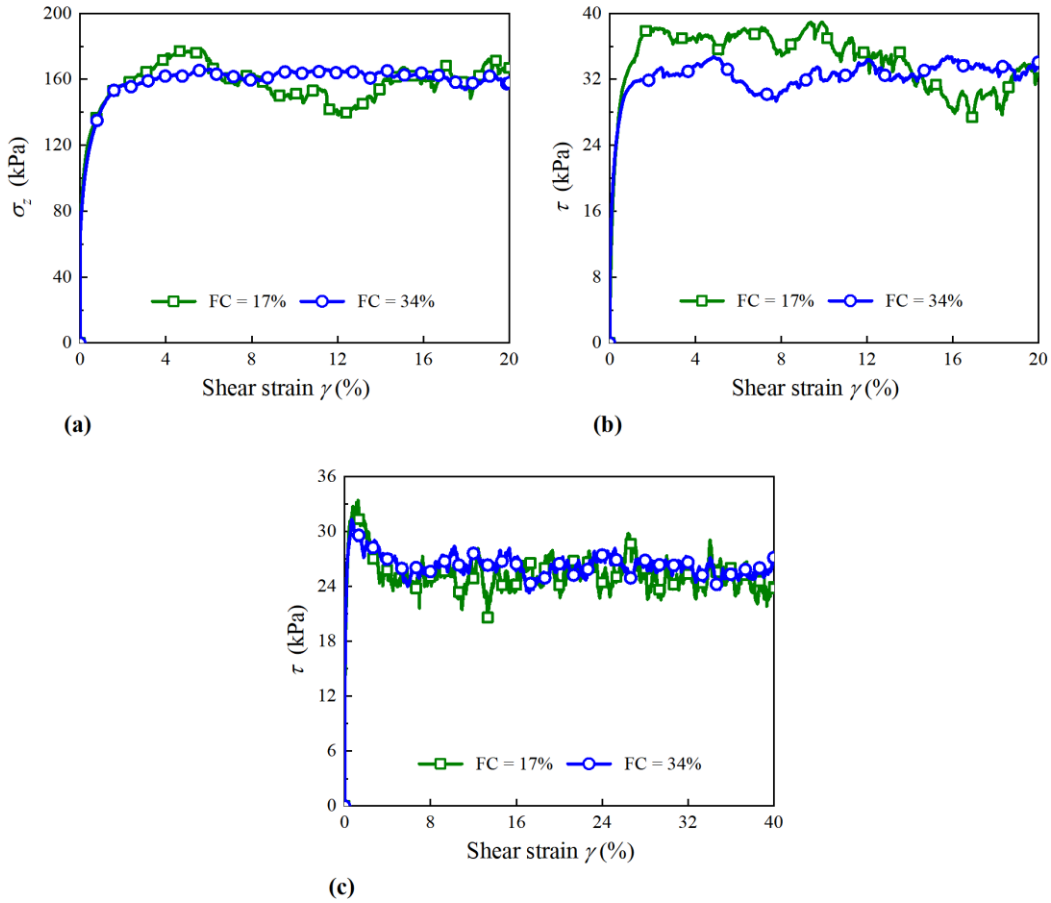

Fig 7.3 Stress-strain relationships for non-eroded specimens: (a) biaxial; (b) direct and (c) ring shear tests.

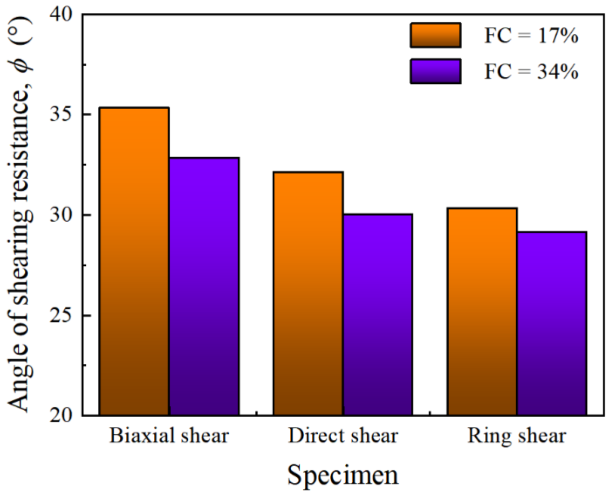

Fig 7.4 Angle of shearing resistance in the non-eroded specimens.

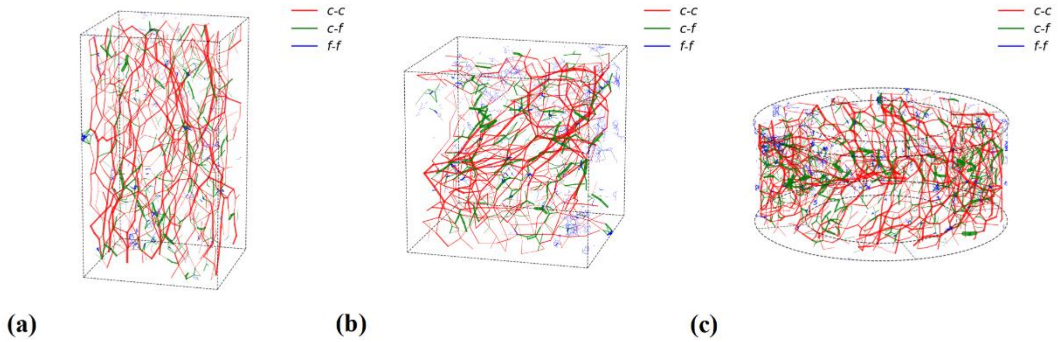

Fig 7.5 Strong force chain networks for non-eroded specimens with FC = 17%: (a) biaxial; (b) direct and (c) ring shear tests.

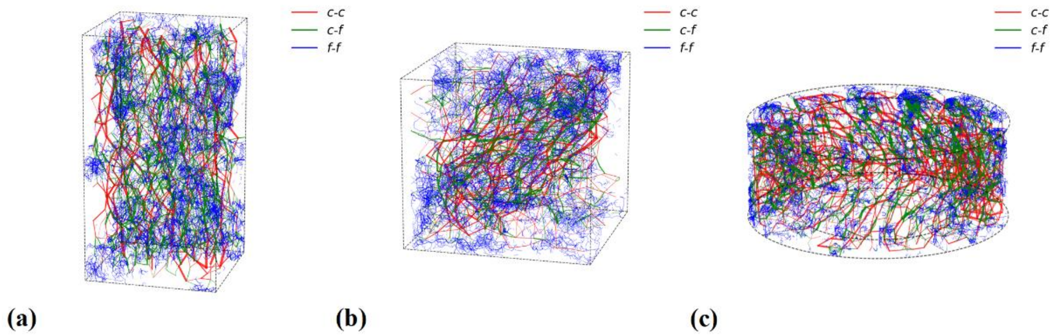

Fig 7.6 Strong force chain networks for non-eroded specimens with FC = 34%: (a) biaxial; (b) direct and (c) ring shear tests.

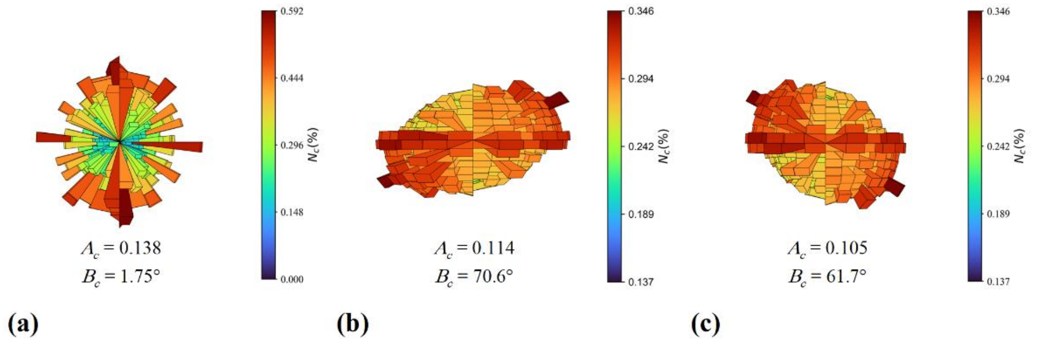

Fig 7.7 Spatial distribution of contact normal at peak strength for non-eroded specimens with FC = 17%: (a) biaxial; (b) direct and (c) ring shear tests.

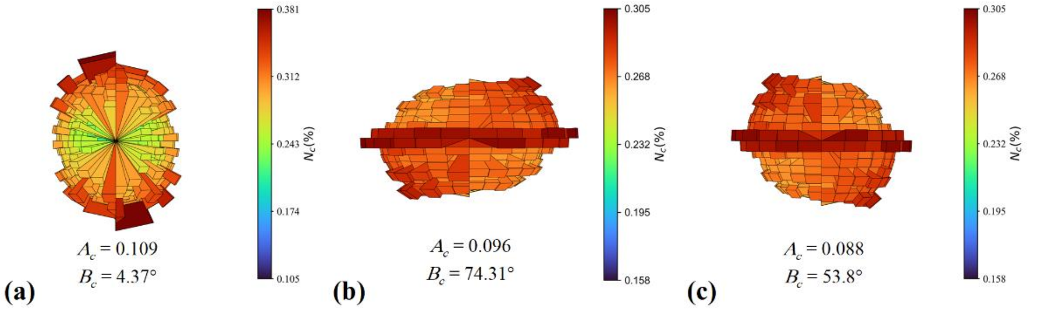

Fig 7.8 Spatial distribution of contact normal at peak strength for non-eroded specimens with FC = 34%: (a) biaxial; (b) direct and (c) ring shear tests.

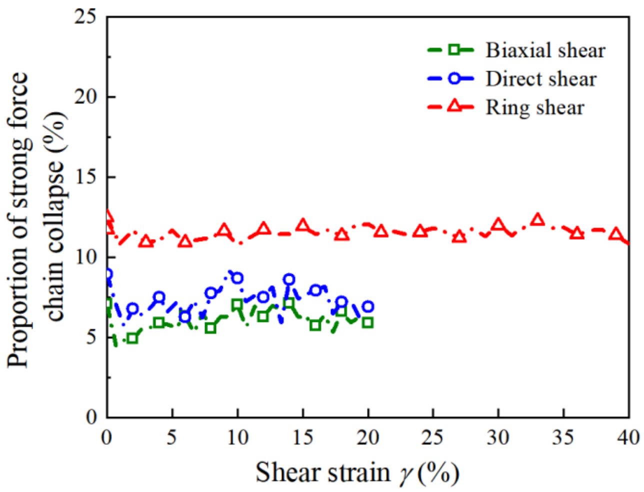

Fig 7.9 Evolution of strong force chain collapse ratio with shear strain for non-eroded specimens with FC = 17%.

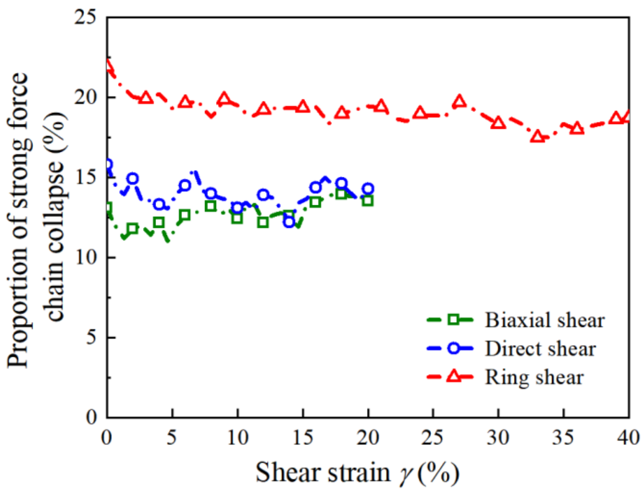

Fig 7.10 Evolution of strong force chain collapse ratio with shear strain for non-eroded specimens with FC = 34%.

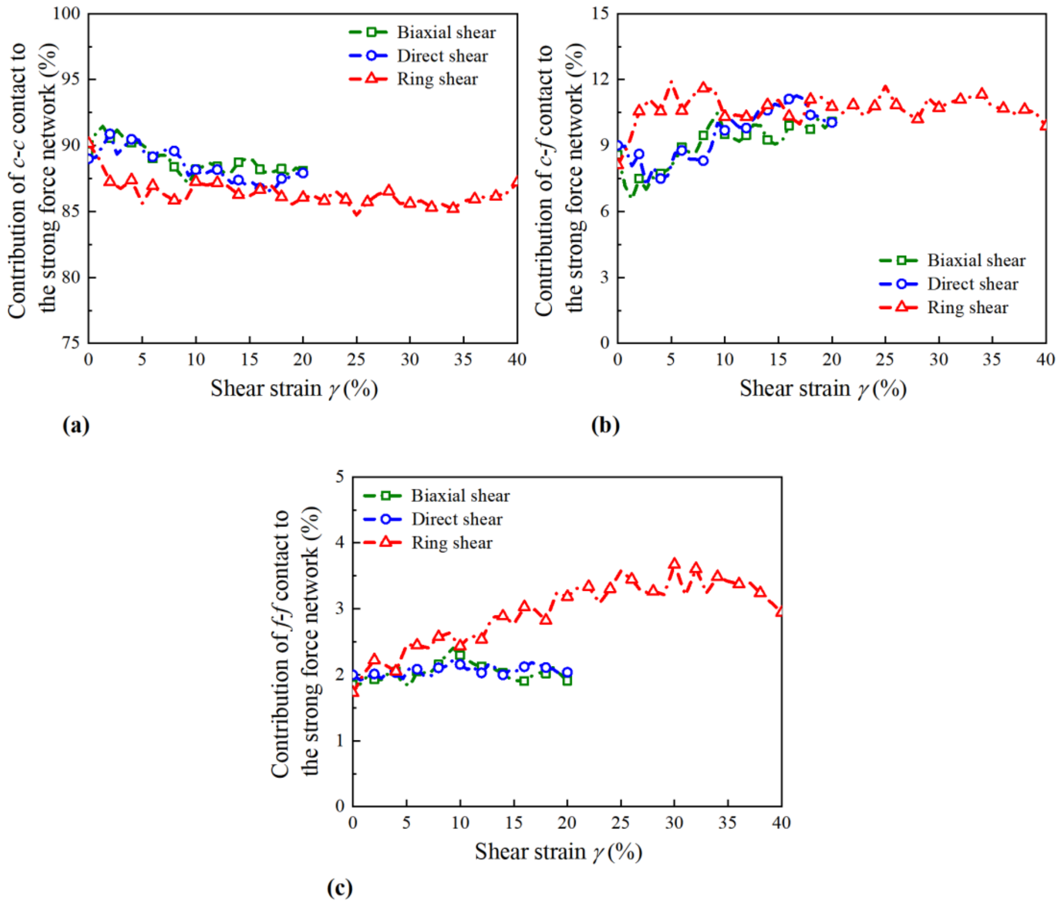

Fig 7.11 Contributions of (a) *c-c*; (b) *c-f* and (c) *f-f* contacts to the strong force chain networks in non-eroded specimens with FC = 17%.

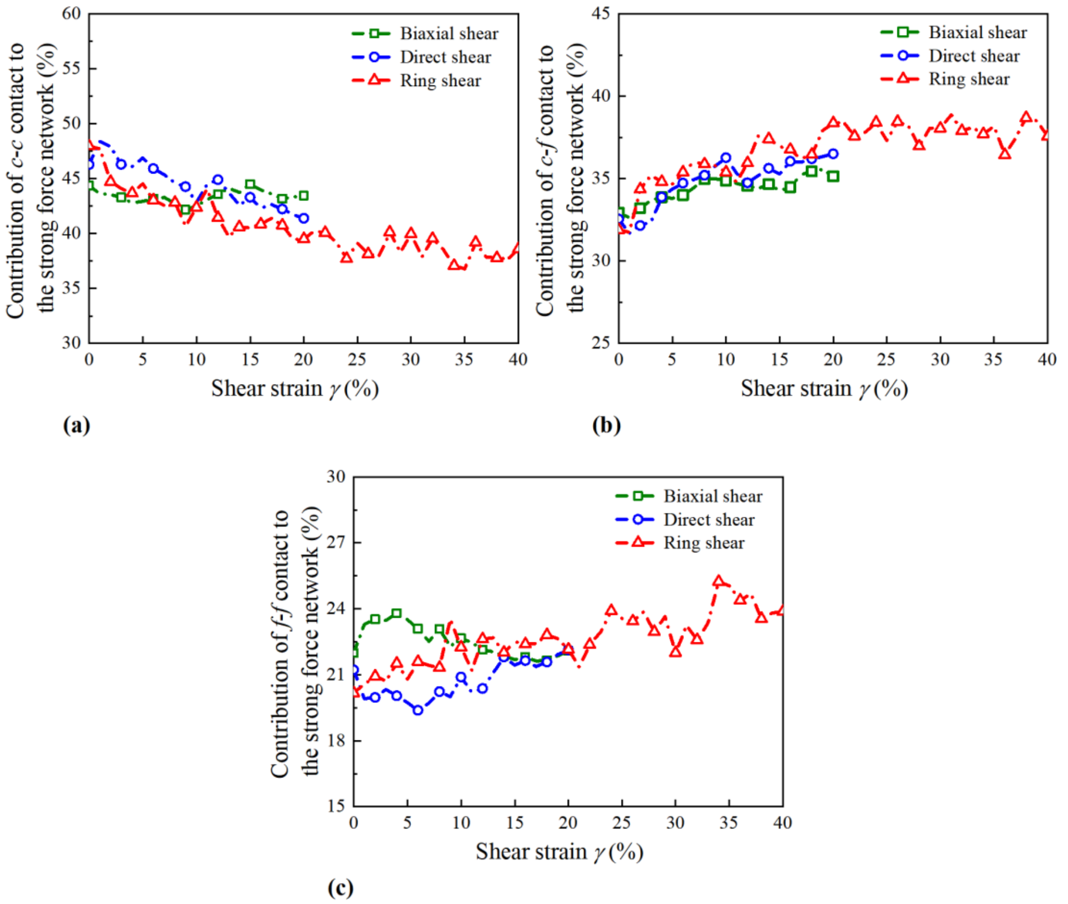

Fig 7.12 Contributions of (a) *c-c*; (b) *c-f* and (c) *f-f* contacts to the strong force chain networks in non-eroded specimens with FC = 34%.

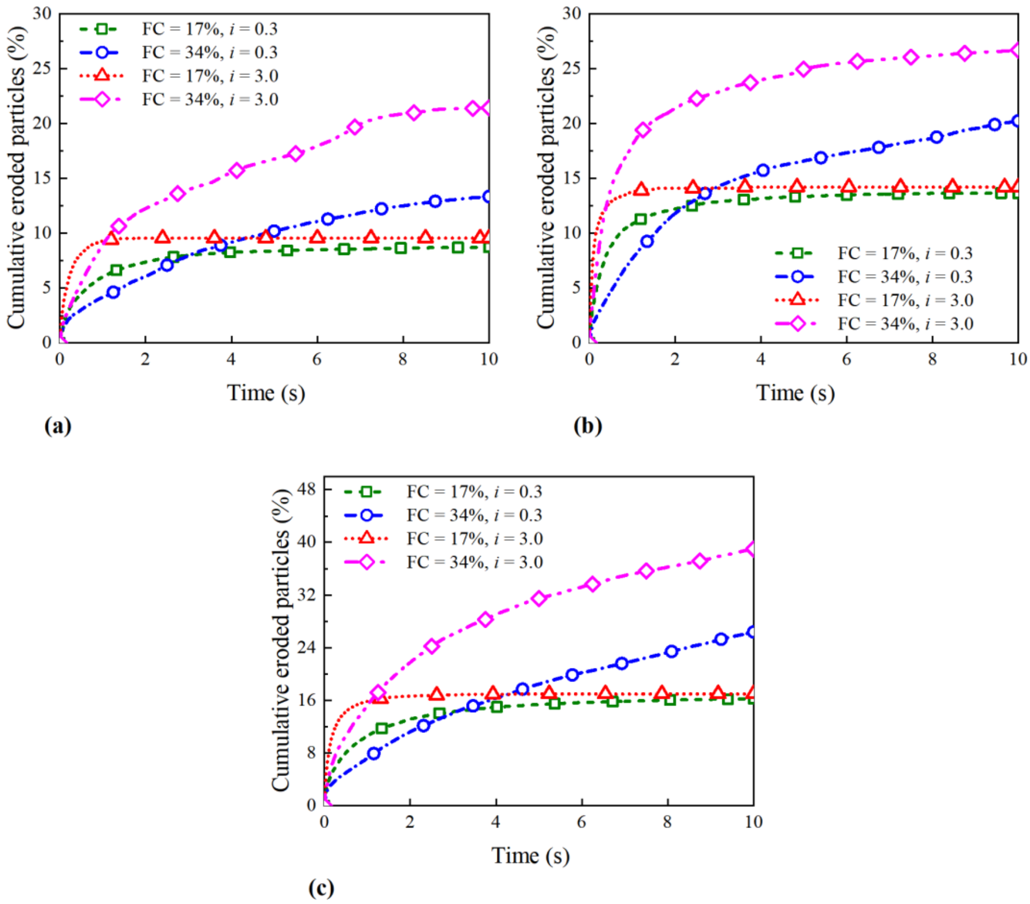

Fig 7.13 Cumulative mass of eroded fines for specimens under (a) biaxial; (b) direct and (c) ring shear tests.

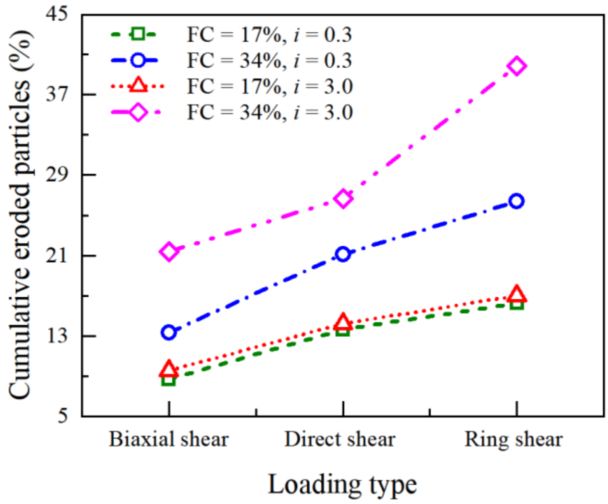

Fig 7.14 Total fine mass loss across all specimens.

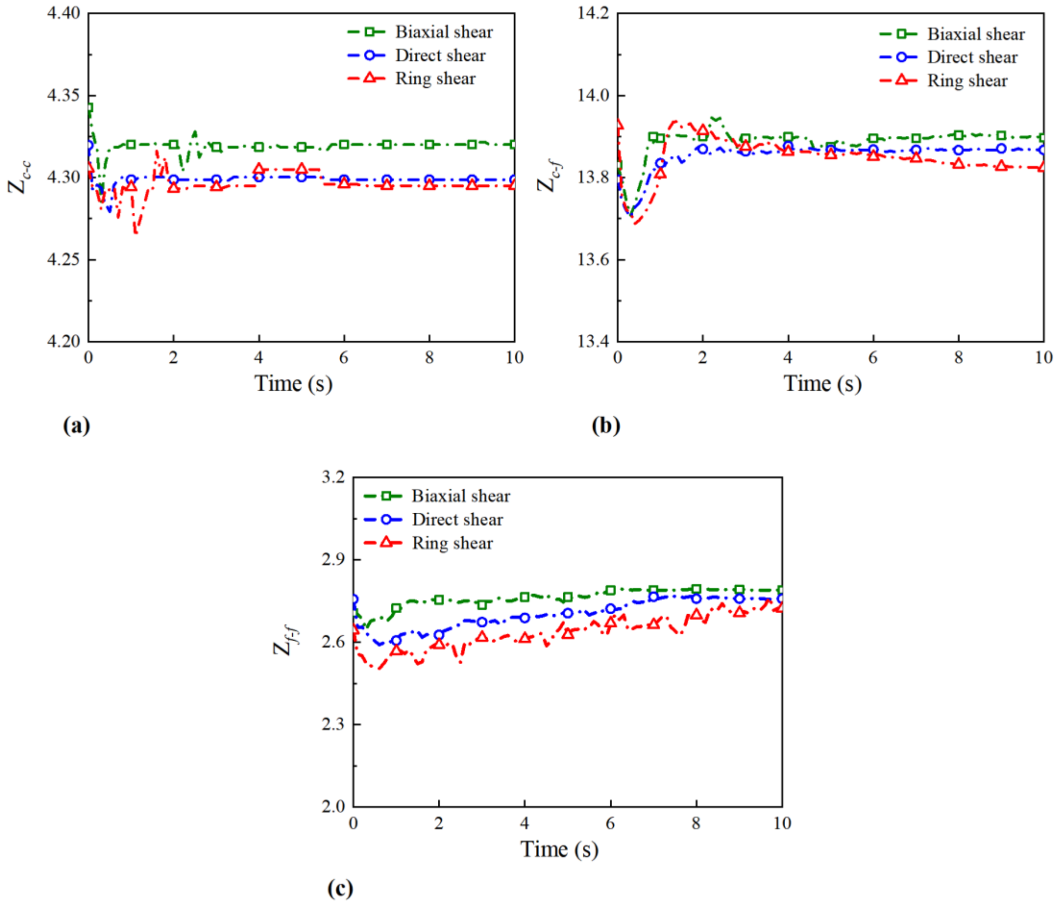

Fig 7.15 Evolution of coordination number for specimens with FC = 17% and i = 0.3 during erosion.

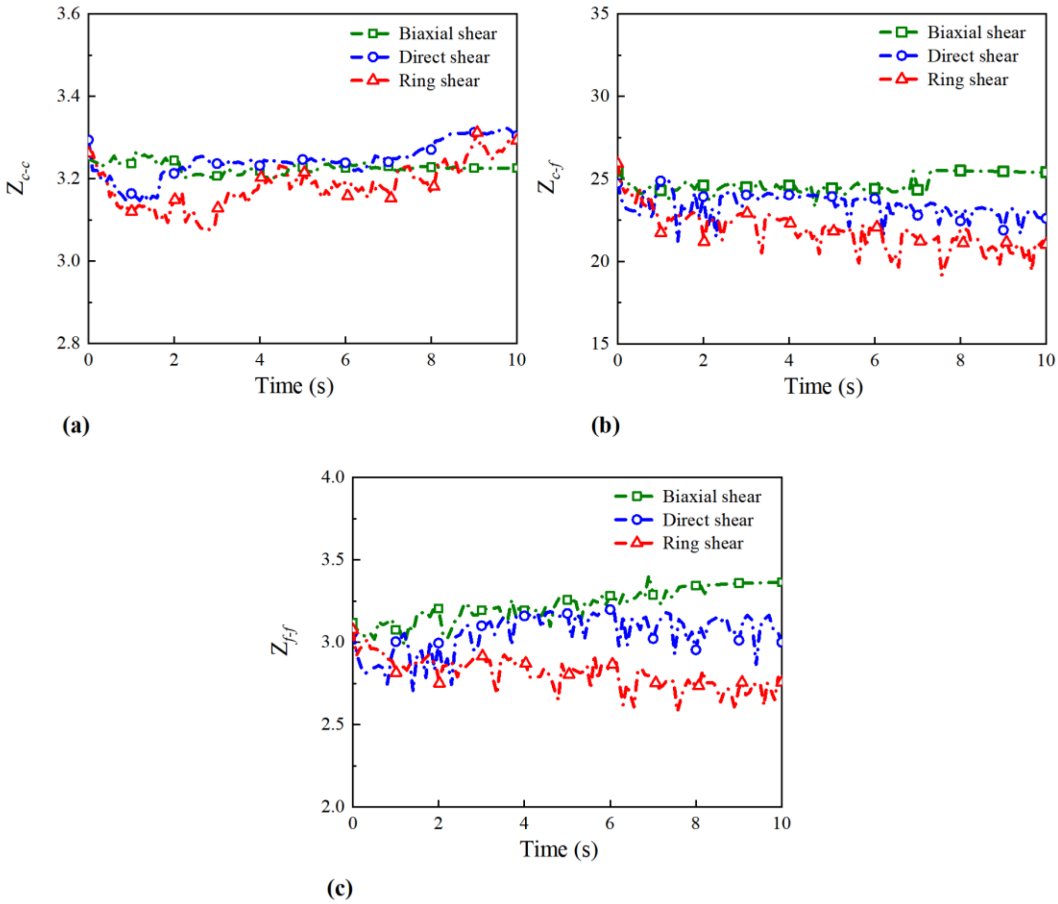

Fig 7.16 Evolution of coordination number for specimens with FC = 34% and i = 0.3 during erosion.

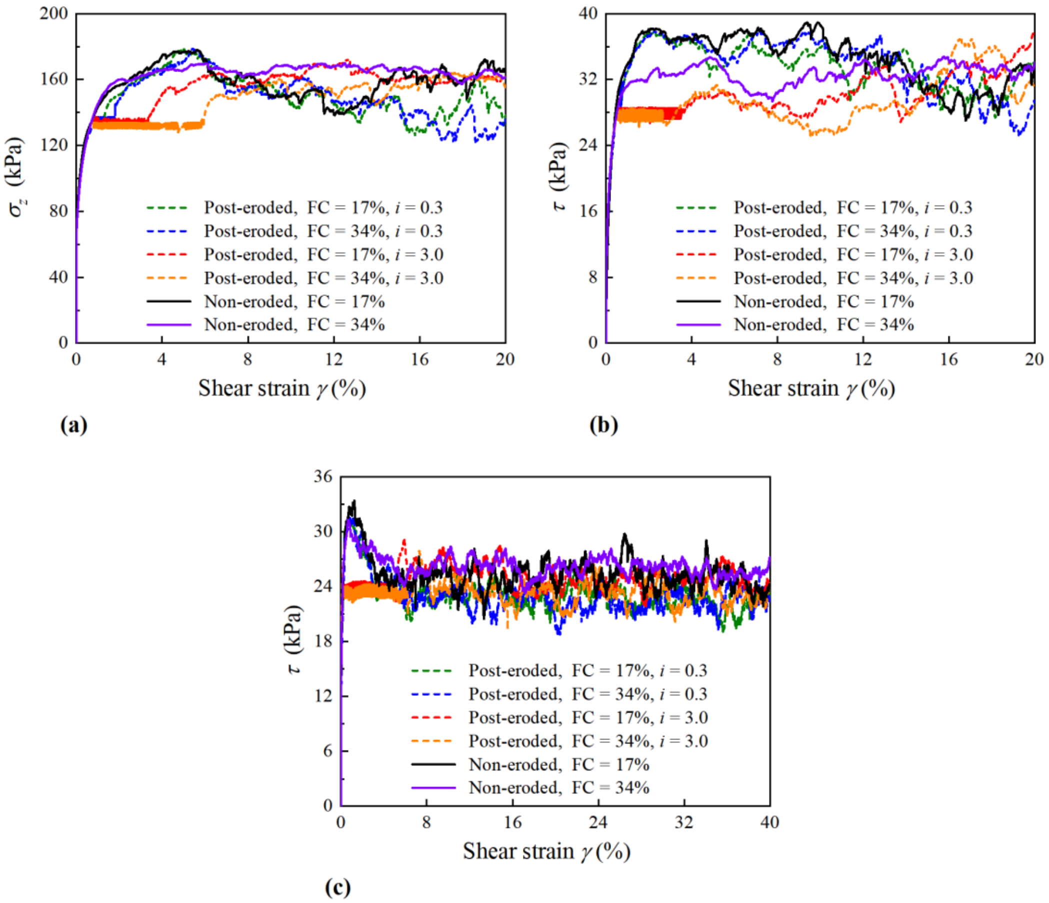

Fig 7.17 Stress-strain curves for specimens subjected to (a) biaxial; (b) direct and (c) ring shear loadings before and after erosion.

Table 7.1 Simulation program

ID	1	2	3	4	5	6	7	8	9	10	11	12
Shear mode	B	B	B	B	D	D	D	D	R	R	R	R
FC (%)	17	17	34	34	17	17	34	34	17	17	34	34
i	0.3	3.0	0.3	3.0	0.3	3.0	0.3	3.0	0.3	3.0	0.3	3.0

Note: The abbreviations B, D, and R denote biaxial, direct, and ring shear modes, respectively.

Table 7.2 DEM and CFD parameters

Parameters			Values
DEM	Elastic modulus	E_{PP} (Pa)	2.0×10^{8}
		E_{PW} (Pa)	2.0×10^{8}
	Stiffness ratio	k_{PP}	3.0
		k_{PW}	3.0
	Friction coefficient	μ_f	0.3
	Rolling friction coefficient	μ_r	0.1
	Density of particles	ρ (kg/m^3)	2650
	Time step	Δt_p (s)	1.0×10^{-7}
CFD	Fluid viscosity	μ (Pa $*$ s)	1.0×10^{-3}
	Density of fluid	ρ_f (kg/m^3)	1000
	Time step	Δt_f (s)	1.0×10^{-5}

CHAPTER 8: CONCLUSIONS AND RECOMMENDATIONS

8.1 Introduction

This thesis presents a computational investigation of internal erosion in gap-graded granular soils using a coupled CFD–DEM approach under different shear loading conditions, including hollow cylinder torsional, biaxial, direct, and ring shear conditions. The framework effectively captures particle migration, pore structure evolution, and force chain reorganization, highlighting the two-way interaction between seepage flow and soil microstructure. Each shear loading condition offers complementary advantages for exploring specific mechanisms: hollow cylinder torsional shear examines the effects of principal stress rotation on erosion; biaxial shear captures plane-strain responses; direct shear focuses on pre-existing shear planes; and ring shear allows large-displacement behaviour analysis.

The influences of stress state, intermediate stress ratio, fines content, hydraulic gradient, and confining pressure are systematically considered, providing insight into both erosion progression and post-eroded mechanical response. Furthermore, this thesis extends the comparative study to evaluate the effect of shear loading conditions on the mechanical behavior and internal erosion susceptibility of gap-graded granular soils. By examining the differences among biaxial, direct, and ring shear tests, this study reveals how boundary constraints, force chain development, and particle mobility influence peak strength, internal erosion, and the ability of the material to recover mechanically after fines loss.

The results clarify the mechanisms controlling internal erosion and post-eroded mechanical behaviour, providing a predictive, engineering-relevant framework for assessing geotechnical stability under coupled hydraulic and mechanical loads. The key findings and potential directions for future research are summarized in the following sections.

8.2 Major conclusions

8.2.1 Effect of stress state on internal erosion under different shear loading conditions

In the internal erosion simulations under biaxial shear, direct shear, and ring shear loading conditions, several stress states were selected to systematically investigate the influence of stress state on particle migration and pore structure evolution. These stress states are characterized by varying levels of mobilized shear stress relative to the peak or residual strength.

In general, fines mass loss intensifies as the stress state approaches the peak stress. From a microstructural perspective, different initial stress states correspond to distinct contact fabric characteristics. As the specimen undergoes progressive loading toward peak stress, contact and force-chain anisotropy increase, and the internal structure becomes more directionally oriented, resulting in a more interconnected pore network. Such structural evolution enhances the hydraulic conductivity and facilitates the free migration and discharge of fine particles under seepage forces. Moreover, the growth of stress state is consistently accompanied by localized contact buckling and structural collapse within the granular assembly. These internal rearrangements release fines that were previously integrated into the load-bearing framework, making them more susceptible to erosion and transport by seepage flow.

Despite this general trend, deviations arise under different shear loading conditions. For example, in direct shear tests, fines loss initially exhibits a reduction during the early stages of shearing, while in ring shear, the increase in fines migration at low stress states is relatively limited. In contrast, biaxial shear tends to show a nearly monotonic increase in fines loss as the stress state approaches the peak. These discrepancies stem from the combined influence of anisotropy magnitude and the orientation of its principal direction. When the principal direction of contact anisotropy deviates significantly from the seepage flow direction, the connectivity of the pore network along the seepage path is diminished, which not only restricts fines migration and increases the likelihood of clogging, but also reduces the overall hydraulic conductivity of the specimen, thereby further limiting the progression of internal erosion. In direct shear and ring shear tests, the orientation of contact anisotropy undergoes significant rotation toward a direction nearly perpendicular to the seepage flow direction, while in biaxial shear, this angle remains relatively small. In addition, during erosion, biaxial shear specimens typically experience an increase in anisotropy magnitude during the initial erosion stage followed by only a minor reduction after clogging and structural adjustments, especially for the specimens under high stress states. In contrast, direct and ring shear conditions exhibit a more pronounced decline in anisotropy after erosion, indicating a sustained structural resistance to seepage forces.

8.2.2 Effect of internal erosion on the mechanical behaviour of post-eroded gap-graded granular soils

Across all shear loading conditions, post-eroded specimens, particularly fine-dominated ones subjected to high stress states during erosion, exhibit lower peak strengths than non-eroded specimens. Pre-existing microstructural damage impedes the formation of robust force chains, leading to abrupt strain softening and steeper post-peak stress drops, reflecting a weakened granular skeleton with reduced load-bearing capacity.

Compared to biaxial shear and direct shear, ring shear offers a clear advantage in studying residual stress because it allows continuous large-displacement shearing after erosion. The result indicated that post-eroded specimens show lower residual stresses, with stress fluctuations characterized by higher peak-to-peak amplitudes but lower frequency, indicating less frequent but more intense intermittent slips. Loss of fine particles shifts the load-bearing function more toward coarse-related contacts and reduces microscale adjustments, indicating progressive internal degradation and a higher risk of abrupt structural instability.

Direct shear provides insight into shear band formation due to its "predetermined" shear plane. Internal erosion modifies shear bands more prominently at higher stress ratios β. In coarse-dominated soils, the contact network remains largely intact, whereas in fine-dominated soils, extensive fines mass loss shifts the load-bearing framework toward coarse skeletons, requiring larger shear strains to re-establish stable force chains. Consequently, post-eroded fine-dominated specimens develop wider, more diffuse shear bands, while coarse-dominated ones, especially those at low β during erosion, maintain relatively narrow, well-defined bands.

Post-eroded specimens exhibit larger-amplitude, low-frequency stress fluctuations, reflecting intermittent slips due to coarse-dominated force chain failure. This behavior can serve as a precursor to large-scale instability. Monitoring systems (e.g., piezometers) could be enhanced to detect not only displacement rate but also irregular pulsing patterns, signaling progressive internal degradation before catastrophic failure.

8.2.3 Effect of shear loading conditions on mechanical response and internal erosion

The choice of shear loading condition strongly influences both the mechanical response of the soil and its susceptibility to internal erosion. Biaxial shear specimens consistently exhibit the highest peak strengths. Strong lateral confinement maintains continuous coarse particle force chains throughout the whole specimens and limits the migration of fine particle during erosion. Direct shear specimens show intermediate behavior. Deformation localizes within a shear band, which preserves some coarse particle networks. Ring shear specimens are subject to weak confinement and continuous large-displacement shearing. They are the most vulnerable, with frequent force chain disruption, lower peak strengths, and higher cumulative fines loss. This implies that using only biaxial may underestimate field-scale erosion risks, particularly in structures experiencing rotational shearing (e.g., circular landslides). Risk assessments should consider results from multiple test types to better capture real-world vulnerability.

Microstructural analysis reveals that strong force chain networks vary significantly among the shear modes. Biaxial shear test maintains a well-connected, axially aligned network, direct shear test localizes force chains within the shear band, and ring shear produces fragmented and discontinuous networks. These differences in network connectivity and constraint govern both stress-strain behavior and the evolution of the pore structure under seepage flow. Moreover, the interaction between fines content and shear mode influences the rate and evolution of erosion. Fine particles can act as structural stabilizers in specimens with high fines content, but their mobility is more sensitive to the degree of particle constraint imposed by the shear mode. Overall, shear loading conditions play a fundamental role in shaping the mechanical behavior, force chain architecture, and internal erosion progression in gap-graded granular soils.

8.2.4 Effect of key factors on internal erosion and subsequent mechanical behaviour

Key factors influencing internal erosion were examined under different shear loading conditions. HCTST-based simulations revealed that specimens with larger principal stress rotation (α) and intermediate principal stress ratio (b) develop distinct pore structures with reduced vertical connectivity. These structural differences direct fine particles along different migration paths, producing variations in fines mass loss and particle redistribution across layers.

Fines content and hydraulic gradient strongly affect both erosion and subsequent shearing. High hydraulic gradients cause rapid detachment of fines and early clogging. Low hydraulic gradients lead to slower erosion and delayed structural collapse. In fine-dominated specimens, this gradual process can trigger localized instabilities and particle rearrangement, increasing the risk of sudden fines loss during the later erosion stage. In addition, fines content also plays an important role in shear banding after erosion.

Higher confining pressures consistently mitigate fines loss by strengthening particle interlocking and increasing average contact forces, which resist detachment and preserve the granular framework. Overall, these factors jointly influence the evolution of pore networks, force chains, and structural stability, highlighting their critical role in determining both the extent of internal erosion and the mechanical behaviour of post-eroded specimens under different loading conditions.

8.3 Future work

This research offers detailed insights into internal erosion and its influence on the behaviour of gap-graded granular soils after erosion under various shear loading conditions using CFD–DEM simulations. While the key objectives have been achieved, some critical aspects remain unexplored. To further enhance the understanding and practical applications, several promising research directions are proposed and discussed below:

(1) This thesis highlights the important role of stress anisotropy in pore structure evolution and internal erosion. However, in real geotechnical systems, such as foundations under wave loading and slopes under seismic excitation, the principal stress axes usually undergo cyclic rotation. This dynamic stress path can induce progressive fabric rearrangement and pore collapse, further accelerating particle migration. Extending the current HCTST-based CFD-DEM framework based on (Yang 2013) to simulate cyclic principal stress rotation would allow investigation of how fluctuating stress rotation affect force chain stability, void redistribution, and erosion susceptibility. Unlike monotonic loading considered in this thesis, cyclic rotation may prevent stable clogging or trigger cumulative fines mobilization. This direction builds on the stress-state-dependent erosion mechanisms identified in this work and is essential for assessing long-term durability of infrastructure under dynamic loading.

(2) This study assumes rigid particles, but particle breakage commonly occurs in coarse-grained soils under high stress. Crushing can alter the grain size distribution, increase fines content, and modify pore connectivity, all of which influence erosion behaviour. For example, fragments generated from breakage may clog pore channels and reduce permeability, potentially suppressing further erosion. Future work should

integrate particle breakage into the CFD-DEM framework by adopting crushable agglomerates or probabilistic fracture criteria. This would enable the modeling of dynamically evolving particle size distributions under seepage-induced erosion. The approach is especially relevant for coarse-dominated soils under elevated confining pressures. Linking particle breakage to hydraulic and mechanical responses will improve the model's realism and predictive accuracy for natural soils subjected to coupled seepage and stress conditions.

(3) While this study has provided valuable insights into erosion under various shear loading conditions at the particle scale, practical geotechnical problems such as embankment piping or foundation instability require continuum-level analysis. A future direction is the development of a multi-scale framework that bridges micromechanical insights from CFD–DEM simulations with finite element (FE) modeling. Key microscale observations, such as erosion-induced softening, reduction of residual strength, and the evolution of fabric anisotropy, can be used to formulate erosion-damage constitutive models. These models can be calibrated using DEM simulation data and subsequently implemented in FE codes to simulate large-scale boundary value problems under realistic hydraulic and stress conditions.

REFERENCES

Al-Douri, R.H.,Poulos, H.G., 1992. Static and cyclic direct shear tests on carbonate sands. Geotech Test J 15 (2), 138-157.

Alshibli, K.,Hasan, A., 2008. Spatial variation of void ratio and shear band thickness in sand using X-ray computed tomography. GEOTECHNIQUE 58 (4), 249-257.

Alshibli, K.A., Batiste, S.N.,Sture, S., 2003. Strain localization in sand: plane strain versus triaxial compression. J Geotech Geoenviron Eng 129 (6), 483-494.

Arand, F.,Hesser, J., 2017. Accurate and efficient maximal ball algorithm for pore network extraction. Computers & Geosciences 101, 28-37.

Babu, G.S.,Srivastava, A. Analytical Solutions for Granular Filters. *In* Proceedings of Indian Geotechnical Conference. 2014.

Barla, G., Barla, M.,Martinotti, M.E., 2010. Development of a new direct shear testing apparatus. Rock Mech Rock Eng 43 (1), 117-122.

Barnett, J.T., 2001. Zero-Crossings of Random Processes with Application to Estimation and Detection. *In* Nonuniform Sampling: Theory and Practice. *Edited by* F. Marvasti. Springer US, Boston, MA. pp. 393-437.

BEEK, V.V., Bezuijen, A.,Sellmeijer, H., 2013. Backward erosion piping. Erosion in geomechanics applied to dams and levees, 193-269.

Benahmed, N.,Bonelli, S., 2012. Investigating concentrated leak erosion behaviour of cohesive soils by performing hole erosion tests. European Journal of Environmental and Civil Engineering 16 (1), 43-58.

Bendahmane, F., Marot, D.,Alexis, A., 2008. Experimental parametric study of suffusion and backward erosion. J Geotech Geoenviron Eng 134 (1), 57-67.

Bishop, A.W., Green, G., Garga, V.K., Andresen, A.,Brown, J., 1971. A new ring shear apparatus and its application to the measurement of residual strength. GEOTECHNIQUE 21 (4), 273-328.

Bonelli, S., FELL, R.,BENAHMED, N., 2013. Concentrated leak erosion. Erosion in geomechanics applied to dams and levees, 271-341.

Bridle, R., 2017. Internal Erosion Mechanics and Risk Estimation Based on ICOLD Bulletin 164. *In* Geo-Risk 2017. pp. 137-146.

Brosse, A.M., 2012. Study of the anisotropy of three British mudrocks using a hollow cylinder apparatus. PhD Thesis. Imperial College London.

Brown, A.J.,Gosden, J.D., 2008. Defra research into Internal Erosion. *In* Ensuring reservoir safety into the future: Proceedings of the 15th Conference of the British Dam Society at the University of Warwick from 10–13 September 2008. *Edited by* H. Hewlett. Emerald Publishing Limited. p. 0.

Cai, Y., Yu, H.-S., Wanatowski, D.,Li, X., 2013. Noncoaxial behavior of sand under various stress paths. Journal of Geotechnical and Geoenvironmental

Engineering 139 (8), 1381-1395.

Chang, D.,Zhang, L., 2011. A stress-controlled erosion apparatus for studying internal erosion in soils. Geotech Test J 34 (6), 579-589.

Chang, D.S.,Zhang, L.M., 2013. Critical Hydraulic Gradients of Internal Erosion under Complex Stress States. J Geotech Geoenviron Eng 139 (9), 1454-1467.

Chen, C., Zhang, L.M.,Chang, D.S., 2016. Stress-Strain Behavior of Granular Soils Subjected to Internal Erosion. J Geotech Geoenviron Eng 142 (12).

Cheng, K., Zhu, J., Qian, F., Cao, B., Lu, J.,Han, Y., 2023. CFD–DEM simulation of particle deposition characteristics of pleated air filter media based on porous media model. PARTICUOLOGY 72, 37-48.

Cividini, A., Bonomi, S., Vignati, G.C.,Gioda, G., 2009. Seepage-induced erosion in granular soil and consequent settlements. Int J Geomech 9 (4), 187-194.

Cui, L.,O'Sullivan, C., 2006. Exploring the macro- and micro-scale response of an idealised granular material in the direct shear apparatus. GEOTECHNIQUE 56 (7), 455-468.

Cundall, P.A.,Strack, O.D., 1979. A discrete numerical model for granular assemblies. GEOTECHNIQUE 29 (1), 47-65.

Di Felice, R., 1994. The voidage function for fluid-particle interaction systems. Int J Multiphase Flow 20 (1), 153-159.

Dong, H.,Blunt, M.J., 2009. Pore-network extraction from micro-computerized-tomography images. Physical Review E—Statistical, Nonlinear, and Soft Matter Physics 80 (3), 036307.

Dong, Z., Su, L., Zhang, C., Liu, Z.,Xiao, S., 2020. Transition of shear flow for granular materials in a numerical ring shear test. Granular Matter 23 (1).

Duan, Y., Zhang, W., Liu, H.,Chen, J., 2024. Dynamics of soil erosion due to underground pipeline fractures: A transparent soil study under varied hydraulic conditions. Journal of Computational Methods in Science and Engineering 24 (4-5), 2429-2445.

Esmaeili, A., George, D., Masters, I.,Hossain, M., 2023. Biaxial experimental characterizations of soft polymers: A review. Polymer Testing 128, 108246.

Fannin, R.,Moffat, R., 2006. Observations on internal stability of cohesionless soils. GEOTECHNIQUE 56 (7), 497-500.

Fannin, R.,Slangen, P., 2014. On the distinct phenomena of suffusion and suffosion. GEOTECH LETT 4 (4), 289-294.

Farhang, B.,Mirghasemi, A.A., 2017. A study of principle stress rotation on granular soils using DEM simulation of hollow cylinder test. Adv Powder Technol 28 (9), 2052-2064.

Fell, R.,Fry, J.-J., 2007. The state of the art of assessing the likelihood of internal erosion of embankment dams, water retaining structures and their foundations. Internal erosion of dams and their foundations, 9-32.

Feng, S.-X., Chai, J.-R., Xu, Z.-G., Qin, Y.,Li, Y.-L., 2020. Test study on the suffusion process of sand-rock mixtures by NMR systems. Geotech Test J 43 (5), 1286-1299.

Foster, M.,Fell, R., 2001. Assessing embankment dam filters that do not satisfy design criteria. J Geotech Geoenviron Eng 127 (5), 398-407.

Foster, M., Fell, R.,Spannagle, M., 2000. The statistics of embankment dam failures and accidents. CAN GEOTECH J 37 (5), 1000-1024.

Gan, J., Fredlund, D.,Rahardjo, H., 1988. Determination of the shear strength parameters of an unsaturated soil using the direct shear test. CAN GEOTECH J 25 (3), 500-510.

Ge, Y., Zhou, A., Nazem, M.,Deng, Y., 2024. Numerical simulation of cone penetration test by using CFD–DEM coupled analysis. Acta Geotech 19 (11), 7635-7653.

Gibo, S., Egashira, K.,Ohtsubo, M., 1987. Residual strength of smectite-dominated soils from the Kamenose landslide in Japan. CAN GEOTECH J 24 (3), 456-462.

Gu, D., Li, B., Shao, Q., Li, C.,Xie, Z., 2025. Development of a New Laboratory Method for Water Erosion Tests Based on Transparent Soil Technique. Hydrological Processes 39 (5), e70138.

Gu, X., Huang, M.,Qian, J., 2014. Discrete element modeling of shear band in granular materials. Theor Appl Fract Mech 72, 37-49.

Guo, Y., Yang, Y.,Yu, X., 2018. Influence of particle shape on the erodibility of non-cohesive soil: Insights from coupled CFD–DEM simulations. PARTICUOLOGY 39, 12-24.

Gutierrez, M., Ishihara, K.,Towhata, I., 1991. Flow theory for sand during rotation of principal stress direction. Soils and foundations 31 (4), 121-132.

Han, C.,Drescher, A., 1993. Shear bands in biaxial tests on dry coarse sand. Soils Found 33 (1), 118-132.

Han, Y.,Cundall, P.A., 2013. LBM–DEM modeling of fluid–solid interaction in porous media. Int J Numer Anal Methods Geomech 37 (10), 1391-1407.

Hanna, A.,Ayadat, T., 2019. Comparative study of shear strength characteristics of dry cohesionless sands from triaxial, plane-strain and direct shear tests. GEOMECH GEOENGIN 16 (2), 150-162.

Hight, D., Gens, A.,Symes, M., 1983. The development of a new hollow cylinder apparatus for investigating the effects of principal stress rotation in soils. Geotechnique 33 (4), 355-383.

Hu, G., Zhou, B., Yang, B., Wang, H.,Liu, Z., 2023. An insight into the interaction between fluid and granular soil based on a resolved CFD-DEM method. Comput Geotech 163, 105722.

Hu, Z., Zhang, Y.,Yang, Z., 2019. Suffusion-induced deformation and microstructural change of granular soils: a coupled CFD–DEM study. Acta Geotech 14 (3), 795-814.

Hu, Z., Zhang, Y.,Yang, Z., 2020. Suffusion-induced evolution of mechanical and microstructural properties of gap-graded soils using CFD-DEM. J Geotech Geoenviron Eng 146 (5), 04020024.

Hu, Z., Li, J.Z., Zhang, Y.D., Yang, Z.X.,Liu, J.K., 2022. A CFD–DEM study on the suffusion and shear behaviors of gap-graded soils under stress anisotropy. Acta Geotech.

Huang, Z.-y., Yang, Z.-x.,Wang, Z.-y., 2008. Discrete element modeling of sand behavior in a biaxial shear test. J ZHEJIANG UNIV-SC A 9 (9), 1176-1183.

Irons, T., Quinn, M.C., Li, Y.,McKenna, J.R., 2014. A numerical assessment of the use of surface nuclear magnetic resonance to monitor internal erosion and piping in earthen embankments. Near Surface Geophysics 12 (2), 325-334.

Iwashita, K.,Oda, M., 2000. Micro-deformation mechanism of shear banding process based on modified distinct element method. Powder Technol 109 (1-3), 192-205.

Jasak, H., Jemcov, A.,Tukovic, Z. OpenFOAM: A C++ library for complex physics simulations. *In* International workshop on coupled methods in numerical dynamics. 2007. pp. 1-20.

Ke, L.,Takahashi, A., 2014. Triaxial erosion test for evaluation of mechanical consequences of internal erosion. Geotech Test J 37 (2), 347-364.

Ke, L.,Takahashi, A., 2015. Drained monotonic responses of suffusional cohesionless soils. J Geotech Geoenviron Eng 141 (8), 04015033.

Kenney, T.,Lau, D., 1986. Internal stability of granular filters: Reply. CAN GEOTECH J 23 (3), 420-423.

Kim, D.H., Kim, S.,Gratchev, I. Unsaturated seepage behavior study using soil column test. *In* 18SEAGC/1AGSSEA. 2013. Research Publishing.

Kim, I.-H., Lee, H.-j.,Chung, C.-K. Assessment of the suffusion sensitivity of Earth-Fill Dam soils in korea through seepage tests. *In* The 29th International Ocean and Polar Engineering Conference. 2019. OnePetro.

Kodicherla, S.P.K., Gong, G., Yang, Z.X., Krabbenhoft, K., Fan, L., Moy, C.K.S.,Wilkinson, S., 2019. The influence of particle elongations on direct shear behaviour of granular materials using DEM. Granular Matter 21 (4).

Kozicki, J., Niedostatkiewicz, M., Tejchman, J.,Muhlhaus, H.B., 2013. Discrete modelling results of a direct shear test for granular materials versus FE results. Granular Matter 15 (5), 607-627.

Kumruzzaman, M.,Yin, J.-H., 2010. Influences of principal stress direction and intermediate principal stress on the stress–strain–strength behaviour of completely decomposed granite. Canadian Geotechnical Journal 47 (2), 164-179.

Kuruneru, S.T.W., Marechal, E., Deligant, M., Khelladi, S., Ravelet, F., Saha, S.C., Sauret, E.,Gu, Y., 2019. A comparative study of mixed resolved–unresolved

CFD-DEM and unresolved CFD-DEM methods for the solution of particle-laden liquid flows. Arch Comput Methods Eng 26 (4), 1239-1254.

Kuwano, R., Santa Spitia, L.F., Bedja, M.,Otsubo, M., 2021. Change in mechanical behaviour of gap-graded soil subjected to internal erosion observed in triaxial compression and torsional shear. Geomech Energy Environ 27.

Labuz, J., Dai, S.-T.,Papamichos, E. Plane-strain compression of rock-like materials. *In* International journal of rock mechanics and mining sciences & geomechanics abstracts. 1996. Elsevier. pp. 573-584.

Li, B., Guo, L.,Zhang, F.-s., 2014. Macro-micro investigation of granular materials in torsional shear test. J CENT SOUTH UNIV 21 (7), 2950-2961.

Li, B., Zhang, F.,Gutierrez, M., 2015. A numerical examination of the hollow cylindrical torsional shear test using DEM. Acta Geotechnica 10 (4), 449-467.

Li, B., Chen, L.,Gutierrez, M., 2017. Influence of the intermediate principal stress and principal stress direction on the mechanical behavior of cohesionless soils using the discrete element method. Comput Geotech 86, 52-66.

Li, M.,Fannin, R., 2012. A theoretical envelope for internal instability of cohesionless soil. GEOTECHNIQUE 62 (1), 77-80.

Li, X.,Yu, H.-S., 2009. Influence of loading direction on the behavior of anisotropic granular materials. Int J Eng Sci 47 (11-12), 1284-1296.

Liang, D., Zhao, X.,Soga, K., 2020. Simulation of overtopping and seepage induced dike failure using two-point MPM. Soils Found 60 (4), 978-988.

Liang, Y., Zhang, B., Yang, Y., Zhang, H.,Dai, L., 2023. Experimental investigation on erosion progression and strength reduction of gap-graded cohesionless soil subjected to suffusion. Environ Earth Sci 82 (7).

Liang, Y., Yeh, T.-C.J., Wang, J., Liu, M., Zha, Y.,Hao, Y., 2019. Onset of suffusion in upward seepage under isotropic and anisotropic stress conditions. European Journal of Environmental and Civil Engineering 23 (12), 1520-1534.

Liu, J.,Iskander, M.G., 2010. Modelling capacity of transparent soil. CAN GEOTECH J 47 (4), 451-460.

Liu, P., Sun, M., Chen, Z., Zhang, S., Zhang, F.-S., Chen, Y., Chen, W.,Bate, B., 2023a. Influencing factors on fines deposition in porous media by CFD–DEM simulation. Acta Geotech 18 (9), 4539-4563.

Liu, S.H., 2006. Simulating a direct shear box test by DEM. CAN GEOTECH J 43 (2), 155-168.

Liu, S.H., Sun, D.a.,Matsuoka, H., 2005. On the interface friction in direct shear test. Comput Geotech 32 (5), 317-325.

Liu, Y., Yin, Z.-Y.,Yang, J., 2023b. Micromechanical analysis of suffusion in gap-graded granular soils considering soil heterogeneity and non-uniform seepage flow. Comput Geotech 159, 105467.

Liu, Y., Yin, Z.-Y., Wang, L.,Hong, Y., 2021. A coupled CFD–DEM investigation of internal erosion considering suspension flow. CAN GEOTECH J 58 (9), 1411-1425.

Liu, Y., Wang, L., Yin, Z.-Y.,Hong, Y., 2022. A coupled CFD-DEM investigation into suffusion of gap-graded soil considering anisotropic stress conditions and flow directions. Acta Geotech.

Liu, Y., Wang, L., Hong, Y., Zhao, J.,Yin, Z.Y., 2020. A coupled CFD-DEM investigation of suffusion of gap graded soil: Coupling effect of confining pressure and fines content. Int J Numer Anal Methods Geomech 44 (18), 2473-2500.

Lominé, F., Scholtes, L., Sibille, L.,Poullain, P., 2013. Modeling of fluid–solid interaction in granular media with coupled lattice Boltzmann/discrete element methods: application to piping erosion. Int J Numer Anal Methods Geomech 37 (6), 577-596.

Luo, Y., Luo, B.,Xiao, M., 2019. Effect of deviator stress on the initiation of suffusion. Acta Geotech 15 (6), 1607-1617.

Lupini, J.F., 1980. The residual strength of soils. PhD Thesis. University of London.

Ma, Q., Wautier, A.,Zhou, W., 2021. Microscopic mechanism of particle detachment in granular materials subjected to suffusion in anisotropic stress states. Acta Geotech 16 (8), 2575-2591.

Ma, Z., Wang, Y., Ren, N.,Shi, W., 2019. A coupled CFD-DEM simulation of upward seepage flow in coarse sands. MAR GEORESOUR GEOTEC 37 (5), 589-598.

Mao, J., Zhao, L., Di, Y., Liu, X.,Xu, W., 2020. A resolved CFD–DEM approach for the simulation of landslides and impulse waves. Comput Methods Appl Mech Eng 359, 112750.

Marot, D., Oli, B., Bendahmane, F., Gelet, R.,Leroy, P., 2024. A hydraulic gradient and stress-controlled erosion apparatus for assessing soil internal erosion. Geotech Test J 47 (6), 1205-1228.

Minh, N.H., Cheng, Y.P.,Thornton, C., 2013. Strong force networks in granular mixtures. Granular Matter 16 (1), 69-78.

Miura, K., Miura, S.,Toki, S., 1986a. Deformation Behavior of Anisotropic Dense Sand Under Principal Stress Axes Rotation. Soils and Foundations 26 (1), 36-52.

Miura, K., Toki, S.,Miura, S., 1986b. Deformation prediction for anisotropic sand during the rotation of principal stress axes. Soils and Foundations 26 (3), 42-56.

Mohajeri, M.J., Do, H.Q.,Schott, D.L., 2020. DEM calibration of cohesive material in the ring shear test by applying a genetic algorithm framework. Adv Powder Technol 31 (5), 1838-1850.

Mu, L., Zhang, P., Shi, Z.,Huang, M., 2023. Coupled CFD–DEM investigation of erosion accompanied by clogging mechanism under different hydraulic gradients. Comput Geotech 153, 105058.

Mukherjee, M., Gupta, A.,Prashant, A., 2017. Instability Analysis of Sand under Undrained Biaxial Loading with Rigid and Flexible Boundary. Int J Geomech 17 (1), 04016042.

Ng, C., Zhan, L., Bao, C., Fredlund, D.,Gong, B.W., 2003. Performance of an unsaturated expansive soil slope subjected to artificial rainfall infiltration. GEOTECHNIQUE 53 (2), 143-157.

Nitka, M.,Grabowski, A., 2021. Shear band evolution phenomena in direct shear test modelled with DEM. Powder Technol 391, 369-384.

Oda, M.,Kazama, H., 1998. Microstructure of shear bands and its relation to the mechanisms of dilatancy and failure of dense granular soils. GEOTECHNIQUE 48 (4), 465-481.

Okada, Y., Sassa, K.,Fukuoka, H. Comparison of shear behaviour of sandy soils by ring-shear test with conventional shear tests. *In* Environmental Forest Science: Proceedings of the IUFRO Division 8 Conference Environmental Forest Science, held 19–23 October 1998, Kyoto University, Japan. 1998. Springer. pp. 623-632.

PHILIPPE, P., BEGUIN, R.,FAURE, Y.H., 2013. Contact erosion. Erosion in geomechanics applied to dams and levees, 101-191.

Pirnia, P., Duhaime, F., Ethier, Y.,Dubé, J.-S., 2020. Hierarchical multiscale numerical modelling of internal erosion with discrete and finite elements. Acta Geotech 15 (10), 2877-2889.

Potts, D., Dounias, G.,Vaughan, P., 1987. Finite element analysis of the direct shear box test. GEOTECHNIQUE 37 (1), 11-23.

Pra-ai, S.,Boulon, M., 2017. Soil–structure cyclic direct shear tests: a new interpretation of the direct shear experiment and its application to a series of cyclic tests. Acta Geotech 12 (1), 107-127.

Qian, J.-G., Zhou, C., Yin, Z.-Y.,Li, W.-Y., 2021. Investigating the effect of particle angularity on suffusion of gap-graded soil using coupled CFD-DEM. Comput Geotech 139.

Radjai, F., Wolf, D.E., Jean, M.,Moreau, J.-J., 1998. Bimodal character of stress transmission in granular packings. Phys Rev Lett 80 (1), 61.

Ramsdell, J.V.,Hinos, W.T., 1971. Concentration fluctuations and peak-to-mean concentration ratios in plumes from a ground-level continuous point source. Atmospheric Environment (1967) 5 (7), 483-495.

Saada, A.S., 1988. State-of-the-art paper: Hollow cylinder torsional devices: Their advantages and limitations. *In* Advanced triaxial testing of soil and rock. ASTM International.

Sassa, K., Fukuoka, H., Wang, G.,Ishikawa, N., 2004. Undrained dynamic-loading ring-shear apparatus and its application to landslide dynamics. Landslides 1 (1), 7-19.

Scarpelli, G.,Wood, D.M. Experimental observations of shear patterns in direct shear tests. *In* IUTAM Deformation and Failure of Granular Materials Conference.

1982. pp. 473-483.

Shi, C., Yang, J., Chu, W., Tang, H.,Zhang, Y., 2021. Macro- and Micromechanical Behaviors and Energy Variation of Sandstone under Different Unloading Stress Paths with DEM. Int J Geomech 21 (8).

Silin, D.,Patzek, T., 2006. Pore space morphology analysis using maximal inscribed spheres. Physica A: Statistical Mechanics and its Applications 371 (2), 336-360.

Silin, D.B., Jin, G.,Patzek, T.W. Robust determination of the pore space morphology in sedimentary rocks. *In* SPE Annual Technical Conference and Exhibition? 2003. SPE. pp. SPE-84296-MS.

Simons, T.A.H., Weiler, R., Strege, S., Bensmann, S., Schilling, M.,Kwade, A., 2015. A Ring Shear Tester as Calibration Experiment for DEM Simulations in Agitated Mixers – A Sensitivity Study. Procedia Engineering 102, 741-748.

Skempton, A., 1964. Long-term stability of clay slopes. GEOTECHNIQUE 14 (2), 77-102.

Song, S., Wang, P., Yin, Z.,Cheng, Y.P., 2024a. Micromechanical modeling of hollow cylinder torsional shear test on sand using discrete element method. Journal of Rock Mechanics and Geotechnical Engineering.

Song, S.X., Yin, Z.Y., Liu, Y.J., Wang, P.,Cheng, Y.P., 2024b. Investigation of Suffusion Under Torsional Shear Conditions With CFD-DEM. Int J Numer Anal Methods Geomech 48 (17), 4274-4290.

Stark, T.D.,Eid, H.T., 1994. Drained residual strength of cohesive soils. Journal of Geotechnical Engineering 120 (5), 856-871.

Sui, W.,Zheng, G., 2018. An experimental investigation on slope stability under drawdown conditions using transparent soils. Bulletin of Engineering Geology and the Environment 77 (3), 977-985.

Symes, M., Gens, A.,Hight, D., 1984. Undrained anisotropy and principal stress rotation in saturated sand. Geotechnique 34 (1), 11-27.

Tatsuoka, F., Masuda, T., Siddiquee, M.,Koseki, J., 2003. Modeling the stress-strain relations of sand in cyclic plane strain loading. J Geotech Geoenviron Eng 129 (5), 450-467.

Tordesillas, A., 2007. Force chain buckling, unjamming transitions and shear banding in dense granular assemblies. Philos Mag 87 (32), 4987-5016.

Toyota, H., Nakamura, K., Sugimoto, M.,Sakai, N., 2009. Ring shear tests to evaluate strength parameters in various remoulded soils. GEOTECHNIQUE 59 (8), 649-659.

USBR, U.S.B.o.R. Report to US Department of the Interior and State of Idaho on Failure of Teton Dam. *In* 1976. The Panel.

Vandenboer, K., van Beek, V.,Bezuijen, A., 2014. 3D finite element method (FEM) simulation of groundwater flow during backward erosion piping. Frontiers of Structural and Civil Engineering 8 (2), 160-166.

Wang, G., Deng, Z., Yang, J., Chen, X.,Jin, W., 2022a. A large-scale high-pressure erosion apparatus for studying internal erosion in gravelly soils under horizontal seepage flow. Geotech Test J 45 (6), 1037-1053.

Wang, J., Dove, J.E.,Gutierrez, M.S., 2007. Discrete-continuum analysis of shear banding in the direct shear test. GEOTECHNIQUE 57 (6), 513-526.

Wang, J., Liu, X., Liu, S., Zhu, Y., Pan, W.,Zhou, J., 2019. Physical model test of transparent soil on coupling effect of cut-off wall and pumping wells during foundation pit dewatering. Acta Geotech 14 (1), 141-162.

Wang, P., Yin, Z.-Y.,Wang, Z.-Y., 2022b. Micromechanical Investigation of Particle-Size Effect of Granular Materials in Biaxial Test with the Role of Particle Breakage. J Eng Mech 148 (1).

Wang, P., Ge, Y., Wang, T., Liu, Q.-w.,Song, S.-x., 2023. CFD-DEM modelling of suffusion in multi-layer soils with different fines contents and impermeable zones. J ZHEJIANG UNIV-SC A 24 (1), 6-19.

Wang, T., Wang, P., Yin, Z.-y., Laouafa, F.,Hicher, P.-Y., 2024a. Hydro-mechanical analysis of particle migration in fractures with CFD-DEM. Eng Geol 335, 107557.

Wang, Y., Yang, Y., Yang, H.,Pang, Z., 2024b. Numerical simulation of fluid-particle interaction in geomechanics using an extended CFD-DEM approach with a super-quadric model of non-spherical particles. Int J Numer Anal Methods Geomech 48 (1), 78-103.

Wang, Z.-Y., Wang, P., Yin, Z.-Y.,Wang, R., 2022c. Micromechanical investigation of the particle size effect on the shear strength of uncrushable granular materials. Acta Geotechnica, 1-20.

Wautier, A., Bonelli, S.,Nicot, F., 2019. DEM investigations of internal erosion: Grain transport in the light of micromechanics. Int J Numer Anal Methods Geomech 43 (1), 339-352.

Xie, L., Zhu, Q., Ge, Y.,Qin, Y., 2023. Instability simulation of the submerged anti-dip slope based on the CFD-DEM coupling method. Frontiers in Earth Science 10, 1013909.

Xiong, H., Guo, L., Cai, Y.,Yang, Z., 2016. Experimental study of drained anisotropy of granular soils involving rotation of principal stress direction. European Journal of Environmental and Civil Engineering 20 (4), 431-454.

Xiong, H., Yin, Z.-Y., Zhao, J.,Yang, Y., 2020. Investigating the effect of flow direction on suffusion and its impacts on gap-graded granular soils. Acta Geotech 16 (2), 399-419.

Xiong, H., Wu, H., Bao, X.,Fei, J., 2021. Investigating effect of particle shape on suffusion by CFD-DEM modeling. Constr Build Mater 289.

Xiong, H., Zhang, Z., Sun, X., Yin, Z.-y.,Chen, X., 2022. Clogging effect of fines in seepage erosion by using CFD–DEM. Comput Geotech 152, 105013.

Xiong, Q., Madadi-Kandjani, E.,Lorenzini, G., 2014. A LBM–DEM solver for fast discrete particle simulation of particle–fluid flows. Continuum Mechanics and

Thermodynamics 26 (6), 907-917.

Xu, W.-J., Xu, Q.,Hu, R.-L., 2011. Study on the shear strength of soil–rock mixture by large scale direct shear test. International Journal of Rock Mechanics and Mining Sciences 48 (8), 1235-1247.

Xu, W.-J., Li, C.-Q.,Zhang, H.-Y., 2015. DEM analyses of the mechanical behavior of soil and soil-rock mixture via the 3D direct shear test. Geomech Eng 9 (6), 815-827.

Yang, L.-T., Li, X., Yu, H.-S.,Wanatowski, D., 2016. A laboratory study of anisotropic geomaterials incorporating recent micromechanical understanding. Acta Geotechnica 11 (5), 1111-1129.

Yang, L., 2013. Experimental study of soil anisotropy using hollow cylinder testing. PhD Thesis. University of Nottingham Nottingham.

Yang, L.T., Li, X., Yu, H.S.,Wanatowski, D., 2015. A laboratory study of anisotropic geomaterials incorporating recent micromechanical understanding. Acta Geotech 11 (5), 1111-1129.

Yerro, A., Rohe, A.,Soga, K., 2017. Modelling internal erosion with the material point method. Procedia engineering 175, 365-372.

Yin, K., Fauchille, A.-L., Di Filippo, E., Kotronis, P.,Sciarra, G., 2021a. A review of sand–clay mixture and soil–structure interface direct shear test. Geotechnics 1 (2), 260-306.

Yin, Y., Cui, Y., Tang, Y., Liu, D., Lei, M.,Chan, D., 2021b. Solid–fluid sequentially coupled simulation of internal erosion of soils due to seepage. Granular Matter 23 (2), 20.

Yousefpour, N.,Mojtahedi, F.F., 2024. Early detection of internal erosion in earth dams: combining seismic monitoring and convolutional AutoEncoders. Georisk: Assessment and Management of Risk for Engineered Systems and Geohazards 18 (3), 570-590.

Yura, H.T.,Hanson, S.G., 2010. Mean level signal crossing rate for an arbitrary stochastic process. J Opt Soc Am A 27 (4), 797-807.

Zhang, C.,Lou, Y., 2024. Influences of the evolving plastic behavior of sheet metal on V-bending and springback analysis considering different stress states. International Journal of Plasticity 173, 103889.

Zhang, J., Wang, X., Yin, Z.-Y.,Liang, Z., 2020a. DEM modeling of large-scale triaxial test of rock clasts considering realistic particle shapes and flexible membrane boundary. Eng Geol.

Zhang, J., Wang, X., Yin, Z.-Y.,Liang, Z., 2020b. DEM modeling of large-scale triaxial test of rock clasts considering realistic particle shapes and flexible membrane boundary. Engineering Geology 279, 105871.

Zhao, J.,Shan, T., 2013. Coupled CFD–DEM simulation of fluid–particle interaction in geomechanics. Powder Technol 239, 248-258.

Zhao, P., Liu, S.,Wu, K., 2024. Study on macro and micro shear strength of continuously graded and gap-graded sand. PARTICUOLOGY 86, 101-116.

Zhou, C., Qian, J.G.,Yin, Z.Y., 2022a. Microscopic investigation of the influence of complex stress states on internal erosion and its impacts on critical hydraulic gradients. Int J Numer Anal Methods Geomech 46 (18), 3377-3401.

Zhou, H.-t., Liu, C.-q., Wang, G.-h., Kang, K.,Liu, Y.-h., 2022b. Study on Drilling Ground Collapse Induced by Groundwater Flow and Prevention Based on a Coupled CFD-DEM Method. KSCE J Civ Eng 26 (5), 2112-2125.

Zhou, H., Wang, G., Jia, C.,Li, C., 2019a. A Novel, Coupled CFD-DEM Model for the Flow Characteristics of Particles Inside a Pipe. Water 11 (11).

Zhou, W.-H., Jing, X.-Y., Yin, Z.-Y.,Geng, X., 2019b. Effects of particle sphericity and initial fabric on the shearing behavior of soil–rough structural interface. Acta Geotech 14 (6), 1699-1716.

Zhou, W., Ma, Q., Ma, G., Cao, X.,Cheng, Y., 2020. Microscopic investigation of internal erosion in binary mixtures via the coupled LBM-DEM method. Powder Technol 376, 31-41.

Zhu, H.-X.,Yin, Z.-Y., 2019. Grain Rotation-Based Analysis Method for Shear Band. J Eng Mech 145 (10).

Zhuang, L., Nakata, Y., Kim, U.-G.,Kim, D., 2013. Influence of relative density, particle shape, and stress path on the plane strain compression behavior of granular materials. Acta Geotech 9 (2), 241-255.

Zou, Y., Chen, C.,Zhang, L., 2020. Simulating progression of internal erosion in gap-graded sandy gravels using coupled CFD-DEM. Int J Geomech 20 (1), 04019135.